

Reactivity of Carbenes with Lewis Acids: A Matrix Isolation Study

Dissertation

To obtain the degree of
Doctor of natural science (Dr. rer. nat.)

by

Akshay Hemant Raut

from Pune, India

**RUHR
UNIVERSITÄT
BOCHUM**

RUB

Bochum 2019

Dedicated to my family.

This work was carried out from September 2015 to February 2019 at the Department of Organic Chemistry II of the Ruhr-Universität Bochum under the supervision of Prof. Dr. Wolfram Sander. Part of the work reported in this thesis was performed during Graduate School of Solvation Science internship under the supervision of Prof. Dr. Jeehiun K. Lee (Department of Chemistry and Chemical Biology, Rutgers, The State University of New Jersey, USA).

First Referee: Prof. Dr. W. Sander

Second Referee: Prof. Dr. P. Nürnberger

Day of submission: 09.05.2019

Publications

A. H. Raut, P. Costa, W. Sander, Reactions of Arylcarbenes with Lewis Acids, *Chem. Eur. J.* **2018**, *24*, 18043-18051.

E. Mendez-Vega, M. Maehara, **A. H. Raut**, J. Mieres-Perez, M. Tsuge, Y. -P. Lee, W. Sander, Activation of Molecular Hydrogen by Arylcarbenes. *Chem. Eur. J.* **2018**, *24*, 18801-18808.

A. H. Raut, P. Costa, W. Sander, Isolation of Dihydrodibenzotropylium Cation in Water Matrix (in preparation).

A. H. Raut, J. Mieres-Perez, G. Richter, W. Sander, Halogen Bonding of Singlet Carbenes (in preparation).

Scientific Meetings

Workshop Graduate School Solvation Science (GSS), Area A, 22.-24.02.2016, Sportschloss Velen, Germany (Poster).

Chemistry and Physics at Low Temperatures, 03.-08.07.2016, Biarritz, France (Poster).

Graduate School of Solvation Science Autumn Workshop, 05.10.2016, Technische Universität Dortmund (Poster).

International Symposium on Reactive Intermediates and Unusual Molecules, 18.-22.06.2017, Sorrento, Italy (Poster).

Symposium of JungChemikerForum (JCF) Ruhr, 12.10.2017, Max-Planck-Institut für Kohlenforschung, Mülheim an der Ruhr, Germany (Oral presentation).

Workshop Graduate School Solvation Science (GSS), Area A, 19.-21.03.2018, Sportschloss Velen, Germany (Poster).

Workshop Graduate School Solvation Science (GSS), Area A, 18.-20.03.2019, Klosterhof, Harsewinkel, Germany (Poster).

International Internship

From 09/2018 to 11/2018 in the group of Prof. Dr. Jeehiun K. Lee at the Department of Chemistry and Chemical Biology, Rutgers, The State University of New Jersey, USA.

“It is our choices that show what we truly are, far more than our abilities.”

J. K. Rowling, Harry Potter and the Chamber of Secrets

Contents

Summary	1
1. General Introduction	9
1.1. Carbene Chemistry.....	9
1.2. Carbocations	16
1.3. Lewis Acids	19
1.4. Matrix Isolation.....	22
1.5. Mass Spectrometry.....	25
2. Reactions of Arylcarbenes with Lewis Acids	29
2.1. Introduction.....	29
2.2. Results and Discussion	31
2.2.1. Computations of S-T gaps of Arylcarbenes.....	31
2.2.2. Reaction of Dibenzocycloheptadienylidene with H ₂ O.....	32
2.2.3. Reaction of Fluorenylidene and Dibenzocycloheptadienylidene with ICF ₃	40
2.2.4. Reaction of Fluorenylidene and Dibenzocycloheptadienylidene with BF ₃	54
2.3. Conclusions.....	70
3. Isolation of Dihydrodibenzotropylium Cation in LDA Water Ice	75
3.1. Introduction.....	75
3.2. Results and Discussion	77
3.2.1. Reaction of Dibenzocycloheptadienylidene with LDA water ice.....	77
3.2.2. Photochemistry of Dihydrodibenzotropylium Cation	83
3.3. Conclusion	86
4. Hydrogenation of Dibenzocycloheptadienylidene	89
4.1. Introduction.....	89
4.2. Results and Discussion	91
4.2.1. Reaction of Dibenzocycloheptadienylidene in Hydrogen Doped Argon Matrices.	91
4.2.2. Reaction of Dibenzocycloheptadienylidene in Solid H ₂ and D ₂ Matrices.	94
4.3. Conclusions.....	99

5. Hydrogen and Halogen Bonding of Singlet Carbenes	101
5.1. Introduction	101
5.2. Results and Discussion	103
5.2.1. Reaction of 1,3-di- <i>tert</i> -butyl-imidazole-2-ylidene with H ₂ O	103
5.2.2. Reactions of Phenylchlorocarbene and 1,3-di- <i>tert</i> -butyl-imidazole-2-ylidene with ICF ₃	110
5.3. Conclusions	122
6. Ammonia Activation by 1,8-diazafluorenylidene	125
6.1. Introduction	125
6.2. Results and Discussion	126
6.2.1. Matrix Isolation Spectroscopic Characterization of 1,8-diazafluorenylidene	126
6.2.2. Reaction of 1,8-diazafluorenylidene with Ammonia	130
Conclusions	143
7. Proton Affinity Bracketing of 2,7-dinitrofluorenylidene	145
7.1. Introduction	145
7.2. Results and Discussion	148
7.2.1. Reaction with <i>N,N,N',N'</i> -tetramethyl-1,3-propanediamine	148
7.2.2. Reaction of with <i>N,N,N',N'</i> -tetramethylethylenediamine	152
7.2.3. Reaction with Tributylamine	154
7.2.4. Reaction with <i>N,N</i> -dimethylcyclohexylamine and <i>N</i> -methylpiperidine	157
7.3. Conclusions	161
Experimental Section	163
Materials	163
Synthesis	163
Matrix Isolation	168
Calculations	169
References	171
Acknowledgements	179
Appendix	181

Summary

A detailed analysis of reactivity of four different arylcarbenes and an *N*-heterocyclic carbene (Chart I) was carried out using matrix isolation IR, UV-Vis and EPR spectroscopy and quantum chemical calculations were performed at B3LYP-D3/def2-TZVP level of theory.

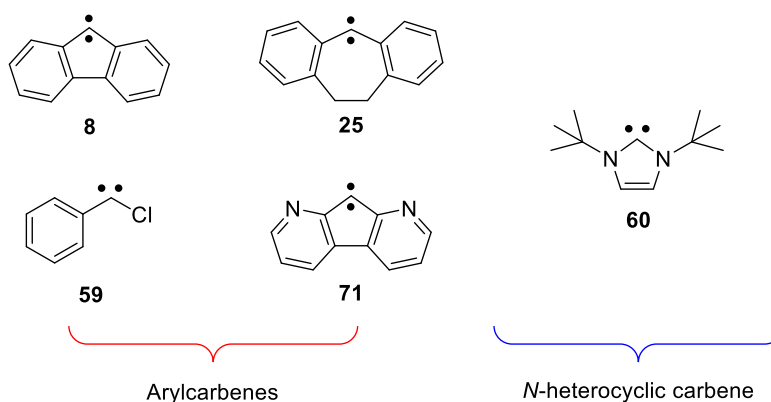
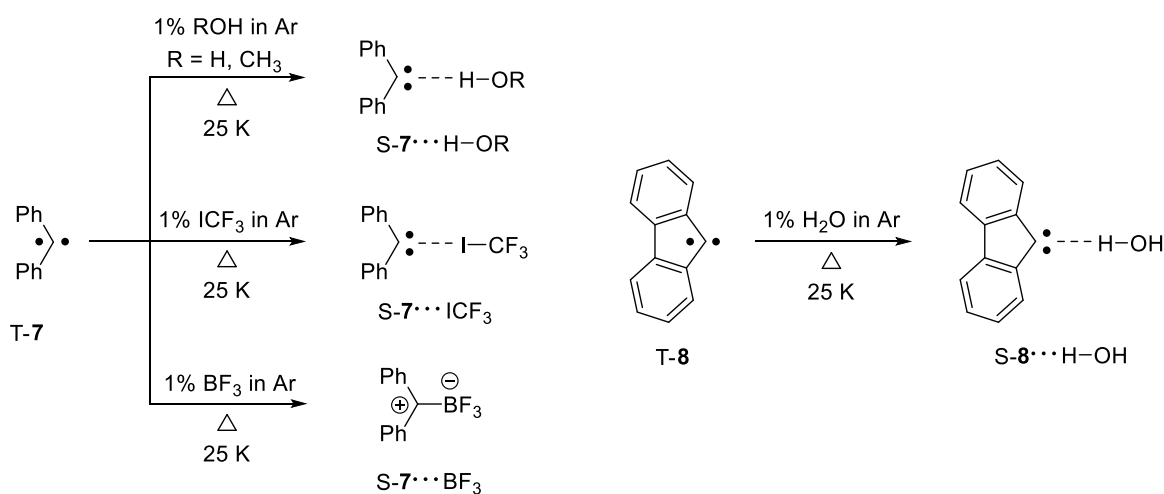


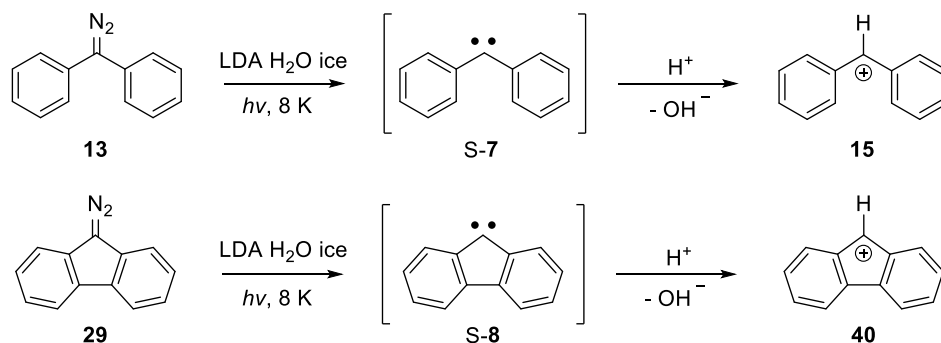
Chart I. Representative structures of four arylcarbenes and *N*-heterocyclic carbene investigated in present study.

Diphenylcarbene **7**, fluorenylidene **8** and dibenzocycloheptadienylidene **25** are archetypical triplet ground state arylcarbenes that differ significantly in their geometries and electronic structures. Previous investigations of **7** with H₂O, ICF₃ and BF₃, and **8** with H₂O under matrix isolation conditions demonstrated the formation of corresponding closed-shell singlet state complexes, switching the spin states of carbenes from triplet to singlet by interactions with Lewis acids (Scheme I).^[1-4] To gain more insight into the reactivity of arylcarbenes towards Lewis acids, the reactions of **8** with ICF₃ and BF₃, and **25** with H₂O, ICF₃ and BF₃ were studied under similar conditions.



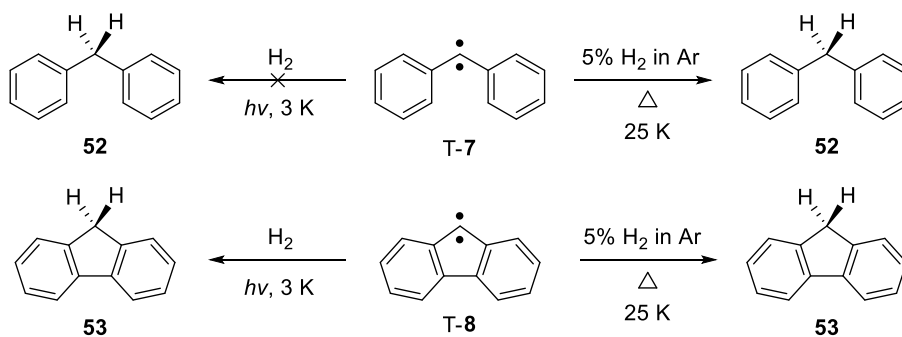
Scheme I. Previously investigated reactions of **7** with H₂O, ICF₃ and BF₃, and **8** with H₂O.^[1-4]

Low density amorphous (LDA) water ice is a highly polar medium and previous studies of **7** and **8** in LDA ice environments have shown the rapid protonation of S-**7** and S-**8** even at 8 K to yield the corresponding **15** and **40** cations upon photolysis of the respective diazo precursors (Scheme II).^[1, 4] To understand the behavior of **25** with H₂O in polar medium compared to argon, the reaction of **25** was investigated in LDA water ice.



Scheme II. Previously investigated reactions of **7** and **8** with LDA water ice.^[1, 4]

In contrast to highly polar singlet states of arylcarbenes **7** and **8**, apolar triplet states interact weakly with Lewis acids. Recent studies on hydrogenation reactions of **7** and **8** (Scheme III) have revealed the reactions of their triplet states via quantum mechanical tunneling (QMT).^[5] Carbene **25** exhibits similar scaffold as that of **7** and **8**, but possess larger singlet-triplet gap and intermediate conformational flexibility. To gain more insight into the balance of these effects on reactivity of carbenes, the reaction of **25** with molecular hydrogen was carried out.

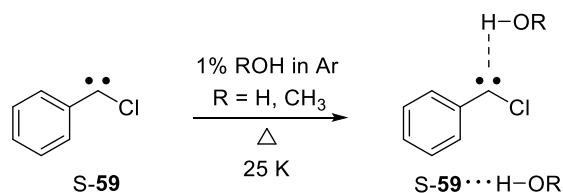


Scheme III. Recent studies on hydrogenation reactions of **7** and **8**.^[5]

1,8-diazafluorenylidene **71** is a triplet ground state arylcarbene which is speculated to exhibit highly electrophilic singlet state where two non-bonding electrons occupy the π -orbital rather than the σ -orbital.^[6] Reagents bearing lone pairs such as NH₃ can interact with the vacant σ -orbital of the upper lying singlet state of the carbene to form ylide as one of the possible products. Carbene

71 can also react from its triplet ground state by abstracting hydrogen from ammonia, since H–H and N–H bond dissociation energies are comparable.^[7] Thus, the reaction of **71** with ammonia was investigated to understand the unusual chemical behavior of **71**.

Unlike triplet ground state carbenes, the singlet ground state carbenes can directly interact with hydrogen or halogen bond donors without a constraint of singlet-triplet gap, for example, singlet phenylchlorocarbene **S-59** is reported to form strong hydrogen-bonded complexes with H₂O and MeOH (Scheme IV).^[8]



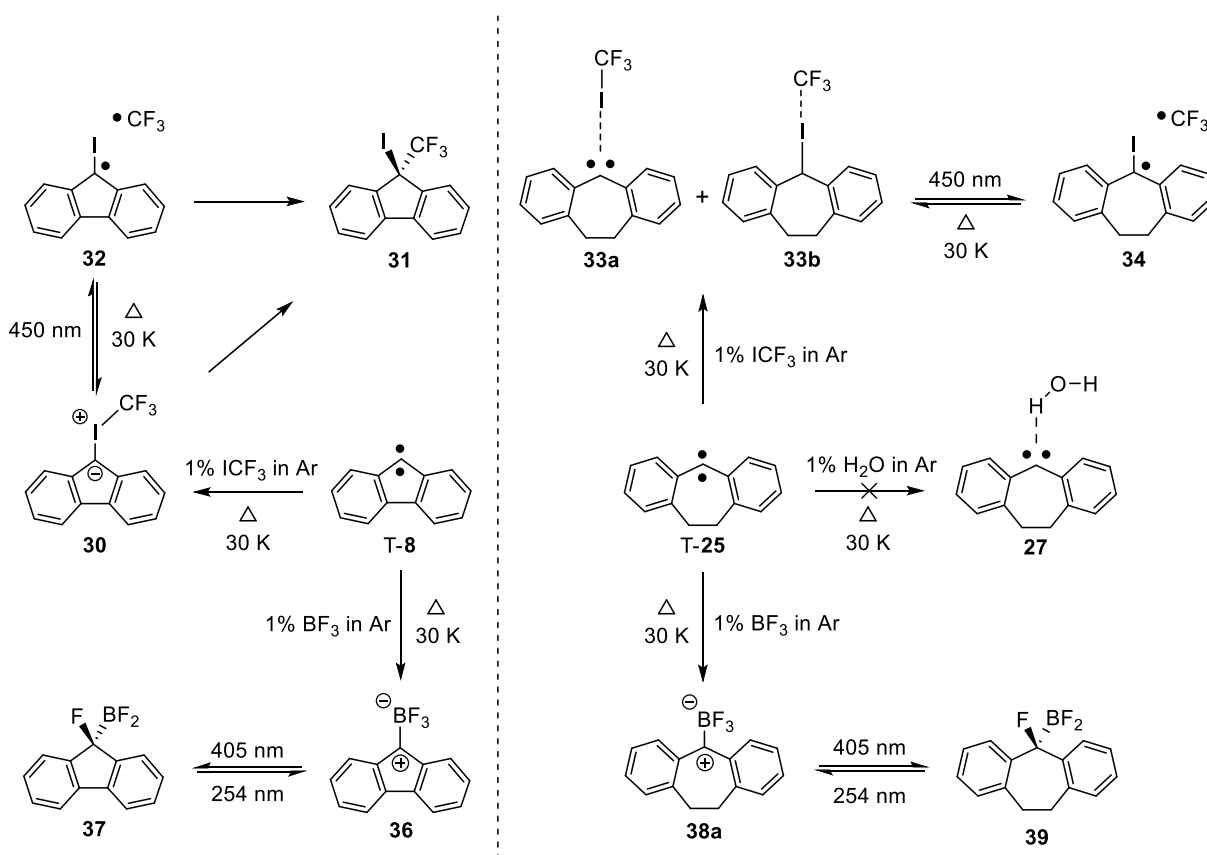
Scheme IV. Previously investigated hydrogen bonding interactions of **59** with proton donors H₂O and MeOH.^[8]

N-heterocyclic carbenes are highly nucleophilic singlet ground state carbenes which can form strong hydrogen as well as halogen bonds. To explore the hydrogen bonding of more nucleophilic carbene, 1,3-di-*tert*-butyl-imidazole-2-ylidene **60**, and to compare hydrogen vs. halogen bonding interactions of the singlet carbenes, the reactions of **59** with ICF₃, and **60** with H₂O and ICF₃ were investigated.

Reaction of Carbene 8 with ICF₃ and BF₃, and Carbene 25 with H₂O, ICF₃ and BF₃.

The reaction of **8** with ICF₃ switches the spin state of the carbene from triplet to singlet and results in the formation of ylide **30** with a negatively polarized fluorenyl unit, avoiding halogen-bonded complex which would transfer a positive charge to the five-membered ring system and lead to an antiaromatic destabilization. Simultaneously, a formal C–I insertion product **31** is also formed due to its high exothermicity of 91 kcal mol⁻¹. Subsequent irradiation (450 nm) converts **30** to a triplet radical pair **32** and this conversion is found to be reversible after several irradiation/annealing cycles producing **31** as byproduct (Scheme V). The interaction of T-**8** with strong Lewis acid BF₃ leads to a formation of zwitterion **36** with a positively charged antiaromatic fluorenyl unit. In this case, antiaromatic destabilization is compensated by the formation of a strong donor-acceptor complex. The adduct **36** is found to be photolabile and undergoes 1,2-fluorine migration (405 nm) from boron to adjacent carbene carbon forming a formal B–F insertion product **37**. This fluorine

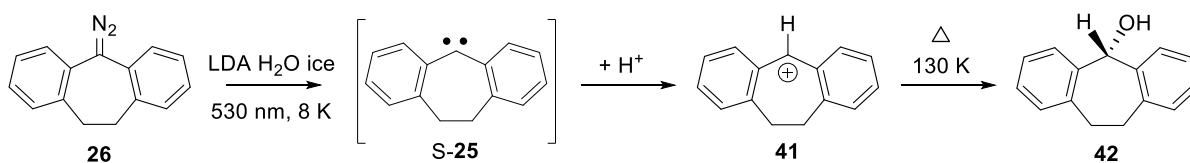
migration is reverted to **36** upon 254 nm irradiation. Unlike **7** and **8**, carbene **25** fails to switch the spin state of carbene on complexation with H₂O and thus could not form singlet hydrogen-bonded complex **27**. This is rationalized by larger S-T gap of **25**, which does not allow to stabilize the singlet state below the triplet by hydrogen bonding. On the other hand, the reaction of T-**25** with ICF₃ results in a formation of both kinds of singlet halogen-bonded complexes, type I **33a** and type II **33b**. This indicates that halogen bonding stabilizes the singlet state more than hydrogen bonding. Upon 450 nm photolysis, the complexes **33a** and **33b** are transformed to a triplet radical pair **34**, which was characterized by EPR spectroscopy. The signals of **33a** and **33b** are restored on subsequent annealing due to recombination of radicals. The formation of a formal C–I insertion product between **25** and ICF₃ is not observed despite of its high exothermicity, probably due to matrix cage effects that inhibit the larger movements of the fragments. With BF₃, carbene **25** forms a Lewis adduct and exhibits photochemistry analogous to BF₃ complex of **8** (Scheme V).



Scheme V. Reaction of **8** with ICF₃ and BF₃, and reaction of **25** with H₂O, ICF₃ and BF₃.

Reaction of Carbene 25 with LDA water ice.

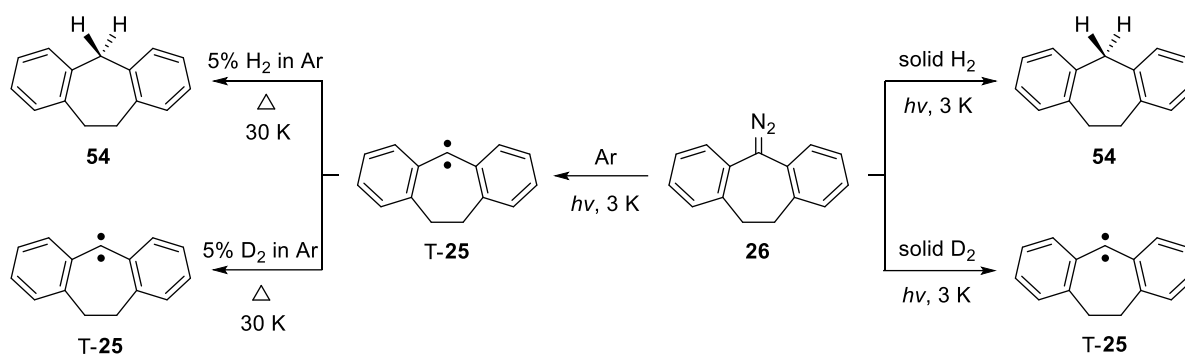
The reaction of **25** with single water molecules embedded in a solid argon differs from the reaction with LDA water ice. Visible light irradiation of dibenzocycloheptadienylidene **26** in amorphous water ice at lowest possible temperatures (8 K) produces dihydrodibenzotropylium cation **41**. This cation is found to be kinetically stable at low temperatures and reacts with surrounding water ice at temperatures above 120 K to form corresponding alcohol **42** (Scheme VI). In comparison to previous findings of benzhydryl and fluorenyl cations in LDA water ice,^[1, 4] it is concluded that protonation of carbenes to form the corresponding cation mainly depends on the proton affinity of the carbene in its singlet state rather than the singlet-triplet energy gap. Carbene **25** is predicted to have a larger proton affinity (283 kcal mol⁻¹) relative to that of **7** and **8** (~ 272 kcal mol⁻¹), which therefore also reflects in protonation of S-**25** to yield cation **41**.



Scheme VI. Reaction of **25** with LDA water ice.

Reaction of Carbene 25 with H₂ and D₂.

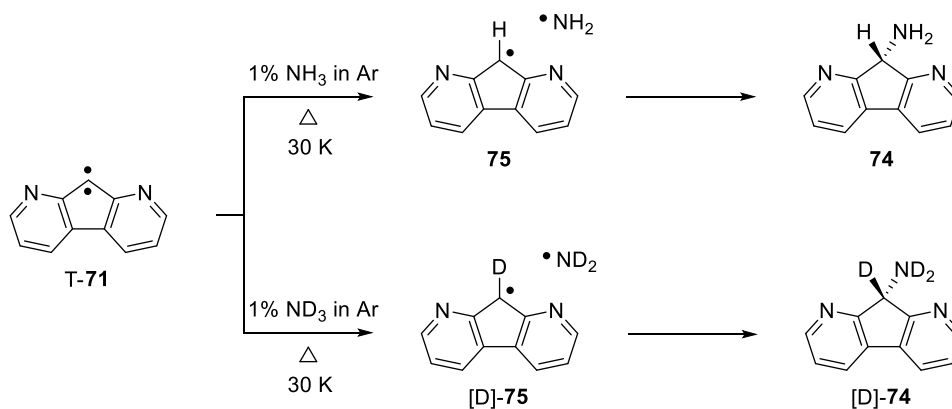
The triplet state of **25** is found to be reactive towards H₂ despite of calculated activation barrier of 7 kcal mol⁻¹ for rate determining hydrogen abstraction step, suggesting that the reactions proceeds via QMT. The product of the hydrogen abstraction reaction, a triplet radical pair, undergoes crossover to the singlet surface and recombines to give the corresponding hydrocarbon **54**. The selective reactivity of **25** in solid H₂ and argon doped H₂ matrices indicates a pronounced kinetic isotopic effect (Scheme VII). The closed-shell singlet state of **25** is predicted to lie 10.2 kcal mol⁻¹ above the triplet ground state. Therefore, H₂ activation reaction from a thermally populated excited singlet state can be excluded under matrix isolation conditions. The reactivity of **25** in solid H₂ is parallel to reactivity of **8** and contrast to stability of **7**, while **8** reacts slowly in solid D₂ opposite to stable behavior of **7** and **25**. This shows an increase in reactivity of carbenes towards molecular hydrogen in the order **7** < **25** < **8**.



Scheme VII. Reactions of **25** with H₂ and D₂.

Reaction of Carbene 71 with NH₃ and ND₃.

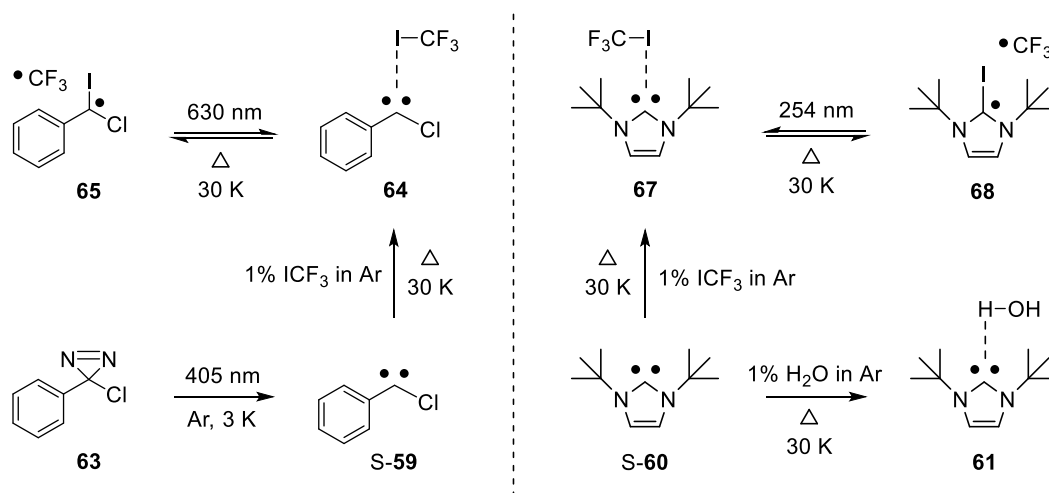
The reaction of 1,8-diazafluorenylidene **71** with ammonia demonstrated triplet state reactivity of the carbene. Despite of considerable activation barrier for ammonia H/D abstraction by T-**71**, the reaction proceeds via QMT to produce triplet radical pair **75**/[D]-**75** as revealed by the radical signals in EPR experiments. The radical pair recombines at 25 – 30 K to form a formal N–H/D insertion product **74**/[D]-**74** (Scheme VIII) which is experimentally identified by comparison of its IR and UV-Vis spectra with that of an authentic matrix-isolated sample and DFT calculations. The absence of kinetic isotopic effect indicates that the carbene center directly interacts with N–H/D bond of ammonia. The large S-T gap of **71** does not allow to stabilize the singlet state below the triplet on complexation with ammonia, hence involvement of the singlet state is ruled out.



Scheme VIII. Reactions of **71** with NH₃ and ND₃.

Reaction of Carbene 59 with ICF₃, and Carbene 60 with H₂O, and ICF₃.

The highly nucleophilic carbene **60** acts as strong base and forms a hydrogen-bonded complex **61** with H₂O. Unlike hydrogen-bonded complex between S-**59** and H₂O, complex **61** formed is found to be stable even after 254 nm photolysis, and a formal O–H insertion product between S-**60** and H₂O is not observed due to endothermicity of this reaction. Analogous to hydrogen bonds, both carbenes S-**59** and S-**60** form the halogen bonds on complexation with ICF₃. The resultant halogen-bonded complexes **64** and **67** are found to be stable at low temperatures, but rearrange photochemically to yield corresponding triplet radical pairs **65** and **68**, respectively. At higher temperatures of 25 – 30 K, the radical pairs recombine to give back the complexes, instead of respective C–I insertion products (Scheme IX). This is rationalized by matrix cage effects that inhibit the larger movements of fragments in the radical pairs. The comparison of computed binding energies of hydrogen and halogen-bonded complexes of S-**59** and S-**60** shows that the stabilization of the singlet states by halogen bonding with ICF₃ is larger than the stabilization by hydrogen bonding with H₂O, provided that steric hindrance has no weakening effect on the strength of halogen bonds.



Scheme IX. Reaction of **59** with ICF₃, and reactions of **60** with H₂O and ICF₃.

1. General Introduction

1.1. Carbene Chemistry

Carbenes are neutral compounds ($:\text{CR}_1\text{R}_2$) having a divalent carbon atom with only six electrons in its valence shell. The unusual valence of the carbon atom in carbenes renders them reactive intermediates, which are unstable at room temperatures and exists only for a short period of time. The electronic structure of carbenes associated with linear and bent forms can be described by referring to the Walsh diagram (Figure 1).^[9] In the linear geometry that exhibits sp hybridization, low-lying CR_1 bonding MO orbital **A** is derived from the $2s$ orbital of carbon, while only one p orbital of the carbon binds with R_2 in the linear form to generate second bonding MO orbital **B**. The degenerate pair of remaining p orbitals (**C** and **D**) is filled by two non-bonding electrons.

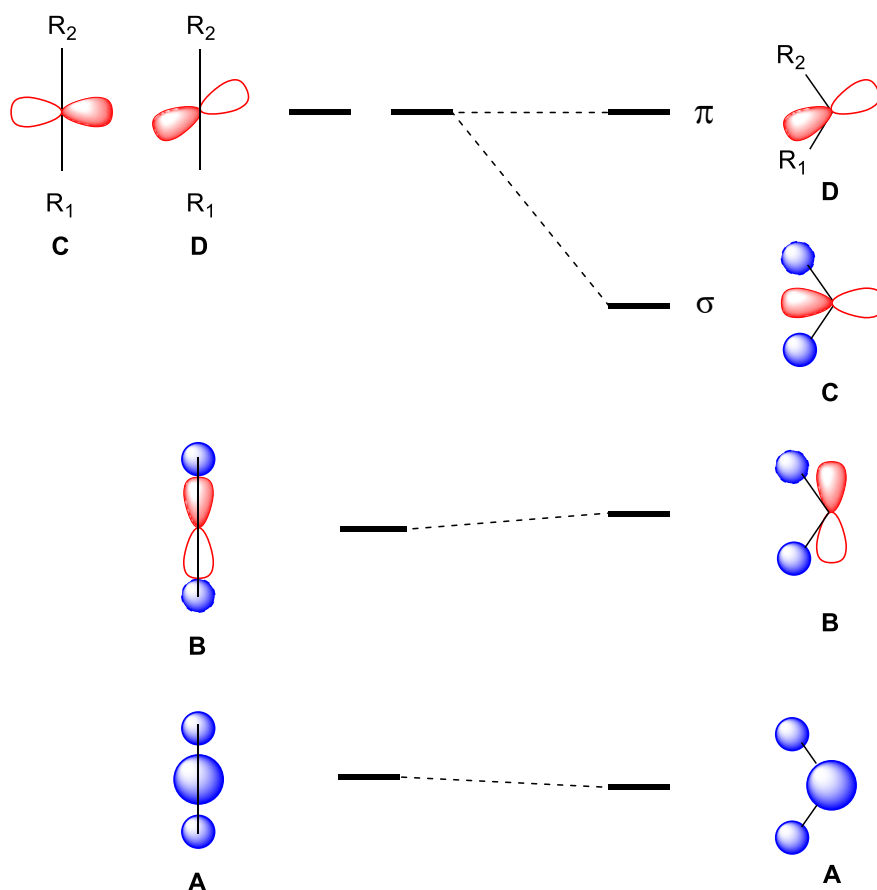


Figure 1. The Walsh diagram showing the electronic structure of the carbene in linear (left) and bent (right) forms.^[9]

As the R_1-C-R_2 angle contracts, the carbon atom adopts sp^2 -like hybridization, where orbital **A** is slightly stabilized due to the $R_1\cdots R_2$ overlap, whereas **B** is destabilized as the $C-R_2$ overlap drops. The dominant change is the drop in energy of **C**, as it gains more s -character, therefore called as σ -orbital and the non-bonding **D** orbital remains unchanged as an isolated π -orbital.

Depending on the occupancy of two non-bonding electrons in **C** and **D** (from here on σ and π , respectively), carbenes can have four possible electronic configurations (Chart 1).^[10] If the electrons are placed, one in each σ and π orbital, with parallel spins, then the molecule is described by $\sigma^1\pi^1$ configuration, often called as triplet state, as the spin state of the system is $S = \frac{1}{2} + \frac{1}{2} = 1$ and thus the multiplicity is $m_s = 2S + 1 = 3$. In contrast, when electrons are paired in the same σ or π orbitals, there are two different states σ^2 and π^2 with spin $S = \frac{1}{2} + (-\frac{1}{2}) = 0$ and $m_s = 1$, which correspond to the closed-shell singlet states of the carbenes. An open shell singlet state of carbene is also expected with $\sigma^1\pi^1$ configuration where the electrons with opposing spins occupy two different σ and π orbitals.

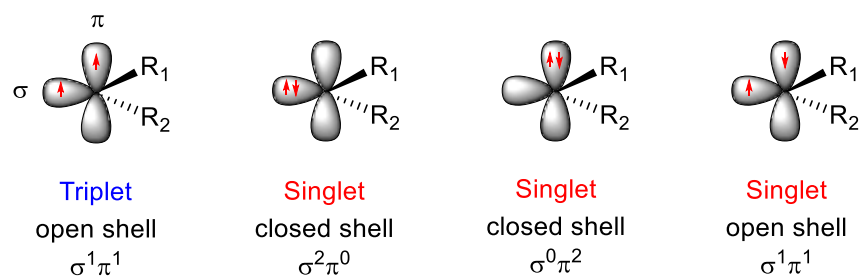


Chart 1. Electronic configuration of carbenes.^[10]

Whether the carbene has a singlet or triplet ground state depends on the relative energy difference between σ and π orbitals as well as the pairing energy of the non-bonding electrons. According to Hund's rule, it takes energy to pair electrons, hence electrons are added to an orbital in such a way that they minimize the total energy of the system. If σ - π separation is greater than the electron repulsion energy, then greater stability is attained by pairing two electrons resulting into singlet ground state. On the other hand, the triplet state is favored by keeping the electrons unpaired when σ - π separation is less than the pairing energy. This approach is quite similar to crystal-field theory describing the formation of low and high spin metal complexes. The spin multiplicity of carbenes can be also correlated to bond angle at the carbene center.^[11-12] The small carbenic bond angle lowers the energy of the σ orbital and thus increases the σ - π separation resulting in singlet state.

In contrast, a large angle at the carbene center leads to smaller σ - π separation and hence the triplet state is preferred.

By appropriate choice of substituents, the relative energies of σ and π orbitals can be perturbed to obtain carbene in its singlet or triplet ground state. For example, the simplest carbene, methylene **1**, is determined to have a triplet ground state with singlet-triplet gap (ΔE_{S-T}) of $\sim 9 \text{ kcal mol}^{-1}$,^[13] whereas fluorine-substituted methylenes **2** and **3** have singlet ground states with ΔE_{S-T} of -14.6 ^[14] and $-56.7 \text{ kcal mol}^{-1}$,^[15] respectively (Chart 2).

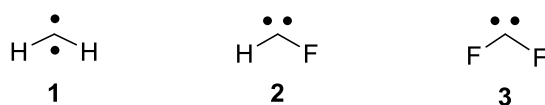


Chart 2. Representative structures of methylene (**1**), monofluoromethylene (**2**) and difluoromethylene (**3**).

The influence of substituents on the carbene ground state multiplicity can be analyzed in terms of electronic and steric effects. In general, σ -electron withdrawing substituents inductively stabilize the σ -orbital of the carbene by increasing its s -character and leave the π -orbital unchanged. The σ - π splitting is thus increased and the singlet state is favored. On the contrary, σ -electron donating substituents induce a small σ - π separation that favors the triplet state. Although inductive effects tune the ground state multiplicity of several carbenes,^[16-20] mesomeric effects can play a more significant role which are consist of the interaction of the carbon orbitals with π orbitals of the substituents.^[11,21] The energy of the π -orbital of the carbene is raised by interaction with π -electron donating substituents, while the σ -orbital remains almost unchanged to an increase in the σ - π separation and the singlet state is preferred. For carbene with π -electron withdrawing substituents, vacant orbitals of the substituents interact with the σ -orbital of the carbene and stabilize it to achieve singlet ground state.^[22-23] Apart from electronic effects, steric bulk of carbene substituents also dictate the relative energies of σ and π orbitals of the carbene and thereby influence the ground state multiplicity. Increasing the steric bulk of the substituents broadens the bond angle at the carbene center, as a result, σ - π separation is minimized and triplet state is desired.^[24] For example, dimethylcarbene **4** has a bent singlet ground state,^[25-26] while di(*tert*-butyl)carbene **5**^[27] and diadamantylcarbenes **6**^[28] are triplets due to wide carbene bond angles.

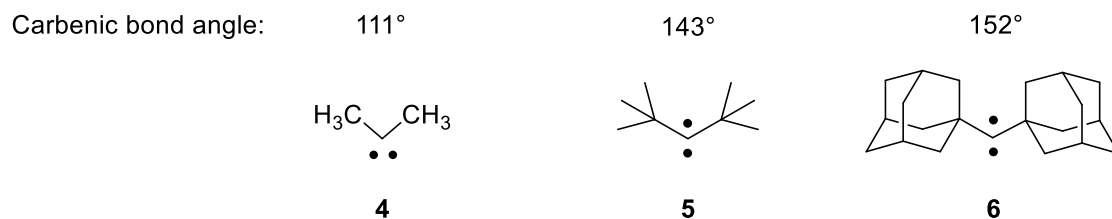
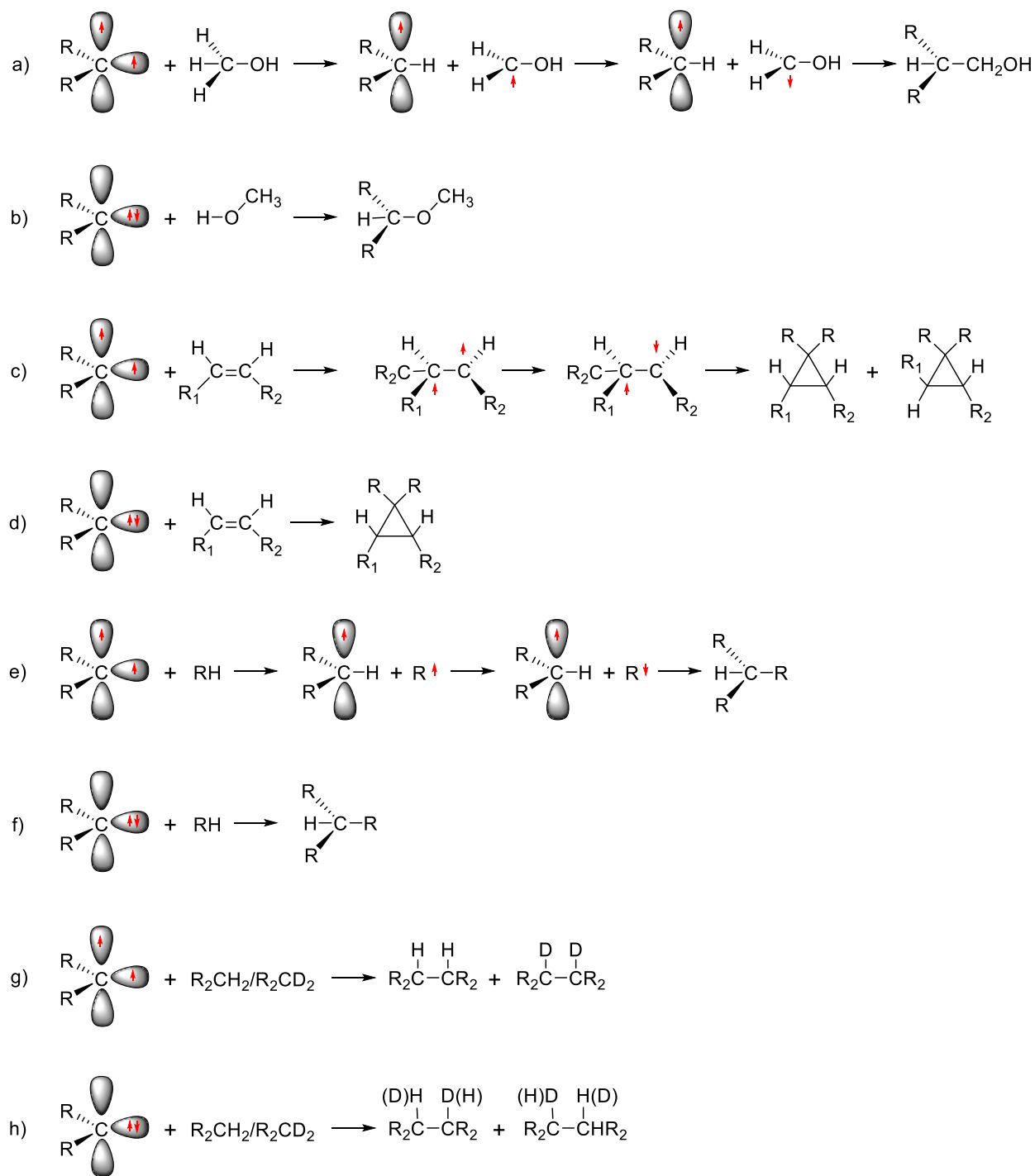


Chart 3. Steric effect governing the carbenic bond angle and ground state multiplicity of carbenes **4**, **5** and **6**.^[25-28]

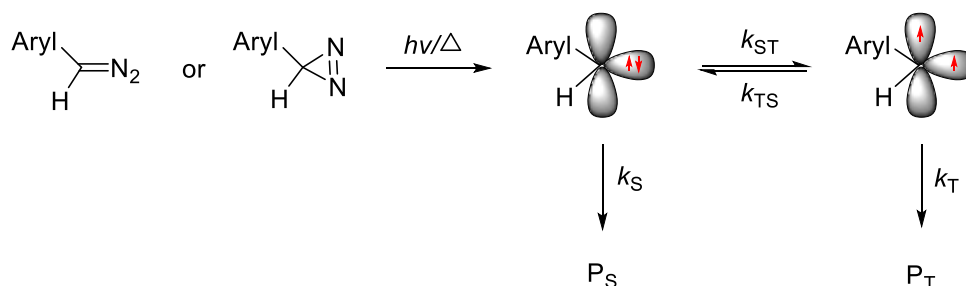
The ground state spin multiplicity is a fundamental feature of carbenes that influences their reactivity.^[29] Due to a filled and a vacant orbital, singlet carbenes possess both electrophilic and nucleophilic character and are likely to react in a single concerted step. Triplet carbenes behave as diradicals because of two singly occupied orbitals and participate in stepwise radical additions (Scheme 1). For instance, singlet carbenes insert into the O–H bonds of alcohols in a concerted reaction to form O–H insertion products,^[30-32] whereas triplet carbenes react with C–H bonds of alcohols yielding a triplet radical pair which recombines after spin-flipping to form C–H insertion products.^[33-37] The reaction of the carbene with an olefin to form cyclopropane is another diagnosis of the multiplicity of the carbene.^[29] The Skell-Woodworth hypothesis suggests that a spin-prohibition requires the addition of a triplet carbene to olefin to occur in two steps via a diradical intermediate.^[38] The intermediate lives long enough to allow the rotation of the substituents around the single bond leading to loss of stereochemistry. The subsequent ring closure of the ring occurs after spin flipping of one of the electrons to give a mixture of isomeric cyclopropanes. In contrast, singlet carbenes add to olefins stereospecifically, yielding only *cis* or *trans* product depending on the starting geometry of the olefin. Moreover, singlet and triplet carbenes react with hydrocarbons in distinctive ways. The singlet carbenes can insert into C–H bonds in a concerted manner which is not expected to generate free radicals.^[39] On the other hand, triplet carbenes are believed to abstract hydrogen atoms to generate radical pairs that recombine in subsequent steps.^[40-42] A straightforward way to distinguish between a direct insertion process of singlet carbene and one going through free radicals is by a crossover experiment.^[43] If a mixture of hydrocarbon R₂CH₂ and its deuterated counterpart R₂CD₂ reacts with singlet carbene, then the reaction products are consist entirely of undeuterated and dideuterated compounds. Alternatively, if the reaction occurs through triplet carbene via a hydrogen abstraction-recombination route, then some monodeuterated cross-products can be formed. It should be noted that the abstraction is expected to exhibit a larger isotopic effect than insertion into a C–H/D bond.



Scheme 1. Reactions of carbenes with methanol, alkene and hydrocarbon. a) Stepwise reaction of triplet carbene with methanol. b) Concerted reaction of singlet carbene with methanol. c) Stepwise reaction of triplet carbene with olefin. d) Concerted reaction of singlet carbene with olefin. e) Stepwise reaction of triplet carbene with hydrocarbon. f) Concerted reaction of singlet carbene with hydrocarbon. g) Reaction of triplet carbene with a mixture of undeuterated and dideuterated hydrocarbon. h) Reaction of singlet carbene with a mixture of undeuterated and dideuterated hydrocarbon.

Intersystem Crossing of Carbenes and the Solvent Effects

Regardless of the nature of the ground state, singlet carbene is expected from the most carbene precursors as a consequence of spin conservation.^[44-45] The first-formed singlet carbene can then undergo either intramolecular or intermolecular reactions to form products P_S or relax to the triplet carbene if it is more favorable in energy and exhibits different reactions to form products P_T (Scheme 2).^[46] Intersystem crossing (ISC) rates between singlet and triplet states (k_{ST} and k_{TS}) play a crucial role in defining the intramolecular dynamics of the carbene and thereby affect its spin dependent chemistry. A well-known class of carbenes, in which one or both hydrogens of the parent methylene are replaced by aromatic rings, are called arylcarbenes and these carbenes mostly possess triplet ground states with a relatively small singlet-triplet splitting. There are several studies on ISC rates reported in literature for such systems due to rapid thermal equilibrium that takes place between their triplet ground states and low-lying singlet states.^[46-50]



Scheme 2. Generation of singlet and triplet carbenes where P_S and P_T are stable products derived from the singlet and triplet carbene, respectively.^[46]

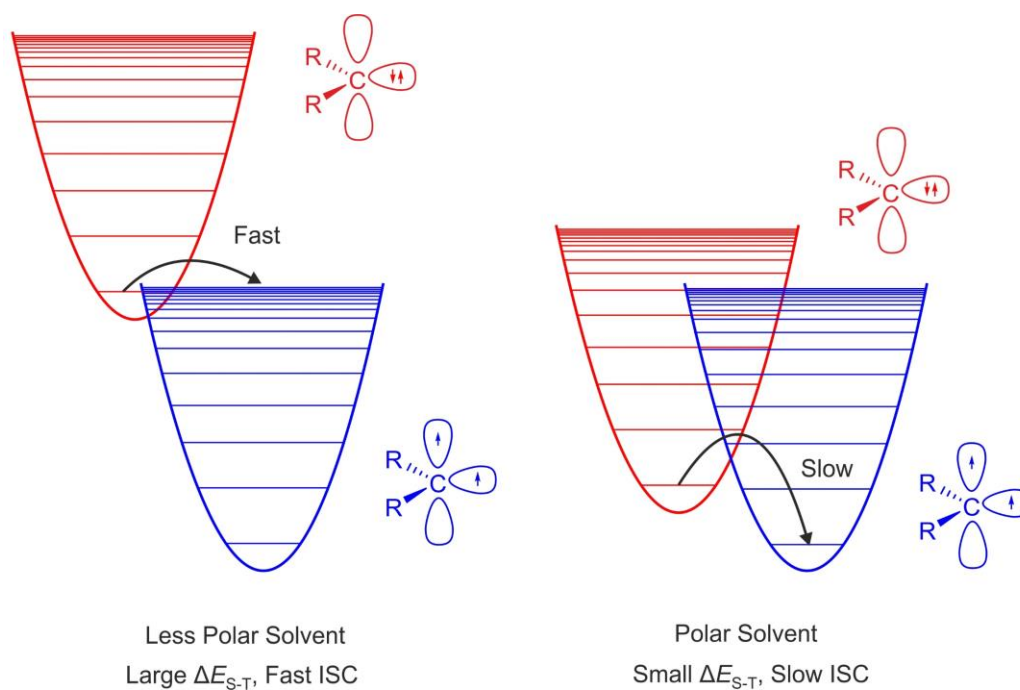
Normally, it is expected that the rate of ISC will increase as the energy gap between the singlet and triplet state (ΔE_{S-T}) decreases, which is also known as the golden rule of ‘radiationless transitions’.^[51-52] However, the solvent environment can considerably affect the intramolecular spin conversion dynamics of the carbene. Eisenthal and co-workers demonstrated that rates of singlet to triplet conversion (k_{ST}) of diphenylcarbene **7** (Scheme 3) decrease as the solvent polarity increases (Table 1).^[49] It was proposed that the singlet state being highly polar, often considered as zwitterionic, is strongly stabilized in polar solvents, whereas the less polar triplet experiences a weak stabilization. Consequently, it leads to a decrease in ΔE_{S-T} with increase in the solvent polarity, but the intersystem crossing from singlet to triplet is slowed down. This is called inverse gap effect, i.e., the intersystem crossing rate decreases as the ΔE_{S-T} decreases.

Table 1. Intersystem crossing rates (k_{ST}) of diphenylcarbene **7** in various solvent.^[49]

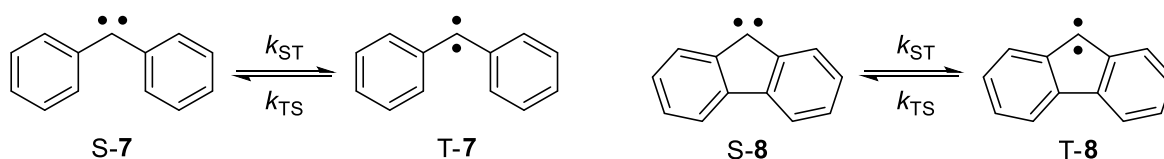
Solvent	$10^{-9} k_{ST}^{[a]}$	$E_T(30)^{[b]}$
isooctane	10.52 ± 0.95	30.9
3-methylpentane	10.52 ± 0.93	30.9
diethyl ether	7.69 ± 0.65	34.6
tetrahydrofuran	5.5 ± 0.45	37.4
butyronitrile	3.57 ± 0.26	43.1
acetonitrile	3.23 ± 0.19	46.0

^[a] k_{ST} in s^{-1} . ^[b] $E_T(30)$ is solvent polarity parameter in $kcal\ mol^{-1}$.

To explain apparent violation of the golden rule of radiationless transitions for carbene ISC processes, it was suggested that when ΔE_{S-T} is small, the singlet carbene overlaps with sparser vibrational levels of the triplet carbene; thus, there will be less vibronic coupling and a slower ISC. On the other hand, when ΔE_{S-T} is larger, the singlet carbene overlaps with denser vibrational levels of the triplet carbene, resulting in greater vibronic coupling and a faster ISC rate (Figure 2). However, the concept of the inverse gap effect does not hold true for carbenes having very large ΔE_{S-T} , where Frank-Condon factors are negligible although the vibronic levels in triplet state are dense and the golden rule is followed in such cases.

**Figure 2.** Illustration of a Franck-Condon-like factor on the ISC process of carbenes.

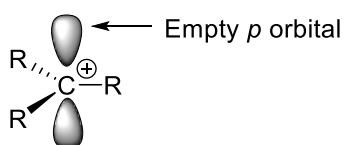
In a study of another triplet ground state arylcarbene fluorenylidene **8** (Scheme 3), Platz et al. found that the ISC rate (k_{ST}) in hexafluorobenzene, a non-polar solvent, is similar to that recorded in polar acetonitrile.^[53] This is a remarkable exception to Eisinger's finding that in non-polar solvents, ISC rates are faster. The similar ISC rates of **8** in polar and non-polar solvent are thought to be the result of a specific interaction between solvent molecules and the carbene imposing a Franck-Condon-like factor on the ISC processes. Therefore, ISC rates of carbenes are not entirely dependent on bulk solvent polarities; the solvent coordinating properties also play a major role.^[46]



Scheme 3. Arylcarbenes **7** and **8** showing ISC between their ground triplet and low-lying singlet states at room temperatures in fluid solutions.^[49, 53]

1.2. Carbocations

Carbocations are reactive intermediates bearing a positive charge on carbon atom. A common model for the carbocation structure is a trivalent carbon species exhibiting sp^2 hybridization, where a vacant p orbital represents the orbital available to accept electrons.



The enthalpies for heterolytic dissociation of alkanes in the gas phase varies with alkyl groups as follows: methyl > ethyl > *iso*-propyl > *tert*-butyl, which is consistent with the generalization that the ease of formation of carbocations is $3^\circ > 2^\circ > 1^\circ$.^[54] This can be explained by the electron-donating ability of methyl or other alkyl group in terms of hyperconjugation, which lowers the energy of a system by delocalization of electrons. In molecular orbital terms, hyperconjugation is the overlap of the filled σ orbitals of the C–H bonds adjacent to the carbocation with the empty p orbital on the positively charged carbon atom. The more alkyl substituents, the more σ bonds are available for hyperconjugation (Figure 3). The carbocation is more stable if its charge is delocalized over more than one atom. The more stable the carbocation, the faster it is formed.^[54]

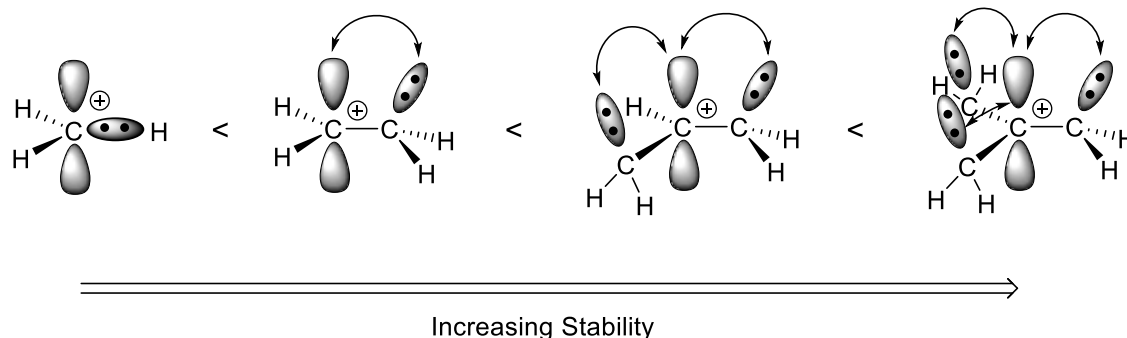
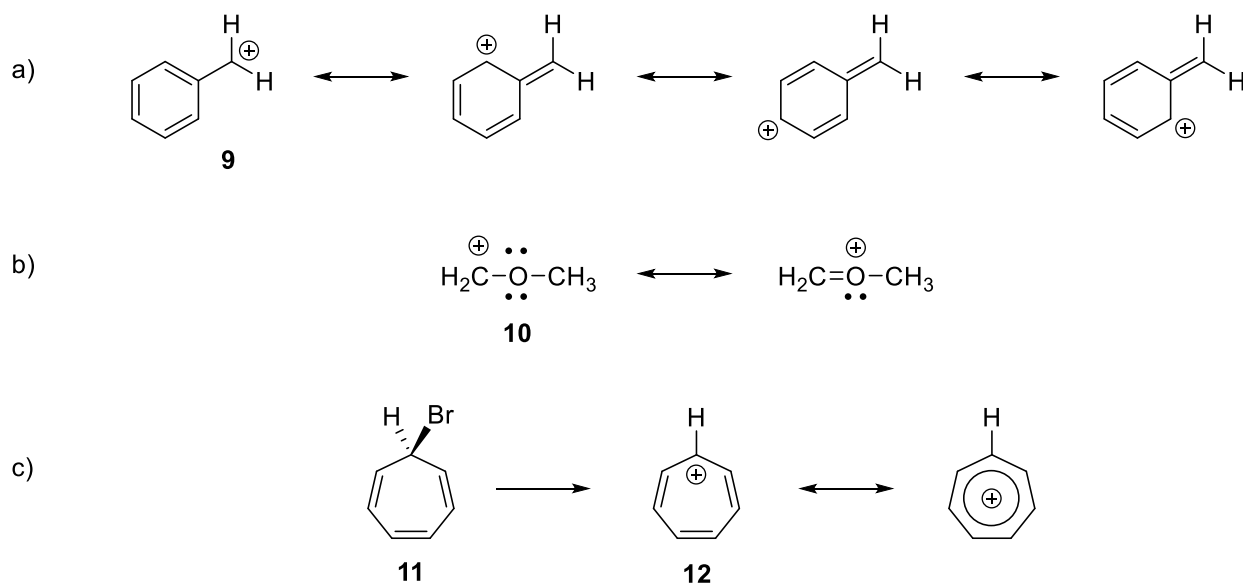


Figure 3. Stabilization of carbocation by hyperconjugation with an adjacent methyl group(s).^[54]

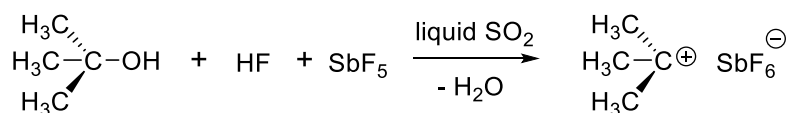
In fact, any factor that leads to delocalization of the positive charge of the electron-deficient carbon should stabilize the carbocation. The neighboring carbon-carbon multiple bonds and atoms with lone pairs stabilize the carbocations by resonance effects.^[54] For example, benzyl cation **9** is stabilized by conjugation with π bonds in the benzene ring, while methoxymethyl cation **10** gains resonance stabilization through lone pair electrons of adjacent oxygen atom of methoxy group. The stabilization by delocalization can also occur through aromatization. Tropylium bromide **11**, a crystalline solid, is highly soluble in water, giving ion pair of tropylium **12** and bromide ions in the solution. The cyclic tropylium cation **12** has 6π electrons delocalized in three molecular orbitals spread over the seven carbon atoms. Thus, it is a Hückel $(4n+2)\pi$ system exhibiting aromaticity (Scheme 4).



Scheme 4. Carbocation charge stabilization through conjugation with a) π bonds, b) lone pair and c) aromatization.^[54]

When considering the importance of hyperconjugation versus resonance as the more stabilizing feature, resonance usually wins out. A primary carbocation with resonance is more stable than a secondary carbocation without resonance and a secondary carbocation with resonance is usually more stable than a tertiary carbocation without resonance.

By developing superacidic chemistry, the Nobel Prize Winner George Olah and his co-workers generated a great number of stable and persistent carbocations.^[55-57] A specific example include the treatment of *tert*-butyl alcohol with SbF₅ and HF in liquid SO₂ to synthesize *tert*-butyl cation (Scheme 5). The ¹³C NMR of this cation showed downfield methyl groups at 47.5 ppm, but the key evidence was the shift of the central carbon atom, which appeared at 335.2 ppm, indicating that the carbon atom is strongly deshielded as it is positively charged and electron deficient.^[58]

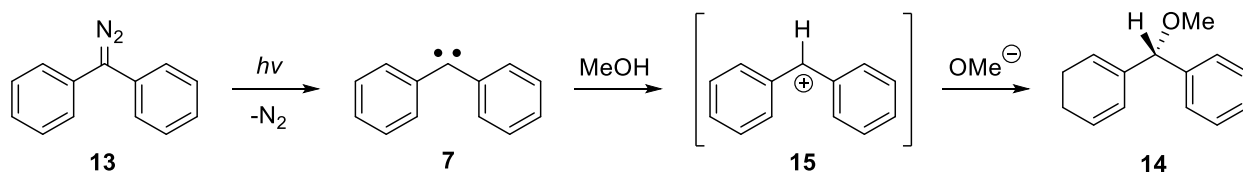


Scheme 5. Generation of *tert*-butyl carbocation under superacidic conditions.

Olah suggested that superacids were so strong that they could donate a proton to simple saturated hydrocarbons to form penta-coordinated positively charged carbon ions.^[59-60] In this respect, he introduced two groups of carbocations namely, trivalent one called *carbenium* ions, where the positively charged carbon is surrounded by three atoms or groups, and those in which the positive carbon atom is surrounded by five atoms or groups called *carbonium* ions. The hypervalent carbonium ions are usually unstable and undergo further reactions.

The carbocations obtained under superacidic conditions are not free species, therefore their reactivity towards solvent and nucleophiles cannot be measured. The advent of laser flash photolysis made a step forward for studying the reactivity of carbocations as free species in nucleophilic environments. In this technique, carbocations are generated by heterolytic scission of a C—X bond of a halide precursor with a short pulse of laser light and their subsequent decay can be monitored using ultrafast UV-vis and IR spectroscopy to obtain the absolute rate constant of the reaction with the nucleophilic environment. Several examples can be found in literature, mainly on the study of diarylcarbocations, since their optical absorptions are quite characteristic and their lifetimes are longer than the laser pulse necessary to cleave the C—X bond.^[61]

The protonation of a carbene is another approach to generate a trivalent carbocation or secondary carbenium ion. Suggestive evidence for the protonation of carbene was uncovered by Kirmse in a photolysis experiment of diphenyldiazomethane **13** in methanol solution producing benzhydryl methyl ether **14**. These results pointed to the diphenylcarbenium ion or benzhydryl cation **15** as an intermediate in the reaction of diphenylcarbene **7** with methanol (Scheme 6).^[32, 62] Thereafter, the chemistry of carbenes in protic media raised the prospect that carbocations could be formed and several fruitful investigations were made for the detection of these reactive intermediates.^[63]



Scheme 6. Photolysis of diphenyldiazomethane **13** in methanol suggesting the formation of benzhydryl cation **15**.^[32]

1.3. Lewis Acids

There are three kinds of theories related to Lewis acids. The first one is the chemical bonding theory proposed by Lewis in 1923.^[64] Lewis suggested that an electron-pair acceptor can be classified as Lewis acid and an electron-pair donor can be classified as Lewis base. The second theory is the Brönsted-Lowry acid-base theory published in the same year,^[65] which states that a Brönsted-Lowry acid as proton donor, while a Brönsted-Lowry base is a proton acceptor. Since the proton can accept an electron-pair into its empty 1s orbital, the proton is also a Lewis acid. Thus, it follows that all Brönsted-Lowry acids are also Lewis acids. The third one is the ‘hard and soft acids and bases’ (HSAB) theory proposed by Pearson in 1963, where Lewis acids and bases are classified according to their hardness or softness.^[66] Hard implies small and non-polarizable atoms having high positive charge in acids and high electronegativity in bases, whereas soft indicates larger atoms that are more polarizable with low positive charge in acids and low electronegativity in bases. In this theory, the strength of adduct formation is predicted based on two key concepts: a) hard acid-hard base interactions are stronger than hard acid-soft base or soft acid-hard base interactions; b) soft acid-soft base interactions are stronger than soft acid-hard base and hard acid-soft base interactions.^[67-70]

According to the IUPAC definition, a Lewis acid is an electron-pair acceptor and therefore can react with a Lewis base to form a Lewis adduct by sharing the electron-pair of the Lewis base.^[71] It implies that a Lewis acid is an atomic or molecular species with a localized empty atomic or molecular orbital of low energy and this lowest energy molecular orbital can accommodate a pair of electrons. The archetype of a Lewis acid-base reaction is:



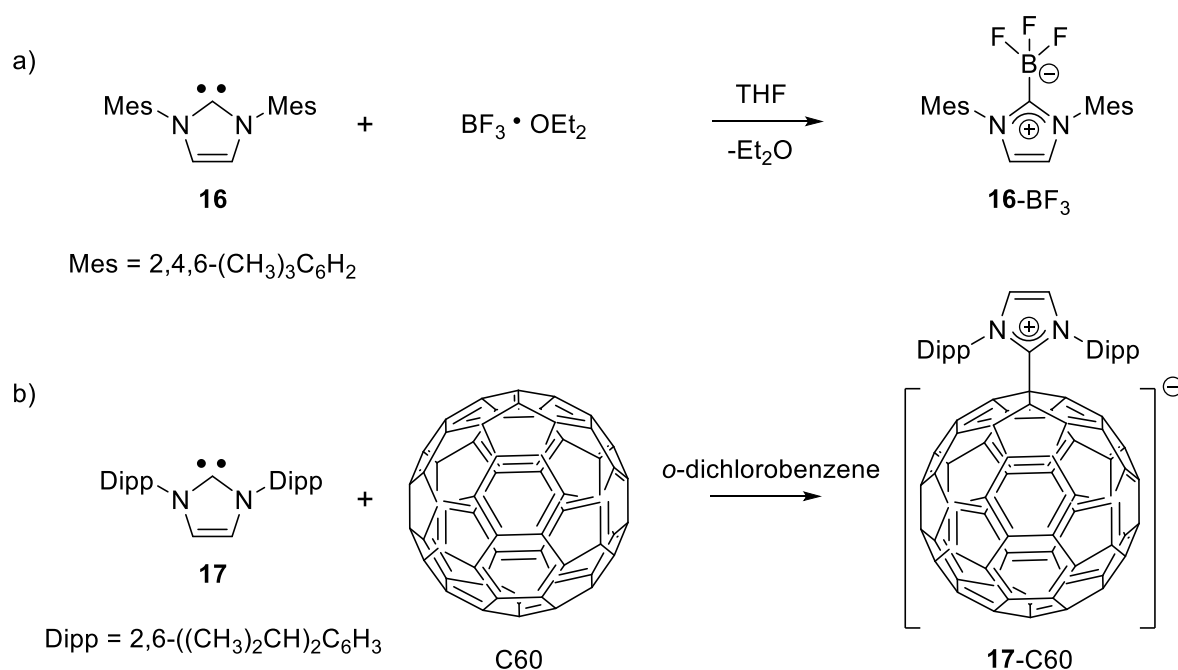
BF_3 is a Lewis acid because the boron atom has only six electrons in its valence shell and, having room for eight, can accept the lone pair of the nitrogen of ammonia.

The translation of Lewis's definition into a quantum mechanical term by Mulliken^[72] further widened the definition, so as to include those reagents that accept a fraction, possibly very small, of an electron. With this extension, compounds that accept electron are considered as Lewis acids. Water, alcohols, phenols, hydrogen halides, carboxylic acids, primary and secondary amines, amides, thiols, 1-alkynes and so on constitute a special class of Lewis acids.^[73] They all contain XH group in which the hydrogen atom is bonded to an electronegative atom X and bears a partial positive charge. Hence, hydrogen is attracted, by means of electrostatic forces towards highly electron density regions, mainly the lone pairs of the bases B, and a hydrogen bond $\text{X-H}\cdots\text{B}$ is formed. In addition to this electrostatic interaction, there is a charge transfer from the base to the antibonding orbital σ^* of the X-H bond. A modern electrostatic model of the hydrogen bond provides a near-quantitative description of structure and properties for a wide range of typical hydrogen bonds.^[74] In contrast, Natural Bond Orbital (NBO) analysis suggests that charge transfer of $n \rightarrow \sigma^*$ type is a characteristic feature of hydrogen bonding.^[75] In any case, the existence of even a small charge transfer allows the hydrogen bond donors to be considered as Lewis acid in nature. Similarly, halogen bond donors such as dihalogens, interhalogens and organic halogens act as Lewis acids by engaging in molecular interactions with electron donor sites of Lewis bases.

To study the Lewis acid-base reactions, it is crucial to understand the fundamental properties such as electronegativity and hardness of interacting molecules which are intimately related to the gain and loss of electrons.^[76] Electronegativity defines whether a compound is an electron acceptor or donor, whereas hardness determines how easily the number of electrons can be changed.^[77] The molecule with higher electronegativity acts as Lewis acid towards a molecule with lower

electronegativity (base) by accepting electrons. The transfer of electron density from base to Lewis acid is driven by their electronegativity difference, and inhibited by the sum of hardness.^[78]

The reactions of Lewis acids with carbon-based Lewis bases have attracted increasing interest because they are useful for developing new coordination complexes featuring acidic centers other than traditional metal ions^[79] and heavier elements.^[80] Due to the presence of a pair of non-bonding electrons, singlet carbenes can act as Lewis bases and interact with various Lewis acids to form a wide variety of carbene adducts.^[81-85] The highly nucleophilic carbenes, imidazole-2-ylidenes **16** and **17** have been shown by Arduengo et al.^[84] and Bazan et al.^[85] to form stable Lewis acid-base adducts with BF_3 and fullerene C_{60} , respectively (Scheme 7).



The formation of strong adducts between a Lewis acid and a given base, depends mainly on their ability to act as electron acceptors i. e., the strength of Lewis acids. Several methods have been used to measure the relative Lewis acidity of boron compounds.^[86-89] Lappert synthesized BX_3L adducts ($\text{X} = \text{F}, \text{Cl}, \text{Br}; \text{L} = \text{ethyl acetate}$) and examined the shift of the CO vibrational frequency of the ethyl acetate ligand upon coordination as a measure of strength of Lewis acidity of boron halides.^[88] Moreover, a linear correlation between the gas phase heats of formation of ethyl acetate ligands and Lappert's CO vibrational frequency shifts was found, providing a reliable estimate of

Lewis acidity.^[90] In the same manner, pyridine and ethanenitrile were used as molecular probes to measure the Lewis acidities of ionic liquids by monitoring the shift of infrared (IR) absorption bands near 1450 cm^{-1} for pyridine and in the range $2250\text{-}2340\text{ cm}^{-1}$ for ethanenitrile.^[91] Varma et al. analyzed the strength of Lewis acidity of boron-containing Lewis acids in terms of Acceptor Number (AN)^[92] derived from ^{31}P NMR shifts of triethylphosphine oxide (TPO) dissolved in these Lewis acid solutions.^[89] The values of AN depend on how well the heteroatom attached to boron competes against the oxygen donor atom of the TPO for the boron acceptor orbital. The boron atom of the strong Lewis acids interacts strongly with oxygen of TPO, leading to deshielding of phosphorous atom and induces a large ^{31}P NMR shift with large AN value.^[89]

1.4. Matrix Isolation

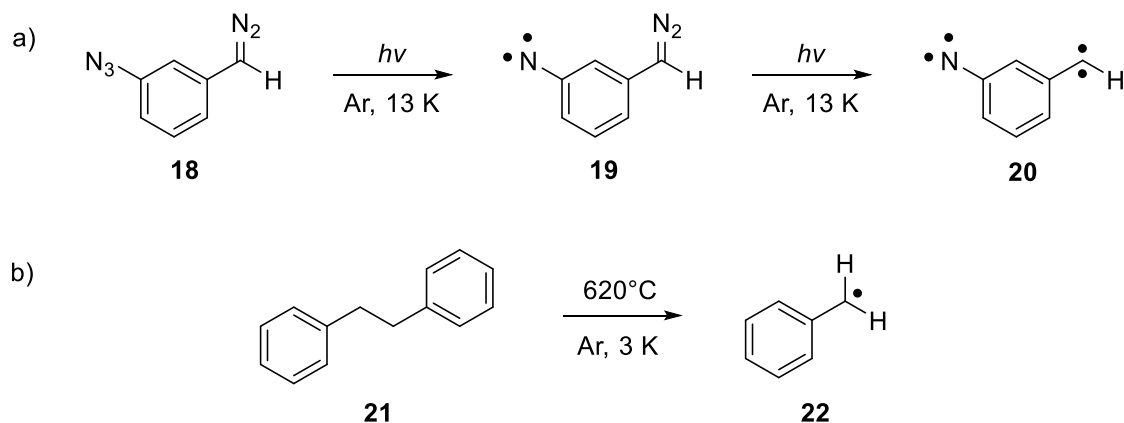
The main objective of this work is to investigate short-lived reactive intermediates which are too unstable to be subjected to conventional spectroscopic methods. In general, there are two techniques used for the detection of this kind of molecules: ultrafast spectroscopy^[93] and matrix isolation spectroscopy.^[94] The first technique uses ultrashort laser pulses for the detection of transient species on extremely short time scales (up to femtoseconds), while the latter technique involves the trapping of reactive species in solid matrices at cryogenic temperatures and thereby extends their lifetimes to carry out conventional spectroscopic analysis. Since most of the work of this thesis was carried out using the matrix isolation technique, further details of this method are given below.

The matrix isolation spectroscopy was pioneered by Pimentel and co-workers in 1954 to study free radicals in solidified CO_2 and xenon matrices.^[95] In the same year, Norman and Porter independently reported isolation of set of radicals trapped in organic glasses formed from different solvents at liquid nitrogen temperatures.^[96] Since then, matrix isolation has been extensively used to examine numerous reactive intermediates and unstable molecules.^[97] In a typical experiment, the sample of interest is deposited in a large excess of inert or reactive host material (N_2 , Ar, Ne, Xe, H_2O , NH_3 , H_2 , etc.) at very low temperatures of $4\text{--}40\text{ K}$ and can be characterized by different spectroscopic methods such as IR, UV-Vis and EPR spectroscopy. Inert gases and nitrogen are considered as the ideal matrix materials, since they possess properties such as optical transparency in the region of interest (UV-Vis and IR), low volatility at cryogenic temperatures, low latent heat of fusion and acceptable thermal conductivity. Since the analyte molecules are isolated in solid

matrices, they do not experience intermolecular interactions. Doppler and collisional broadening are also absent as the molecules are immobilized in the frozen matrix. The low temperature conditions ensure that only the lowest electronic and vibrational level of the molecules of interest are populated and rotational transitions are mostly suppressed by rigid matrix environment. Owing to all these reasons, the matrix isolated spectra are generally sharp, unlike vapour and condensed phase spectra, which usually show large linewidths and spectral congestion.

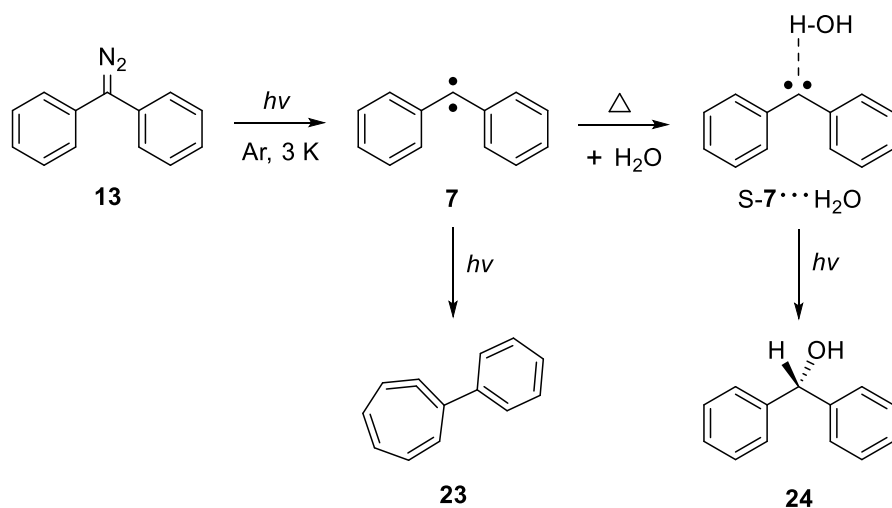
The matrix environmental effects usually perturb the spectra of trapped species to a small extent due to various reasons such as matrix trapping sites, molecular rotations, aggregations or matrix shifts.^[98] The sample molecules are trapped either in substitutional sites or interstitial holes in the matrix. Different trapping sites will have different kind of weak intermolecular forces existing between the matrix and sample. It is therefore possible that different trapping matrix sites may induce different shifts leading to broadening and splitting of bands. Although free rotations are inhibited in the frozen matrix, quantized rotational features may be possible for small molecules which are identified by reversible intensity changes on temperature cycling. The modification in vibrational band can be observed when two or more guest species are trapped very nearby causing the overlap of respective cages to form dimers or higher aggregates. The weak interactions between trapped species and matrix material can also result in a shift in a frequency or splitting of bands. The frequency shift in a solid matrix with respect to the gas phase value arises from electrostatic, inductive, dispersive and repulsive interactions. The long range London dispersion forces and the short range repulsive forces are the two dominant interactions in inert gas matrices.

The reactive species studied by the matrix isolation technique are usually generated by two methods: 1) *in situ* generation by photodissociation of a matrix-isolated precursor and 2) external generation by flash vacuum pyrolysis where the reactive species is prepared shortly before being trapped in the matrix. Many carbenes and nitrenes have been synthesized in low temperature matrices using *in situ* generation,^[99] while the second method is particularly useful for generating radicals, since it avoid the cage effect (Scheme 8).^[100] Apart from these methods, there are various methods such as pulsed pyrolysis, carrier gas pyrolysis, etc. also available for generating reactive species.^[101] For depositing metals, laser evaporation techniques are frequently adopted.^[102]



Scheme 8. a) In situ generation of triplet *m*-diazomethylphenyl nitrene **19** and quintet *m*-methylenephényl nitrene **20** by photolysis of corresponding precursor **18**.^[103] b) External generation of benzyl radical **22** by flash vacuum pyrolysis of the precursor **21**.^[104]

Apart from the isolation of analyte molecules, the matrix isolation technique also can be used to study bimolecular reactions. In that case, the matrix containing the analyte can be additionally doped with an appropriate reactant, particularly small molecules. Noble gas matrices become softer upon raising the temperature from 4 K to higher temperatures (e.g. 25 – 30 K for argon) and allow the diffusion of small molecules, making it possible to spectroscopically investigate their interactions. In addition, photochemically induced reactions can also be studied using the matrix isolation techniques. The reaction of triplet diphenylcarbene **7** with water and photoinduced ring expansion of **7** are examples of the versatility of this technique (Scheme 9).^[105-106]



Scheme 9. Reaction of diphenylcarbene **7** with water and its rearrangement to 1-phenyl-1,2,4,6-cycloheptatetraene **23** using the matrix isolation technique.^[105-106]

1.5. Mass Spectrometry

Mass spectrometry has become a powerful tool for investigating gas phase properties of organic compounds due to newly developed ionization methods, such as electrospray ionization (ESI).^[107] In chapter 7 of this dissertation, liquid chromatography quadrupole instrument is used in combination with an ESI ionization source and a quadrupole mass analyzer to measure proton affinity (PA) of carbenes.

The electrospray ionization-mass spectrometry (ESI-MS) technique was developed by John Brennet Fenn in the 1980s.^[108-109] An electrospray ionizes the sample at atmospheric pressure and is often considered as ‘soft ionization’ method, since the process often generates a molecular ion or pseudo molecular ion without fragmentation. In this process, the electrospray is generated under atmospheric conditions by applying a strong electric field to a slow flow of solution (Figure 4). The solution containing protonated carbene species in a volatile solvent such as methanol is injected into a stainless steel or silicon capillary. The solution is pushed through the capillary by a pump at a speed of 1 – 1000 $\mu\text{L}/\text{min}$ and comes out at the end of capillary tip. Between the capillary tip and counter electrode or heated capillary, a potential difference of 3 – 6 kV is applied. The capillary tip and the counter electrode is usually separated by 0.3 – 2.0 cm, thus a very strong electric field is generated in the atmospheric region between the tip and the counter electrode.^[110]

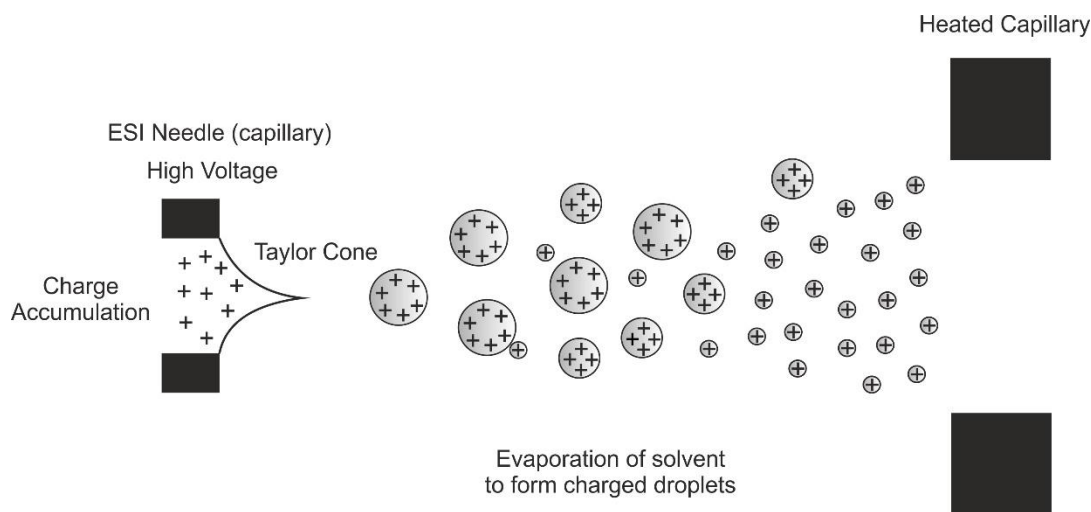


Figure 4. Process of electrospray ionization^[110]

Due to the strong electric field of the capillary tip, charged ions accumulate at the end of the capillary tip and form a conical shape named ‘Taylor cone’. The solution can break to form highly

charged droplets at the Taylor cone.^[111] Being directed by the electric field, the charged droplet can travel from the capillary to the heated capillary. During this process, the evaporation of solvents from the droplet can increase the repelling coulombic force of the ions to reach a limit, at which the droplet becomes unstable and breaks into even smaller droplets. Eventually, all solvent is evaporated and the ionized carbenium ions are released into the quadrupole mass analyzer.

The quadrupole ion trap is a mass analyzer with high sensitivity and specificity,^[112] which was invented by Wolfgang Paul who received the Nobel Prize in 1989 for his work.^[113] This configuration of the ion trap is also known as 3D (Paul) trap. The 3D trap consists of three hyperbolic electrodes, one ring and two end cap electrodes (Figure 5). Initially, the ions generated by ESI are focused using two Octapole transmission systems (Ion Focusing), then the ions can be trapped, excited and ejected in the cavity formed by these three electrodes that are applied by both AC and DC (Ion analysis). Each endcap electrode has a small hole through which ions can travel in and out. Helium (~ 1 mTorr) is introduced in the ion trap to dampen the kinetic energy of hot ions. The additional gas inlet is attached to the 3D ion trap for injecting the vapors of reference bases. The reference base can react with the carbenium ion to generate the protonated base species. With aid of AC applied to the ring electrode, all the ionic species move towards the center of the ion trap. By altering the amplitude of the AC, the ions are activated and ejected through the holes in the endcap electrodes according to their mass-to-charge ratios. At last, the separated ions are detected by a collision dynode and an electron multiplier system (Detection).^[114]

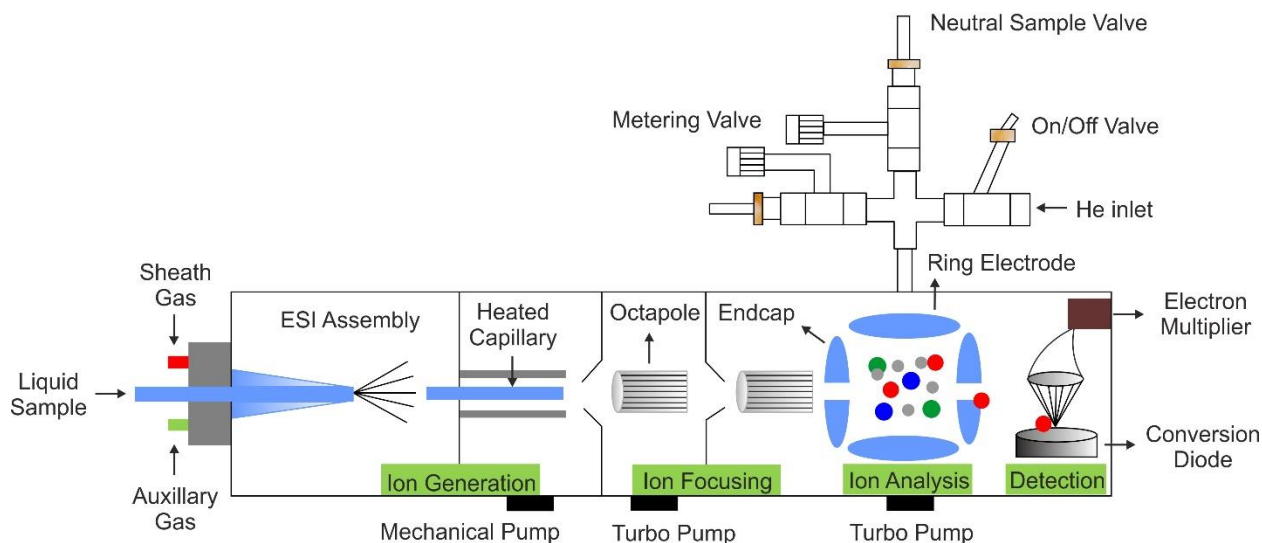
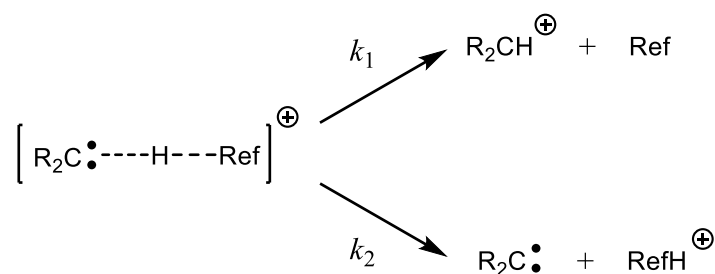


Figure 5. Schematic of the house-modified liquid chromatography quadrupole mass spectrometer (LCQ-MS).

Two methodologies are generally used to determine the PA of carbenes and other organic base compounds: bracketing method and Cook's kinetic method. The bracketing method uses the bases with known PAs as the reference bases.^[115-117] By changing the voltages of parallel metal plates, the gas phase carbenium ions are transferred from the cell on the left 'source cell' to the cell on the right 'analyzer cell' to react with the neutral reference base. By monitoring the proton transfer reaction between the protonated carbene species and references, the PA of the carbene can be compared to that of the reference base. For example, if a protonated carbene can be deprotonated by a reference base, then the PA of the carbene should be lower than the PA of the reference base. By using a series of reference bases, the PA of carbene or base compound can be bracketed into a narrow range and thus can be measured. A detailed description of the bracketing method is given in Chapter 7, where the PA of one of the arylcarbenes is bracketed employing this method.



Scheme 10. Collision induced dissociation of proton-bound complex of a carbene and reference base.^[118-119]

Cook's kinetic method requires the formation of a hydrogen-bonded dimer between carbene and reference base. This dimer is isolated in the gas phase and subjected to collision induced dissociation (CID). It is assumed that only two fragmentation pathways can occur upon CID which gives the protonated carbene and protonated reference base respectively (Scheme 10).^[118-120] With these assumptions, the kinetic features of the two pathways can be used to calculate the PA of the carbene. The ratio of the rate constants for the two fragmentation pathways (k_1/k_2) can be represented by the relative ion abundance of the product ion. The PA of the carbene under study relative to the references can be calculated using Eq. 1,^[114] in which T_{eff} is the effective temperature of the proton-bound dimer in Kelvin. By plotting the natural logarithm of k_1/k_2 versus the known PA for a series of reference bases, the PA of the carbene or base under study equals to the intercept of the resulting straight line.

$$\ln(k_1/k_2) = -(PA_{\text{ref}} - PA_{\text{carbene or base}}) / RT_{\text{eff}} \quad (1)$$

2. Reactions of Arylcarbenes with Lewis Acids

2.1. Introduction

Diphenylcarbene **7**, fluorenylidene **8** and dibenzocycloheptadienyliene **25** are similar looking triplet ground state arylcarbenes that differ in descriptors determining carbene reactivity: the geometry, the singlet-triplet gap ΔE_{S-T} ,^[121-122] the philicity (electrophilicity vs. nucleophilicity),^[123] and the basicity (or proton affinity).^[31]

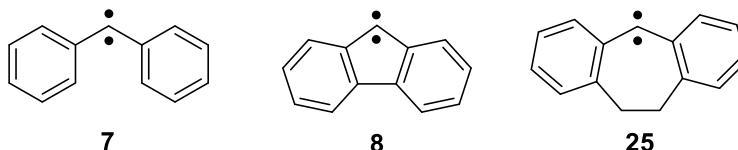


Chart 4. Representative structures of diphenylcarbene **7**, fluorenylidene **8** and dibenzocycloheptadienyliene **25**.

The arylcarbenes **7**, **8** and **25** have been investigated extensively by time-resolved spectroscopy in solution,^[124] by low-temperature spectroscopy in organic glasses,^[125] and in inert gases matrices,^[126] and by computational methods.^[127] By time-resolved fluorescence spectroscopy, ΔH_{S-T} of **7** in isooctane at room temperature was determined to 4.6 ± 0.3 kcal mol⁻¹, which is lowered to 3.2 ± 0.3 kcal mol⁻¹ in the more polar acetonitrile.^[128] In similar experiments, ΔH_{S-T} of **8** and **25** in acetonitrile were determined to 1.1 and 4.9 kcal mol⁻¹, respectively.^[47, 129] Wright and Platz have investigated the reactions of these arylcarbenes in methanol matrices at 77 K and correlated ΔE_{S-T} of these carbenes from the ratios of the resulting O–H and C–H insertion products. Carbene **25**, which showed the least amount of O–H insertion product and maximum amount of C–H insertion product was determined to have a larger singlet-triplet gap as compared to **7** and **8**.^[130] The larger S-T gap of **25** relative to **7** and **8** can be rationalized by the larger bond angle at the carbene center. The phenyl rings in **8** are fixed in a planar conformation, whereas in **7** the phenyl rings are twisted to adopt a propeller-like conformation to avoid steric repulsion of the *ortho* hydrogen atoms. In **25**, the *ortho* positions of the phenyl rings are bridged by an ethano linker leading to a larger bond angle at the carbene center and a reduced conformational flexibility. The energy of the singlet state of carbenes increases rapidly as the angle at the carbene center increases due to loss of s-character in σ -orbital, whereas the energy of the triplet state is less sensitive to angular distortion.^[130] Carbene **8** contains a conjugated five-membered ring that is expected to be destabilized by antiaromaticity if positive charge builds up in the π -system. This should lead to a destabilization of the singlet state, however, the smaller S-T gap of **8** compared to

7 and **25** indicates that this destabilization of singlet state by antiaromaticity is overcompensated by the smaller bond angle at the carbene center. The proton affinities for the closed-shell singlet states **S-7** and **S-8** (275 and 272 kcal mol⁻¹) were estimated to be higher than that of *N*-heterocyclic carbenes (in the order of 250 kcal mol⁻¹),^[131-132] making the closed-shell singlet carbenes one of the strongest neutral bases.^[8] Lewis acids can strongly interact with the in-plane lone pair of such carbenes and selectively stabilize the singlet states.^[133] This can be utilized to switch the spin state of carbenes from triplet to singlet and thus to control carbene reactivity.^[3]

Under the conditions of matrix isolation at cryogenic temperatures, all three carbenes **7**, **8** and **25** show triplet ground states that have been characterized by EPR spectroscopy.^[134-135] Recently, it was found that interaction of matrix-isolated triplet diphenylcarbene **T-7** with a single molecule of water^[1] or methanol^[105] results in the formation of strong hydrogen-bonded complex **S-7**⋯H-OR (R = H or CH₃), switching the spin state of carbene from triplet to singlet. However, the hydrogen-bonded singlet carbene complexes are only metastable, and upon irradiation slowly rearrange to form the corresponding O-H insertion products. The halogen bond donor ICF₃ stabilizes the singlet state **S-7** in a similar fashion by forming the halogen-bonded complex **S-7**⋯I-CF₃.^[2] Interaction of **T-7** with the much stronger Lewis acid BF₃ leads to a formation of a highly stabilized Lewis adduct **S-7**⋯BF₃, composed of a positively charged benzhydryl unit and a negatively charged BF₃ fragment.^[3]

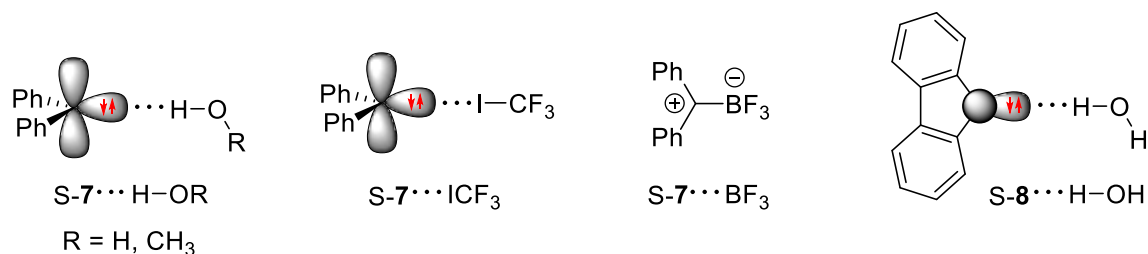


Chart 5. Singlet state complexes of **7** with H₂O, MeOH, ICF₃ and BF₃, and **8** with H₂O.

This reactivity pattern is not limited to carbene **7**, the smaller S-T gap in **8** makes the spin inversion quite obvious. As expected, the reaction of the triplet state of fluorenylidene **T-8** with a single molecule of water also results in the formation of the hydrogen-bonded singlet carbene complex **S-8**⋯H-OH.^[4] However, the reactions of **8** with stronger Lewis acids should exhibit intriguing chemistry. The fluorenyl unit is expected to be destabilized upon interaction with BF₃ due to accumulation of positive charge at the carbene center leading to antiaromaticity. Moreover, the

singlet state of dibenzocycloheptadienylidene **25** has not been observed due to its larger S-T gap which should make switching of spin state more difficult. To gain more insight into reactivity of carbenes towards Lewis acids, we therefore investigated the reactions of **8** with ICF₃ and BF₃ and of **25** with H₂O, ICF₃ and BF₃.

2.2. Results and Discussion

2.2.1. Computations of S-T gaps of Arylcarbenes

The singlet-triplet energy separation in carbenes is a function of bond angle at the carbene center. According to calculations at the B3LYP-D3/def2-TZVP level of theory, the central carbene bond angle decreases from 141.6° in T-**7** to 119.4° in S-**7**. The smaller bond angle in S-**7** indicates a larger s-character of the lone pair (σ -orbital) as compared to the SOMO in T-**7**. Fluorenylidene **8** has a fixed planar conformation in both spin states S-**8** and T-**8**, and bond angle at the carbene center is therefore restricted to smaller values as compared to **7**. It can be seen that the carbene central angle is not varied much, as it is decreased by only 11° from T-**8** to S-**8**. On the other hand, the seven-membered ring in dibenzocycloheptadienylidene is predicted to have carbene central bond angle of 142.6° in T-**25**, similar to that in T-**7**, and of 126.1° in S-**25**, larger than that of S-**7** and S-**8**. Accordingly, the energy of S-**25** raises relative to T-**25**, leading to larger S-T energy separation in **25** (Figure 6).

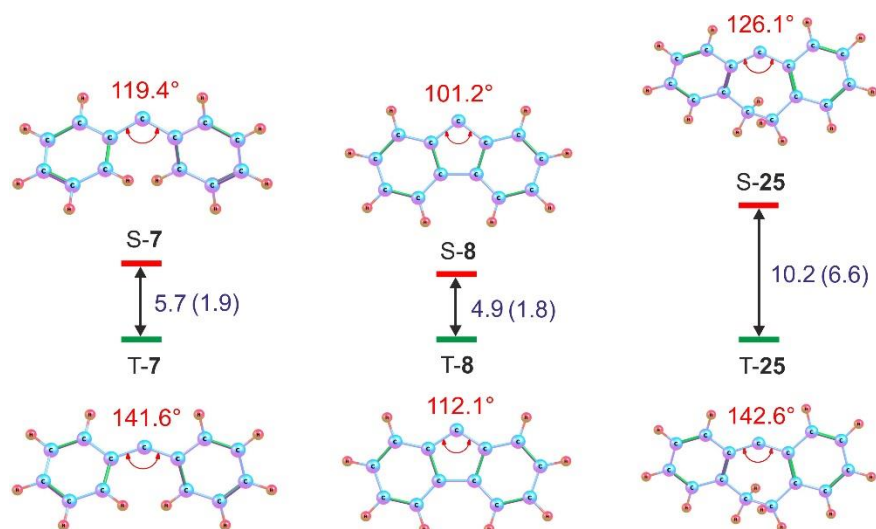


Figure 6. Singlet-triplet gaps (kcal mol⁻¹) of **7**, **8** and **25** and their bond angles at the carbene centers computed at the B3LYP-D3/def2-TZVP level of theory. Values in parenthesis correspond to singlet-triplet gaps computed at the CCSD(T)/def2-TZVP//B3LYP-D3/def2-TZVP level of theory.

The computations of the S-T gaps of **7**, **8** and **25** were performed at the B3LYP-D3/def2-TZVP and CCSD(T)/def2-TZVP//B3LYP-D3/def2-TZVP level of theory (Table 2, Figure 6). Since the B3LYP functional overestimates ΔE_{S-T} by 2 – 3 kcal mol⁻¹, depending on the basis sets and the gaps calculated with CCSD(T) seem to be underestimated, an empirical correction suggested by Woodcock et al.^[136] was employed on the S-T gaps computed at the B3LYP-D3/def2-TZVP level of theory. The correction of 2.32 kcal mol⁻¹ was obtained by taking the difference between the computed S-T energy gap of methylene at the B3LYP-D3/def2-TZVP level of theory (11.37 kcal mol⁻¹) and its accurately determined experimental S-T gap (9.05 kcal mol⁻¹).^[13] If we take this correction into account, then S-T gaps of **7**, **8** and **25** are estimated to be 3.4, 2.6, and 7.9 kcal mol⁻¹, respectively, in reasonable agreement with experimental data. The stabilization energies of the most stable complexes of **7**, **8** and **25** in both spin states with H₂O, ICF₃ and BF₃ were also computed as shown in Table 2, which are discussed in next sections describing the reactions of these carbenes with the respective Lewis acids.

Table 2. Calculated singlet-triplet energy gaps (ΔE_{S-T}) of **7**, **8** and **25** and binding energies of the most stable singlet and triplet complexes with H₂O, ICF₃ and BF₃. Energies in kcal mol⁻¹.

#	$\Delta E_{S-T}^{[a]}$	$\Delta E_{S-T}^{[b]}$	$\Delta E_{S-T}^{[c]}$	H ₂ O complexes ^[d]		ICF ₃ complexes ^[d]		BF ₃ complexes ^[d]	
				S	T	S	T	S	T
7	5.7	1.9	3.4	-9.3	-4.1	-14.4	-5.0	-36.2	-3.8
8	4.9	1.8	2.6	-10.0	-3.4	-22.4	-4.9	-41.9	-3.7
25	10.2	6.6	7.9	-11.5	-3.9	-14.6	-5.4	-36.2	-4.3

^aB3LYP-D3/def2-TZVP. ^bCCSD(T)/def2-TZVP//B3LYP-D3/def2-TZVP. ^cCorrection of 2.32 kcal mol⁻¹ to adjust for the difference between the experimental and the B3LYP computed S-T gap for CH₂. ^dEnergy of complex formation, B3LYP-D3/def2-TZVP.

2.2.2. Reaction of Dibenzocycloheptadienylidene with H₂O.

Previously, the bimolecular reactions of triplet ground state carbenes **7** and **8** in argon matrices doped with 1% of H₂O showed the formation of the corresponding hydrogen-bonded singlet carbene complexes by switching the spin states of the carbenes from triplet to singlet.^[1, 4] The reaction of carbene **25** with H₂O was therefore studied under similar conditions. Prior to this, carbene **25** was characterized by IR, UV-Vis and EPR spectroscopy in pure argon matrices.

Experiments in pure argon matrices. Diazodibenzocycloheptadienylidene **26** was deposited by thermal decomposition of its sodium salt in an argon matrix at 20 K. The IR absorption at 2045.3 cm^{-1} is attributed to the asymmetric stretching vibration of C=N=N group, which is characteristic of the diazo compound **26**. Irradiation of the matrix isolated diazo precursor **26** with 530 nm at 3 K produces dibenzocycloheptadienylidene **25** in its triplet ground state. The IR spectrum is in a good agreement with a DFT calculated spectrum of T-**25** (Figure 7, Table 3).

Carbene **25** is non-planar mainly due to ethano linkage and therefore it has two enantiomers, with one of the CH₂ groups in ethano linkage above the plane, and one CH₂ group below the plane. The activation barrier between these enantiomers is calculated to be 14 kcal mol^{-1} . In the same manner, diazo precursor **26** also has two enantiomers. Since the energies and IR frequencies of the enantiomers are same, IR experiments could not achieve the enantiomeric distinction.

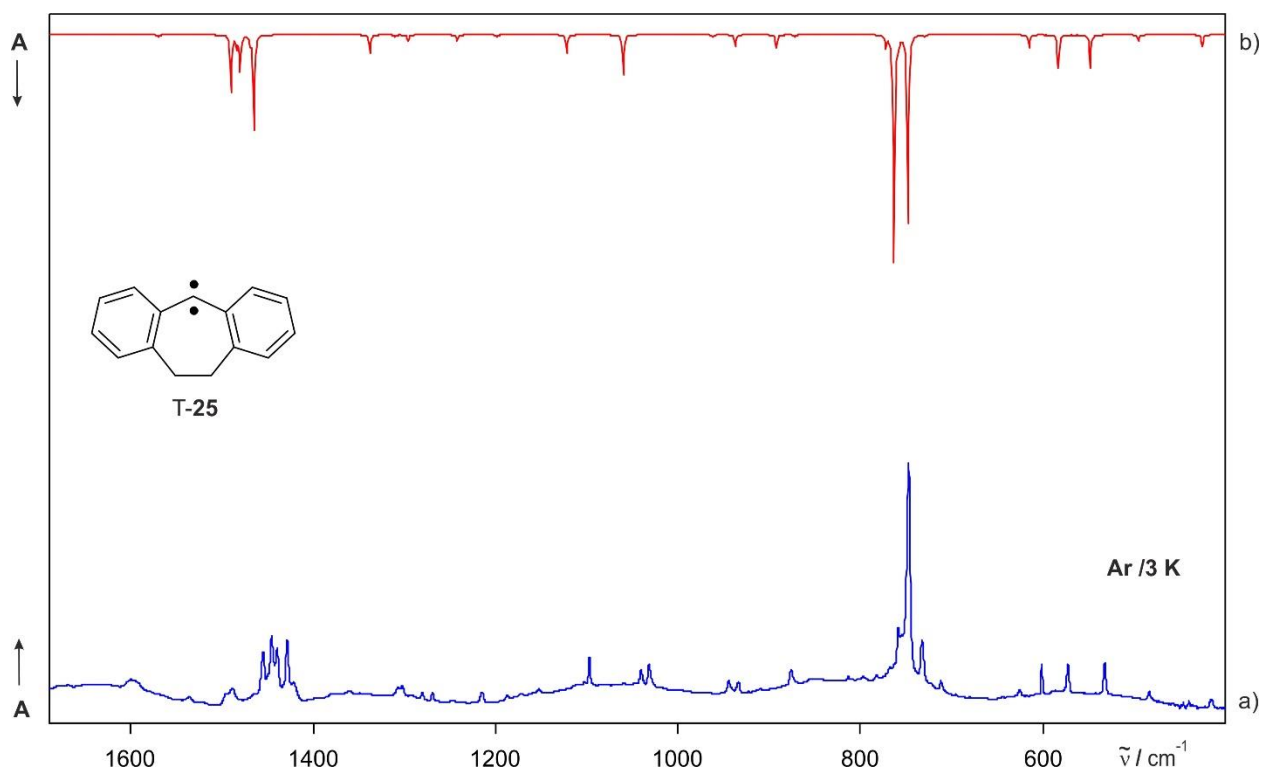


Figure 7. IR spectra of carbene **25** in its triplet ground state. a) IR spectrum obtained after 530 nm irradiation of diazo precursor **26** in an argon matrix at 3 K. b) Computed IR spectrum of T-**26** at the B3LYP-D3/def2-TZVP level of theory.

Table 3. IR vibrational frequencies of triplet dibenzocycloheptadienyliene T-25.

Mode	Sym	DFT ^[a]		Argon ^[b]		Assignment
		$\tilde{\nu}$ / cm ⁻¹	I _{rel}	$\tilde{\nu}$ / cm ⁻¹	I _{rel}	
10	B	425.4	5	415.3	4	CH ₂ bend
12	B	495.2	4	483.2	4	Ethano bridge str.
14	B	548.9	16	532.3	14	C–H bend
16	B	583.9	15	572.5	14	C–H bend
17	B	615.5	9	601.2	15	Ring def.
21	B	748.9	81	732.6	20	C–H wagging
23	B	763.5	100	747.3	100	C–H wagging
24	B	772.3	6	758.8	27	Ring def.
28	B	892.1	9	876.3	7	CH ₂ bend
30	B	937.5	6	934.3	7	C–H wagging
36	B	1060.9	22	1031.9 + 1040.8	17	Ring def.
38	A	1122.1	10	1097.3	13	C–H bend
50	A	1338.2	10	1302.5 + 1307.6	14	C=C stretch

^[a]Calculated at the B3LYP-D3/def2-TZVP level of theory. ^[b]Argon matrix at 3 K.

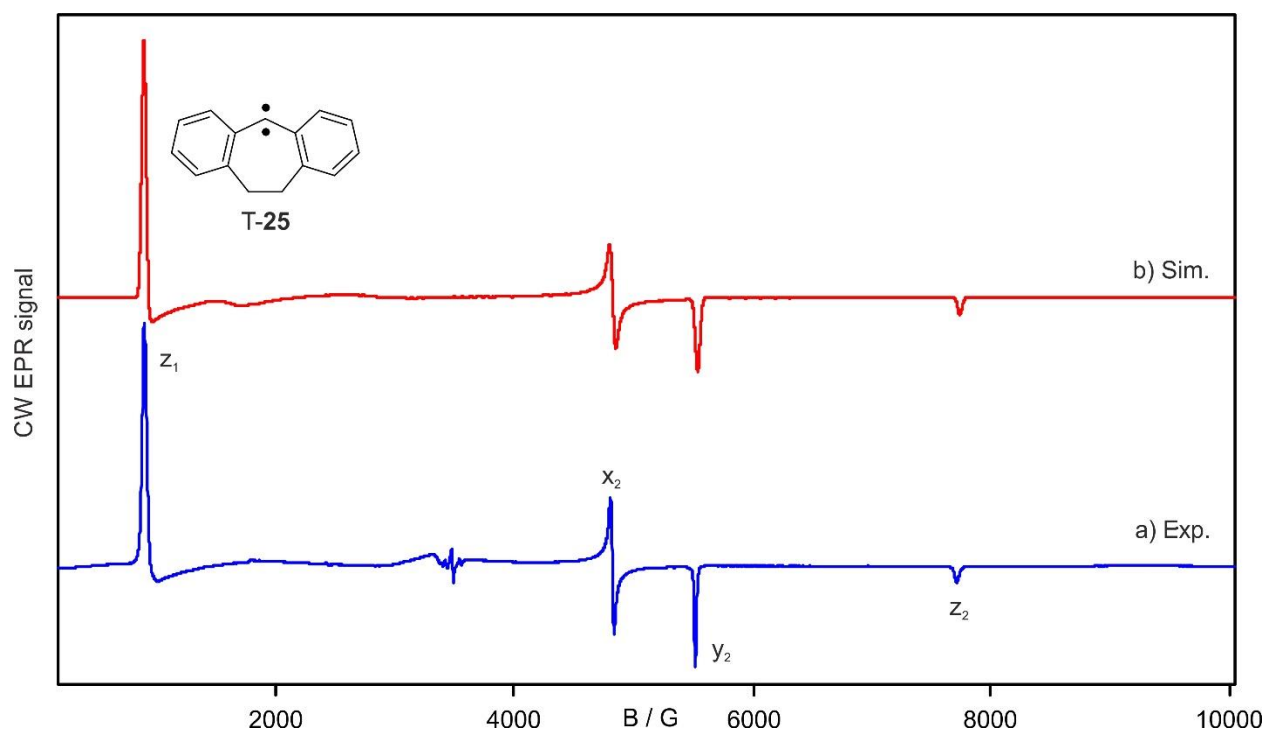


Figure 8. EPR spectra of the carbene **25** in its triplet ground state. a) X-Band CW EPR spectrum obtained after 530 nm irradiation of diazo precursor **26** in an argon matrix at 3 K. b) Simulated EPR spectrum of T-**25** with zfs parameters $|D/hc| = 0.398$ cm⁻¹ and $|E/hc| = 0.018$ cm⁻¹.

The formation of **25** in its triplet state was also followed by EPR spectroscopy. Irradiation of diazo precursor **26** with 530 nm in an argon matrix at 5 K produces the characteristic signals of T-**25** with zero field splitting parameters $D = 0.398 \text{ cm}^{-1}$, $E = 0.018 \text{ cm}^{-1}$ (Figure 8), in good agreement with Moritani et al.'s pioneering study of carbene **25** in organic glasses at 77 K ($D = 0.393 \text{ cm}^{-1}$, $E = 0.017 \text{ cm}^{-1}$).^[134]

In the same manner, UV-Vis spectra showed the formation of T-**25** with strong absorptions observed at $\lambda_{\text{max}} = 302, 320$ and 332 nm and a weak visible absorption centered at $\lambda_{\text{max}} = 500 \text{ nm}$ (Figure 9), consistent with flash photolysis studies of **25** by Moritani^[137] and Platz.^[138] The characteristic visible absorption of T-**25** is assigned to an electronic transition from π -orbital of the carbene carbon to the antibonding π -electrons of the adjacent phenyl rings, which is in reasonably agreement with TD-DFT calculations ($\lambda = 435 \text{ nm}$, $f = 0.0068$). No new signals were detected after the irradiation with different wavelengths between 650 and 254 nm at 3 K, suggesting the stability of T-**25** in argon matrix under these conditions.

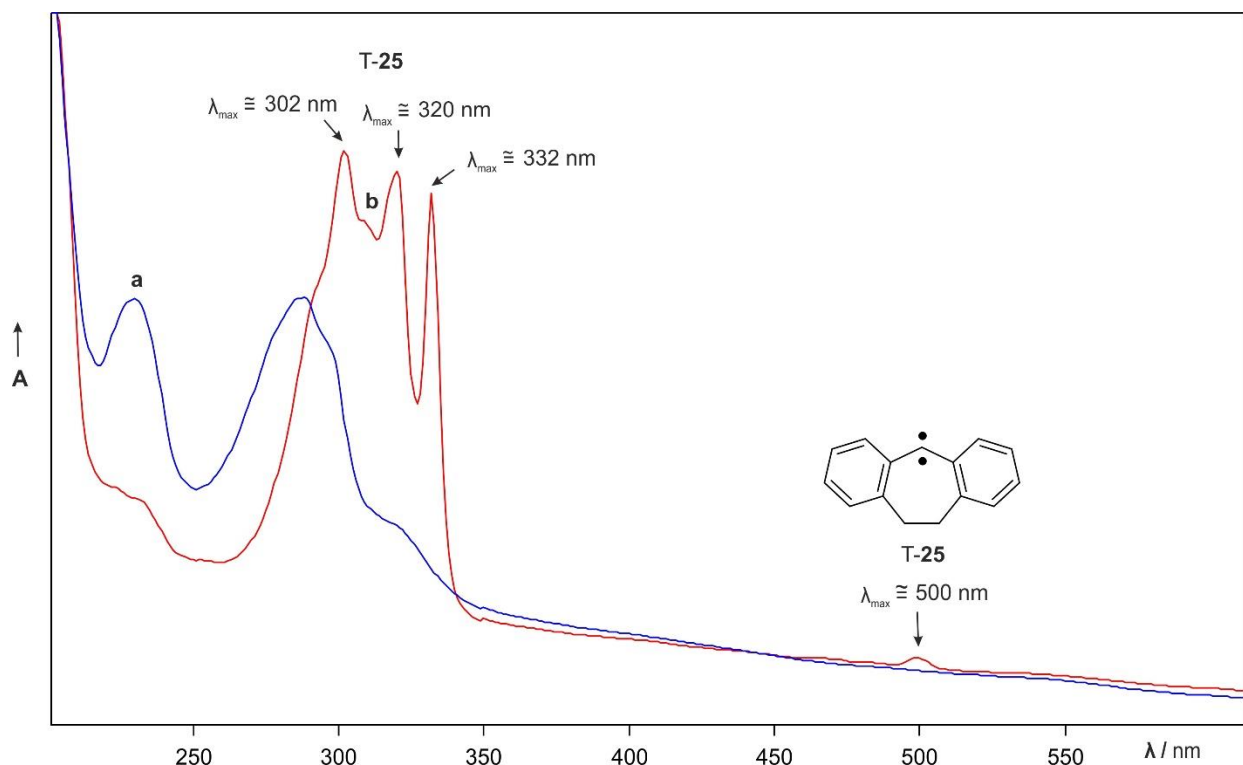


Figure 9. UV-Vis spectra showing the formation of carbene **25** in its triplet ground state. a) UV-Vis spectrum of diazodibenzocycloheptadienyliene **26** isolated in an argon matrix at 8 K. b) UV-Vis spectrum of T-**25** generated upon 530 nm irradiation of the same matrix, in a good agreement with literature spectra.^[137-138]

Experiments in argon matrices doped with 1% of H₂O. Visible light photolysis (530 nm) of dibenzocycloheptadienylidene **26** in argon doped with 1% of H₂O at 3 K produces triplet carbene T-**25** in high yields and no traces of reaction products between **25** and H₂O were observed. Annealing at 25 – 30 K allows H₂O to diffuse in argon matrix, and leads to a decrease in intensities of the IR bands of isolated water molecules accompanied by an increase of IR bands of dimers and higher aggregates. Several bands of T-**25** are slightly shifted and decrease in intensity, most likely due to small conformational changes taking place on annealing. The hydrogen-bonded singlet carbene complex **27** (S-**25**···H₂O) is predicted to show a strong C–C–C asymmetric stretching vibration at 1384.3 cm⁻¹, and a similar vibration was experimentally observed at 1327.8 cm⁻¹ for S-**7**···H₂O.^[1] However, no such feature is observed in the experiments. The formation of the most stable triplet water complex **28a** is also not observed due to less intense bands appearing on annealing (Figure 10).

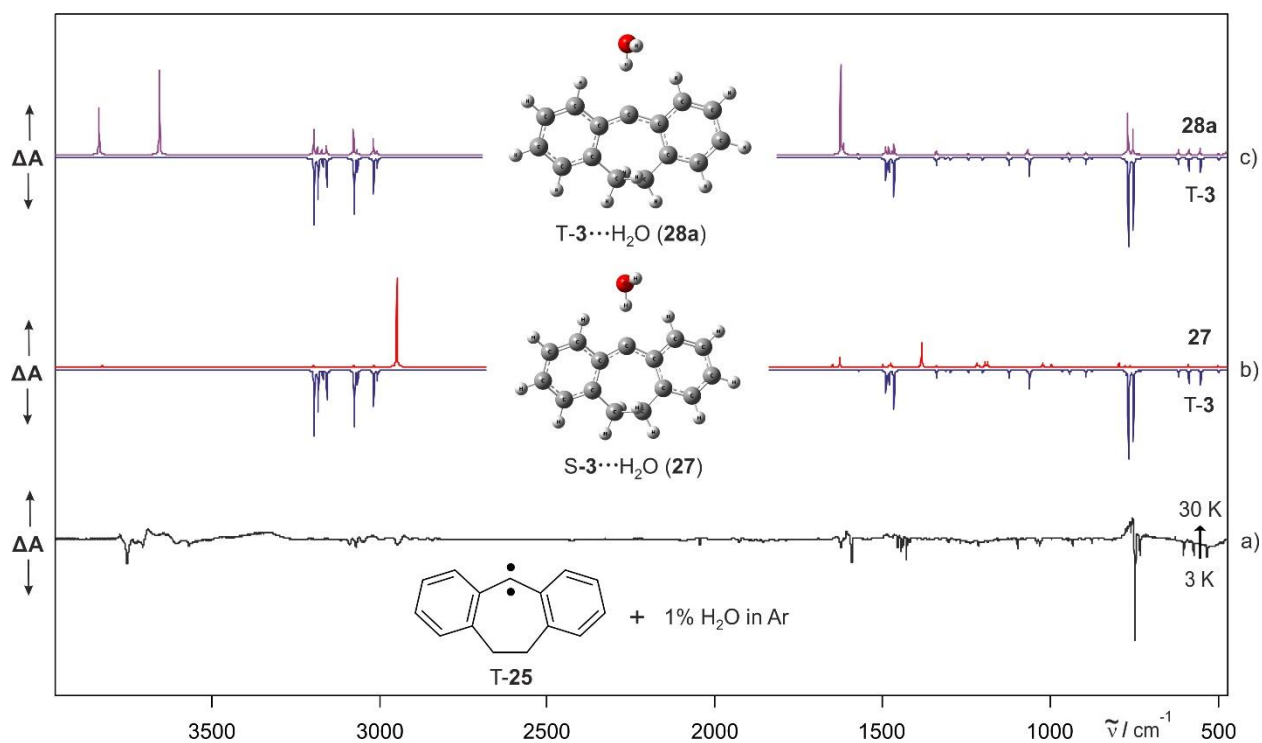


Figure 10. IR spectra showing the reaction of T-**25** with H₂O. a) Difference IR spectrum of an argon matrix doped with 1% of H₂O containing T-**25**, showing changes after annealing at 30 K. Bands pointing downwards assigned to T-**25** and H₂O are disappearing. b) Computed IR spectrum of T-**25** (multiplied by -1, peaks pointing downwards) and computed IR spectrum of singlet water complex **27** (peaks pointing upwards) at the B3LYP-D3/def2-TZVP level of theory. c) Computed IR spectrum of T-**25** (multiplied by -1, peaks pointing downwards) and computed IR spectrum of triplet water complex **28a** (peaks pointing upwards) at the B3LYP-D3/def2-TZVP level of theory.

It is important to note that the shifts observed for the computed vibrational features of T-**25** and water with respect to computed vibrational bands of the possible triplet complexes **28a** and **28b** are very small, suggesting weak interactions of T-**25** with H₂O (Figure 11).

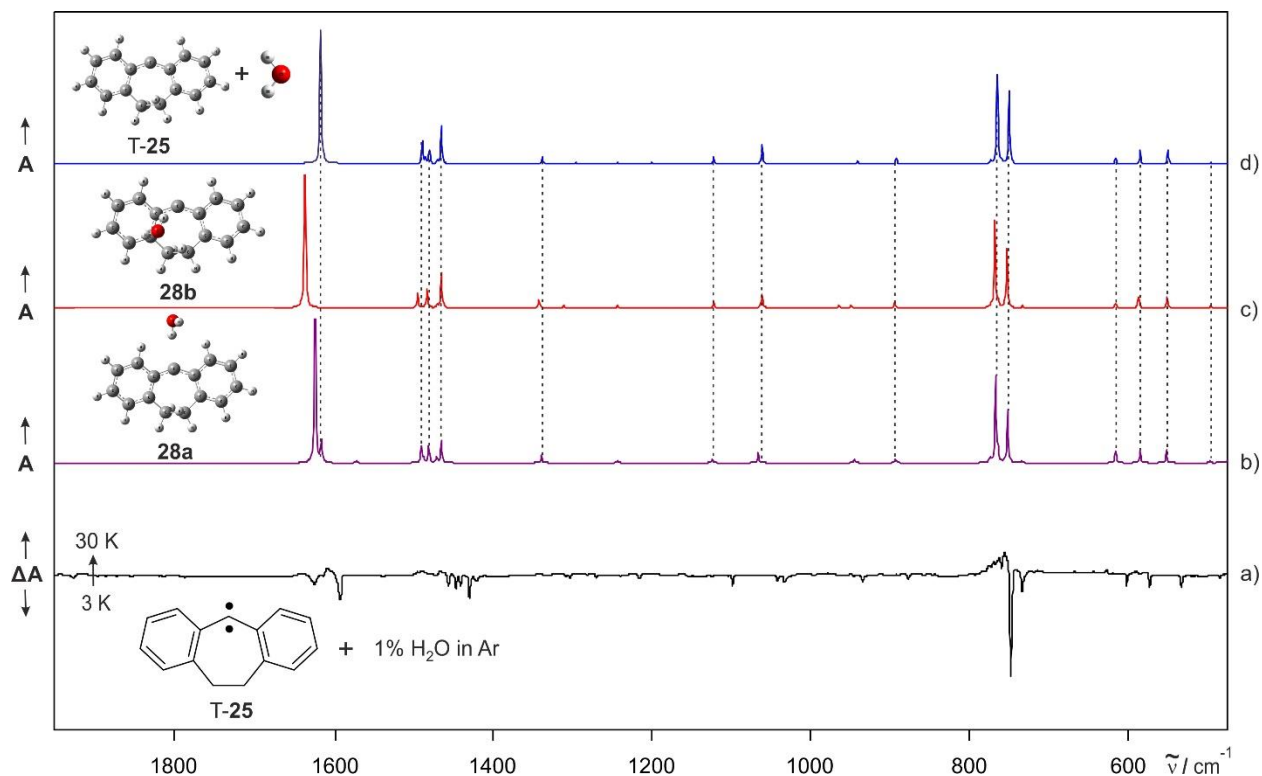


Figure 11. IR spectra showing possible weak complexes formed between T-**25** and H₂O. a) Difference IR spectrum of an argon matrix doped with 1% of H₂O containing T-**25**, showing changes after annealing at 30 K. Bands pointing downwards assigned to T-**25** and H₂O are disappearing. b) Computed IR spectrum of the most stable triplet water complex **28a** at the B3LYP-D3/def2-TZVP level of theory. c) Computed IR spectrum of triplet water complex **28b** at the B3LYP-D3/def2-TZVP level of theory. d) Superposition of computed IR spectra of T-**25** and H₂O at the B3LYP-D3/ def2-TZVP level of theory.

The reaction of T-**25** with water was also studied by UV-Vis spectroscopy under similar conditions (Figure 12). On annealing of an argon matrix doped with 1% of H₂O containing T-**25** at 30 K, the intensity of the characteristic UV and visible absorptions of T-**25** ($\lambda_{\text{max}} = 302, 320, 332$ and 500 nm) decrease and a very broad absorption centered around 396 nm appears (Figure 12c). However, it must be noted that the same broad absorption is observed upon annealing of an argon matrix containing T-**25** at 30 K (Figure 12d), which is therefore not related to the interaction between T-**25** and water molecules. Thus, both IR and UV-Vis experiments show no evidence signifying the formation of the hydrogen-bonded singlet carbene complex **27**.

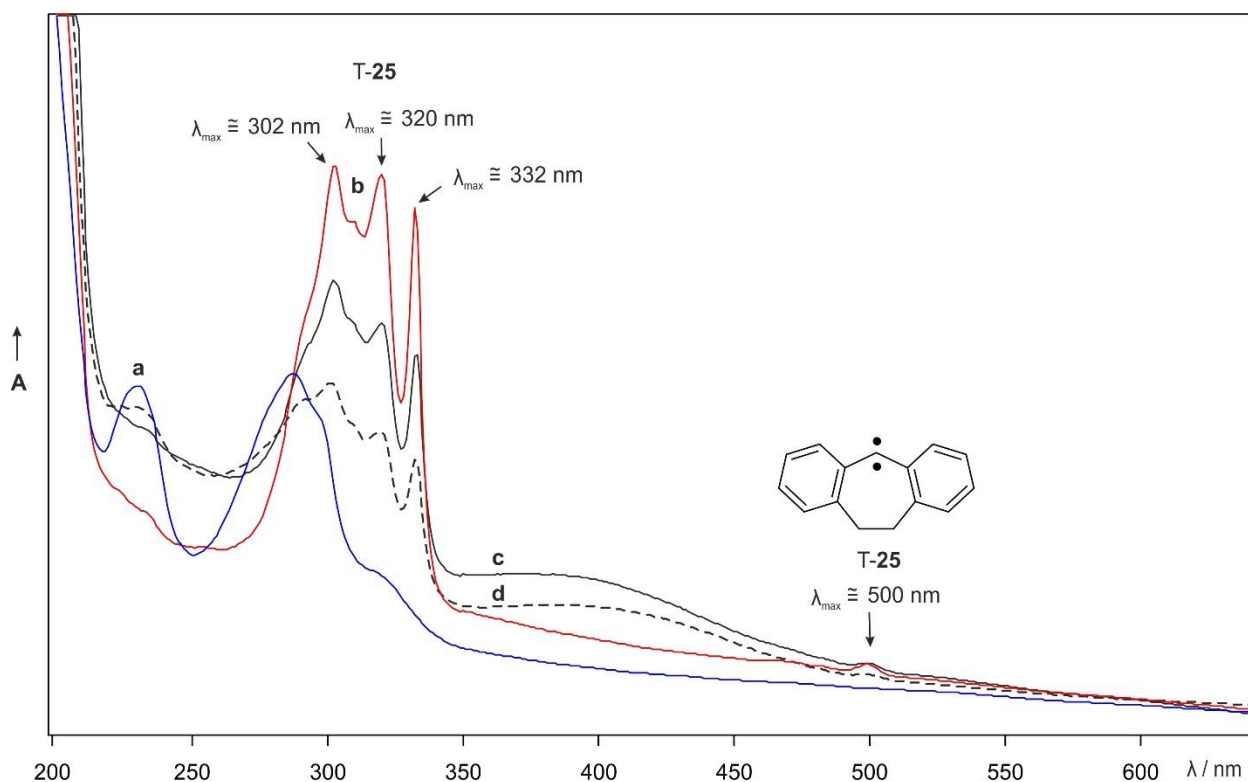


Figure 12. UV-Vis spectra showing the reaction of T-**25** with H₂O (except trace d). a) UV-Vis spectrum of diazo precursor **26** in an argon matrix doped with 1% of H₂O at 8 K. b) UV-Vis spectrum of T-**25** generated upon irradiation of the same matrix with 530 nm. The bands with $\lambda_{\text{max}} = 302, 320, 332$ and 500 nm are assigned to T-**25**. c) UV-Vis spectrum of the same matrix showing changes after annealing at 30 K. d) UV-Vis spectrum of T-**25** in pure argon matrix showing changes after annealing at 30 K. The argon matrices containing T-**25**, and T-**25** doped with 1% H₂O show almost the same broad absorption on annealing at 30 K, which excludes the possibility of formation of singlet water complex **27**.

Computations. At the B3LYP-D3/def2-TZVP level of theory, **25** is predicted to have a larger singlet-triplet energy separation ($10.2 \text{ kcal mol}^{-1}$) than **7** ($5.7 \text{ kcal mol}^{-1}$) and **8** ($4.9 \text{ kcal mol}^{-1}$). Highly basic S-**7**, S-**8** and S-**25** are calculated to be strongly stabilized upon hydrogen bonding interaction with water by 9.3, 10.0, and $11.5 \text{ kcal mol}^{-1}$, respectively, whereas the triplet states of the carbenes are expected to form weak van der Waals complexes with stabilization energies of $3.4 - 4.1 \text{ kcal mol}^{-1}$ (Figure 13, Table 2). For carbene **7**, the stabilization of S-**7** is larger than that of T-**7** by $5.2 \text{ kcal mol}^{-1}$, and this stabilization is slightly lower than its S-T gap of $5.7 \text{ kcal mol}^{-1}$, which therefore predicts marginal stabilization of T-**7**···H₂O relative to S-**7**···H₂O by $0.5 \text{ kcal mol}^{-1}$. In case of **8**, the difference in stabilization of S-**8** and T-**8** is $6.6 \text{ kcal mol}^{-1}$, which is larger than its S-T gap of $4.9 \text{ kcal mol}^{-1}$, due to which spin state of **8**···H₂O complex is predicted

to change from triplet to singlet. In contrast, carbene **25** is calculated to have a S-T gap of 10.2 kcal mol⁻¹, larger than the stabilization of S-**25** relative to T-**25** of 7.6 kcal mol⁻¹, and thus T-**25**···H₂O is predicted to be more stable than S-**25**···H₂O by 2.6 kcal mol⁻¹.

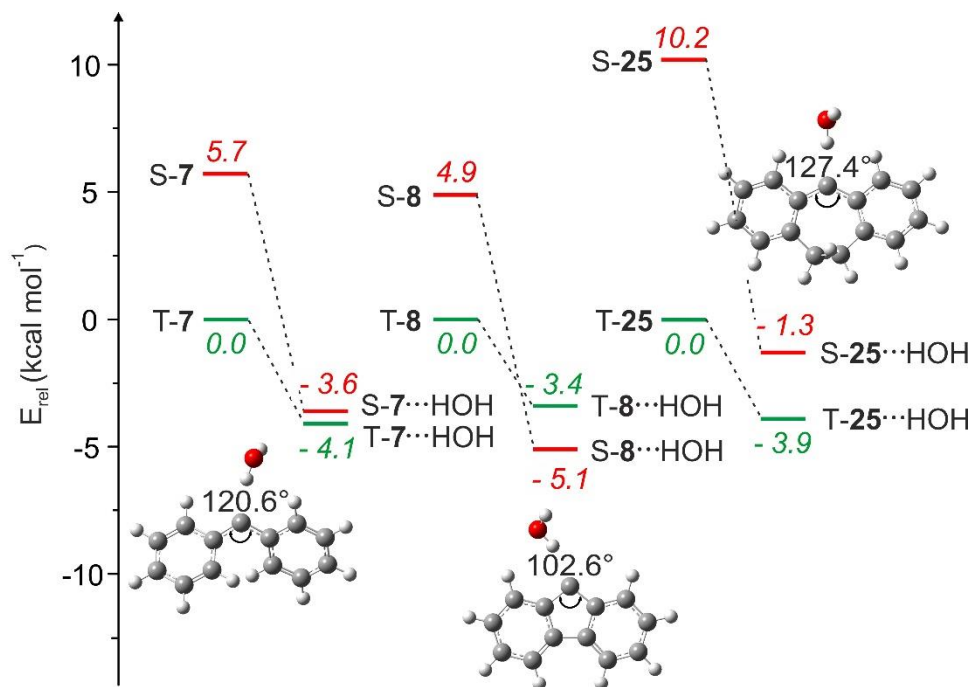


Figure 13. Relative energies (kcal mol⁻¹) of **7**, **8** and **25** in both spin states, and their most stable complexes with H₂O computed at the B3LYP-D3/def2-TZVP level of theory. Representative structures of the most stable singlet complexes are shown with their bond angles at the carbene centers.

After applying the empirical correction mentioned above, the S-T gaps of the carbenes are reduced by 2.32 kcal mol⁻¹. Consequently, the S-T gaps of **7** (3.4 kcal mol⁻¹) and **8** (2.6 kcal mol⁻¹) are now estimated to be lower than the relative stabilization of singlet as compared to the triplet states (5.2 kcal mol⁻¹ in **7** and 6.6 kcal mol⁻¹ in **8**) by 1.8 kcal mol⁻¹ and 4.0 kcal mol⁻¹, respectively. As a result, the spin states of **7**···H₂O and **8**···H₂O are expected to switch from triplet to singlet, in accordance with the experiments.^[1, 4] Even after employing the empirical correction, the S-T gap of **25** (7.9 kcal mol⁻¹) is found to be slightly larger than the difference in stabilization of S-**25** relative to T-**25** (7.6 kcal mol⁻¹) by 0.3 kcal mol⁻¹. Therefore, the singlet and triplet states of **25**···H₂O should be energetically nearly degenerate. Our experiments clearly show that a single water molecule fails to switch the spin state of **25** from triplet to singlet, in contrast to **7** and **8**.

2.2.3. Reaction of Fluorenylidene and Dibenzocycloheptadienyliidene with ICF₃.

Previous findings on interaction of **7** with halogen bond donor ICF₃ showed that the spin state of the carbene can be switched from triplet to singlet by forming a halogen-bonded singlet carbene complex $S\text{-7}\cdots\text{ICF}_3$,^[2] similar to the hydrogen bonding interaction of **7** with H₂O^[1] and MeOH.^[105] To extend this work, the reactions of carbenes **8** and **25** with ICF₃ were investigated under similar conditions. In pure argon matrices, the triplet ground state of **8** was previously characterized using IR, UV-Vis and EPR spectroscopy.^[4]

Reaction of fluorenylidene **8 with ICF₃.** Triplet carbene T-**8** is generated as main product by photolysis (365 nm) of diazofluorene **29** in an argon matrix doped with 1% of ICF₃ at 3 K. Annealing of the matrix at 30 K leads to a decrease in the IR bands of T-**8** and ICF₃, and new signals are formed. The weakly bound dimers of ICF₃ showing small shifts of the IR bands compared to that of the monomer are previously identified.^[139] Other newly formed bands are assigned to two compounds: compound **30** with the most intense signal centered at 963.5 cm⁻¹ and the formal C-I insertion product of **8** into C-I bond of ICF₃, iodotrifluoromethyl-9H-fluorene **31**, with two strong signals at 1119.6 and 1240.9 cm⁻¹.

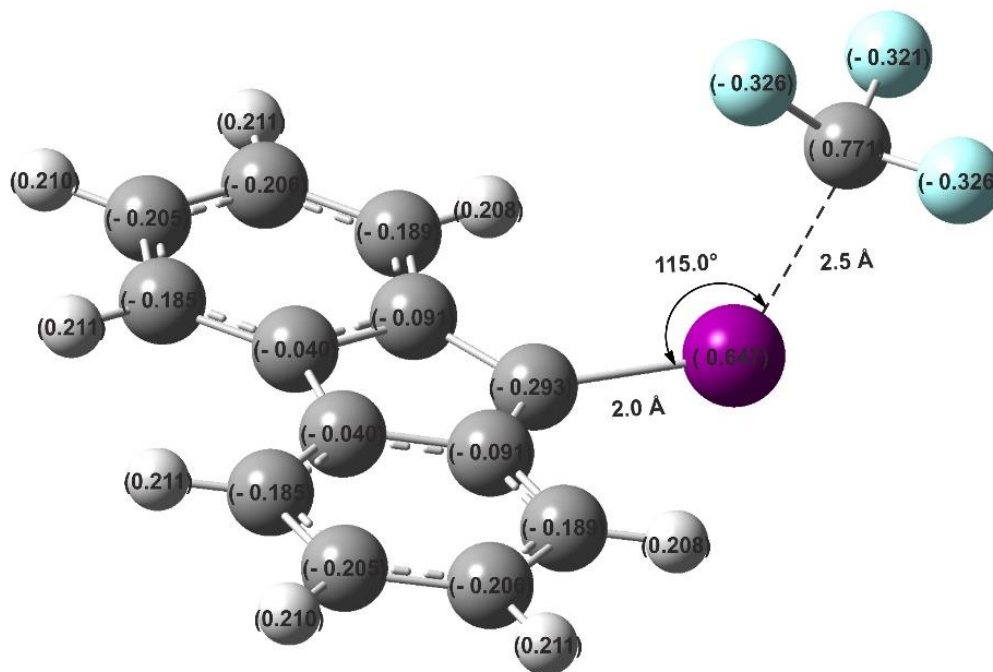


Figure 14. Structure of compound **30** formed from **8** and ICF₃ with natural charges calculated at the B3LYP-D3/def2-TZVP level of theory.

Compound **30** is predicted to have a structure different from that of the conventional singlet halogen-bonded complex **S-8**···ICF₃, as it exhibits an ylide structure with a partially positively charged iodine atom bridging the negatively charged fluorenyl unit and the weakly negative CF₃ fragment. The NBO charges on the iodine atom, the fluorene ring and the CF₃ fragment in **30** are calculated to be +0.65, -0.45, and -0.20, respectively (Figure 14). The bond length of F₃C–I (2.5 Å) in **30** is considerably longer than in uncomplexed ICF₃ (2.2 Å), indicating a substantially weakened C–I bond in **30**. It is important to note that the five-membered ring in **8** prefers to acquire a negative charge instead of acting as halogen bond acceptor. In latter case, build-up of positive charge of the ring would lead to destabilization due to antiaromaticity. Recently, similar ylides in the reactions of ICF₃ with cyclopentadienylidene and tetrachlorocyclopentadienylidene were reported.^[140] The observed IR bands formed in the reaction of **8** and ICF₃ correlate well with calculated spectra for both **30** and **31** (Figure 15c, Table 4 and Table 5).

Table 4. IR vibrational frequencies of ylide **30**.

Mode	Sym	DFT ^[a]		Argon ^[b]		Assignment
		$\tilde{\nu}$ / cm ⁻¹	I _{rel}	$\tilde{\nu}$ / cm ⁻¹	I _{rel}	
21	A'	569.5	1	556.2	5	Ring def.
26	A'	699.0	4	674.5	3	CF ₃ str.
27	A'	737.6	5	720.2	20	C–H wagging
37	A'	950.0	11	936.7	20	C–F str.
40	A'	997.2	100	963.5	100	C–H bend
57	A'	1463.9	5	1441.3	8	Ring def.

^[a]Calculated at the B3LYP-D3/def2-TZVP level of theory. ^[b]Argon matrix at 3 K.

Table 5. IR vibrational frequencies of Iodotrifluoromethyl-9H-fluorene **31**.

Mode	Sym	DFT ^[a]		Argon ^[b]		Assignment
		$\tilde{\nu}$ / cm ⁻¹	I _{rel}	$\tilde{\nu}$ / cm ⁻¹	I _{rel}	
25	A'	695.1	31	690.7	18	Ring def.
27	A'	761.5	64	732.3	48	C–H wagging
31	A'	849.7	26	873.8	17	C–I str.
35	A'	947.0	16	917.9	15	Ring def.
44	A''	1144.2	100	1119.6	100	CF ₃ str.
52	A'	1259.3	84	1240.9	92	F ₃ C–C str.
58	A''	1488.5	17	1453.7	19	C–H bend

^[a]Calculated at the B3LYP-D3/def2-TZVP level of theory. ^[b]Argon matrix at 3 K.

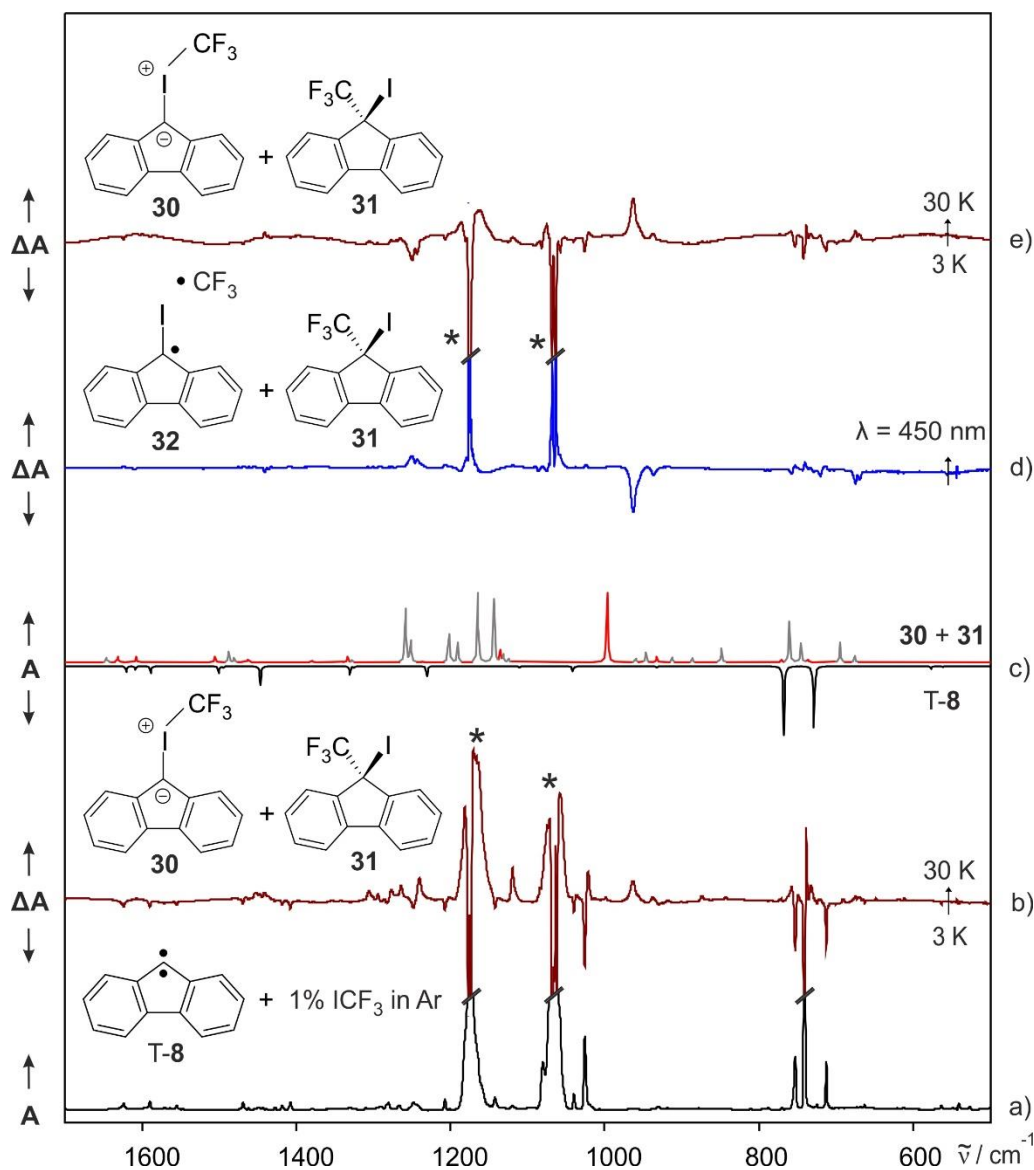


Figure 15. IR spectra showing the reaction between T-8 and ICF₃. a) IR spectrum of T-8 in an argon matrix doped with 1% of ICF₃ at 3 K. b) Difference IR spectrum of the same matrix showing changes after annealing at 30 K. Bands pointing downwards assigned to T-8 and ICF₃ are disappearing, and bands pointing upwards are assigned to ylide **30**, iodotrifluoromethyl-9H-fluorene **31**, the formal insertion product of **8** into C-I bond of ICF₃ are appearing. c) Computed IR spectrum of T-8 (multiplied by -1, peaks pointing downwards) and superposition of computed IR spectra of **30** - red line and **31** - grey line (peaks pointing upwards) at the B3LYP-D3/def2-TZVP level of theory. d) Difference IR spectrum of the annealed matrix showing the changes after 450 nm irradiation at 3 K. Bands pointing downwards assigned to ylide **30** are disappearing, and bands pointing upwards assigned to radical pair **32** and formal insertion product **31** are appearing. e) Difference IR spectrum of the same matrix showing the changes after annealing at 30 K. Bands pointing downwards assigned to radical pair **32** are disappearing, and bands pointing upwards correspond to ylide **30** and formal insertion product **31** are appearing. The bands marked with asterisks are assigned to ICF₃ and its higher aggregates.

When a matrix containing the product mixture of **30** and **31** is irradiated with 450 nm, all IR bands assigned to **30** disappear, and concomitantly triplet radical pair **32** is formed. The IR spectrum of the radical pair **32** shows the characteristic IR vibrations of the CF₃ radical at 1242.7 and 1249.9 cm⁻¹.^[139] A good agreement between experimental and calculated spectrum is observed for the radical pair **32** (Figure 16, Table 6). Further annealing of the same matrix results in a decrease of the intensities of all IR bands assigned to **32** and reappearance of the signals assigned to **30** (Figure 15e). This interconversion between **30** and **32** is found to be reproducible even after multiple cycles of annealing and irradiation. It should be noted that the formal C–I insertion product **31** is formed as byproduct during these cycles (Scheme 11). The annealing steps could generate **31** by reaction of unconsumed T-8 with ICF₃ or via recombination of triplet radical pair **32**, whereas irradiation presumably rearranges **30** to **31**. DFT calculations predict the formation of **31** from T-8 and ICF₃ to be highly exothermic by 91 kcal mol⁻¹.

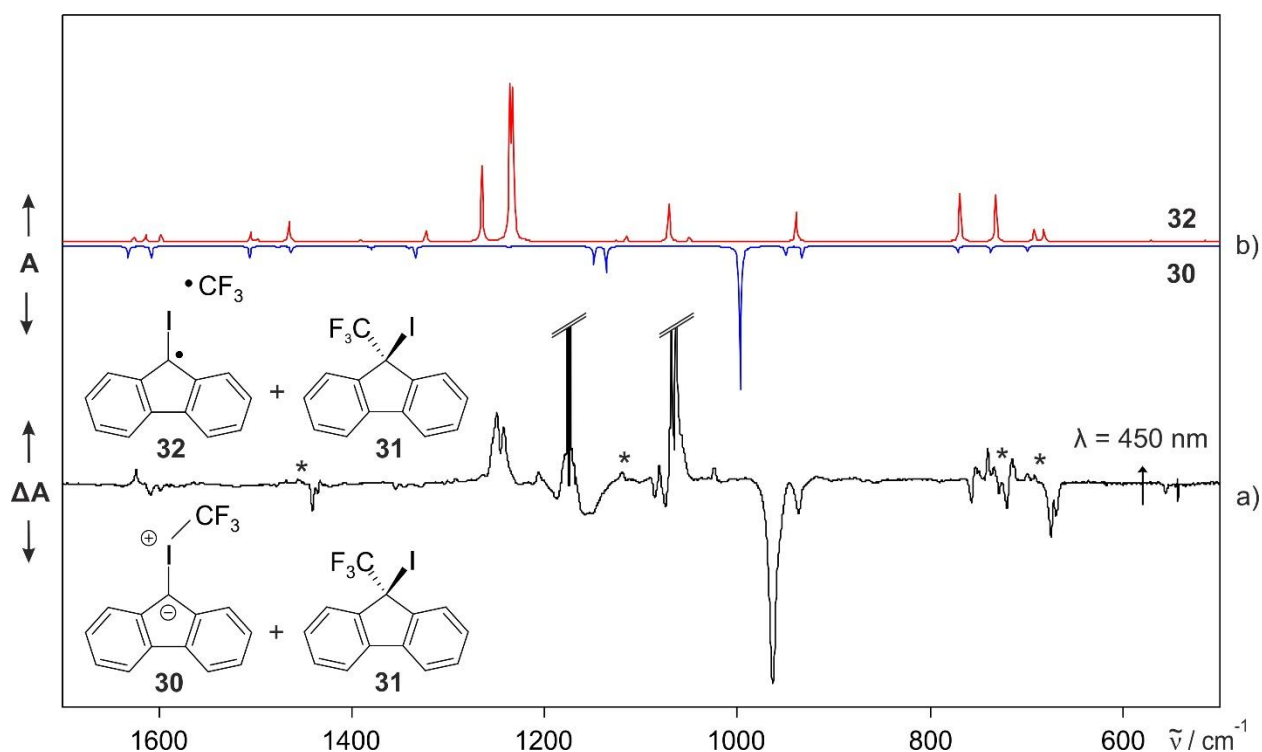
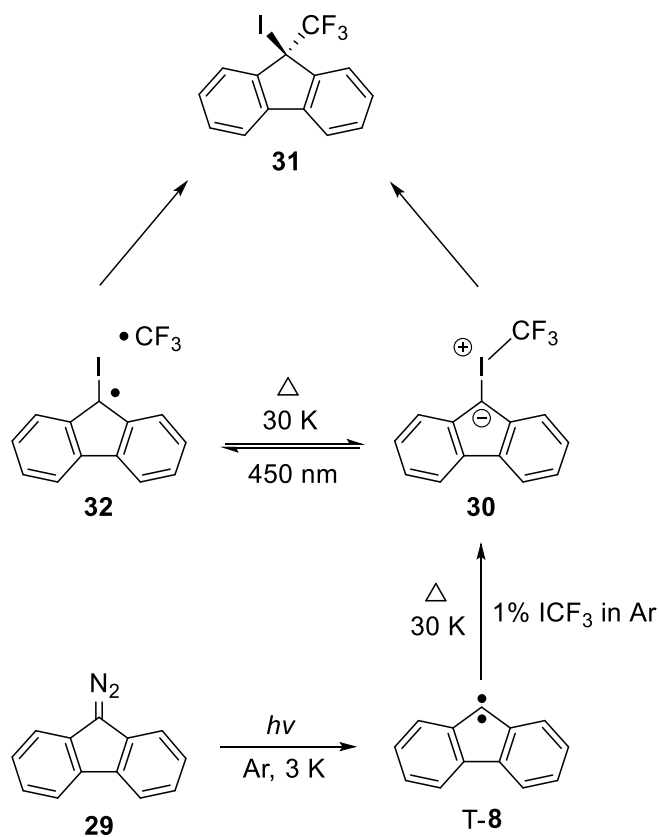


Figure 16. IR spectra showing the formation of radical pair **32**. a) Difference IR spectrum obtained after 450 nm irradiation of the matrix containing **30** and **31**. Bands marked with asterisk assigned to the formal C–I insertion product **31** are also appearing in addition to bands of triplet radical pair **32**, bands pointing downwards assigned to ylide **30** are disappearing. b) Computed IR spectrum of **30** (multiplied by -1, peaks pointing downwards) and computed IR spectrum of **32** (peaks pointing upwards) at the B3LYP-D3/def2-TZVP level of theory.

Table 6. IR vibrational frequencies of radical pair **32** formed by interaction of T-**8** and ICF₃.

Mode	Sym	DFT ^[a]		Argon ^[b]		Assignment
		$\tilde{\nu}$ / cm ⁻¹	I _{rel}	$\tilde{\nu}$ / cm ⁻¹	I _{rel}	
26	A	692.9	8	699.3	10	Sym. C–F str.
27	A	732.4	32	715.8	30	C–H wagging
30	A	769.1	33	740.5	35	C–H wagging
43	A	1071.3	25	1024.3	19	C–F str.
50	A	1233.6	96	1242.7	80	C–F str.
51	A	1236.7	100	1249.9	100	C–F str.
52	A	1265.9	52	1206.8	17	C–C–C sym. str.
53	A	1323.7	8	1292.3	7	C–H bend
58	A	1465.9	13	1433.0	8	C–H bend
60	A	1505.5	6	1468.3	5	C–H bend

^[a]Calculated at the B3LYP-D3/def2-TZVP level of theory. ^[b]Argon matrix at 3 K.


Scheme 11. Reaction of fluorenylidene **8** with ICF₃.

Reaction of dibenzocycloheptadienylidene 25 with ICF₃. The reaction of **25** with ICF₃ was studied in argon matrices doped with 1% of ICF₃ using IR, UV-Vis and EPR spectroscopy.

IR spectroscopy. The carbene is obtained in its triplet ground state T-**25** by visible light irradiation (530 nm) of a matrix containing diazo precursor **26** and 1% of ICF₃. Subsequent annealing of the matrix at 30 K gives rise to new IR bands at 772.6, 1075.2, 1307.8, 1346.5 and 1586.9 cm⁻¹ assigned to the classical ‘type I’^[141] halogen-bonded singlet carbene complex **33a**. The IR spectrum obtained after annealing matches well with calculated spectrum of **33a** (Figure 17c, Table 7). The possibility of formation of the triplet complex T-**25**···ICF₃ is excluded by comparing the spectrum after annealing with a calculated spectrum of the triplet complex. Thus, it is concluded that halogen bonding interaction of T-**25** with ICF₃ switches the spin state from triplet to singlet. The signal centered at 1346.5 cm⁻¹ is assigned to C–C–C asymmetric stretching vibration across carbene center in **33a**. In addition to IR bands of **33a**, signals at 679.5, 941.7, and 960.1 cm⁻¹ are also observed on annealing, which are assigned to unconventional ‘type II’^[141] halogen-bonded singlet carbene complex **33b**. The signal at 960.1 cm⁻¹ is assigned to C–I stretching vibration of **33b**. The halogen bonding interaction of diphenylcarbene **7** with ICF₃ under the same conditions similarly results in a formation of two types of halogen-bonded complexes, of which one has been classified as the unconventional type II halogen-bonded complex and shows a similar intense signal at 949.0 cm⁻¹.^[2]

Table 7. IR vibrational frequencies of classical type I halogen-bonded complex **33a** between S-**25** and ICF₃.

Mode	Sym	DFT ^[a]		Argon ^[b]		Assignment
		$\tilde{\nu}$ / cm ⁻¹	I _{rel}	$\tilde{\nu}$ / cm ⁻¹	I _{rel}	
27	A	585.2	4	570.3	8	C–H bend
28	A	621.9	2	606.4	9	Ring def.
36	A	793.2	8	772.6	27	C–H wagging
48	A	1069.6	100	1075.2	100	F ₃ C–I str.
51	A	1099.8	32	1101.9	26	C–F str.
59	A	1208.1	4	1186.1	10	C–H bend
65	A	1340.8	3	1307.8	7	CH ₂ bend
67	A	1376.2	57	1346.5	66	C–C–C asym. str.
73	A	1498.2	6	1461.1	11	C=C str.
77	A	1628.5	22	1586.9	29	C=C str.

^[a]Calculated at the B3LYP-D3/def2-TZVP level of theory. ^[b]Argon matrix at 3 K.

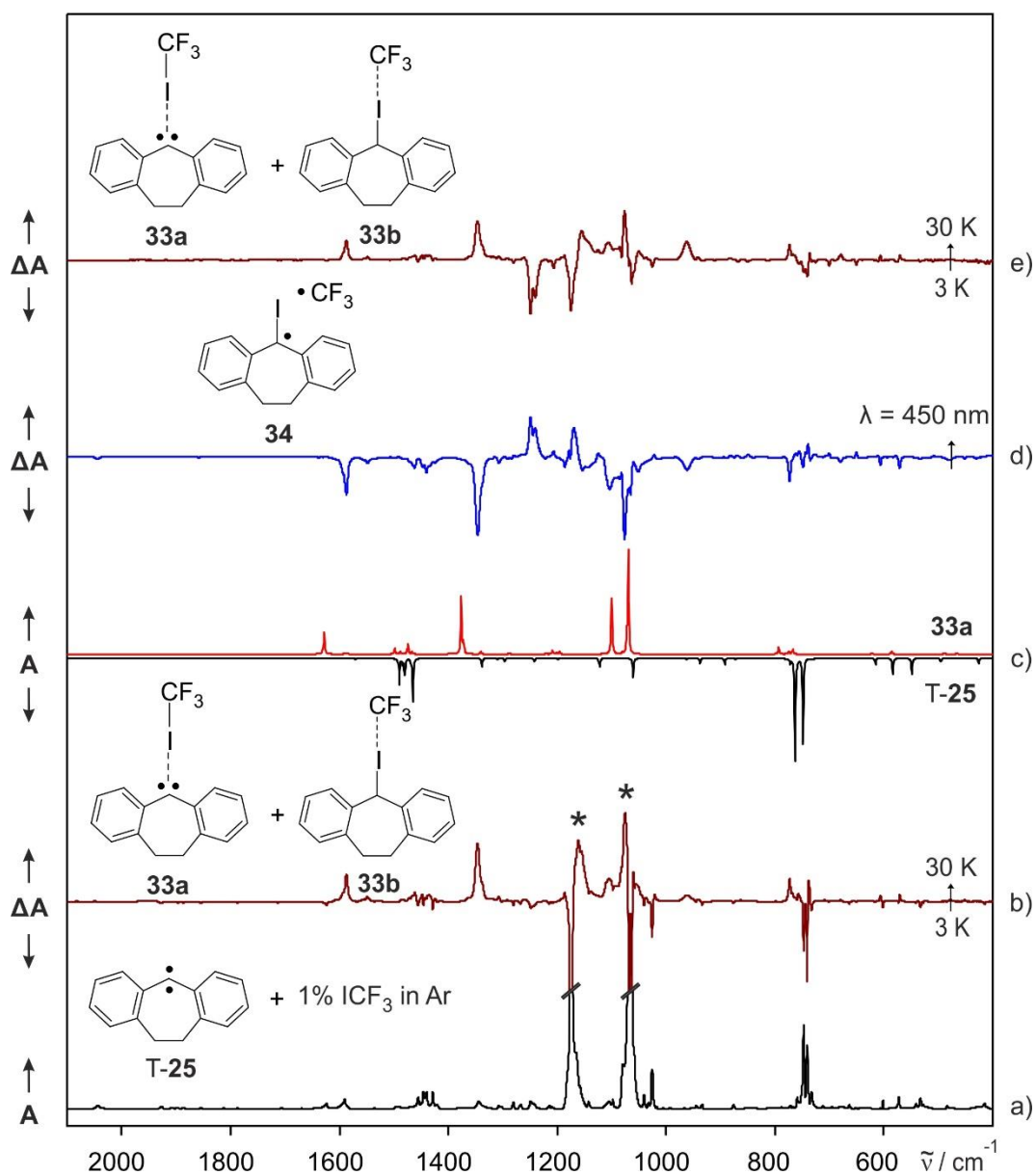


Figure 17. IR spectra showing the reaction between T-25 and ICF₃. a) IR spectrum of T-25 in an argon matrix doped with 1% of ICF₃ at 3 K. b) Difference IR spectrum of the same matrix showing changes after annealing at 30 K. Bands pointing downwards assigned to T-25 and ICF₃ are disappearing, and bands pointing upwards are assigned to complexes between S-25 and ICF₃ (**33a** and **33b**) are appearing. The bands marked with asterisks are assigned to ICF₃ and its higher aggregates. c) Computed IR spectrum of T-25 (multiplied by -1, peaks pointing downwards) and computed IR spectrum of **33a** (peaks pointing upwards) at the B3LYP-D3/def2-TZVP level of theory. d) Difference IR spectrum of the annealed matrix showing the changes after 450 nm irradiation at 3 K. Bands pointing downwards assigned to halogen bonded complexes **33a** and **33b** are disappearing, and bands pointing upwards assigned to radical pair **34** are appearing. e) Difference IR spectrum of the same matrix showing the changes after annealing at 30 K. Bands pointing downwards assigned to radical pair **34** are disappearing, and bands pointing upwards corresponding to halogen-bonded complexes **33a** and **33b** are appearing.

Irradiation of the matrix isolated halogen-bonded complexes **33a** and **33b** with 450 nm leads to conversion of these complexes and formation of triplet radical pair **34** (Figure 17d). In addition to characteristic IR absorptions of the CF₃ radical observed at 700.1, 1240.6 and 1248.8 cm⁻¹, bands appearing at 650.4, 738.8, 755.6, 849.3 and 1170.3 cm⁻¹ are assigned to radical pair **34** based on comparison with DFT calculations (Figure 18, Table 8). Interestingly, subsequent annealing of the same matrix restores the signals of the halogen-bonded complexes **33a** and **33b**, accompanied by a decrease in intensity of **34** (Figure 17e). This interconversion is found to be reversible for multiple cycles of photolysis and annealing. The formation of the formal C–I insertion product **35** between **25** and ICF₃ is estimated to be highly exothermic (~ 61 kcal mol⁻¹), but it is not observed in the experiments (Scheme 12).

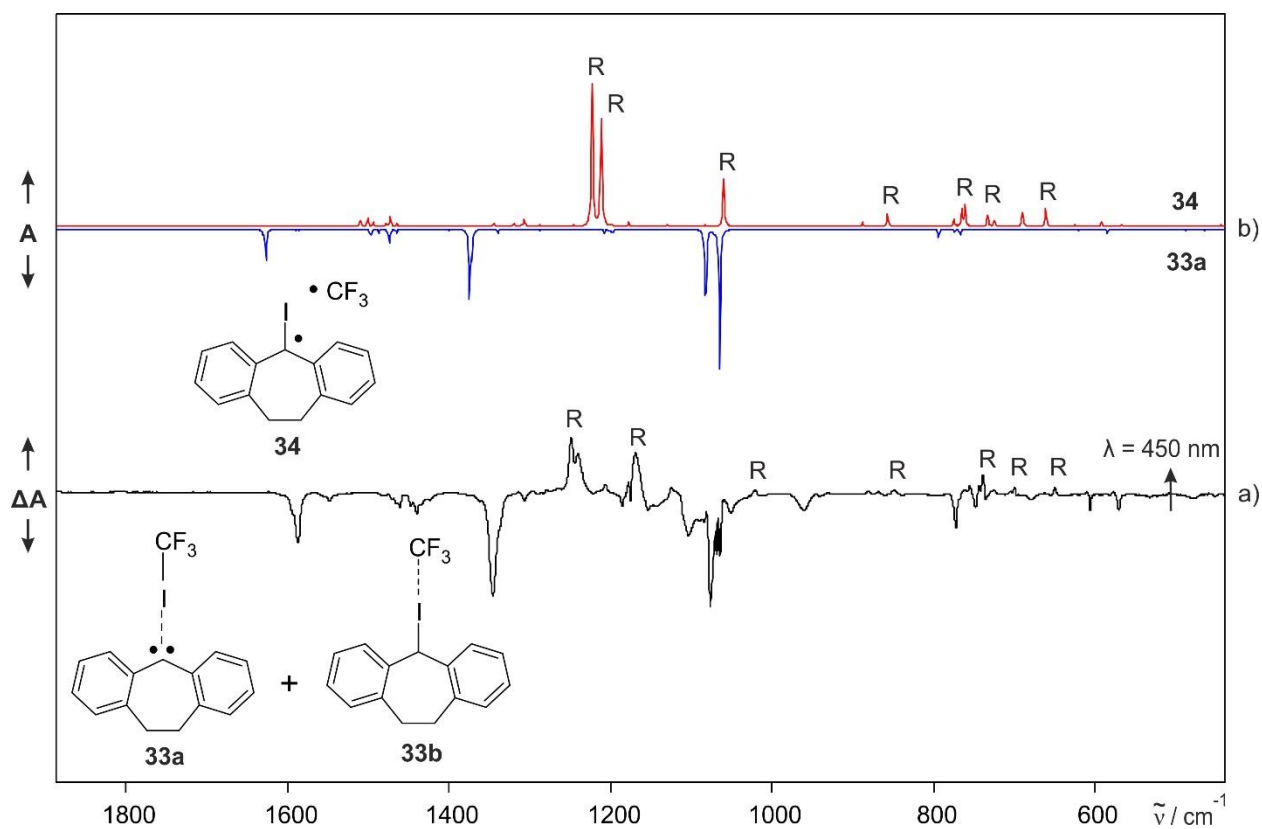
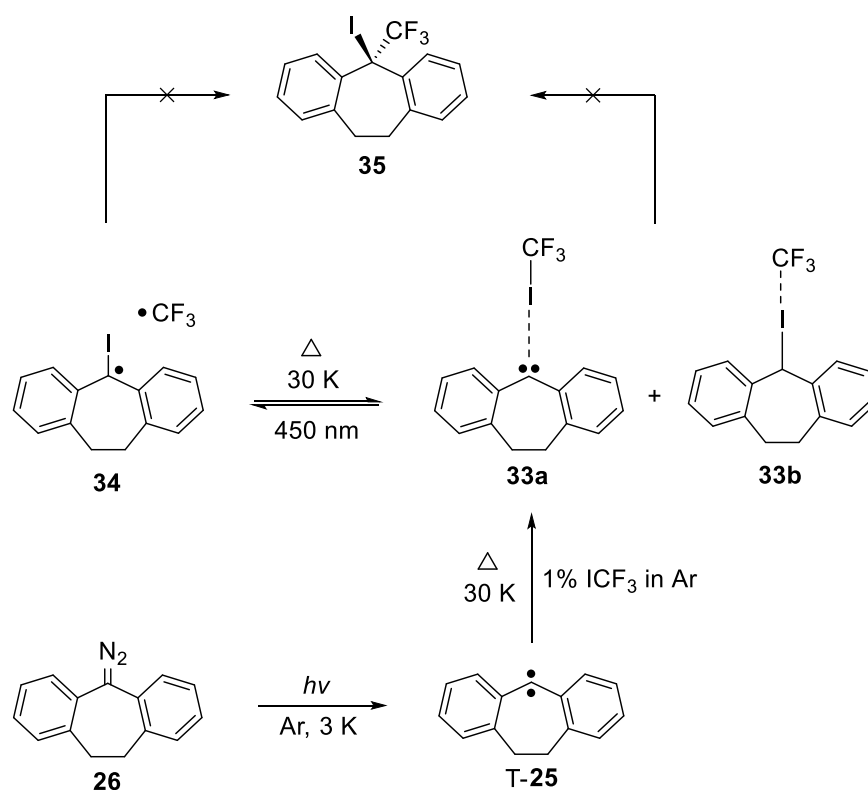


Figure 18. IR spectra showing the formation of radical pair **34** formed from T-**25** and ICF₃. a) Difference IR spectrum showing the changes after 450 nm irradiation of the halogen-bonded complexes **33a** and **33b**. Bands pointing downwards assigned to halogen-bonded complexes **33a** and **33b** are disappearing, and bands pointing upwards assigned to radical pair **34** are appearing. b) Computed IR spectrum of **33a** (multiplied by -1, peak pointing downwards) and computed IR spectrum of **34** (peaks pointing upwards) at the B3LYP-D3/def2-TZVP level of theory.

Table 8. IR vibrational frequencies of radical pair **34** between **25** and ICF₃.

Mode	Sym	DFT ^[a]		Argon ^[b]		Assignment
		$\tilde{\nu}$ / cm ⁻¹	I _{rel}	$\tilde{\nu}$ / cm ⁻¹	I _{rel}	
29	A	661.7	13	650.4	9	C–C–C bend + C–I str.
30	A	691.1	11	700.1	8	Sym. C–F str.
33	A	760.8	16	738.8	12	C–H wagging
35	A	775.5	6	755.6	7	C–H wagging
37	A	858.5	10	849.3	7	C–I str.
58	A	1217.4	61	1170.3	68	C–F str.
59	A	1230.2	100	1240.6 + 1248.8	100	C–F str.

^[a]Calculated at the B3LYP-D3/def2-TZVP level of theory. ^[b]Argon matrix at 3 K.

**Scheme 12.** Reaction of Dibenzocycloheptadienyldiene **25** with ICF₃.

UV-Vis spectroscopy. Experiments were performed following the reaction of **T-25** with ICF₃ using UV-vis spectroscopy. Annealing of an argon matrix doped with 1% of ICF₃ containing **T-25** at 30 K results in a decrease in UV-Vis absorptions of **T-25** (λ_{\max} = 302, 320, 332 and 500 nm) and formation of a new absorption centered at λ_{\max} = 381 nm, which is assigned to the classical type I

halogen-bonded complex **33a** (Figure 19c). The transition of an electron from bonding π -orbitals of the phenyl rings adjacent to the central seven-membered ring to the empty π -orbital of carbene carbon is assigned to this absorption (Figure A1), which is in good agreement with TD-DFT calculations ($\lambda = 346$ nm, $f = 0.2231$). The reaction of **7** with ICF_3 exhibits a similar absorption at 372 nm corresponding to classical type I halogen-bonded singlet carbene complex $\text{S-7}\cdots\text{ICF}_3$.^[2]

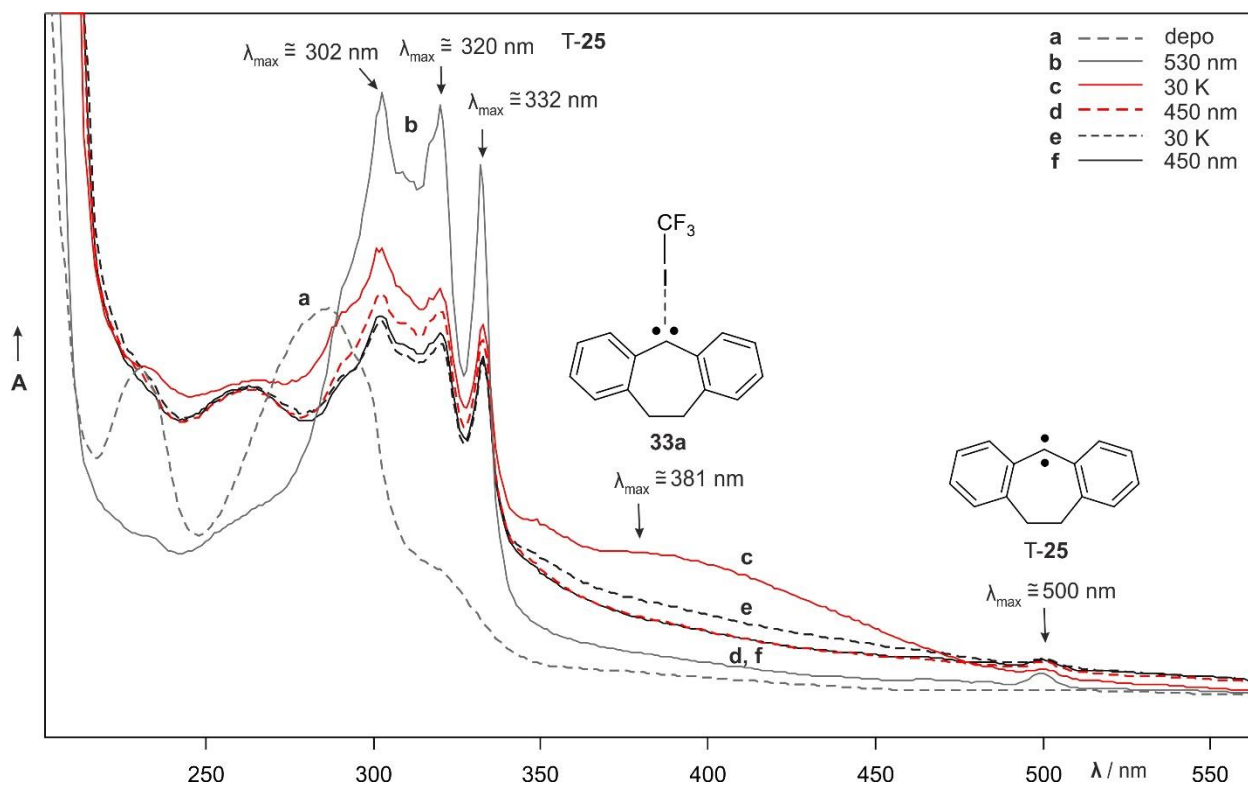


Figure 19. UV-Vis spectra showing the reaction of **T-25** with ICF_3 . a) Dashed grey line: UV-Vis spectrum of diazo precursor **26** in an argon matrix doped with 1% of ICF_3 at 8 K. b) Solid grey line: UV-Vis spectrum of **T-25** ($\lambda_{\text{max}} = 302, 320, 332,$ and 500 nm) generated upon irradiation with 530 nm. c) Solid red line: UV-Vis spectrum of the same matrix showing the changes after annealing at 30 K. The band at $\lambda_{\text{max}} = 381$ nm is assigned to **33a**. d) Dashed red line: UV-Vis spectrum of the same matrix after 450 nm irradiation, showing decrease in intensity of the band of **33a**. e) Dashed black line: UV-Vis spectrum of the same matrix after subsequent annealing at 30 K. The band assigned to **33a** increases in intensity. f) Solid black line: UV-Vis spectrum of the same matrix after 450 nm irradiation showing reduction in intensity of band of **33a** as observed earlier.

Upon 450 nm photolysis, the signal assigned to **33a** decreases, while the formation of radical pair **34** is not detected as observed in IR experiments (Figure 19d). Subsequent annealing of the same matrix recovers the signal of **33a** (Figure 19e), which provides indirect evidence for the formation of **34** in the photolysis experiments. If the matrix is further irradiated with 450 nm again, the

absorption of **33a** again decreases signifying the reversible interconversion between **33a** and **34** (Figure 19f).

EPR spectroscopy. To confirm the assignment of the triplet radical pair **34**, EPR spectroscopic measurements were carried out. As expected, photolysis (530 nm) of diazo precursor **26** in an argon matrix doped with 1% of ICF₃ at 5 K produces strong signals of T-**25**. Annealing of the matrix at 30 K leads to decrease of the signals of T-**25** due to the formation of EPR inactive singlet halogen-bonded complexes **33a** and **33b**. Subsequent photolysis with 450 nm does not affect the signals of T-**25**, but forms an intense radical pattern around 3400 G (Figure 20). Based on the IR observations, the radical signals appearing upon the photolysis should correspond to the triplet radical pair **34**. It can be seen that most of these signals in the radical region correlate well with a simulated spectrum of CF₃ radicals (Figure 21).^[142] The broad feature underlying CF₃ radical is tentatively assigned to C₁₅H₁₂I radical.

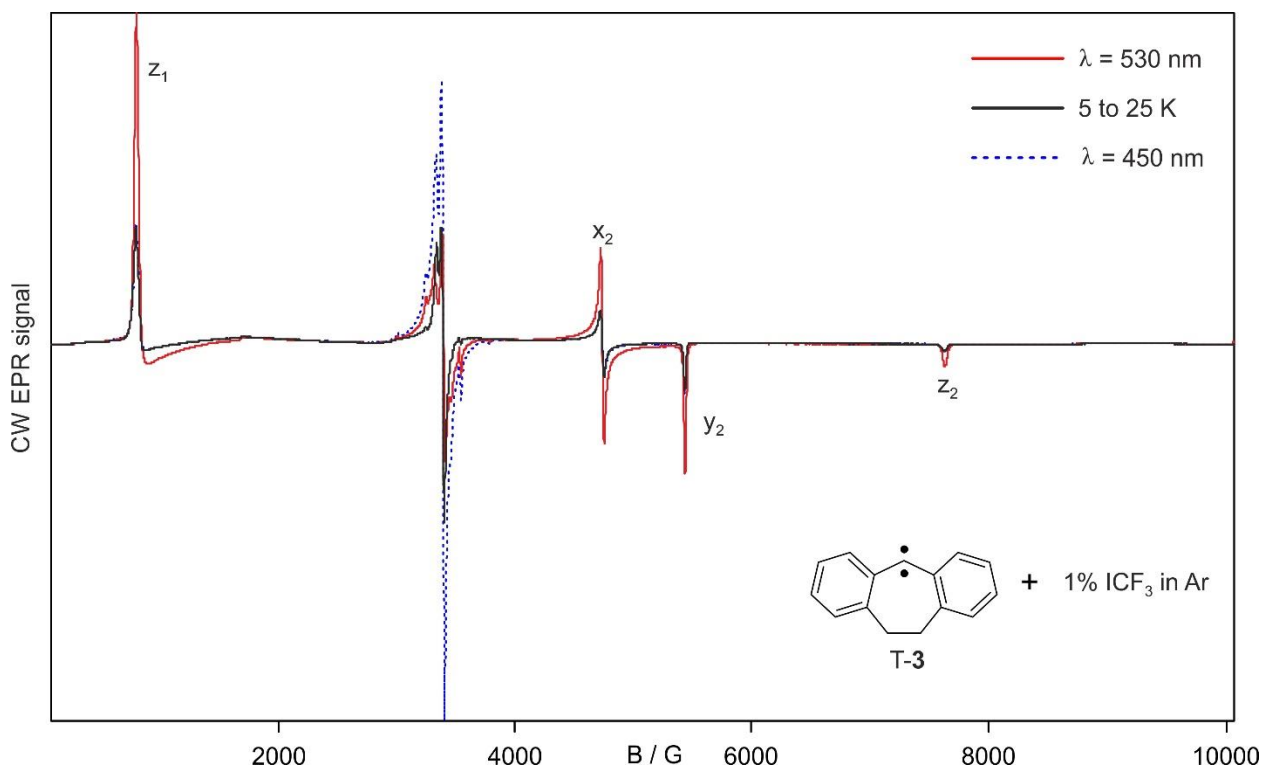


Figure 20. EPR spectra showing the reaction of T-**25** with ICF₃. Red line: spectrum of T-**25** generated upon 530 nm photolysis of diazo precursor **26** in a solid argon matrix doped with 1% of ICF₃ at 5 K. Black line: spectrum of the same matrix showing the changes after annealing at 30 K for 30 minutes. Dashed blue line: spectrum of the same matrix after 450 nm irradiation showing the formation of new signals in radical region assigned to radical pair **34**.

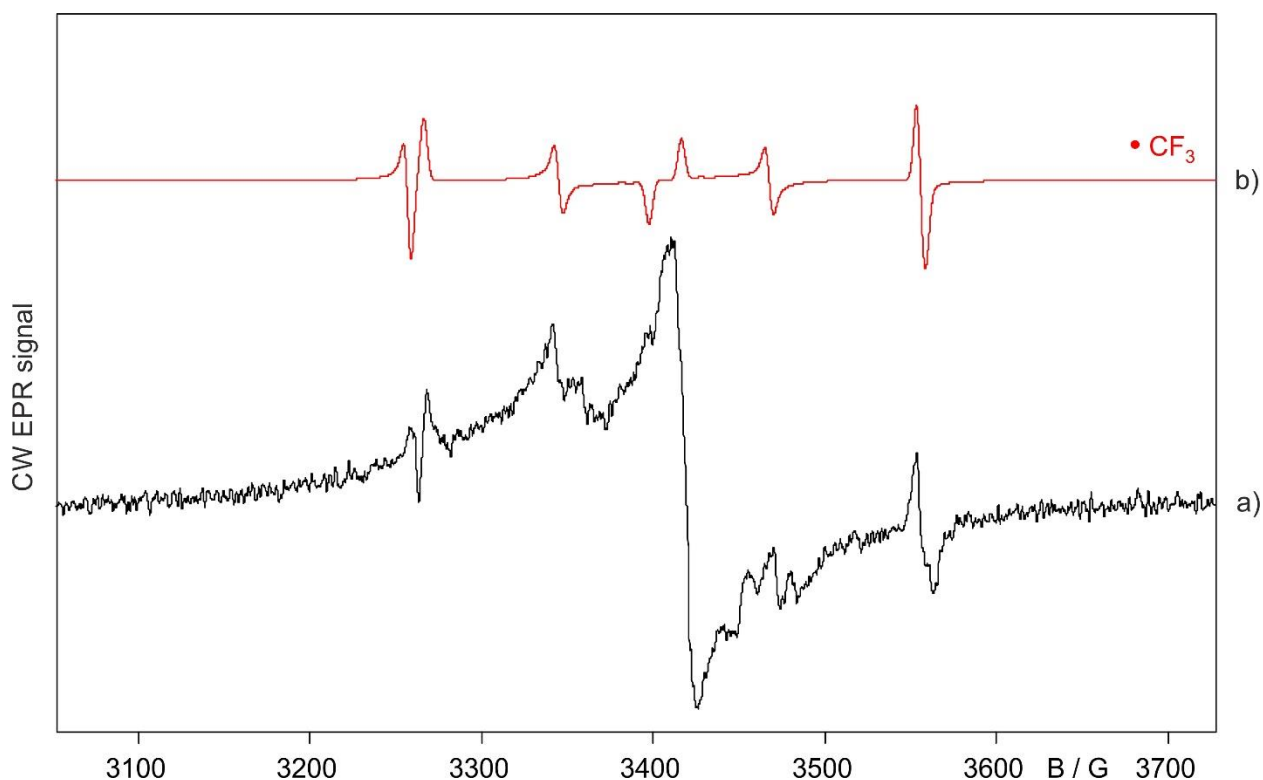


Figure 21. EPR spectrum of CF_3 radicals. a) EPR spectrum obtained upon 450 nm irradiation of the annealed argon matrix containing **T-25** and 1 % of ICF_3 . b) Simulated EPR spectrum of CF_3 radicals.^[142]

Computations. For all three carbenes **7**, **8** and **25**, the gas phase DFT calculations at the B3LYP-D3/def2-TZVP level of theory predict a larger stabilization of the singlet states relative to the triplet upon interaction with ICF_3 (Table 2). The singlet states **S-7** and **S-25**, stabilized by $\sim 15 \text{ kcal mol}^{-1}$, are expected to form halogen-bonded singlet carbene complexes **S-7** $\cdots\text{ICF}_3$ and **S-25** $\cdots\text{ICF}_3$. On the other hand, **S-8** is calculated to be highly stabilized by 22 kcal mol^{-1} on complexation with ICF_3 to give ylide **30** (**S-8-I-CF₃**) instead of the halogen-bonded singlet carbene complex **S-8** $\cdots\text{ICF}_3$. All attempts to computationally locate **S-8** $\cdots\text{ICF}_3$ as minimum structure converged to ylide **S-8-I-CF₃** (Figure 22). The triplet states **T-7**, **T-8** and **T-25** are predicted to form weak ICF_3 complexes with stabilization energies of $\sim 5 \text{ kcal mol}^{-1}$, where partially filled π -orbital of carbene interacts with iodine of ICF_3 .

The relative stabilization of **S-7** as compared to **T-7** ($9.4 \text{ kcal mol}^{-1}$) upon complexation with ICF_3 is larger than the S-T gap of **7** ($5.7 \text{ kcal mol}^{-1}$) which results in the switching of the spin state of **7** $\cdots\text{ICF}_3$ complex from triplet to singlet.^[2] Since **25** has a larger S-T gap ($10.2 \text{ kcal mol}^{-1}$) as

compared to **7**, the predicted relative stabilization of S-**25**···ICF₃ compared to T-**25**···ICF₃ (9.2 kcal mol⁻¹) is not sufficient to invert the spin state from triplet to singlet. However, if the empirical correction is taken into account, then S-T gap of **25** is reduced to 7.9 kcal mol⁻¹ and as a result, the spin state of **25**···ICF₃ complex is switched from triplet to singlet, in agreement with the experimental findings.

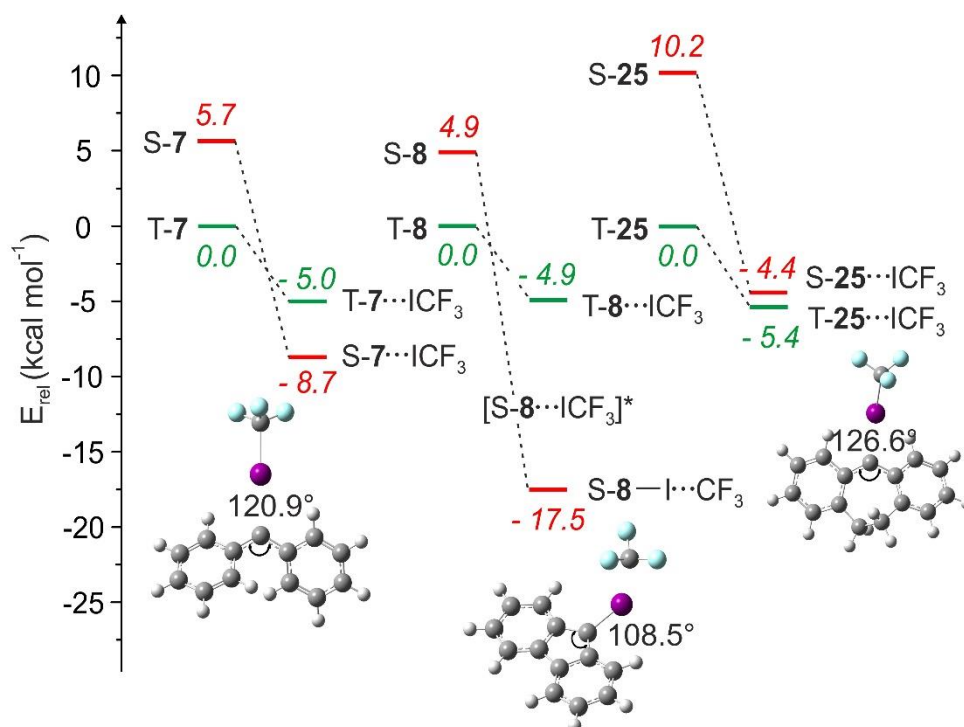


Figure 22. Relative energies (kcal mol⁻¹) of **7**, **8** and **25** in both spin states, and their most stable complexes with ICF₃ computed at the B3LYP-D3/def2-TZVP level of theory. Representative structures of the most stable singlet complexes are shown with their bond angles at the carbene centers.

It is important to note that the argon matrix stabilizes the polar singlet state more than apolar triplet states.^[1] The gas phase computations places the triplet complex T-**25**···ICF₃ slightly below the corresponding singlet complex S-**25**···ICF₃ by 1.0 kcal mol⁻¹. The computations with the continuum argon model at the same level of theory (Table 9) reveal additional stabilization of S-**25**···ICF₃ by 1.6 kcal mol⁻¹ and of T-**25**···ICF₃ by 0.6 kcal mol⁻¹, making both spin states of **25**···ICF₃ complex degenerate. This explains possible formation of S-**25**···ICF₃ as observed experimentally, whereas T-**25**···ICF₃ complex could not be observed probably due to weak interaction of T-**25** and ICF₃ which does not predict significant shifts with respect to monomers.

Table 9. Stabilization of spin states, both S and T, of **7**, **8** and **25** and their most stable Lewis acid complexes including solvation of argon, computed using the B3LYP-D3/def2-TZVP/IEFPCM (argon) level of theory. The ‘Argon correction’ is calculated by taking the difference between zero-point corrected energies with and without argon solvation keywords. Energies in kcal mol⁻¹.

Geometries	Argon correction	ΔE_{S-T}	$\Delta E_{S-T}/\text{argon}$
S- 7	0.9	5.7	5.2
T- 7	0.4		
S- 7 ...H ₂ O	1.8	0.5	-0.2
T- 7 ...H ₂ O	1.2		
S- 1 ...MeOH	1.5	0.3	-0.3
T- 7 ...MeOH	0.9		
S- 7 ...ICF ₃	1.6	-3.7	-4.7
T- 7 ...ICF ₃	0.6		
S- 7 ...BF ₃	2.8	-26.7	-28.8
T- 7 ...BF ₃	0.7		

S- 8	1.3	4.9	4.1
T- 8	0.5		
S- 8 ...H ₂ O	1.8	-1.7	-2.4
T- 8 ...H ₂ O	1.1		
S- 8 ...MeOH	1.5	-1.9	-2.6
T- 8 ...MeOH	0.8		
S- 8 -I...CF ₃	0.8	-12.7	-12.9
T- 8 ...ICF ₃	0.6		
S- 8 ...BF ₃	3.0	-33.3	-35.6
T- 8 ...BF ₃	0.7		

S- 25	1.0	10.2	9.7
T- 25	0.5		
S- 25 ...H ₂ O	1.7	2.6	2.1
T- 25 ...H ₂ O	1.2		
S- 25 ...MeOH	1.5	2.4	1.8
T- 25 ...MeOH	0.9		
S- 25 ...ICF ₃	1.6	1.0	0.0
T- 25 ...ICF ₃	0.6		
S- 25 ...BF ₃	2.9	-21.7	-23.8
T- 25 ...BF ₃	0.6		

2.2.4. Reaction of Fluorenylidene and Dibenzocycloheptadienyliidene with BF₃.

BF₃ is a much stronger Lewis acid than H₂O and ICF₃, therefore it is expected to interact more strongly with the highly basic singlet states of carbenes. Recent work on the reaction of triplet diphenylcarbene T-7 with BF₃ in doped argon matrices demonstrated the spin inversion of 7 by forming a strong Lewis acid-base adduct between the singlet state of diphenylcarbene S-7 and BF₃.^[3] To gain more insight on the reactivity of carbenes towards BF₃, the reactions of carbenes 8 and 25 with BF₃ were carried out under the similar conditions.

Reaction of Fluorenylidene 8 with BF₃. The reaction of T-8 with BF₃ was studied in argon matrices doped with 1% of BF₃ using IR and UV-vis spectroscopy.

IR spectroscopy. As expected, photolysis (365 nm) of diazofluorene 29 isolated in argon matrices doped with 1% of BF₃ produces T-8. When such matrix is annealed from 3 to 30 K, the IR bands of T-8 and BF₃ decrease, and new signals are formed. Dimers and higher oligomers of BF₃ are observed on annealing at 650, 655, 821, 1415, 1418, 1421, 1456, 1461, 1469, 1473, 1475, 1498, 1514 cm⁻¹, indicating the diffusion of BF₃ in a solid argon.^[143] The signals at 728.7, 900.8, 1082.8, 1101.2, 1573.0, and 1609.8 cm⁻¹ are assigned to Lewis adduct 36 between S-8 and BF₃ by comparison with DFT calculations (Figure 23c, Table 10).

Table 10. IR vibrational frequencies of Lewis adduct 36 formed from S-8 and BF₃.

Mode	Sym	DFT ^[a]		Argon ^[b]		Assignment
		$\tilde{\nu}$ / cm ⁻¹	I _{rel}	$\tilde{\nu}$ / cm ⁻¹	I _{rel}	
20	A	623.7	8	599.8	16	BF ₃ bend
24	A	751.3	18	728.7	76	C–H wagging
30	A	908.3	35	900.8 ^c	37	BF ₃ sym. str.
37	A	1014.9	23	974.4 ^c	20	C–B str.
41+42	A	1077.2 + 1101.9	100	1082.8 + 1101.2	100	B–F str.
48	A	1243.5	29	1231.6 ^c	20	C–C–C asym. str.
49	A	1310.9	12	1301.4	16	Ring def.
52	A	1335.0	8	1326.9	16	C–H bend
58	A	1612.7	23	1573.0	47	C=C str.
61	A	1643.4	22	1609.8	42	C=C str.

^[a]Calculated at the B3LYP-D3/def2-TZVP level of theory. ^[b]Argon matrix at 3 K. ^[c]Broad peaks.

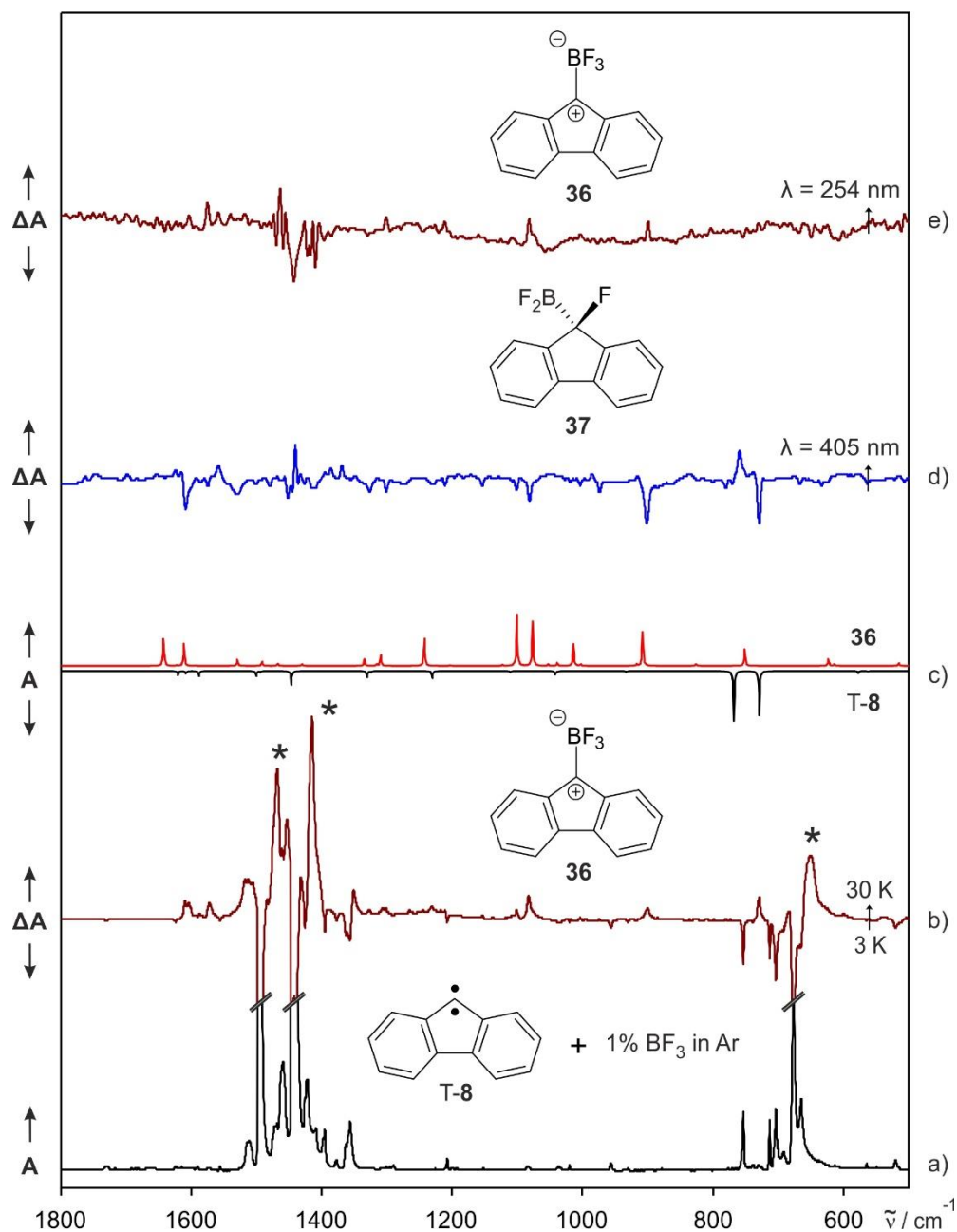


Figure 23. IR spectra showing the reaction between T-8 and BF₃. a) IR spectrum of T-8 in an argon matrix doped with 1% of BF₃ at 3 K. b) Difference IR spectrum of the same matrix showing the changes after annealing at 30 K. Bands pointing downwards assigned to T-8 and BF₃ are disappearing, and bands pointing upwards assigned to 36 are appearing. The bands marked with asterisks are assigned to higher aggregates of BF₃. c) Computed IR spectrum of T-8 (multiplied by -1, peaks pointing downwards) and computed IR spectrum of 36 (peaks pointing upwards) at the B3LYP-D3/def2-TZVP level of theory. d) Difference IR spectrum of the annealed matrix showing the changes after 405 nm irradiation at 3 K. Bands pointing downwards assigned to the Lewis adduct 36 are disappearing, and bands pointing upwards assigned to B-F insertion product 37 are appearing. e) Difference IR spectrum of the same matrix after 254 nm irradiation at 3 K, showing the conversion of 37 into 36.

The observation of **36** implies that the interaction of T-**8** with BF_3 flips the spin state of carbene **8** from triplet to singlet analogous to the interactions of T-**8** with H_2O ^[4] and ICF_3 . Subsequent photolysis of the same matrix with 405 nm results in a decrease of the IR bands of **36** and formation of a new compound with strong absorptions at 759.3, 984.9, 1369.1, and 1440.6 cm^{-1} . By comparison with DFT calculations, this new compound is identified as the formal B–F insertion product, difluoro(fluoro-9F-fluorenyl)borane **37** (Figure 24, Table 11). Interestingly, the migration of the fluorine atom from boron to adjacent carbene carbon is reverted upon irradiation with 254 nm, which converts **37** back to the Lewis adduct **36** (Figure 23e, Scheme 13) and indicates a reversible photochemical interconversion between **36** and **37**. This reversible rearrangement is rationalized by the formation of highly electrophilic carbon and boron atom centers upon the migration of fluorine atom in both directions. A similar photoinduced reversible fluorine migration was previously observed for the reaction of **7** with BF_3 .^[3]

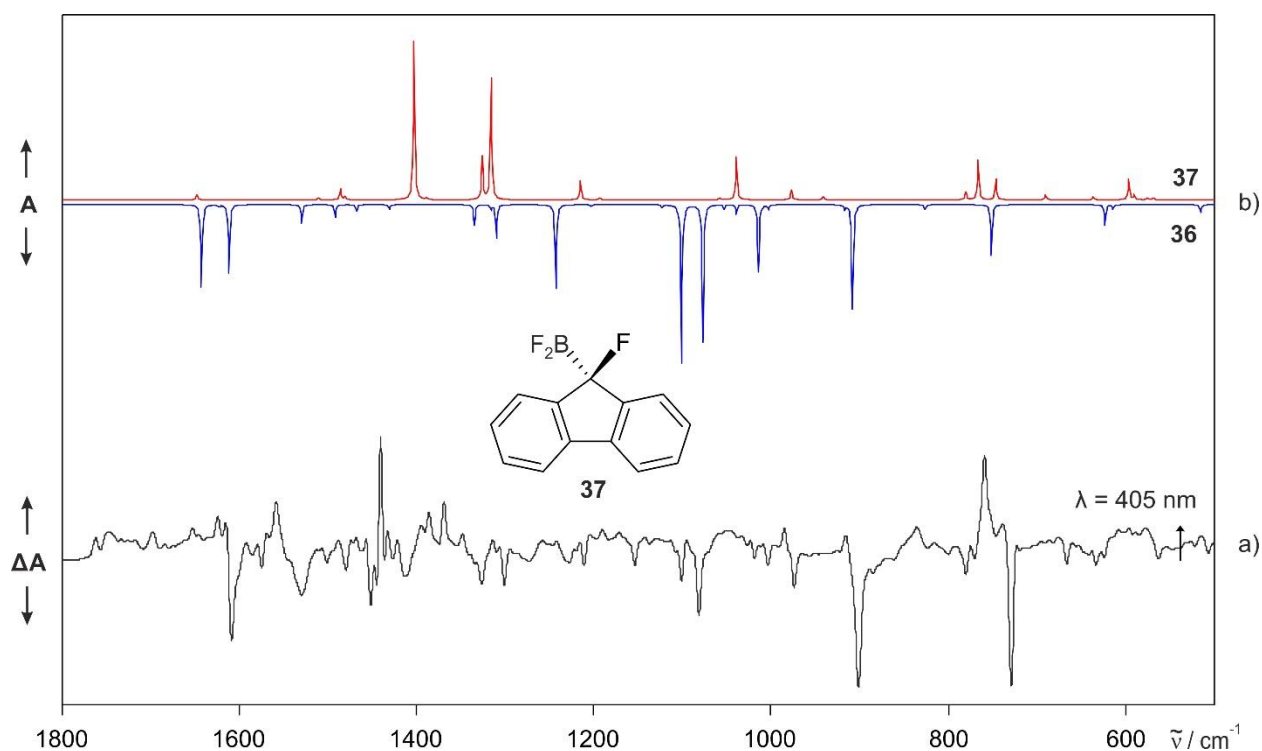
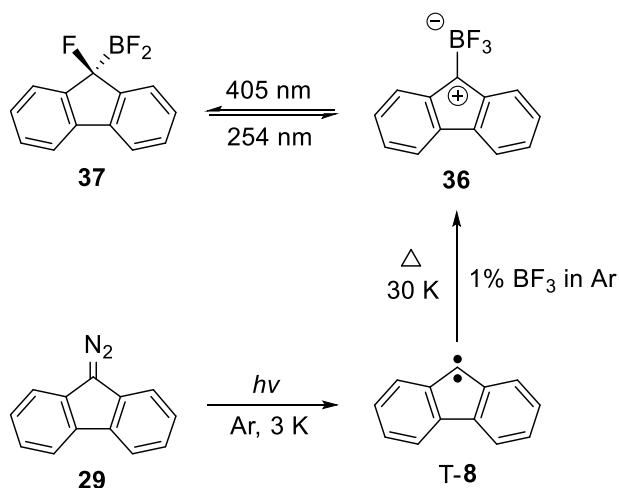


Figure 24. IR spectra showing the formation of the formal B–F insertion product of fluorenylidene **8** and BF_3 , difluoro(fluoro-9F-fluorenyl)borane **37**. a) Difference IR spectrum of photolyzed Lewis adduct **36** showing the changes after 405 nm irradiation. Bands pointing downwards assigned to **36** are disappearing, and bands pointing upwards assigned to **37** are appearing. b) Computed IR spectrum of **36** (multiplied by -1, peak pointing downwards) and computed IR spectrum of **37** (peaks pointing upwards) at the B3LYP-D3/def2-TZVP level of theory.

Table 11. IR vibrational frequencies of difluoro(fluoro-9F-fluorenyl)borane **37**.

Mode	Sym	DFT ^[a]		Argon ^[b]		Assignment
		$\tilde{\nu}$ / cm ⁻¹	I _{rel}	$\tilde{\nu}$ / cm ⁻¹	I _{rel}	
24	A	746.4	14	738.1	22	C–H wagging
25	A	766.8	25	759.3	55	C–H wagging
27	A	780.6	7	774.9	20	C–C–C bend
38	A	1039.8	28	984.9	20	C–F str.
46	A	1215.2	13	1190.8	11	C–C–C sym. str.
48	A	1316.0	76	1369.1	31	C–B str.
50	A	1326.1	28	1385.9	10	C–H bend + C–B str.
53	A	1403.6	100	1440.6	100	B–F str.

^[a]Calculated at the B3LYP-D3/def2-TZVP level of theory. ^[b]Argon matrix at 3 K.

**Scheme 13.** Reaction of fluorenylidene **8** with BF_3 .

UV-Vis spectroscopy. The reaction of **8** with BF_3 was monitored by UV-Vis spectroscopy. Annealing of an argon matrix containing T-**8** and 1% of BF_3 at 30 K leads to a decrease in the UV-Vis absorptions of T-**8** at $\lambda_{\text{max}} = 257, 321, 436, 454,$ and 462 nm, and concurrently the matrix turns orange-yellow corresponding a strong visible absorption at $\lambda_{\text{max}} = 492$ nm assigned to the Lewis adduct **36** (Figure 25c). This absorption of **36** is assigned to a transition of bonding

π -electrons of the adjacent phenyl rings to the empty π -orbital of carbene carbon (Figure A2), which is in reasonably good agreement with TD-DFT calculations ($\lambda = 405$ nm, $f = 0.1728$).

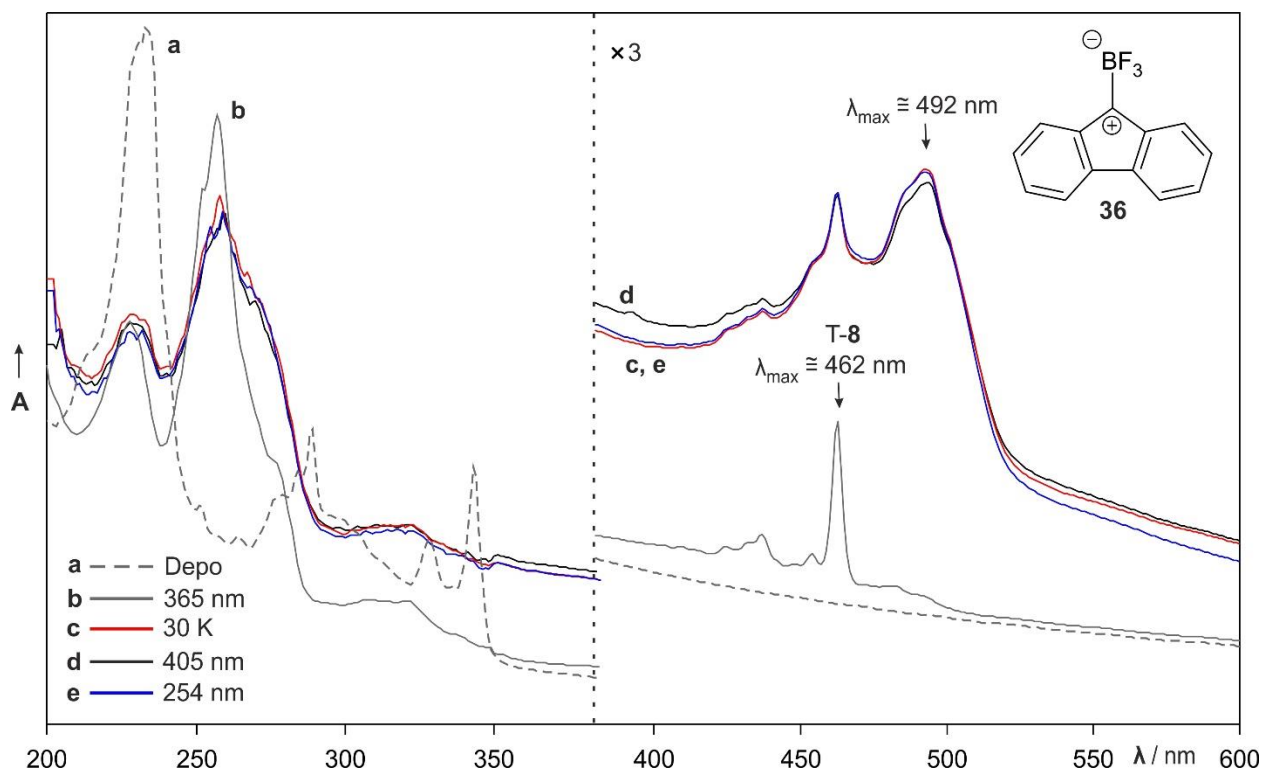


Figure 25. UV-Vis spectra showing the reaction of T-8 with BF_3 . a) UV-Vis spectrum of diazo precursor **29** in an argon matrix doped with 1% of BF_3 at 8 K. b) UV-Vis spectrum of T-8 ($\lambda_{\text{max}} = 257, 321, 436, 454$ and 462 nm) generated upon 365 nm irradiation of **29**. c) UV-Vis spectrum of the same matrix showing the changes after annealing at 30 K. The band at $\lambda_{\text{max}} = 492$ nm is assigned to **36**. d) UV-Vis spectrum of the same matrix after 405 nm irradiation, showing decrease in intensity of band of **36**. e) UV-Vis spectrum of the same matrix after subsequent 254 nm irradiation. The band assigned to **36** increases in intensity.

Subsequent irradiation of the matrix with 405 nm results in a decrease of the absorption assigned to **36** without affecting the triplet carbene signal at $\lambda_{\text{max}} = 462$ nm. The formal B-F insertion product **37** which was identified as photoproduct of **36** by IR spectroscopy does not show any characteristic signal in the UV-Vis spectral range. Photolysis of the same matrix with 254 nm recovers the visible absorption of the adduct **36**, in agreement with the observations in the IR experiments. It should be noted that the intensity of the absorptions of T-8 remains the same even during 254 nm photolysis, which suggests that **36** is formed back from **37** and unreacted T-8 is not playing any role in this interconversion.

Reaction of Dibenzocycloheptadienylidene 25 with BF₃. The reaction of **25** with BF₃ was investigated in argon matrices doped with 1% of BF₃ using IR and UV-Vis spectroscopy.

IR spectroscopy. When a matrix containing T-**25** and 1% of BF₃ is annealed at 25 – 30 K for several minutes, BF₃ diffuses to react with T-**25** and the matrix turns yellow. During this annealing process, the IR bands of T-**25** and BF₃ decrease in intensity, and new signals appear at 613.4, 754.6, 889.1, 982.7, 1076.7, 1112.2, 1351.2 and 1593.3 cm⁻¹. By comparison with DFT calculations, these bands are assigned to Lewis adduct **38a** formed from S-**25** and BF₃ (Figure 26c, Table 12). This observation implies that the reaction of T-**25** with BF₃ results in the switching of the spin state of **25** from triplet to singlet, in analogy to reaction of T-**7** and T-**8** with BF₃.^[3] The signal centered at 1351.2 cm⁻¹ is assigned to the characteristic C–C–C asymmetric stretching vibration across the carbene center in **25**, close to the corresponding vibration of the Lewis adduct between S-**7** and BF₃ at 1349.5 cm⁻¹.^[3]

Table 12. IR vibrational frequencies of Lewis adduct **38a** between S-**25** and BF₃.

Mode	Sym	DFT ^[a]		Argon ^[b]		Assignment
		$\tilde{\nu}$ / cm ⁻¹	I _{rel}	$\tilde{\nu}$ / cm ⁻¹	I _{rel}	
23	A	585.9	5	557.7	14	C–H bend
24	A	621.4	10	613.4	24	BF ₃ sym. str.
25	A	629.3	3	619.9	18	Ring def.
30	A	771.5	11	754.6	24	C–H wagging
36	A	902.5	12	889.1	18	BF ₃ sym. str.
39	A	966.5	28	982.7	17	B–F str.
47	A	1080.4	35	1076.7 ^[c]	18	B–F str. + C–H str.
49	A	1119.3	40	1112.2 ^[c]	18	B–F str.
63	A	1375.3	100	1351.2	100	C–C–C asym. str.
74+75	A	1633.7 + 1637.5	45	1593.3	86	C=C str.

^[a]Calculated at the B3LYP-D3/def2-TZVP level of theory. ^[b]Argon matrix at 3 K. ^[c]Broad peaks.

The BF₃ fragment in **38a** exhibits the characteristic E and A₁ symmetrical BF stretching vibrations that are highly sensitive to charge at this fragment.^[144-145] The comparison of the characteristic vibrations of the BF₃ fragment in **38a** with that of BF₃ anion, neutral BF₃ and BF₃ cation reveals that the BF₃ fragment in **38a** carries a negative charge. The BF₃ anion is characterized by an IR band at 1026 cm⁻¹ assigned to degenerate, E symmetrical BF and FBF stretching vibration, and by two IR bands at 595 and 847 cm⁻¹ assigned to A₁ symmetrical BF₃ stretching vibrations.^[145]

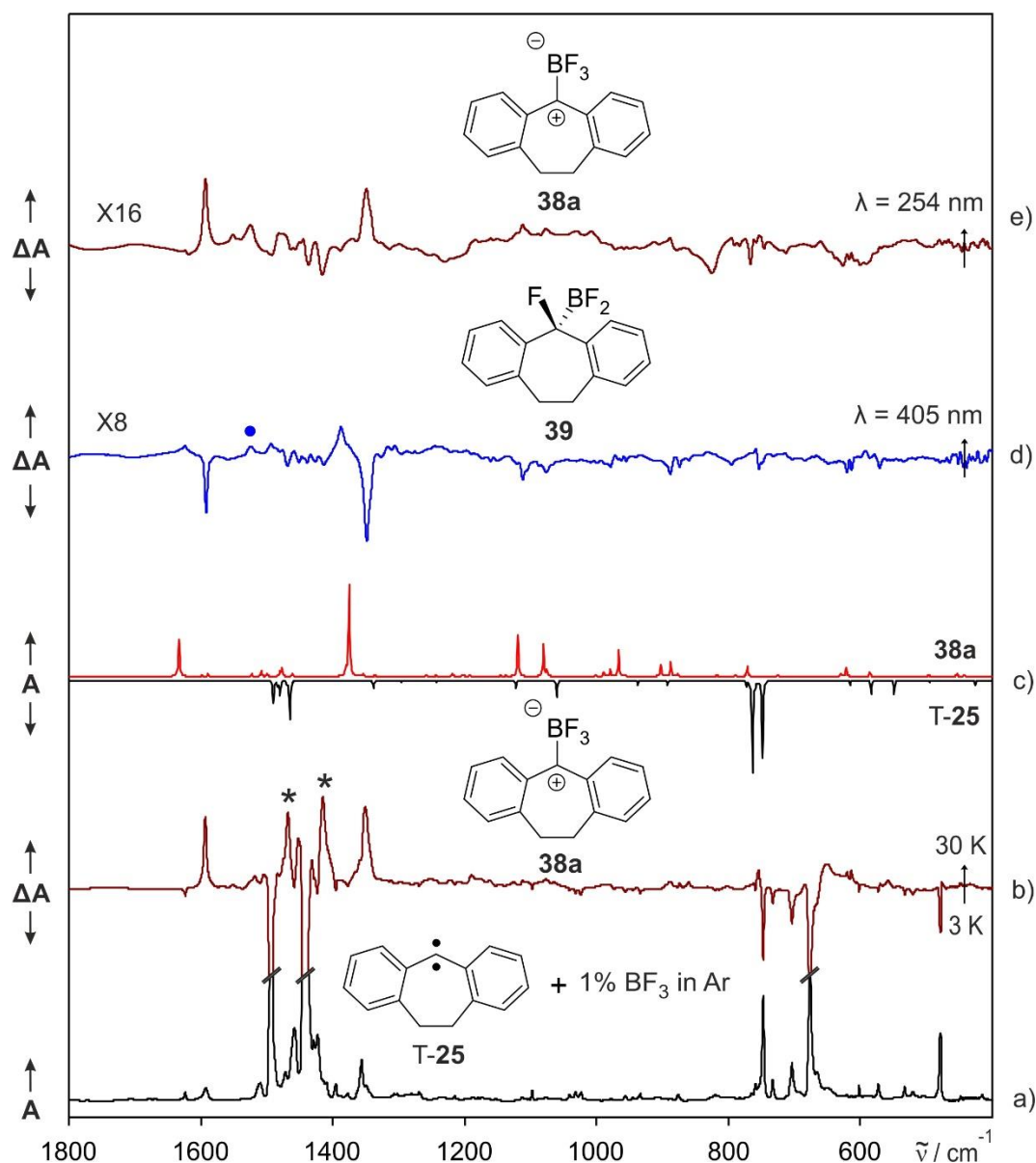


Figure 26. IR spectra showing the reaction between T-25 and BF₃. a) IR spectrum of T-25 in an argon matrix doped with 1% of BF₃ at 3 K. b) Difference IR spectrum of the same matrix showing the changes after annealing at 30 K. Bands pointing downwards assigned to T-25 and BF₃ are disappearing, and bands pointing upwards assigned to **38a** are appearing. The bands marked with asterisks are assigned to higher aggregates of BF₃. c) Computed IR spectrum of T-25 (multiplied by -1, peaks pointing downwards) and computed IR spectrum of **38a** (peaks pointing upwards) at the B3LYP-D3/def2-TZVP level of theory. d) Difference IR spectrum of the annealed matrix showing the changes after 405 nm irradiation at 3 K. Bands pointing downwards assigned to the Lewis adduct **38a** are disappearing, and bands pointing upwards assigned to B-F insertion product **39** are appearing. Blue dot denotes IR band of an unidentified photoproduct. e) Difference IR spectrum of the same matrix showing the changes after 254 nm irradiation at 3 K. Bands pointing downwards assigned to **39** are disappearing and bands pointing upwards assigned to **38a** are appearing, confirming the conversion from **38a** to **39**.

For neutral BF_3 and the BF_3 cation, the degenerate E symmetrical BF stretching vibrations are found at 1448 and 1790 cm^{-1} .^[144-145] In the Lewis adduct **38a**, the degeneracy of the E vibration is lifted due to interaction between **25** and BF_3 leading to two blue-shifted vibrations at 1077 and 1112 cm^{-1} , and the A_1 symmetrical BF_3 stretching vibrations in **38a** are blue-shifted to 613 and 889 cm^{-1} compared to those of the BF_3 anion (Figure 27).

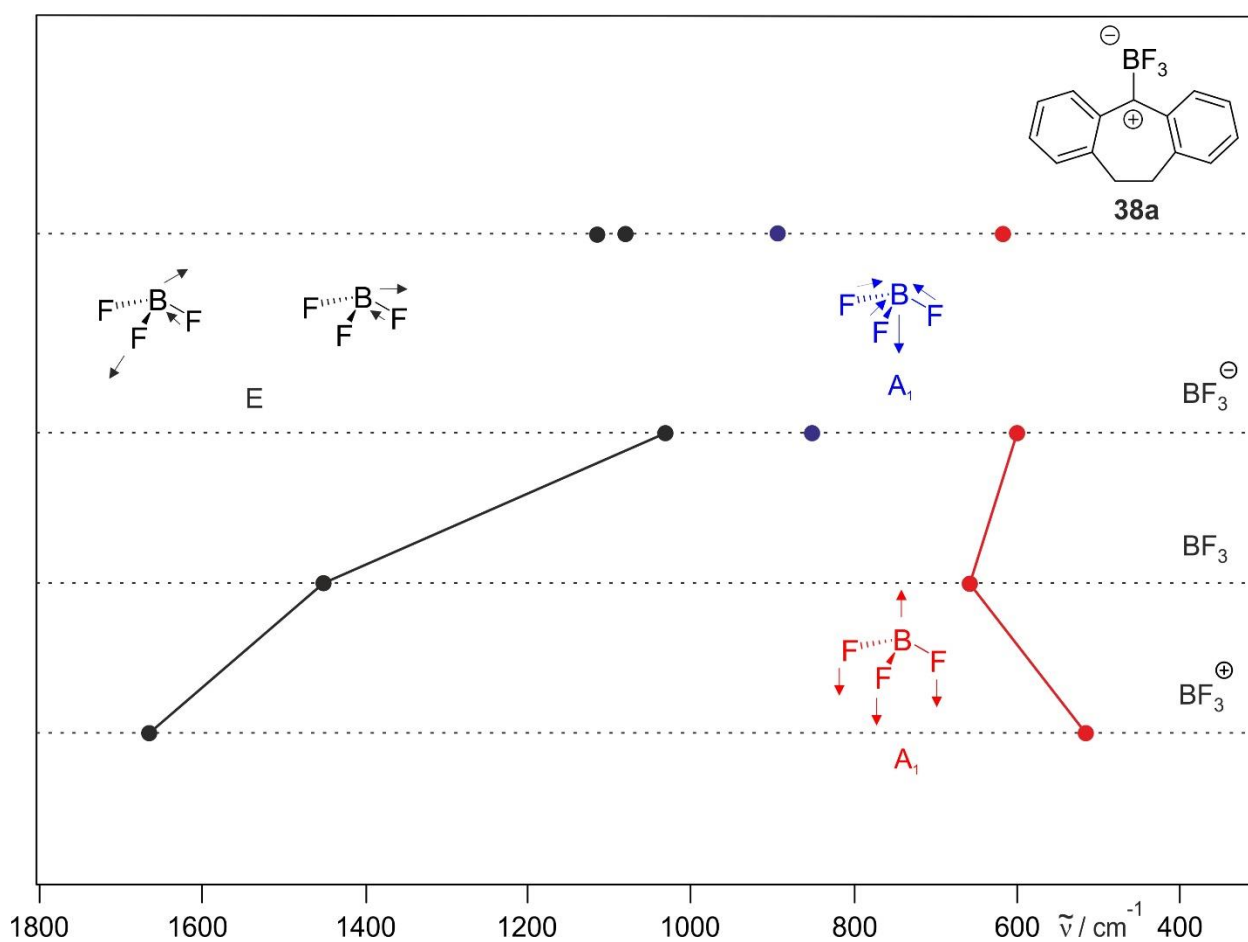


Figure 27. Characteristic IR vibrations of BF_3 fragments. The experimental frequencies of the degenerate, E symmetrical BF and FBF stretching vibrations (black), A_1 symmetric BF_3 stretching vibrations (blue and red) of the cation BF_3^+ , of the anion BF_3^- , and for the neutral BF_3 are compared to those of **38a** (upper trace).^[145]

The Lewis adduct **38a** is found to be photolabile and a new photoproduct, characterized by a strong signal at 1388.4 cm^{-1} and other two low intense bands at lower intensity 1306.3 and 1317.7 cm^{-1} , is formed upon irradiation with 405 nm. The IR spectrum of this new product matches with DFT calculation of difluoro(5-fluorodibenzo[a,d]cycloheptadien-5-yl)borane **39**, the formal insertion product of **25** into a B–F bond of BF_3 (Figure 28, Table 13).

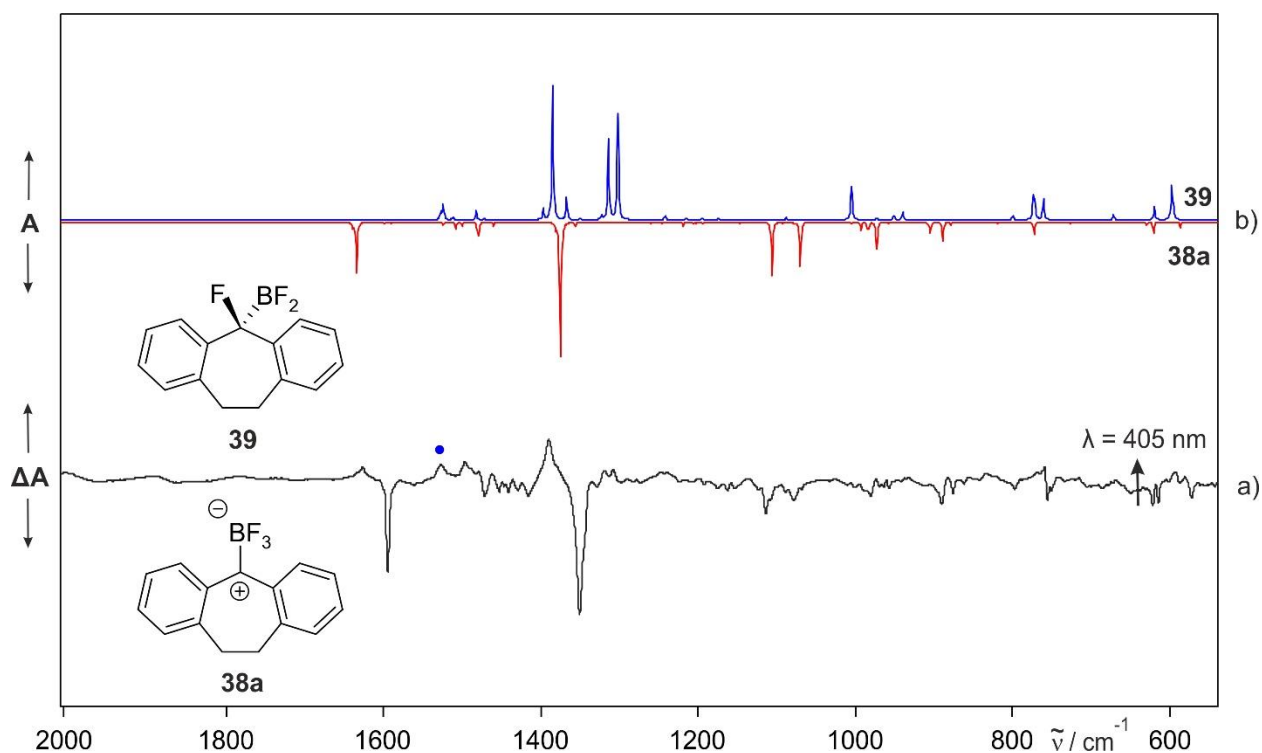


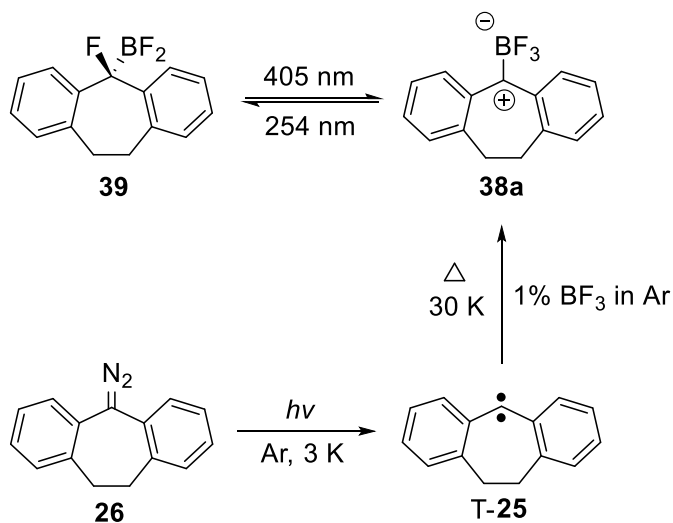
Figure 28. IR spectra showing the formation of the formal B–F insertion product, difluoro(5-fluorodibenzo[a,d]cycloheptadien-5-yl)borane **39**. a) Difference IR spectrum of photolyzed Lewis adduct **38a** showing the changes after 405 nm irradiation. Bands pointing downwards assigned to **38a** are disappearing, and the bands pointing upwards assigned to **39** are appearing. Blue dot denotes an IR band of an unidentified photoproduct. b) Computed IR spectrum of **38a** (multiplied by -1, peak pointing downwards) and computed IR spectrum of **39** (peaks pointing upwards) at the B3LYP-D3/def2-TZVP level of theory.

Table 13. IR vibrational frequencies of difluoro(5-fluorodibenzo[a,d]cycloheptadien-5-yl)borane **39**.

Mode	Sym	DFT ^[a]		Argon ^[b]		Assignment
		$\tilde{\nu} / \text{cm}^{-1}$	I_{rel}	$\tilde{\nu} / \text{cm}^{-1}$	I_{rel}	
24	A	596.3	32	594.6	47	C–C–C bend + C–I str.
29	A	759.3	14	746.4	17	Sym. C–F str.
30+31	A	770.6 + 772.4	24	766.5	30	C–H wagging
58	A	1300.0	64	1306.3	41	C–H wagging
59	A	1312.8	48	1317.7	32	C–I str.
64	A	1383.0	100	1388.4	100	C–F str.
70+71	A	1522.9 + 1525.5	15	1494.9	32	C–F str.

^[a]Calculated at the B3LYP-D3/def2-TZVP level of theory. ^[b]Argon matrix at 3 K.

Subsequent irradiation of matrix containing **39** with 254 nm leads to a decrease of bands assigned to **39**, accompanied by an increase of the bands of **38a**, suggesting the reversible photochemical interconversion between **38a** and **39** (Figure 26e, Scheme 14). This is in analogy to the photochemistry of the BF_3 complexes of **7** and **8**.^[31]



Scheme 14. Reaction of dibenzocycloheptadienyldiene **25** with BF_3 .

In addition to the IR bands of insertion product **39**, 405 nm photolysis shows an increase in intensity of an absorption at 1526 cm^{-1} (marked with blue dot in Figure 26d and Figure 28a). Although this band appears on initial annealing at 30 K with very low intensity, it is not assigned to the Lewis adduct **38a** based on subsequent 405 nm photochemical behaviour. The feature at 1526 cm^{-1} continues to increase in intensity on photolysis with 254 nm, which induces the rearrangement of **39** back to **38a**, ruling out the possibility that this band belongs to the insertion product **39**. Additionally, the possible stable complexes between **S-25** and BF_3 (**38a-e**) were computed using the Multiple Minima Hypersurface (MMH) approach.^[146] However, none of the calculated IR spectra of these complexes contains a signal that can be correlated well to the band at 1526 cm^{-1} (Figure 29). Recently, the reaction of tetrachlorocyclopentadienyldiene with two BF_3 molecules was investigated, which shows that the Lewis adduct formed between the singlet state of the carbene and BF_3 is stabilized upon interaction with second molecule of BF_3 .^[147] Therefore, several complexes of **S-25** with two BF_3 molecules (**40a-e**) were computed, but no convincing assignment is found for the band at 1526 cm^{-1} after comparison with computed IR spectra of these complexes (Figure 30).

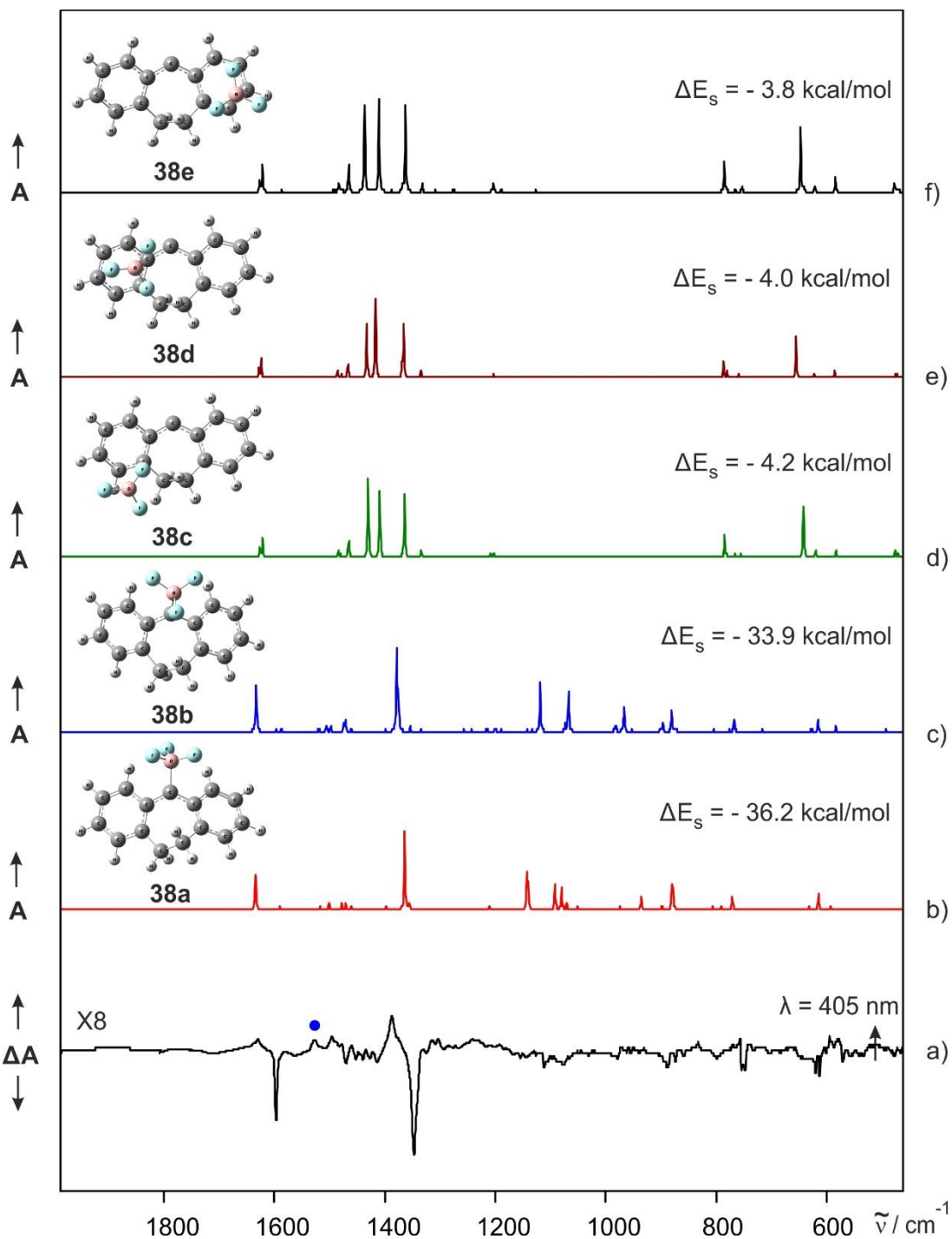


Figure 29. IR spectra showing the comparison of the unidentified photoproduct with IR spectra of possible stable complexes between S-25 and BF₃. a) Difference IR spectrum of photolyzed Lewis adduct **38a** showing the changes after 405 nm irradiation. Bands pointing downwards assigned to **38a** are disappearing, and the bands pointing upwards assigned to **39** are appearing. Blue dot denotes an IR band of an unidentified photoproduct. Computed IR spectra of stable complexes (**38a-e**) between S-25 and BF₃ at the B3LYP-D3/def2-TZVP level of theory with binding energies (ΔE_s) of b) -36.2, c) -33.9, d) -4.2, e) -4.0, and f) -3.8 kcal mol⁻¹ relative to monomers S-25 and BF₃.

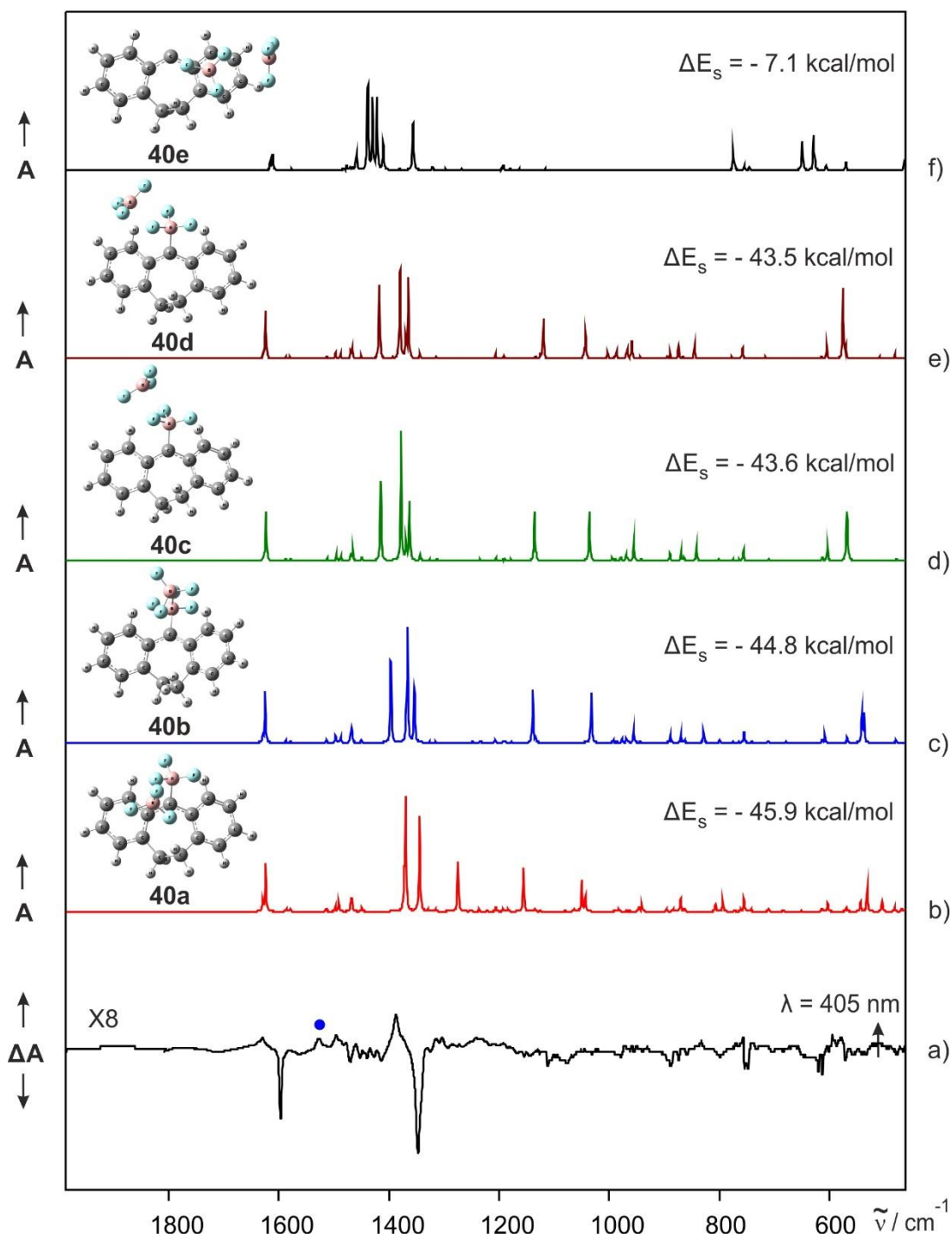


Figure 30. IR spectra showing the comparison of unidentified photoproduct with possible stable complexes between **S-25** and two BF_3 molecules. a) Difference IR spectrum of photolyzed Lewis adduct **38a** showing the changes after 405 nm irradiation. Bands pointing downwards assigned to **38a** are disappearing, and the bands pointing upwards assigned to **39** are appearing. Asterisk denotes IR band of an unidentified photoproduct. Computed IR spectra of stable complexes (**40a-e**) between **S-25** and two molecules of BF_3 at the B3LYP-D3/def2-TZVP level of theory with binding energies (ΔE_s) of b) -7.1, c) -43.5, d) -43.6, e) -44.8, and f) -45.9 kcal mol⁻¹ relative to **S-25** and two BF_3 molecules.

UV-Vis spectroscopy. The reaction of T-**25** with BF₃ could also be monitored by UV-Vis spectroscopy (Figure 31). The characteristic absorptions of T-**25** at $\lambda_{\text{max}} = 302, 320, 332$ and 500 nm decrease in intensity on annealing of an argon matrix doped with 1% of BF₃ containing T-**25** at 30 K, and the resulting yellow matrix features a strong visible absorption centered at $\lambda_{\text{max}} = 427$ nm, assigned to **38a** (Figure 31c). This absorption is analogous to the matrix-isolated Lewis adduct between S-**7** and BF₃ observed at $\lambda_{\text{max}} = 438$ nm.^[3] The assignment of the band at $\lambda_{\text{max}} = 427$ nm to **38a** is in reasonable agreement with TD-DFT calculations ($\lambda = 372$ nm, $f = 0.2792$) for electronic excitation from the σ -orbital of the carbene carbon–boron bond to the empty π -orbital of carbene carbon (Figure A3).

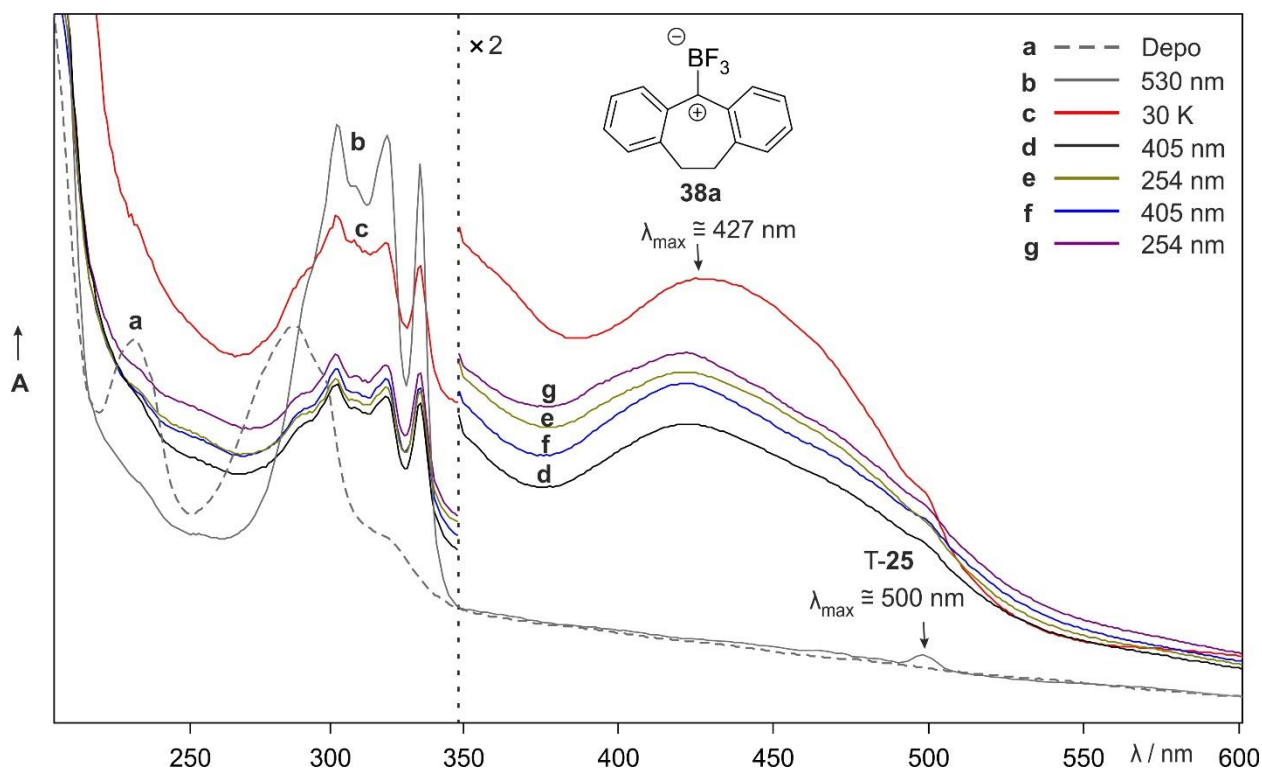


Figure 31. UV-Vis spectra showing the reaction of T-**25** with BF₃. a) UV-Vis spectrum of diazo precursor **26** in an argon matrix doped with 1% of BF₃ at 8 K. b) UV-Vis spectrum of T-**25** ($\lambda_{\text{max}} = 302, 320, 332,$ and 500 nm) generated upon 530 nm irradiation of **26**. c) UV-Vis spectrum of the same matrix showing the changes after annealing at 30 K. The band at $\lambda_{\text{max}} = 427$ nm is assigned to **38a**. d) UV-Vis spectrum of the same matrix after 405 nm irradiation, showing decrease in intensity of band of **38a**. e) UV-Vis spectrum of the same matrix after subsequent 254 nm irradiation. The band assigned to **38a** increases in intensity. f) UV-Vis spectrum of the same matrix after 405 nm irradiation showing reduction in intensity of band of **38a** as observed earlier.

The photolysis of the annealed matrix with 405 nm light results in a decrease of the intensity of the band of **38a** (Figure 31d), but does not produce any detectable absorption corresponding to the formal B–F insertion product **39** in the UV-Vis range. Nevertheless, further UV irradiation with 254 nm of the same matrix recovers the signal of **38a** (Figure 31e), providing indirect evidence for the intermediate formation of **39**. Increase and decrease of visible absorption of **38a** is reproducible by photolysis with 405 nm and 254 nm respectively (Figure 31f and Figure 31g) and therefore indicates the reversible interconversion between **38a** and **39**.

Computations. At the B3LYP-D3/def2-TZVP level of theory, the singlet states of **S-7**, **S-8** and **S-25** are predicted to be highly stabilized upon complexation with BF_3 by 36.2, 41.9, and 36.2 kcal mol^{-1} , respectively, whereas the corresponding triplet states are expected to form weakly interacting triplet complexes with binding energies of $\sim 4 \text{ kcal mol}^{-1}$ (Table 2). The higher binding energy of the **S-8** $\cdots\text{BF}_3$ complex as compared to that of the **S-7** $\cdots\text{BF}_3$ and **S-25** $\cdots\text{BF}_3$ complexes can be explained by the higher s-character of **S-8** relative to that of **S-7** and **S-25**. According to NBO calculations at the same level of theory, the s-characters of **S-7**, **S-8** and **S-25** are estimated to be 46, 35, and 34%, respectively, making **S-8** more acidic (or less basic) than **S-7** and **S-25**.

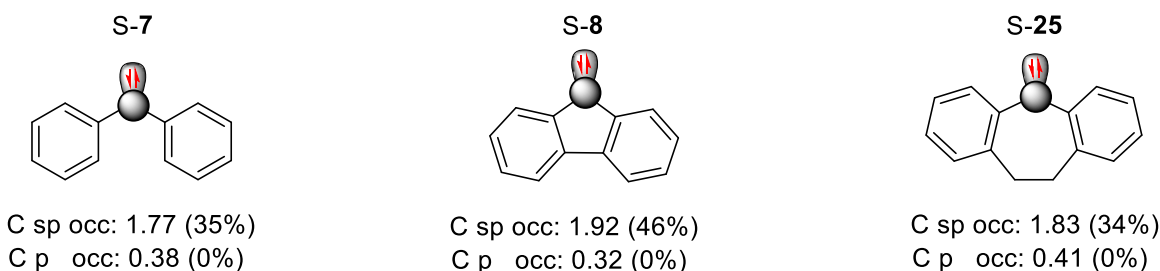


Chart 6. NBO calculations showing the occupancies of s-characters of **S-7**, **S-8** and **S-25**.

DFT calculations predict a shorter B–C bond (1.65 Å) for **S-8** $\cdots\text{BF}_3$, while the same bond is found to be elongated for **S-7** $\cdots\text{BF}_3$ (1.69 Å) and **S-25** $\cdots\text{BF}_3$ (1.70 Å). The complex **S-7** $\cdots\text{BF}_3$ can be compared to acetylene, in which the C–H bond is shorter and thus stronger than those of ethylene and ethane. In the same manner, the carbene carbon in **S-8** is more acidic and electrons are closer to the carbon nucleus, making the B–C bond more polar and shorter, explaining the higher binding energy of **S-8** $\cdots\text{BF}_3$ complex. Accordingly, the strong interaction between **S-8** and BF_3 overcompensates the antiaromatic destabilization of the conjugated five-membered ring in **S-8** $\cdots\text{BF}_3$ complex with a NICS value of 23 calculated at the same level of theory.

For each of the carbenes **7**, **8** and **25** the relative stabilization of the singlet state upon complexation with BF_3 as compared to that of the triplet is larger than S-T gap of the carbene and thus the spin ground state of the carbene- BF_3 complex is predicted to switch from triplet to singlet (Figure 32).

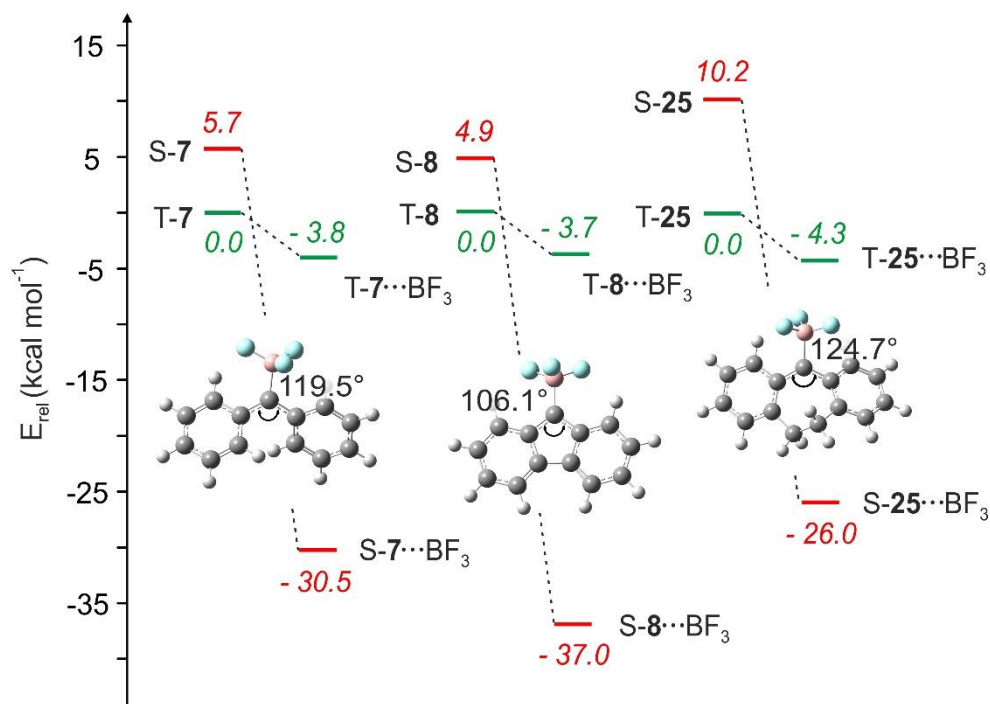


Figure 32. Relative energies (kcal mol^{-1}) of **7**, **8** and **25** in singlet and triplet states, and their most stable complexes with BF_3 computed at the B3LYP-D3/def2-TZVP level of theory. Representative structures of the most stable singlet complexes are shown with their bond angles at the carbene centers.

AIM analysis.

Atoms-in-molecule (AIM) analysis developed by Bader^[148] was carried out for the complexes **30**, **33a**, **36** and **38a** which were observed experimentally using the wavefunctions generated at the B3LYP-D3/def2-TZVP level of theory. The bond critical (3, -1) and ring critical (3, +1) points associated with the interactions in **30**, **33a**, **36** and **38a** are shown in Figure 33. The values of electron density $\rho(r_c)$, eigenvalues of Hessian λ_1 , λ_2 , λ_3 , the Laplacian of electron density ($\nabla^2\rho$) of electron density and ($|\lambda_1/\lambda_3|$) for all complexes computed at bond critical points (BCPs) are given in Table 14.

The complex **30** between S-**8** and ICF_3 presents a BCP1 for the $\text{C-I}\cdots\text{CF}_3$ type of intermolecular interaction (Figure 33a). The BCP1 has a ratio of $|\lambda_1/\lambda_3|$ less than 1, which corresponds to a closed-

shell interaction. The complex **33a** ($S\text{-25}\cdots\text{ICF}_3$) exhibits two interactions, a primary interaction (BCP1) between the carbene carbon of $S\text{-25}$ and the iodine atom of ICF_3 , and second interaction (BCP2) between a hydrogen atom of the aromatic ring of $S\text{-25}$ and the iodine atom of ICF_3 (Figure 33b). The electron density at BCP1 in **33a** is 3.6 times larger than at the BCP2. The values of the ratio $|\lambda_1/\lambda_3|$ at both BCPs are less than 1, which is an indication of closed shell interaction. The Laplacian $\nabla^2\rho(r_c)$ at both BCP1 and BCP2 is less than zero, implying that the charge is locally concentrated. As revealed by $\rho(r_c)$ and $(\nabla^2\rho)$ at the corresponding BCPs, the carbene carbon-iodine interaction in **30** is stronger than in **33a**.

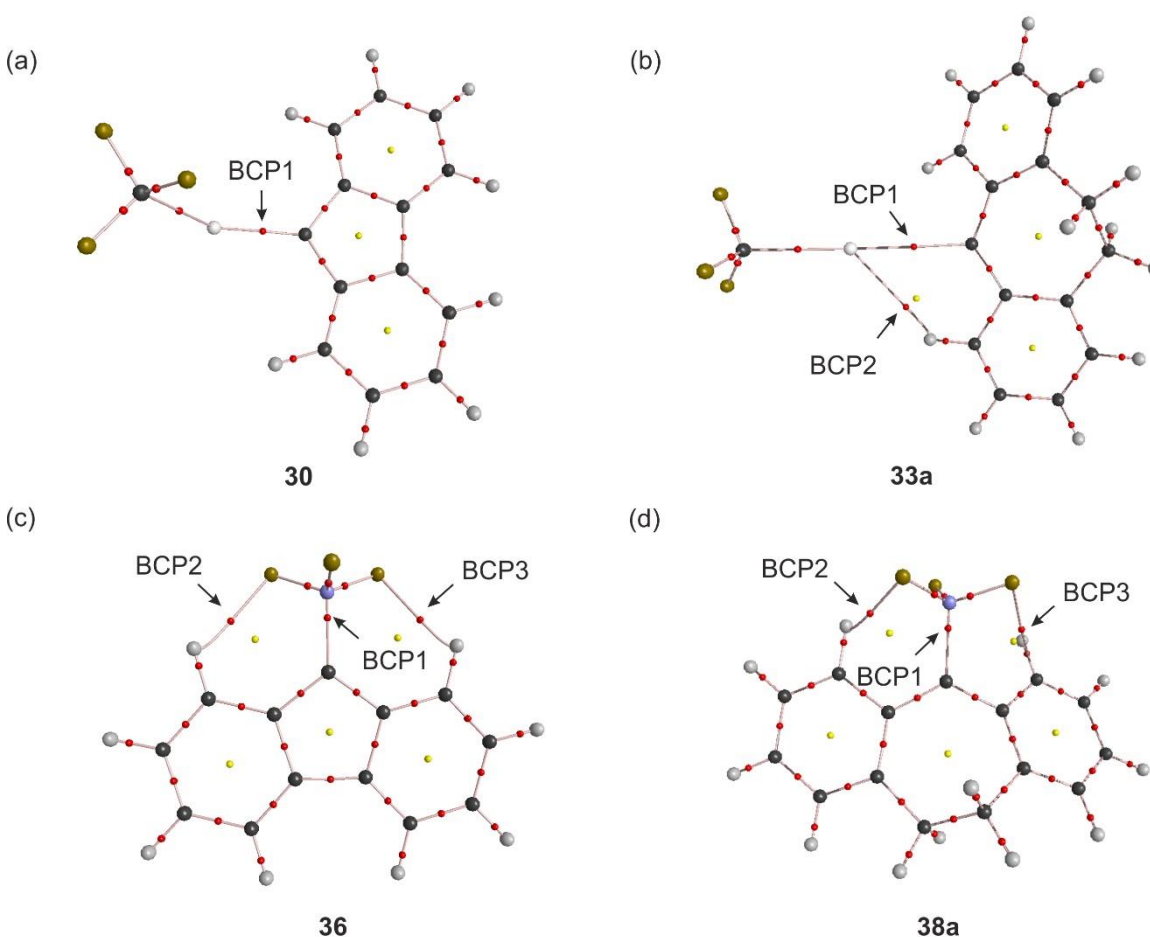


Figure 33. Structures of carbene-Lewis acid complexes (a) **30**, (b) **33a**, (c) **36** and (b) **38a** showing the bond critical points computed at the B3LYP-D3/def2-TZVP level of theory.

AIM analysis shows three interactions in complex **36**: strong carbene carbon-boron interaction (BCP1) and two relatively weak interactions (BCP2 and BCP3) between a fluorine atom of BF_3 and one of the aromatic hydrogen atoms of $S\text{-8}$ (Figure 33c). BCP1 has an electron density about

12 times larger than that of BCP2 and BCP3. The values of $|\lambda_1/\lambda_3| < 1$ at all three BCPs, indicating closed-shell interactions. BCP1 has $\nabla^2\rho(r_c) > 0$, implying the local depletion of charge due to the strong Lewis acidity of BF_3 , whereas the charge is locally concentrated in case of BCP2 and BCP3 since $\nabla^2\rho(r_c) < 0$. As in $\text{S-8}\cdots\text{BF}_3$, the complex **38a** between **S-25** and BF_3 shows three interactions with roughly similar topological parameters (Figure 33d). Larger electron density located between the carbene carbon atom and the boron in $\text{S-8}\cdots\text{BF}_3$ relative to that in $\text{S-25}\cdots\text{BF}_3$ results from the greater s-character of **8**. From the prominent interactions in all these complexes, the interaction of the singlet carbene center with BF_3 is stronger than that with ICF_3 , which evidences BF_3 to be stronger Lewis acid than ICF_3 .

Table 14. Summary of AIM calculations for the complexes **30**, **33a**, **36** and **38a** computed at the B3LYP-D3/def2-TZVP level of theory. All quantities are expressed in a.u.

Complexes	Bond critical point	$\rho(r_c)$	λ_1	λ_2	λ_3	$\nabla^2\rho(r_c)$	$ \lambda_1/\lambda_3 $
S-8 $\cdots\text{ICF}_3$ (30)	BCP 1	0.1386	-0.1569	-0.1326	0.2905	-0.0003	0.5399
S-25 $\cdots\text{ICF}_3$ (33a)	BCP1	0.0369	-0.0278	-0.0265	0.1089	-0.0136	0.2556
	BCP2	0.0103	-0.0073	-0.0042	0.0413	-0.0075	0.1764
S-8 $\cdots\text{BF}_3$ (36)	BCP1	0.1483	-0.2596	-0.2510	0.4390	0.0044	0.5266
	BCP2	0.0119	-0.0124	-0.0106	0.0682	-0.0113	0.1825
	BCP3	0.0119	-0.0124	-0.0106	0.0682	-0.0113	0.1825
S-25 $\cdots\text{BF}_3$ (38a)	BCP1	0.1393	-0.2278	-0.2240	0.3658	0.0215	0.6226
	BCP2	0.0176	-0.0152	-0.0150	0.1042	-0.0185	0.1461
	BCP3	0.0145	-0.0105	-0.0052	0.0798	-0.0160	0.1312

2.3. Conclusions

The highly polar closed-shell singlet states of carbenes **7**, **8** and **25** can be described as 1,1-zwitterions with a highly asymmetric charge distribution at the carbene center, whereas the triplet states are described as unpolar 1,1-diradicals. As a result, the singlet states are much more stabilized by hydrogen bonding, halogen bonding, and Lewis acid-base interactions than the triplet states. Interestingly, the stabilization of the singlet states of the three carbenes with H_2O , ICF_3 , and BF_3 lies in wide range of 9 – 42 kcal mol⁻¹, whereas the triplet states are stabilized only by 3 – 5 kcal mol⁻¹, irrespective of the chemical nature of the interacting molecule (Table 2). ICF_3 stabilizes the triplet states slightly more than H_2O or BF_3 , indicating that van der Waals dispersion

interactions are more important than the Lewis acidity. In contrast, the singlet states of the carbenes are highly stabilized by interactions with the Lewis acids, and the amount of stabilization varies considerably between the carbenes and between the Lewis acids. The stabilization is the largest for the complexation with BF_3 and the least for the complexes with H_2O .

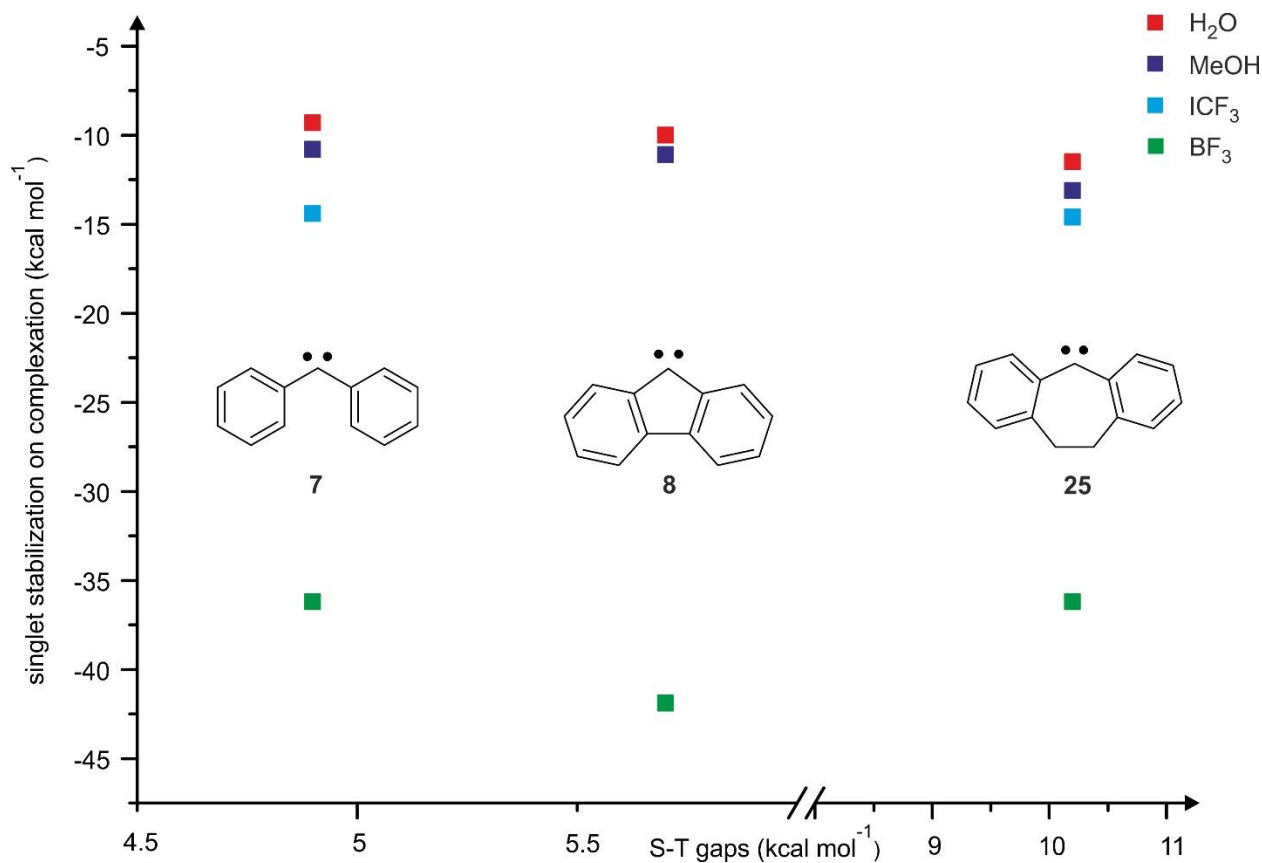


Figure 34. Complexation energies of different Lewis acids with the singlet states of carbenes **7**, **8** and **25**: Red, blue, cyan and green squares correspond to stabilization energies of the singlet state of the carbenes with H_2O , CH_3OH , ICF_3 , and BF_3 , respectively. Since carbene **8** does not form a halogen-bonded complex, but rather forms a singlet ylidic complex as shown in Figure 14, the stabilization energy of singlet state of **8** on complexation with ICF_3 is not considered. All the computations are performed at the B3LYP-D3/def2-TZVP level of theory.

It must be noted that the switching of the triplet ground state of the carbene on interaction with a given Lewis acid does not only depend on the stabilization energy of the corresponding singlet and triplet states, but also on the singlet – triplet energy gaps of the carbenes. For example, the singlet states of carbenes **7** and **25** are stabilized in a very similar manner by interactions with Lewis acids (Figure 34, Table 2). However, while carbene **7** forms singlet complexes with all three reagents, carbene **25** forms a singlet complex only with ICF_3 and BF_3 , but not with H_2O .

The stabilization of *S*-**25** upon formation of a hydrogen-bonded complex with water is not large enough to overcome the singlet-triplet splitting of carbene **25**. An important conclusion from this observation is that the stabilization of singlet carbenes by halogen bonding with ICF₃ is larger than the stabilization by hydrogen bonding with H₂O. Also, NBO analysis does not reveal any considerable difference in natural charges developed on the carbenes in the corresponding singlet complexes for a given Lewis acid (Figure 35, Table 15).

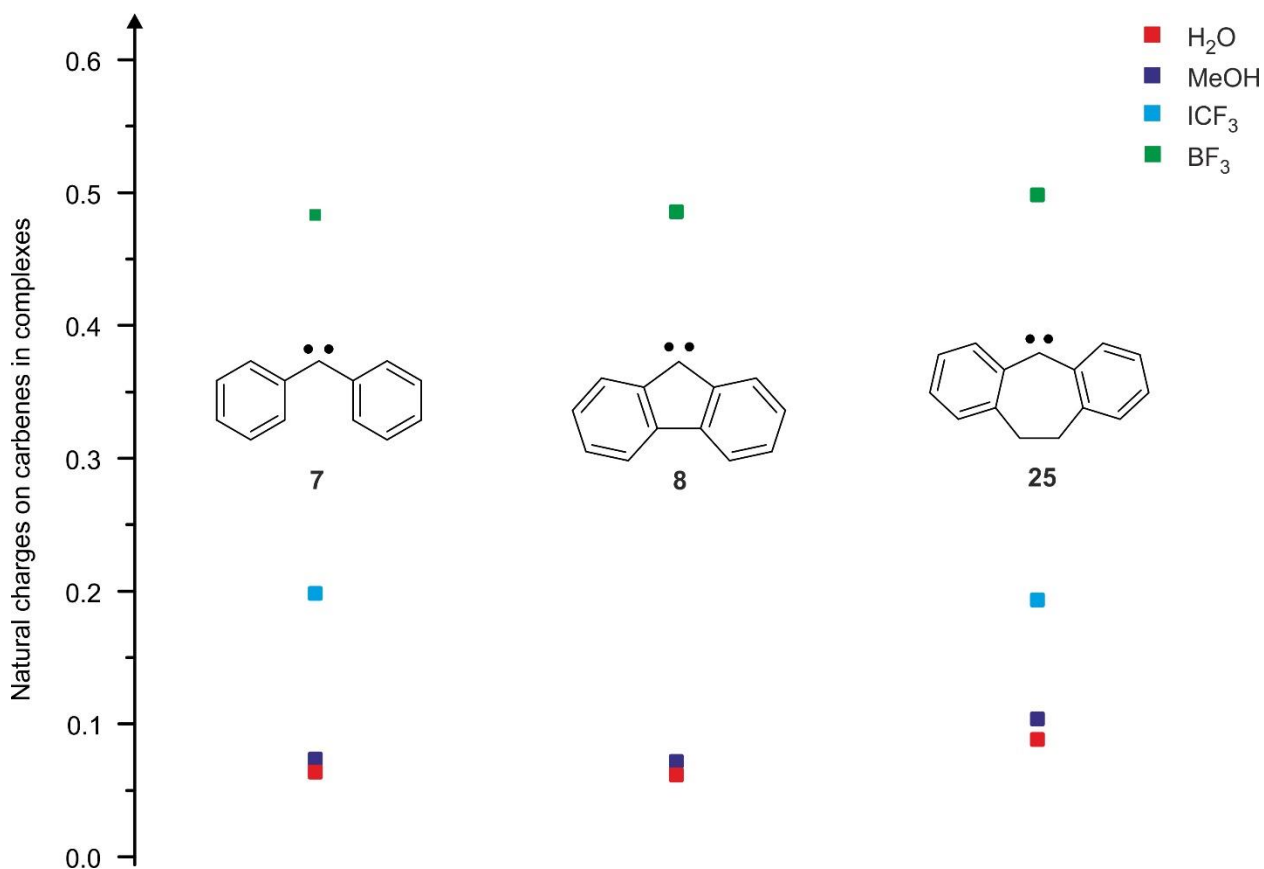


Figure 35. Natural charges on carbenes **7**, **8** and **25** in their most stable singlet complexes with H₂O (red), MeOH (blue), ICF₃ (cyan) and BF₃ (green) calculated at the B3LYP-D3/def2-TZVP level of theory. Since carbene **8** does not form the halogen-bonded complex, but rather forms a singlet ylidic complex as shown in Figure 14, the natural charge on carbene **8** in singlet ICF₃ complex is not compared here.

Table 15. Natural charges on the carbenes **7**, **8** and **25** in their most stable singlet and triplet complexes with H₂O, ICF₃ and BF₃.

#	H ₂ O complexes ^[a]		MeOH complexes ^[a]		ICF ₃ complexes ^[a]		BF ₃ complexes ^[a]	
	S	T	S	T	S	T	S	T
7	0.0634	0.0002	0.0735	0.0026	0.1982	0.0233	0.4830	0.0067
8	0.0615	-0.0147	0.0717	-0.0069	-0.4454	0.0084	0.4853	0.0125
25	0.0881	-0.0039	0.1036	0.0012	0.1932	0.0173	0.4981	0.0041

^aNatural charges on carbenes on complex formation, B3LYP-D3/def2-TZVP.

The different behavior of carbenes **7** and **25** can be understood in terms of the different S-T gaps resulting from the larger carbene bond angle in **25** compared to that in **7**. Fluorenylidene **8** shows a slightly smaller S-T gap than diphenylcarbene **7**, but the bond angle at the carbene center of S-**8** is with 101.2° considerably smaller than that of S-**7** with 119.4° (Figure 6). Consequently, the in-plane lone pair of S-**8** exhibits a higher s-character (46%) than that of S-**7** (35%) and thus lower basicity. In addition, reactions of carbene **8** are governed by the aromatic stabilization vs. anti-aromatic destabilization of the fluorenyl anion compared to the cation.

The interaction of S-**8** with the strong Lewis acid BF₃ results in the formation of the zwitterion **36** with a positively charged, and thus antiaromatic, fluorenyl unit resembling the fluorenyl cation. In this case, the antiaromatic destabilization is compensated by the formation of a strong donor-acceptor complex with a short C–B bond. The interaction of **8** with ICF₃, on the other hand, results in the formation of ylide **30** with a negatively polarized fluorenyl unit, avoiding a halogen-bonded complex, which would transfer positive charge to the five-membered ring system. In this respect, the reactivity of fluorenylidene **8** is closer to that of cyclopentadienyldiene and its chlorine derivative^[140] than to diphenylcarbene **7**.

Parts of chapter 2 were adapted with permission from Chem. Eur. J., **2018**, *24*, pp. 18043–18051.

Copyright 2018 WILEY-VCH.

3. Isolation of Dihydrodibenzotropylium Cation in LDA Water Ice

3.1. Introduction

The intramolecular spin conversion dynamics of carbenes strongly depends on the polarity of the solvent. Since the singlet states are highly polar, they are strongly stabilized in polar solvents, whereas the apolar triplet states experience only a weak stabilization.^[49]

Previous studies on carbenes **7**, **8**, and **25** by laser-induced fluorescence spectroscopy have shown that the singlet to triplet intersystem crossing rate (k_{ST}) of the carbene decreases as the polarity of the solvent increases.^[49, 149-150] By ultrafast time-resolved spectroscopy, the lifetimes of S-**7**, S-**8**, and S-**25** in more polar acetonitrile were determined to 340, 440, and 83 ps, whereas in less polar cyclohexane, the lifetimes are shortened to 110, 88, and 72 ps, respectively.^[53, 127, 151] The longer lifetimes of the singlet carbenes in more polar solvents are due to reduction of the rate constants of intersystem crossing; for example, the rate constants of singlet fluorenylidene S-**8** were determined to $1.4 \times 10^{-9} \text{ s}^{-1}$ in acetonitrile and to $9.5 \times 10^{-9} \text{ s}^{-1}$ in cyclohexane.^[53] In methanol, the lifetimes of the singlet states are drastically reduced to 9 ps for S-**7**, 22 ps for S-**8**, and 9 ps for S-**25** due to the rapid reactions with the solvent to give the corresponding benzhydryl **15**, fluorenyl **40**, and dihydrodibenzotropylium **41** cations.^[53, 127, 151]

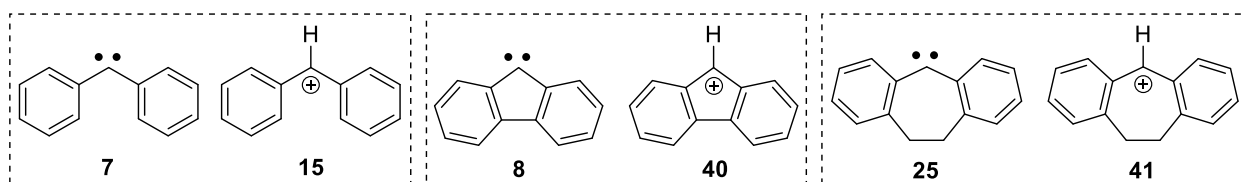


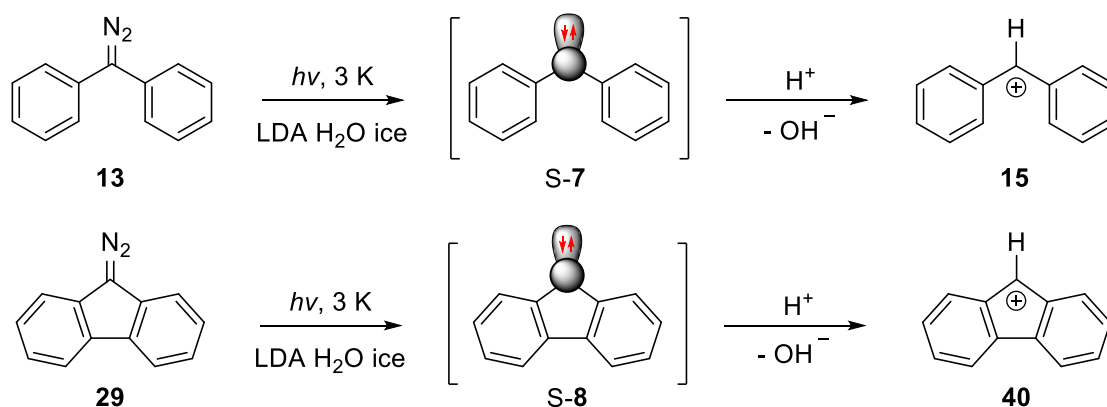
Chart 7. Structures of Benzhydryl **15**, fluorenyl **40** and dihydrodibenzotropylium **41** cations with their respective carbenes **7**, **8** and **25**.

The longer lifetime of S-**8** in methanol was explained by the antiaromaticity of the fluorenyl cation **40**, since formation of such species is less exothermic and governed by a higher activation barrier and slower rate.^[53] The strongly electrophilic secondary cations **15**, **40** and **41** are short-lived in methanol and react with surrounding methanol molecules. Interestingly, cation **41** decays slower in methanol with a time constant of 81 ps, compared to **15** (31 ps) and **40** (5 ps).^[53, 127, 151] The stability of these cations **15**, **40** and **41** has been investigated by measurement of their pK_R values by Looker and O'Ferrall et al.^[152-153] Cation **41** with a pK_R value of -8.0 was determined to be

significantly more stable than **15** with a pK_R value of -11.7 and **40** with a pK_R value of -15.9, explaining its relatively longer lifetime in methanol.

Under the conditions of matrix isolation, it was demonstrated that the reactions of the triplet ground state carbenes **7** and **8** in argon matrices doped with 1% of H₂O result in the formation of strongly hydrogen-bonded complexes by switching the spin states of carbenes from triplet to singlet.^[1, 4] On the contrary, as discussed in chapter 2, the reaction of T-**25** with single water molecules fails to form the hydrogen-bonded singlet carbene complex S-**25**···H₂O by switching the spin state of the carbene from triplet to singlet. This is rationalized by the large S-T gap of **25**, which does not allow to stabilize S-**25** below T-**25** by hydrogen bonding.^[154]

Low density amorphous (LDA) water ice is a highly polar medium and recent studies of **7** and **8** in LDA ice environments have shown the rapid protonation of S-**7** and S-**8** even at 8 K to yield the corresponding **15** and **40** cations upon photolysis of the respective diazo precursors (Scheme 15).



Scheme 15. Protonation of diphenylcarbene **7** and fluorenylidene **8** in LDA water ice.

To gain more insight into the reactivity of **25** in polar media considering the larger S-T gap of carbene **25** compared to **7** and **8**, the reaction of **25** with H₂O was studied in LDA water ice.

LDA water ice

The solid state of ice can be classified as a crystalline and amorphous phase. The crystalline phase is reported to have at least 15 different forms,^[155] whereas the amorphous ice can be grouped into two forms depending on their densities, low density (LDA) and high density (HDA) amorphous water ice.^[156] The deposition of low-pressure vapour of water onto a cold substrate forms LDA ice, while pressurized crystalline ice (~ 13 Kbar) produces HDA ice. Unlike crystalline ice, both

forms of amorphous water ice lack the long-range periodic structure, which makes them structurally similar to liquid water.^[157] This can be observed by analysis of the O–H stretching region in the infrared region.^[158] The O–H stretching vibration in LDA water ice exhibits a broad band like in liquid water, whereas this band is much sharper in crystalline ice. Due to the higher mobility of water molecules in the liquid phase, the exchange of hydrogen bonds takes place on an ultra-fast time scale of a few ps. On the other hand, in LDA water ice, the reorientation of the water molecules is a very slow process, which leads to stronger hydrogen bonding.^[159] In matrix isolation spectroscopy, LDA water ice can be used instead of inert gases to generate matrices with unique properties. However, as compared to inert gas matrices, the IR transparency in LDA water ice is reduced due to strong absorptions around 3600, 1600, 700, and 400 cm^{-1} .^[160] In contrast to the IR spectral region, LDA water ice is transparent in the UV-Vis region above 160 nm, which is comparable to inert gas matrices. Gudipati et al. have demonstrated the application of LDA water ice using matrix isolation reporting series of experiments on reactive species.^[161-164]

3.2. Results and Discussion

3.2.1. Reaction of Dibenzocycloheptadienylidene with LDA water ice

IR spectroscopy. Diazodibenzocycloheptadienylidene **26** generated by sublimation of its sodium salt was deposited with an excess of water onto a cold spectroscopic window at 50 K to form a LDA water ice matrix, which was then cooled to 8 K. An absorption appearing at 2044.4 cm^{-1} can be assigned to the asymmetric stretching vibration of the C=N=N group identifying the deposited compound as diazo precursor **26**. The peak broadening compared to an argon is mainly due to inhomogeneity of the matrix cages of the LDA ice (Figure A4, Table A1). Visible light irradiation (530 nm) of **26** trapped in LDA water ice at 8 K gives rise to a set of IR bands at 778.4, 1180.6, 1360.3, 1476.6, 1521.4 and 1591.3 cm^{-1} which are assigned to dihydrodibenzotropylium cation **41** by comparison with a DFT calculation (Figure 36, Table 16). The signal centered at 1521.4 cm^{-1} is assigned to the characteristic C–C–C asymmetric stretching vibration at the cationic center of **41** and is almost identical to corresponding signal of the benzhydryl cation **15** in LDA water ice at 1521.6 cm^{-1} .^[1] The singlet carbene S-**25** is not observed under these conditions, and trace amounts of T-**25** could be detected by UV-Vis experiments. Cation **41** is presumed to be formed by abstraction of a proton of water by singlet state of **25** even at 8 K and the OH^- ion produced during the proton transfer from the water molecule is stabilized and immobilized in LDA water ice.

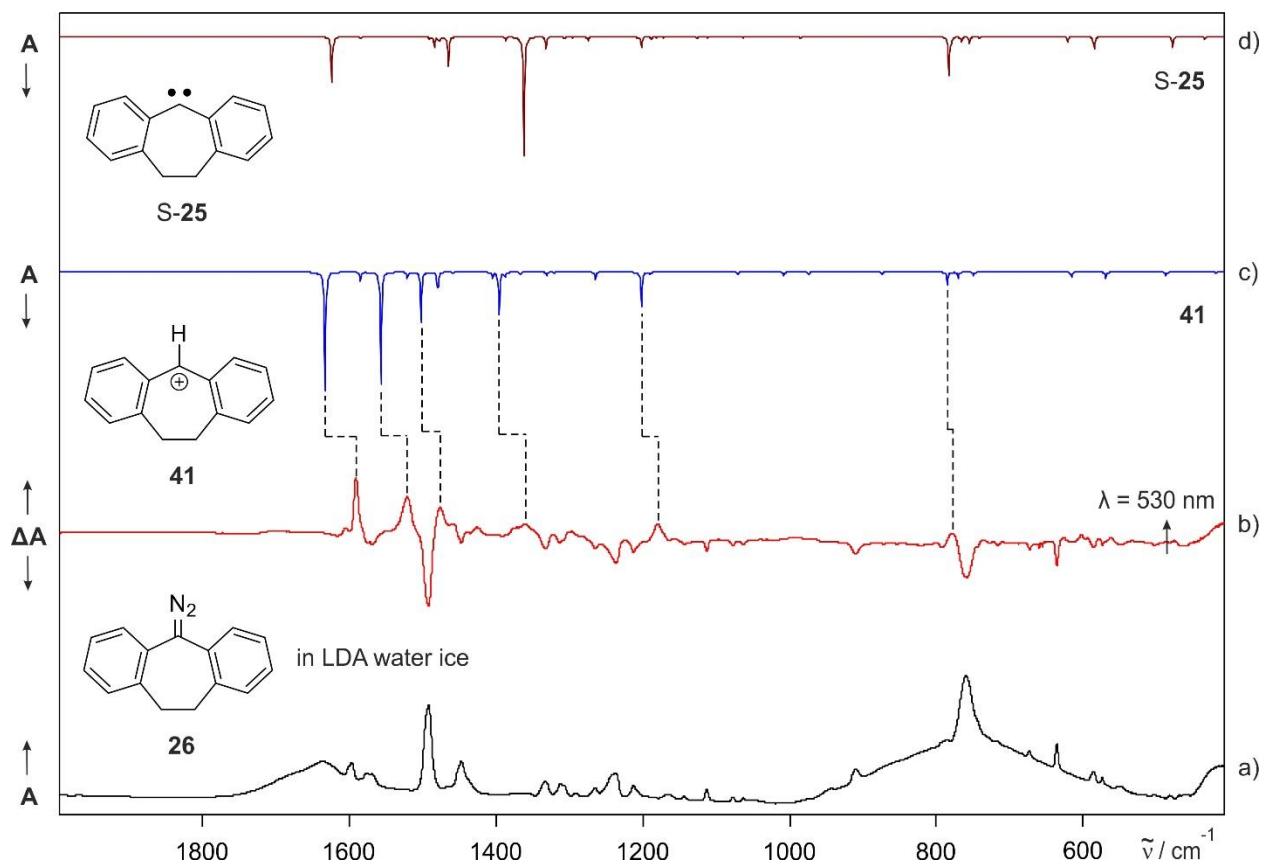


Figure 36. IR spectra showing the formation of dihydrodibenzotropylium cation **41** in LDA water ice. a) IR spectrum of diazodibenzocycloheptadienyliene **26** trapped in a LDA water ice matrix at 8 K. b) Difference IR spectrum showing the changes after 530 nm irradiation at 8 K. Bands pointing downwards assigned to **26** are disappearing, and bands pointing upwards assigned to the cation **41** are appearing. c) Computed IR spectrum of **41** at the B3LYP-D3/def2-TZVP level of theory (multiplied by -1). d) Computed IR spectrum of S-25 at the B3LYP-D3/def2-TZVP level of theory (multiplied by -1).

Cation **41** is kinetically stabilized and does not react with the water matrix at low temperatures. Annealing of the matrix from 8 to 130 K results in a decrease of the intensities of the bands of **41**, and concurrently new signals are formed, which are assigned to dihydrodibenzotropylium alcohol **42** by comparison with an IR spectrum of an authentic matrix-isolated sample (Figure 37). It is worth to note that the alcohols resulting from the reactions of **15** and **40** with LDA water ice were observed at 100 and 50 K respectively,^[1,4] suggesting the greater stability of **41** in LDA water ice. The stability of these cations can be elucidated from their pK_R values, which are $pK_R = -8.0$ for **41**, $pK_R = -11.7$ for **15** and $pK_R = -15.9$ for **40**, indicating that the latter two ions are less stable.^[152-153]

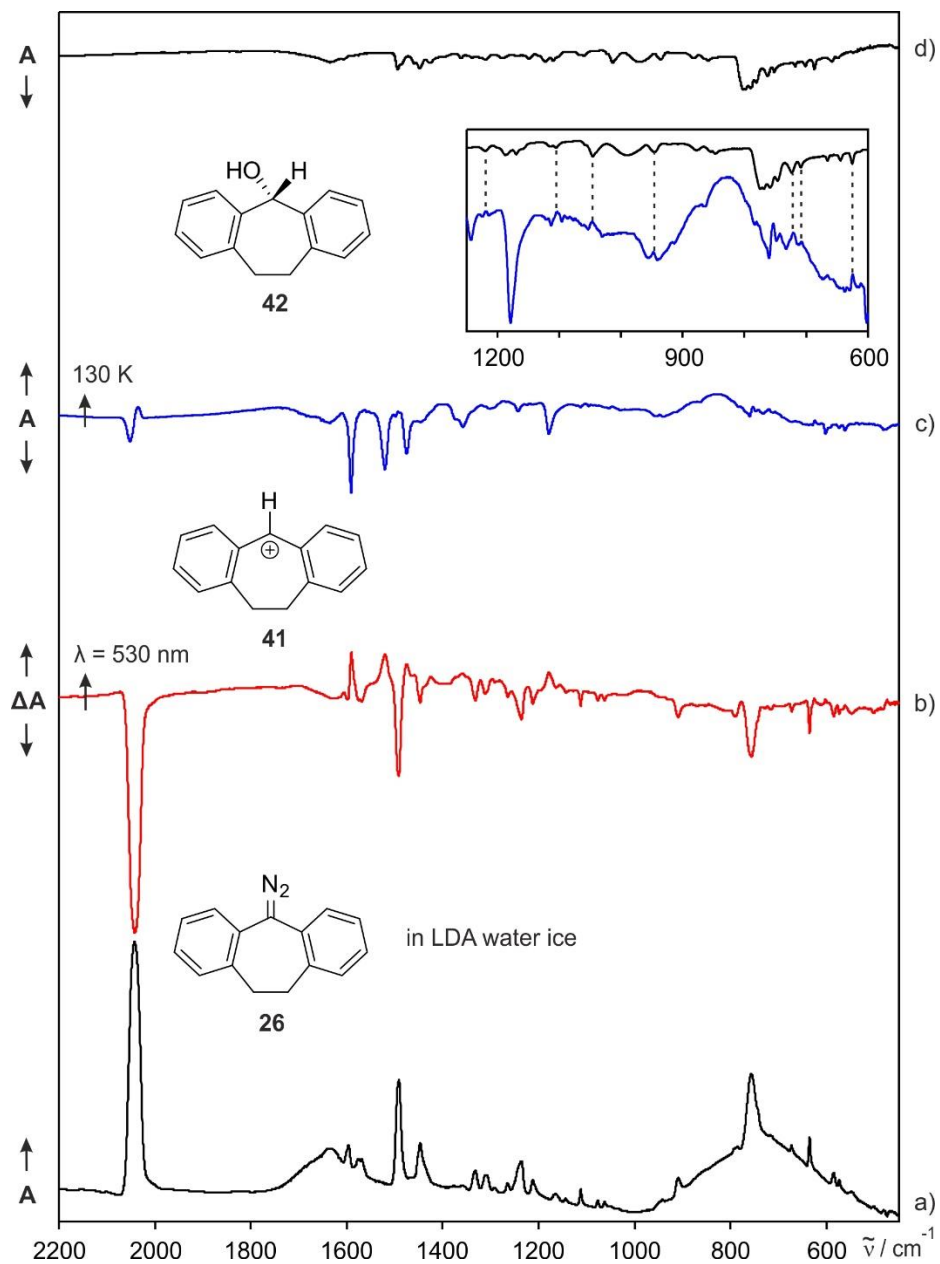


Figure 37. IR spectra showing the formation of dihydrodibenzotropylium cation **41** and its disappearance on annealing. a) IR spectrum of diazo precursor **26** trapped in a LDA water ice matrix at 8 K. b) Difference IR spectrum showing the changes after 530 nm irradiation at 8 K. Bands pointing downwards assigned to **26** are disappearing, and bands pointing upwards assigned to the cation **41** are appearing. c) Difference IR spectrum of the same matrix showing the changes after annealing from 8 to 130 K. Bands pointing downwards assigned to cation **41** are disappearing, and bands pointing upwards assigned to formal O–H insertion product **42** are appearing. d) IR spectrum of **42** in a LDA water ice matrix at 8 K. The inset shows the spectral region between 600 – 1250 cm^{-1} of spectra c) and d), showing a good agreement.

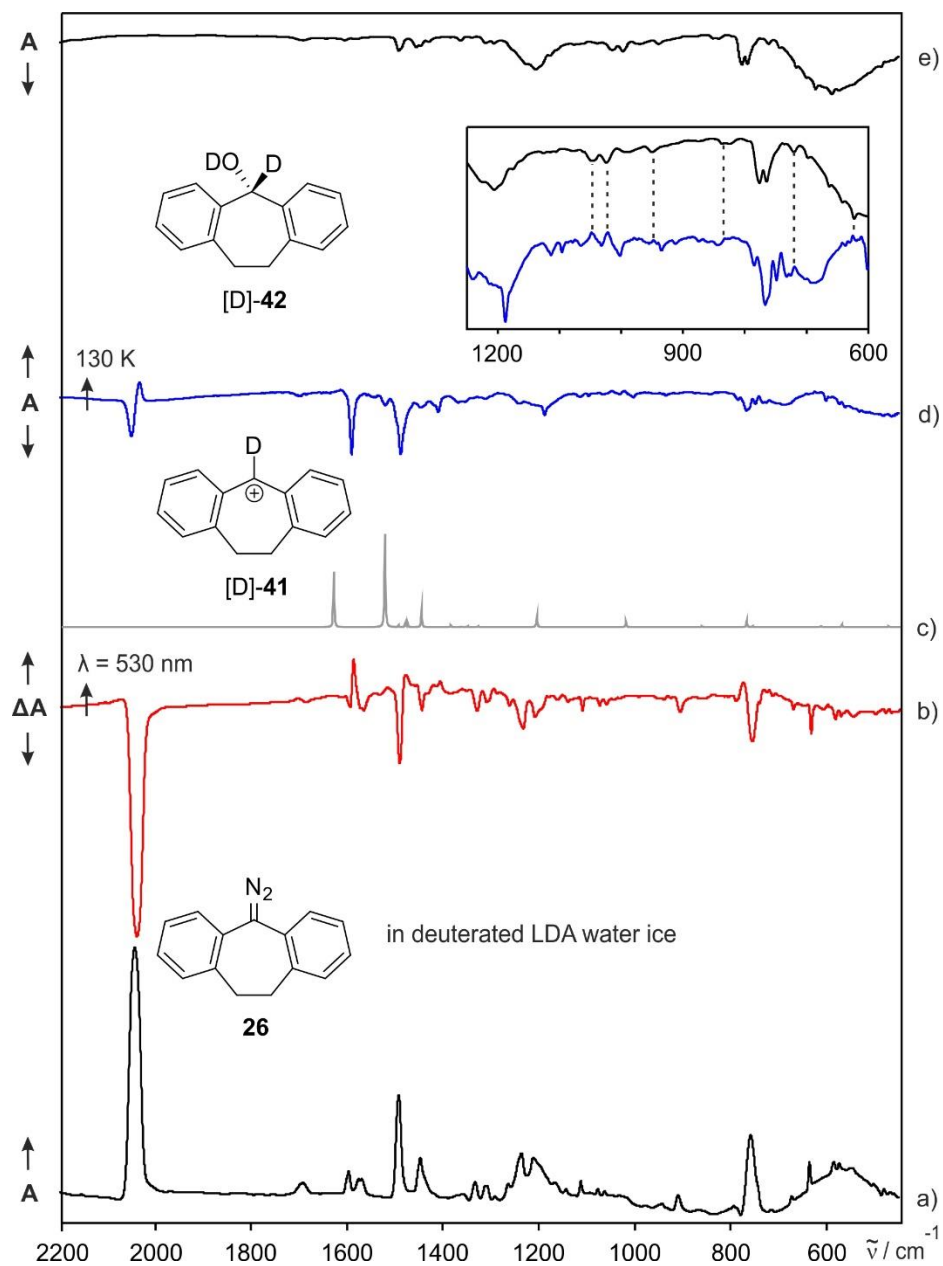


Figure 38. IR spectra showing the formation of deuterated dihydrodibenzotropylium cation [D]-41 and its disappearance on annealing. a) IR spectrum of diazodibenzocycloheptadienyliene **26** trapped in LDA D_2O ice matrix at 8 K. b) Difference IR spectrum showing the changes after 530 nm irradiation at 8 K. Bands pointing downwards assigned to **26** are disappearing, and bands pointing upwards assigned to cation [D]-41 are appearing. c) Computed IR spectrum of [D]-41 at the B3LYP-D3/def2-TZVP level of theory. d) Difference IR spectrum of the same matrix showing the changes after annealing from 8 to 130 K. Bands pointing downwards assigned to [D]-41 are disappearing, and bands pointing upwards assigned to formal O-D insertion product [D]-42 are appearing. e) IR spectrum of [D]-42 in LDA water ice matrix at 8 K. The inset shows the spectral region between 600 – 1250 cm^{-1} of spectra d) and e), showing a good agreement.

In analogy to H₂O, the experiments were performed in D₂O LDA ice. Photolysis of **26** with 530 nm resulted in formation of the deuterated cation [D]-**41**. The observed IR bands fit nicely with a calculated spectrum of [D]-**41** (Figure 38, Table 16). A strong signal at 1487.9 cm⁻¹ is assigned to the characteristic C–C–C asymmetric stretching vibration of undeuterated **41** and shows a pronounced isotopic shift of -33.0 cm⁻¹ in [D]-**41**, in excellent agreement with theoretical predictions (Figure 39).

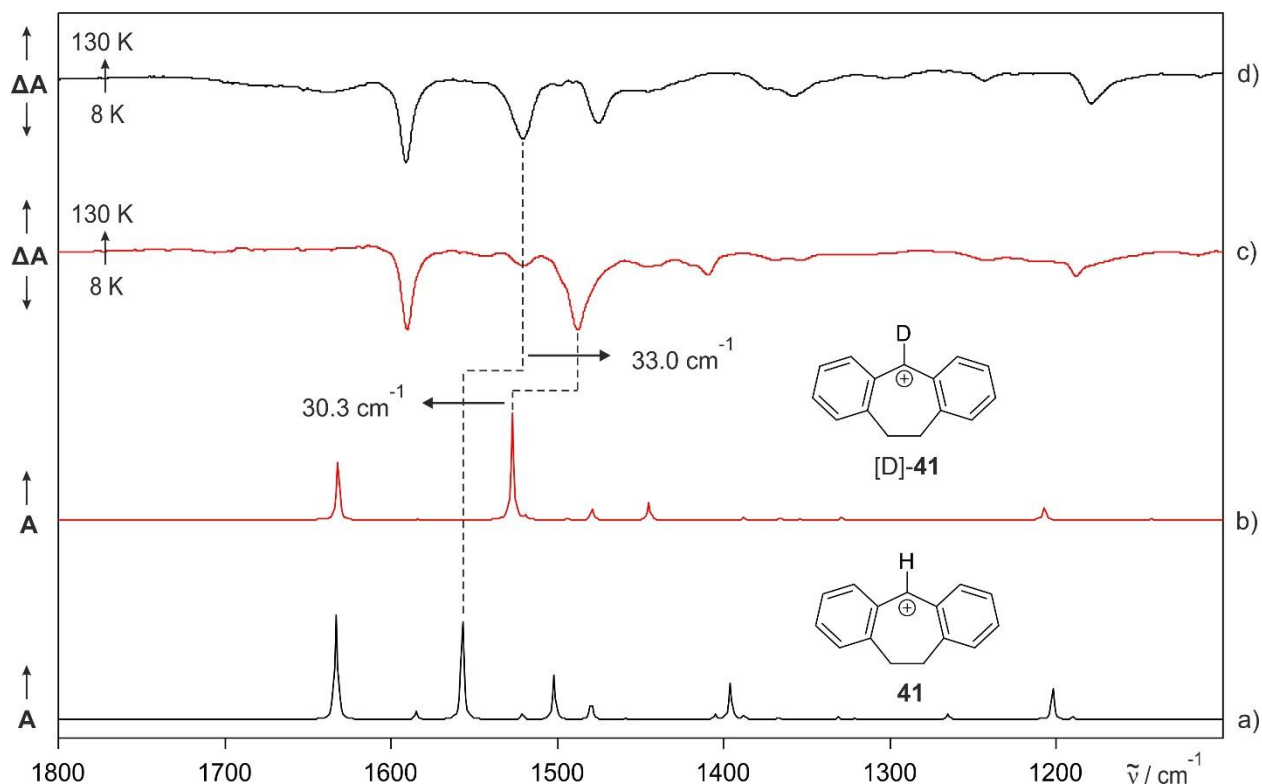


Figure 39. IR spectra showing the isotopic shift of the C–C–C asymmetric stretching vibrations of cation **41** and its corresponding isotopomer [D]-**41**. a) IR spectrum of cation **41** at the B3LYP-D3/def2-TZVP level of theory. b) Computed IR spectrum of deuterated cation [D]-**41** at the B3LYP-D3/def2-TZVP level of theory. c) IR difference spectrum of D₂O ice matrix containing [D]-**41** showing the changes after annealing at 130 K, peaks pointing downwards are assigned to [D]-**41**. d) IR difference spectrum of the H₂O ice matrix containing **41** showing the changes after annealing at 130 K, peaks pointing downwards are assigned to **41**.

Warming up the LDA matrix containing [D]-**41** from 3 to 130 K leads to decrease of the IR bands assigned to [D]-**41**, and concomitantly the corresponding alcohol [D]-**42** is produced (Figure 38d). The assignment of [D]-**42** is confirmed by comparison with an IR spectrum of an authentic matrix-isolated sample (Figure 38e).

Table 16. IR vibrational frequencies of dihydrodibenzotropylium cation **41** and its deuterated isotopomer [D]-**41**.

Mode	Sym	DFT ^[a]		LDA ice ^[b]		Assignment
		$\tilde{\nu}$ /cm ⁻¹ (shift) ^[c]	I _{rel} ([D]- 41) ^[d]	$\tilde{\nu}$ /cm ⁻¹ (shift) ^[c]	I _{rel} ([D]- 41) ^[d]	
12	B	489.6	4	476.5	6	Skel. vib.
16	B	573.1 (-0.4)	6 (3)	562.7 (-1.1)	9 (7)	C-H bend
17	B	618.2 (-1.8)	6 (3)	603.3 (-1.5)	10 (8)	Skel. vib.
21	B	754.2	4	738.0	7	C-H bend
23	B	793.2 (-22.2)	11 (8)	778.4 (-29.6)	21 (11)	C-H wagging
42	B	1204.2 (+5.6)	31 (12)	1180.6 (+7.9)	31 (14)	C-H def. (in plane)
53	B	1398.1	35	1360.3	24	C=C str.
57, 58	B, A	1479.8, 1484.3	18	1425.8	14	CH ₂ bend
59	B	1504.7	42	1476.6	36	C=C str.
61	B	1558.8 (-32.5)	93 (100)	1521.4 (-33.3)	72 (100)	C-C-C asym. str.
64	B	1633.9 (-0.4)	100 (54)	1591.3 (-0.7)	100 (83)	C=C str.

^[a]Calculated at the B3LYP-D3/def2-TZVP level of theory. ^[b]LDA water ice matrix at 8 K. ^[c]Deuterium isotopic shift of [D]-**41** relative to **41** in parentheses. ^[d]Relative intensity of [D]-**41** isotopomer in parentheses.

UV-Vis spectroscopy. The formation of cation **41** in LDA water ice was also monitored by UV-Vis spectroscopy. Under reaction conditions similar to the IR experiments, photolysis (530 nm) of a LDA water ice matrix containing **26** at 8 K produces **41** and the matrix turns intensely yellow, featuring a strong visible absorption centered at $\lambda_{\text{max}} = 416$ nm, in accordance with the reported absorption in methanol at 420 nm.^[127] The absorption at $\lambda_{\text{max}} = 416$ nm is also in a fair agreement with TD-DFT calculations ($\lambda = 346$ nm, $f = 0.2231$) for the transition from bonding π -orbitals of adjacent phenyl rings to the empty π -orbital of the carbene carbon (Figure A5). In addition, trace amounts of triplet carbene T-**25** are detected showing UV absorptions at $\lambda_{\text{max}} = 323$, 337, and 349 nm. No traces of singlet carbene S-**25** are observed under these conditions. It is interpreted that the highly basic singlet state S-**25** is immediately protonated by water to form **41**, whereas T-**25** interacts weakly. On annealing of the water matrix above 50 K, the visible band of **41** and the UV bands of T-**25** slowly disappear (Figure 40). Unfortunately, the UV signals of the insertion product **42** appearing at 265 and 273 nm are overlapping with the broad absorptions of precursor **26**, so that an unambiguous assignment is not possible.

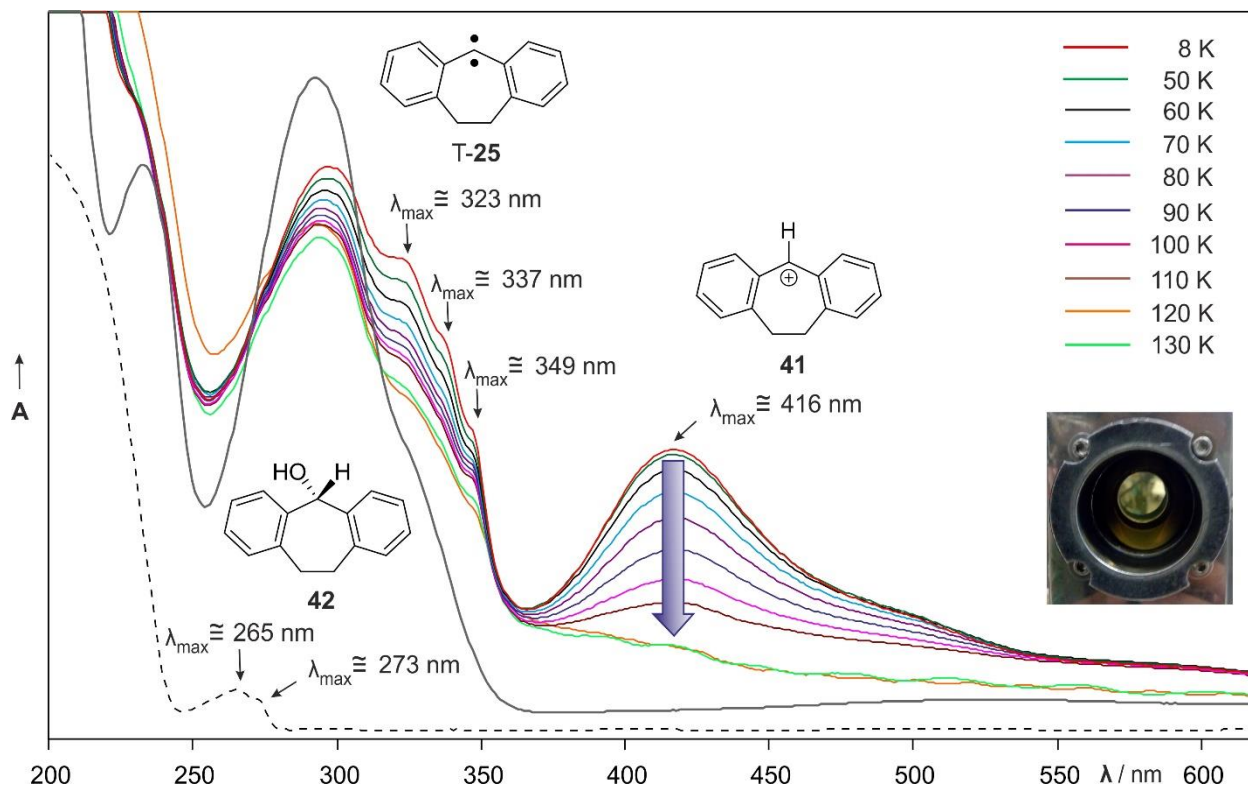


Figure 40. UV-Vis spectra showing the decay of dihydrodibenzotropylium cation **41** ($\lambda_{\text{max}} = 416 \text{ nm}$) and T-**25** ($\lambda_{\text{max}} = 323, 337 \text{ and } 349 \text{ nm}$) on warming the LDA water ice matrix from 8 to 130 K. Grey line represents the UV-Vis spectrum of diazo precursor **26** isolated in LDA water ice at 8 K. Dotted line represents the UV-Vis spectrum of **42** isolated in a LDA water ice matrix. The formation of cation **41** leads to intense yellow colour of the matrix (Photograph).

3.2.2. Photochemistry of Dihydrodibenzotropylium Cation

Irradiation of the cation **41** in LDA water ice with 450 nm results in the decrease of the intensity of the visible band of **41**, and concurrently the intensity of one of the UV absorptions of T-**25** at 349 nm increases. Previously, Scaiano and Wright reported that the absorption maxima of T-**25** and dihydrodibenzotropylium radical **43** are very similar and it was observed that T-**25** has a larger extinction coefficient than the radical **43** at 324 nm, whereas the radical absorbs more strongly than T-**25** at 348 nm.^[165] The rise of the absorption centered at 349 nm in our experiment is therefore assigned to the formation of radical **43**. Interestingly, subsequent irradiation of the same matrix with 365 nm recovers the signal of **41**, accompanied by the decrease of the UV band of **43** at 349 nm. This electron transfer reaction is found to be reversible by UV/Vis irradiations, interconverting between **41** and **43** (Figure 41). The observed phenomenon is in analogy to the

photoinduced equilibrium reported for the benzhydryl radical and benzhydryl cation in amorphous water ice.^[104]

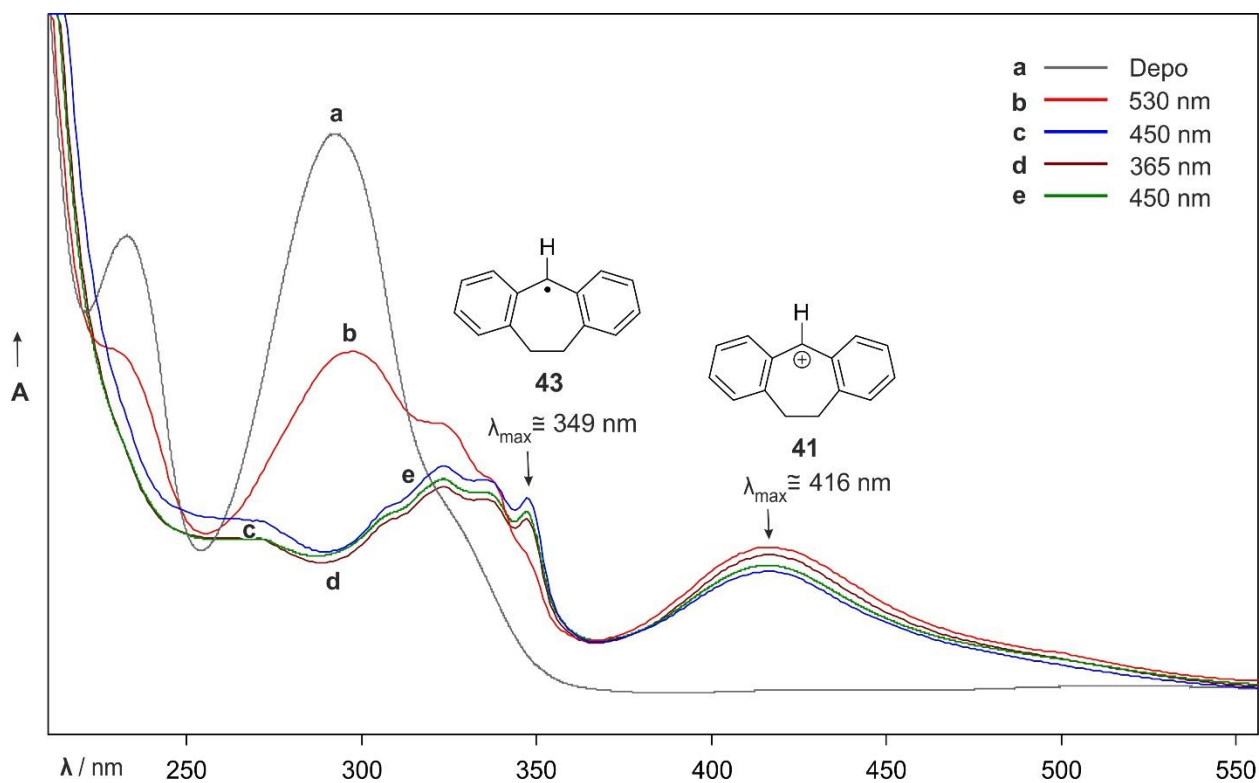


Figure 41. UV-Vis spectra showing the photochemistry of dihydrodibenzotropylium cation **41** in LDA water ice. a) UV-Vis spectrum of diazo precursor **26** isolated in LDA water ice at 8 K. b) UV-Vis spectrum obtained after irradiation of the matrix with 530 nm, showing the formation of cation **41** ($\lambda_{\max} = 416$ nm) and T-**25**. c) UV-Vis spectrum of the same matrix showing the changes after 450 nm irradiation. The intensity of the band assigned to **41** decreases, and simultaneously the intensity of the band at $\lambda_{\max} = 349$ nm assigned to radical **43** increases. d) UV-Vis spectrum of the same matrix showing the changes after 365 nm irradiation. The intensity of the absorption of **41** is increased accompanied by a decrease of the intensity of the band of **43**. e) UV-Vis spectrum of the same matrix obtained after irradiation with 450 nm confirming the interconversion between cation **41** and radical **43**.

The reversible interconversion between **41** and **43** was also examined by IR spectroscopy. Upon 450 nm photolysis of cation **41** in LDA water ice, all IR bands assigned to **41** disappear, however, no signals corresponding to radical **43** are detected in these experiments. This is rationalized by the low yield of **43** as the radical is a secondary photoproduct in the reaction and also it has lower absorption coefficient relative to that of **41**. Further irradiation of the same matrix with 365 nm restores the signals of **41**, suggesting the formation of **43** as the intermediate photoproduct (Figure 42).

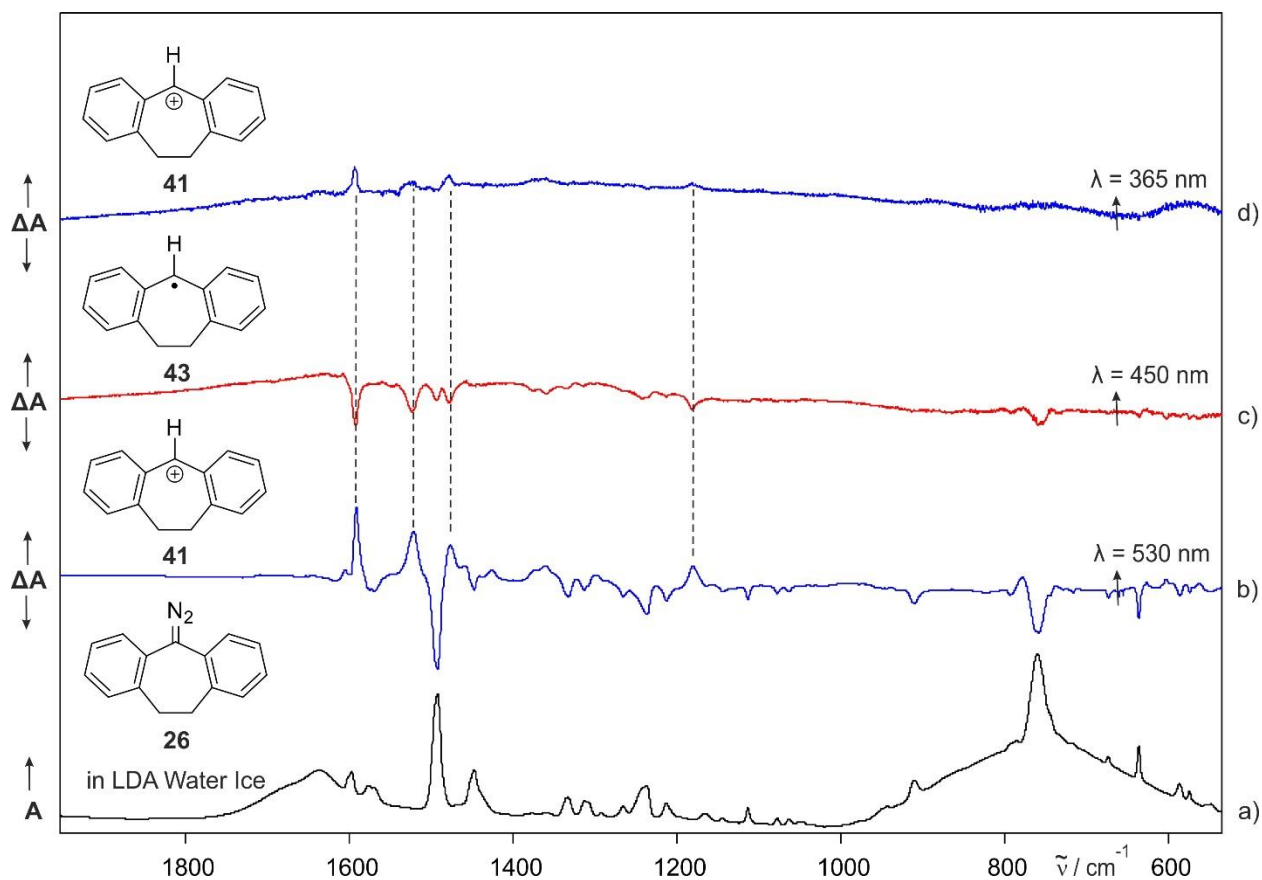
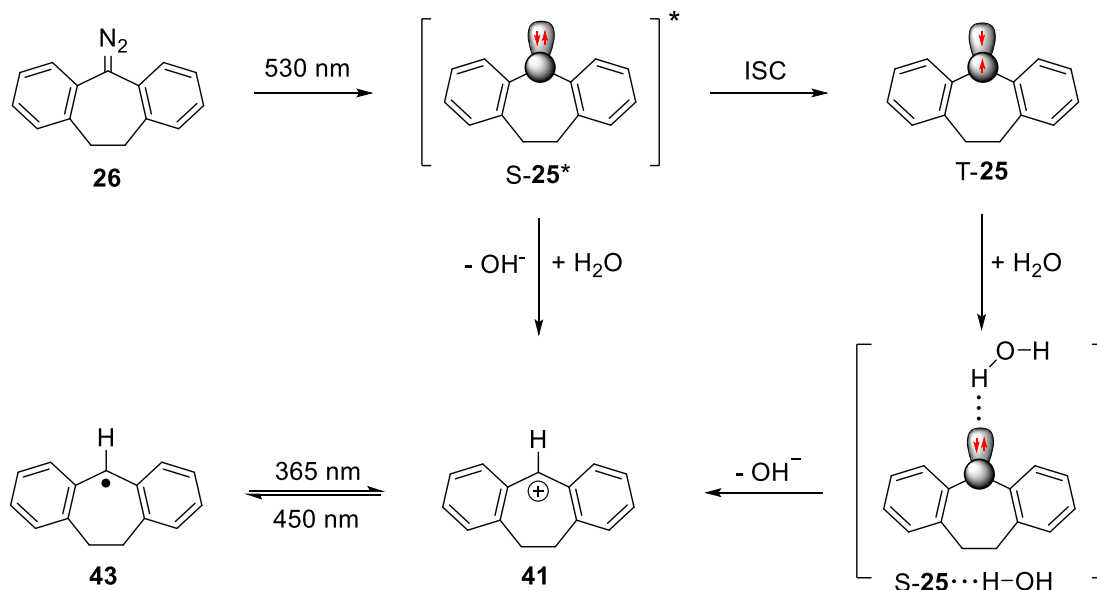


Figure 42. IR spectra showing the photochemistry of dihydrodibenzotropylium cation **41** in LDA water ice. a) IR spectrum of diazo precursor **26** trapped in LDA water ice at 8 K. b) Difference IR spectrum showing the changes after 530 nm irradiation at 8 K. Bands pointing downwards assigned to **26** are disappearing, and peaks pointing upwards assigned to cation **41** are appearing. c) Difference IR spectrum of the same matrix showing the changes after 450 nm irradiation. Bands pointing downwards assigned to **41** are disappearing. d) Difference IR spectrum of the same matrix showing the changes after 365 nm irradiation. Bands pointing upwards assigned to **41** are reappearing, suggesting the formation of radical **43** as intermediate photoproduct.

The mechanism of reaction of carbene **25** with LDA water ice to yield the cation **41** can be proposed in two ways (Scheme 16): a) Interaction of **25** with highly polar LDA ice switches the spin state of the carbene from triplet to singlet, followed by rapid protonation of singlet state S-**25** to produce **41**. However, as discussed in previous chapter, single water molecule fails to stabilize S-**25** enough to overcome the S-T gap of **25**.^[154] Therefore, more than one water molecules might be required to switch the spin state from T-**25** to S-**25** in LDA water ice. b) The singlet excited state S-**25**^{*} generated upon photolysis of diazo precursor **26** is immediately protonated before relaxing to the triplet ground state T-**25**.



Scheme 16. Reaction of dibenzocycloheptadienyldene **25** with LDA water ice.

It is interesting to compare the reactivity of **7** and **8** in LDA water ice reported in literature with that of **25**. Diphenylcarbene **7** and fluorenylidene **8** were shown to produce benzhydryl **15** and fluorenyl **40** cations respectively in amorphous water ice,^[1, 4] and in the experiments described above, dihydrodibenzotropylium cation **41** is obtained by the reaction of **25** with amorphous water ice (Figure 37). The tendency of carbenes **7**, **8** and **25** to form the corresponding cations by rapid protonation can be quantified from the proton affinity values of these carbenes in their singlet states. According to DFT calculations at the B3LYP-D3/def2-TZVP level of theory, carbene S-**25** is predicted to have a larger proton affinity value of 283 kcal mol⁻¹, compared to that of S-**7** (274 kcal mol⁻¹) and S-**8** (273 kcal mol⁻¹), which reflects a more exothermic protonation of S-**25** to yield cation **41**.

3.3. Conclusion

LDA water ice proves to be a potent and polar matrix material which allows to isolate and kinetically stabilize dihydrodibenzotropylium cation **41**. The visible absorption of **41** matches with that previously observed by ultrafast absorption spectroscopy,^[127] and its IR spectrum is in good agreement with a spectrum calculated at the B3LYP-D3/def2-TZVP level of theory. Cation **41** can be formed either by protonation of the hot singlet state S-**25*** obtained by photolysis of **26** or by protonation of S-**25** generated after spin switching induced by LDA water ice. It remains an

interesting challenge for future research to provide detailed insight into these processes. The formation of **41** can be correlated to a proton affinity value of $283 \text{ kcal mol}^{-1}$ calculated at the B3LYP-D3/def2-TZVP level of theory, indicating the ability of highly basic singlet state **S-25** to abstract proton. Below 50 K, **41** is stable and does not react with the surrounding water molecules or hydroxyl ions. Annealing of the LDA water matrix containing **41** from 3 to 130 K results in the formation of dihydrodibenzotropylium alcohol **42**, which demonstrates the stability of **41** as evident by its pK_R value of -8.0 .^[153]

The stability of the cation **41** can also be explained by the extent to which the empty π -orbital of the cationic carbon acquires electron density through conjugation. The more it acquires electron density, the higher will be the stability of the cation. In case of cation **41**, the phenyl rings adjacent to the cationic carbon are bridged by an ethano linkage, and therefore the π -orbitals of these rings are in appropriate alignment with respect to the empty π -orbital of the cationic carbon, which facilitates conjugation and delocalizes the positive charge into the π -system. In contrast, the phenyl rings of benzhydryl cation **15** are twisted to avoid steric repulsion of *ortho* hydrogens. Accordingly, the π -orbitals of one of the phenyl rings of the benzhydryl cation **15** adopt a coplanar geometry with respect to the empty π -orbital of the cationic carbon and therefore comparatively less electron density is transferred which accounts for the lower stability of **15** with respect to **41** ($pK_R = -11.7$).^[152] On the other hand, fluorenyl cation **40** is highly destabilized with a pK_R value of -15.9 ^[152] due to antiaromaticity despite of its planar geometry where the π -orbitals of the adjacent phenyl rings are in the same plane as that empty π -orbital of the cationic carbon.

The photochemistry of cation **41** in LDA water ice was also investigated in the present study. Photoinduced (450 nm) electron capture by **41** either from OH^- or electrons trapped in ice matrix leads to the formation of radical **43** which can be rationalized by the high electron affinity of **41**. This electron transfer is found to be reversible upon 365 nm irradiation yielding back cation **41** implying the higher electron affinity of the LDA water ice with respect to **43**. In conclusion, for the first time, dihydrodibenzotropylium cation **41** is isolated in a neutral and weakly interacting environment, which also shows interesting photochemistry.

4. Hydrogenation of Dibenzocycloheptadienylidene

4.1. Introduction

The chemistry of carbenes is controlled by their spin states, which is either singlet or triplet.^[39, 126] In particular, it has been assumed that reactions of singlet carbenes with alcohols give O–H insertion adducts, whereas triplet carbenes yield C–H insertion adducts.^[130] As discussed in Chapters 2 and 3, the highly polar closed-shell singlet states of arylcarbenes **7**, **8** and **25** are reactive towards Lewis acids, while the triplet states interact weakly. The triplet states of the carbenes are less polar and therefore show radical-like reactivity such as atom abstractions. Laser flash photolysis studies on carbenes **7**, **8** and **25** in cyclohexane at room temperature have demonstrated triplet derived reactions for carbenes **7** and **25**, while singlet chemistry was observed for **8**.^[43, 165] Both **7** and **25** were found to abstract hydrogen atoms from the solvent to form corresponding radicals which further recombine to give respective radical dimers as main product, however the formal C–H insertion products were observed in small amounts. In contrast, carbene **8** produces smaller amounts of radical-recombination products and predominantly forms the formal C–H insertion product under similar conditions. These results are consistent with the smaller S-T energy separation of **8** than that of **7** and **25**.^[166] Platz and co-workers investigated **7**, **8** and **25** in hydrocarbon solvent matrices such as ether, 2-methyltetrahydrofuran, 2-propanol and toluene at 77 K by ESR spectroscopy and detected the radical pairs generated by abstraction of hydrogen from these organic solvents.^[33, 167]

In addition to C–H bonds, carbenes have been shown to activate H–H bonds from their singlet as well as triplet states (Chart 8). Bertrand et al. reported the H₂ insertion reactions of two stable singlet (alkyl)(amino)carbenes **44** and **45** at room temperature.^[7] Under the conditions of matrix isolation, several carbenes **46-50** were reported to insert into H₂ despite of considerable activation barriers that are higher than the thermal energy available at cryogenic temperatures.^[168-171] It clearly indicates that these reactions proceed via quantum mechanical tunneling (QMT). Likewise, singlet difluorovinylidene **51**, an extremely reactive and highly electrophilic carbene, was found to react rapidly with H₂ under similar conditions, as this reaction is predicted to have no activation barrier.^[172]

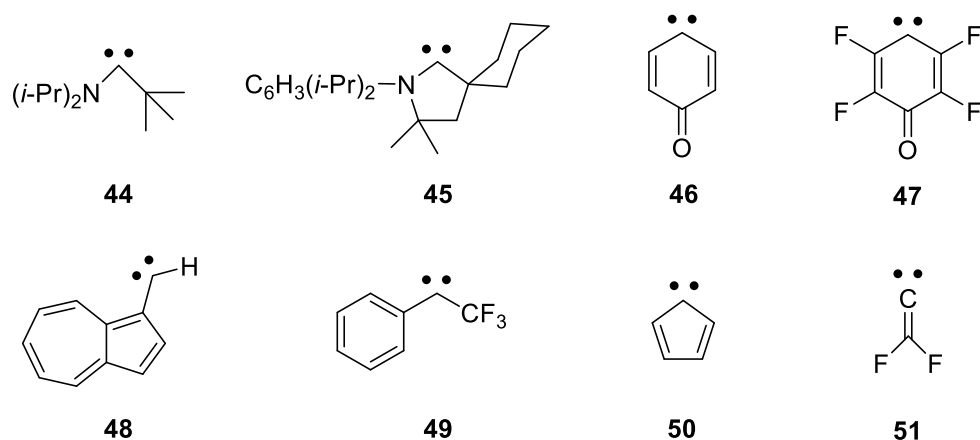
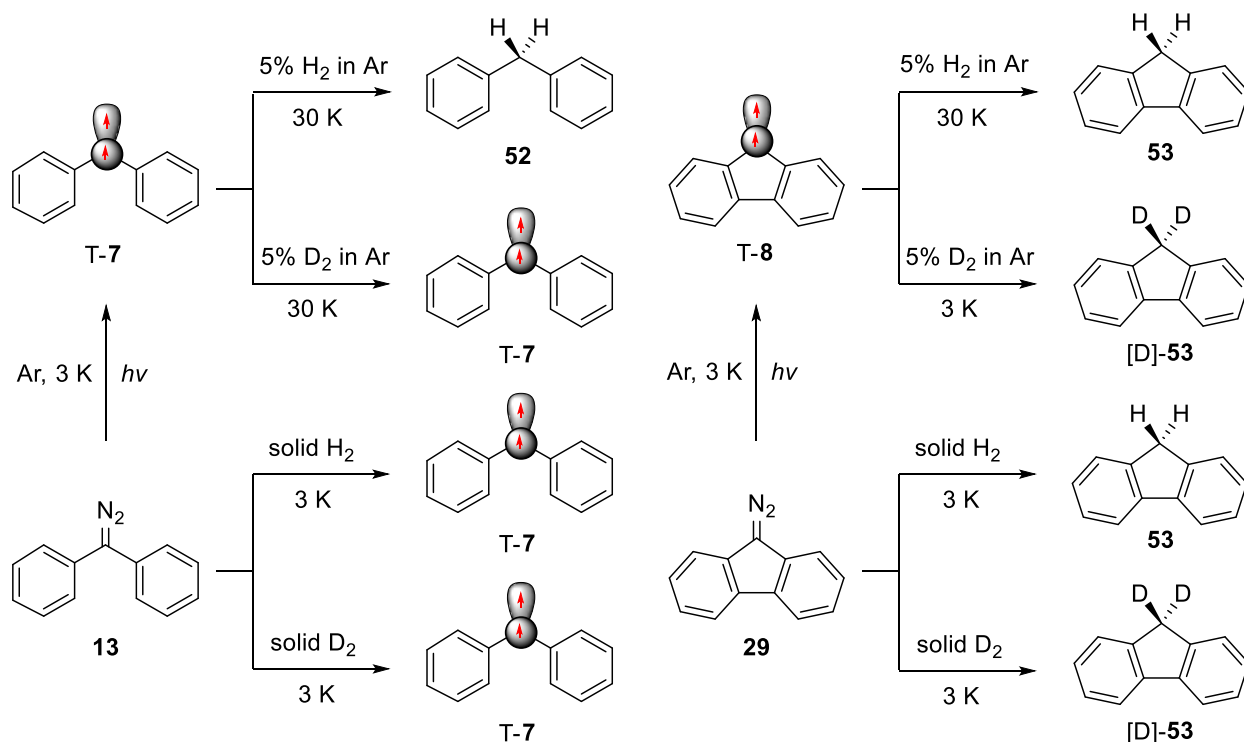


Chart 8. Representative structures of carbenes **44** – **51** reacting with H₂.

The insertion of carbenes into H₂ proceeds through two pathways, depending on the spin multiplicity of the carbene. Singlet carbenes have a filled *sp*² and an empty π -orbital, and therefore, like transition metal centers, they are suited for donation and back-donation that could activate H₂ in a concerted mechanism.^[7, 169, 172] On the other hand, a stepwise reaction pathway is expected for H₂ activation by triplet carbenes, which involves the hydrogen abstraction to yield a triplet radical pair, followed by its recombination.^[168, 170-171]

Recently, hydrogenation reactions of **7** and **8** were investigated in 5% H₂-doped argon, solid H₂ and D₂ matrices using matrix isolation IR and EPR spectroscopy.^[5] In 5% H₂-doped argon matrices, the reactions of T-**7** and T-**8** with H₂ at 30 K produced diphenylmethane **52** and fluorene **53**. Surprisingly, T-**7** was found to be stable in solid H₂ at 3 K even upon intense IR and UV-Vis irradiations. Experiments performed in solid H₂ showed instantaneous hydrogenation of **8** even at 3 K, and in solid D₂, T-**8** decays slowly, suggesting a large kinetic isotope effect (Scheme 17). The hydrogen abstraction reactions by the triplet states of **7** and **8** are predicted to have activation barriers of 2.6 and 7.0 kcal mol⁻¹ (B3LYP-D3/def2-TZVP level of theory), respectively, which clearly indicate that these reactions proceed via QMT. This discrepancy in reactivity of **7** with H₂ at 3 and 30 K can be rationalized by softening of matrix at higher temperatures that might leads to the structural changes required for the tunneling of **7**.

Dibenzocycloheptadienylidene **25** has a larger S-T gap and intermediate conformational flexibility as compared to **7** and **8**. To gain more insight into the balance of these effects on carbene reactivity, the hydrogenation reaction of **25** was studied under similar conditions.



Scheme 17. Reactions of diphenylcarbene **7** and fluorenylidene **8** with H₂ and D₂.

4.2. Results and Discussion

4.2.1. Reaction of Dibenzocycloheptadienylidene in Hydrogen Doped Argon Matrices.

Irradiation of diazodibenzocycloheptadienylidene **26** in an argon matrix doped with 5% of H₂ with 530 nm at 3 K produces triplet dibenzocycloheptadienylidene T-**25** in good yields. The IR spectrum of T-**25** shows a good agreement with that in pure argon matrix. Subsequent annealing at 30 K allows H₂ to diffuse in the argon matrix, and results in a decrease of the intensities of the bands of T-**25**, and gives rise to a set of IR bands. The new signals appearing at 586.1, 625.2, 711.5, 739.6, and 762.6 cm⁻¹ are assigned to the formal H₂ insertion product dibenzosuberane **54** by comparison with the IR spectrum of its authentic matrix isolated sample (Figure 43). The formation of **54** as a result of the reaction between T-**25** and H₂ at 30 K was monitored for an extended period of time and kinetics is obtained by monitoring the signal intensities of T-**25** at 723 cm⁻¹ and **54** at 625 cm⁻¹ as a function of time.

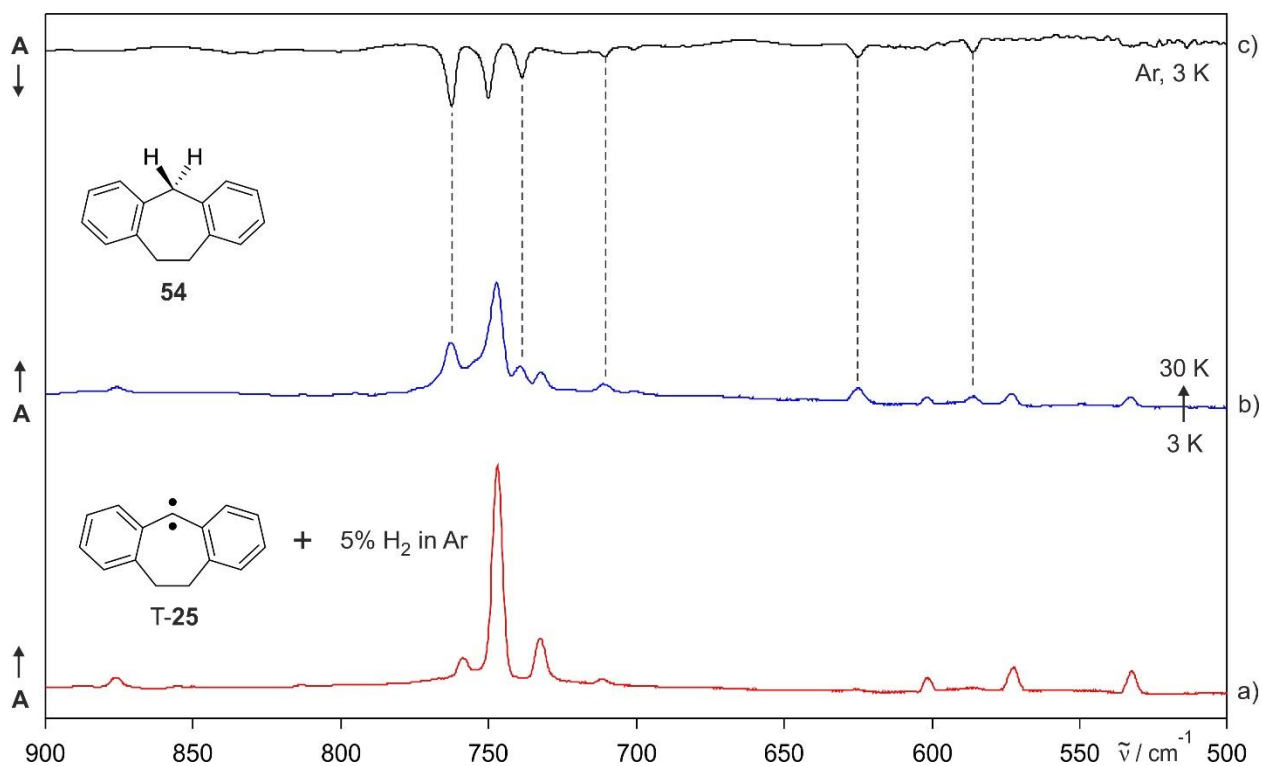


Figure 43. IR spectra showing the reaction between T-25 and H₂. a) IR spectrum of T-25 in an argon matrix doped with 5% of H₂ at 3 K. b) IR spectrum of the same matrix showing changes after annealing at 30 K. Bands assigned to T-25 are disappearing, and bands assigned to the formal H₂ insertion product **54** are appearing. d) IR spectrum of **54** in an argon matrix at 3 K (multiplied by -1).

Assuming a pseudo-first order reaction, the kinetic data is fitted using the equation of Wildman and Siebrand (Eq. 2).^[173] Noteworthy, a distribution of rate constants arising from matrix cage effects is taken into account by dispersion coefficient β .

$$I = I_0 e^{-(kt)^\beta} + C \quad \text{with } 0 < \beta < 1 \quad (2)$$

Considering $\beta = 0.75$, the reaction rate at 30 K was determined to be $6.4 \times 10^{-5} \text{ s}^{-1}$. The decay of the carbene T-25 signal at 723 cm^{-1} and rise of a new signal assigned to **54** at 625 cm^{-1} indicate that the carbene remaining after initial annealing slowly converts into the corresponding insertion product upon keeping the matrix at 30 K for 24 hrs, and approximately 67% of T-25 converts into **54** (Figure 44).

In contrast, no reaction was observed between T-25 and D₂ in argon matrices doped with 5% of D₂, where T-25 was found to be stable on annealing at 30 K. The reactions of **7** and **8** with H₂ under the similar conditions result in the formation of corresponding H₂ insertion products **52** and **53**, respectively, whereas only **8** was observed to slowly insert into D₂ with a reaction rate of $4 \times 10^{-5} \text{ s}^{-1}$ at 30 K.^[5] To avoid complications that might arise from the diffusion of H₂ or D₂ in solid argon, experiments were also performed in solid H₂ and D₂ to understand the mechanism of the hydrogen insertion reaction. Due to high volatility of H₂, temperatures below 4 K are necessary to prevent sublimation of H₂, whereas D₂ matrices are stable up to 6 K under the conditions of matrix isolation.

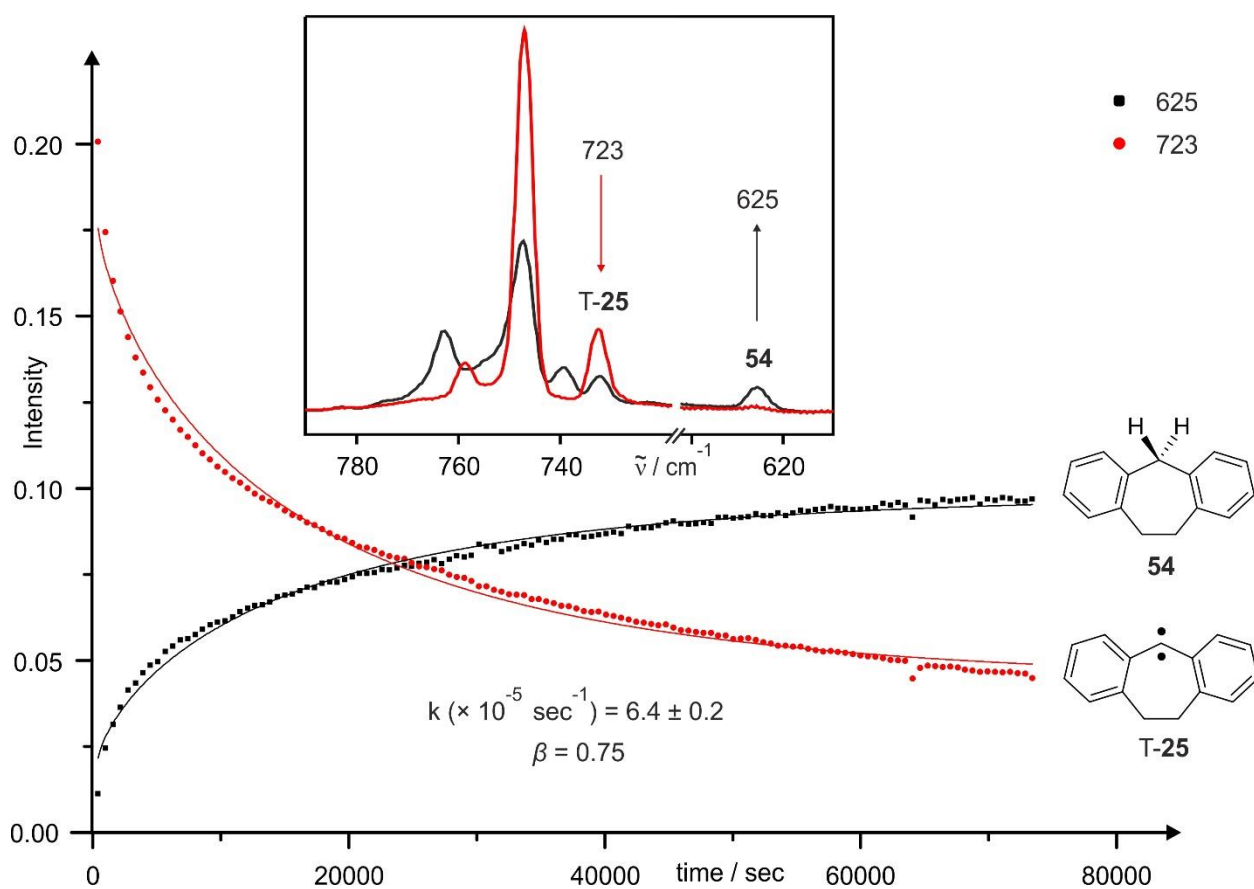


Figure 44. Plot showing the progress of reaction between T-25 and H₂ at 30 K during a period of 24 hrs. Red and black dots indicate integrated intensities of IR signals at 723 cm⁻¹ assigned to carbene T-25 and 625 cm⁻¹ assigned to formal H₂ insertion product **54**, respectively. Inset shows IR spectra of argon matrix containing T-25 and 5% of H₂ at 3 K (red line) and 30 K (black line). The red line represents a set of IR bands of carbene T-25 and black line shows disappearance of IR bands assigned to T-25, accompanied by appearance of new IR bands assigned to **54**.

4.2.2. Reaction of Dibenzocycloheptadienylidene in Solid H₂ and D₂ Matrices.

Visible light photolysis (530 nm) of **26** trapped in solid H₂ at 3 K results in the almost complete bleaching of **26**, and concurrently a new compound is formed. The resulting IR spectrum reveals the formation of **54** based on the comparison with IR spectrum of an authentic matrix isolated sample (Figure 45c). At no instance, carbene **25** is detected in solid H₂ upon photolysis, suggesting the instantaneous reaction of **25** with surrounding H₂ molecules. It may be recalled that the reaction of T-**25** with H₂ in argon doped matrices also leads to the formation of **54** at 30 K. The reactivity of **25** towards H₂ even at 3 K shows that the reaction rate is temperature independent. A similar behavior was previously observed for **8** in solid H₂ matrices.^[5]

When D₂ is used as matrix, irradiation (530 nm) of **26** produces only carbene in its triplet state T-**25** and no traces of reaction products between **25** and D₂ are observed (Figure 45e, Scheme 18), analogous to the reaction of **7** with D₂.^[5] In order to induce reaction between T-**25** and D₂, broadband IR irradiation (730 – 2500 nm) was carried out to excite D–D vibration or its overtone, however no such reaction was observed. Even after keeping the matrix at 6 K for 24 hrs, no traces of deuterated product [D₂]-**54** are observed. The unreactive behavior of carbene **25** towards D₂ indicates a very large H₂/D₂ kinetic isotope effect (KIE) and shows remarkable isotope selectivity towards H₂. Previous studies of **8** in solid H₂ and D₂ matrices also demonstrated the large KIE, where T-**8** is found to react instantaneously with H₂ and insert slowly in D₂ ($4 \times 10^{-5} \text{ s}^{-1}$).^[5] It is important to note that the photolysis (530 nm) of **26** in solid H₂ matrices presumably does not play any role in hydrogenation reaction, because the same photolysis conditions could not induce any reaction of T-**25** in solid D₂ matrices. As observed in argon matrices doped with 5% of H₂ and D₂, the photolysis of **26** yields carbene **25** in its triplet ground state (Figure 43a). Thus, reaction of carbene **25** in solid H₂ matrices should also involve the formation of T-**25**, followed by its instantaneous hydrogenation.

It is interesting to compare the reactivities of the three similar looking arylcarbenes **7**, **8** and **25** towards H₂ and D₂. Carbene **7** is stable in solid H₂ and D₂, and only reacts at higher temperatures in H₂-doped argon matrices. On the other hand, carbene **8** reacts with H₂ and D₂ in both solid and doped matrices, and only the reaction with D₂ is slow enough to be monitored. Carbene **25** reacts with H₂, but is stable in D₂ matrices, displaying reactivity between carbenes **7** and **8**.

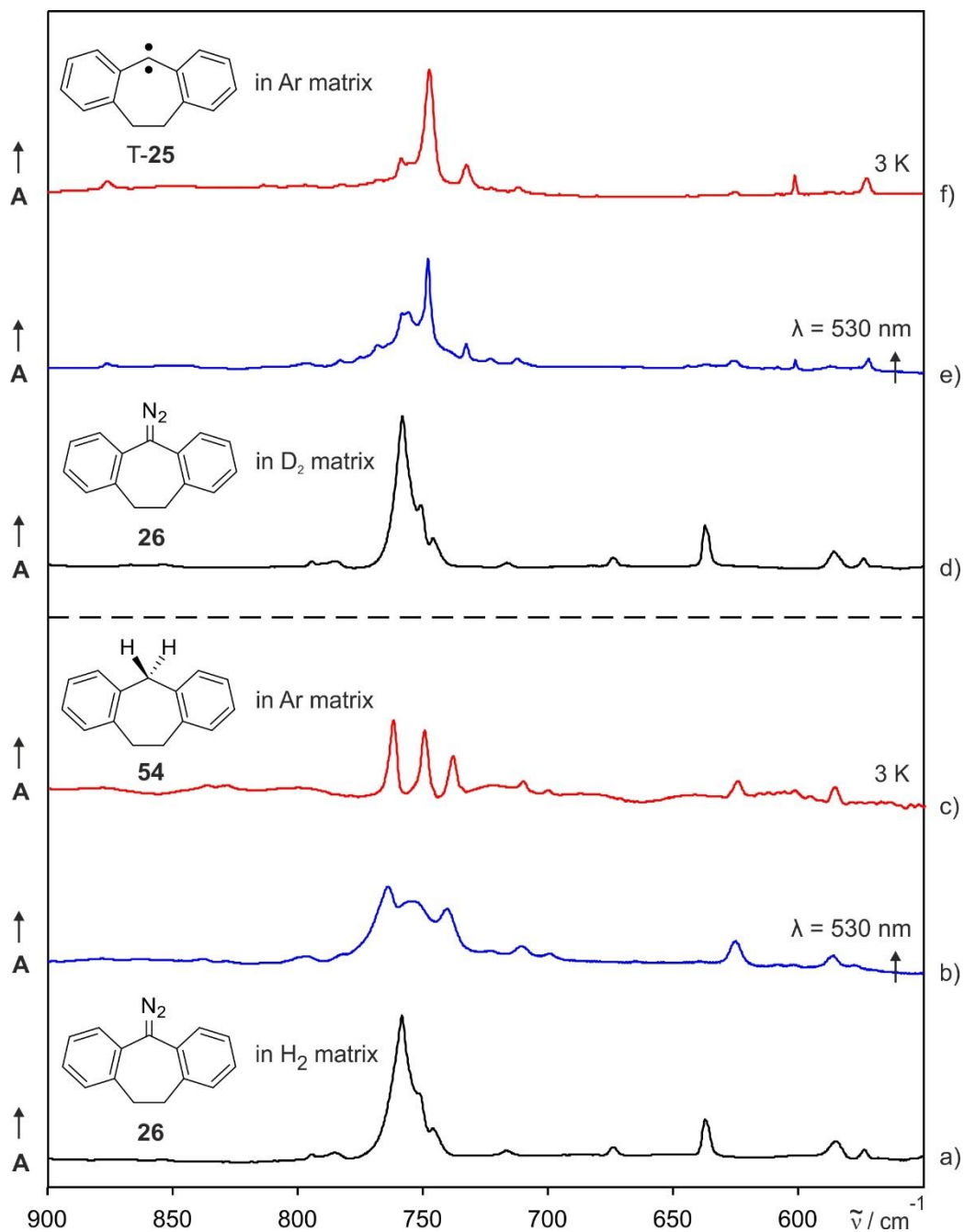
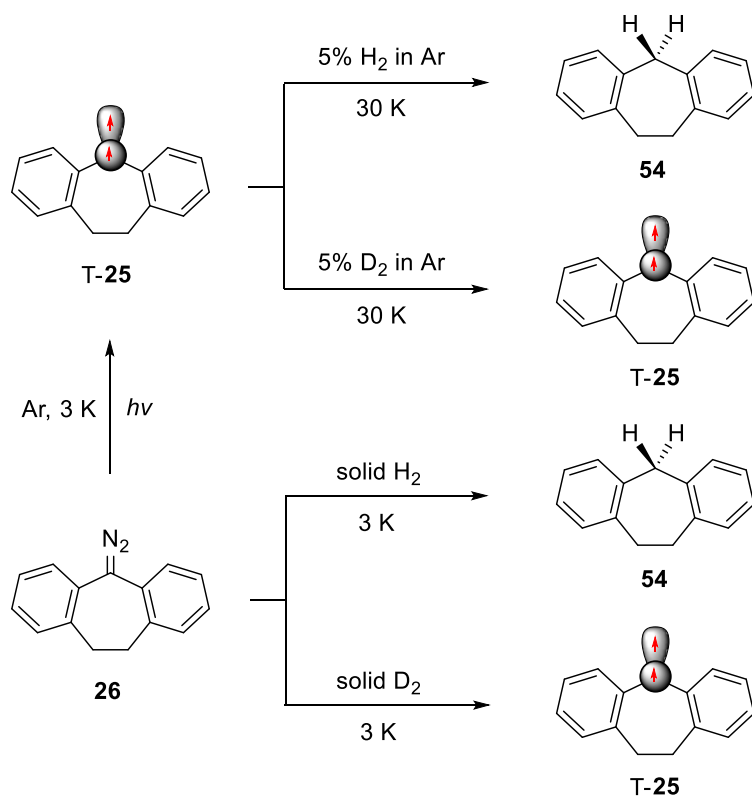


Figure 45. IR spectra showing the photochemistry of diazodibenzocycloheptadienyldiene **26** in solid H₂ and D₂ matrices. a) IR spectrum of **26** trapped in a H₂ matrix at 3 K. b) IR spectrum of the same matrix showing the changes after 530 nm irradiation. Bands assigned to **26** are disappearing, and bands assigned to the formal H₂ insertion product **54** are appearing. c) IR spectrum of **54** in an Ar matrix at 3 K. d) IR spectrum of **26** trapped in a D₂ matrix at 3 K. e) IR spectrum of the same matrix showing the changes after 530 nm irradiation. Bands assigned to **26** are disappearing, and bands assigned to T-**25** are appearing. f) IR spectrum of T-**25** isolated in an Ar matrix at 3 K.



Scheme 18. Reaction of dibenzocycloheptadienylidene **25** with H_2 and D_2 .

Computations (Provided by Enrique Mendez-Vega). At the B3LYP-D3/def2-TZVP level of theory, intrinsic reaction coordinate (IRC) calculations were performed to study the reaction pathway for the hydrogenation of **7**, **8** and **25** (Figure 46). The first step of the reaction is hydrogen abstraction by the triplet carbene to form the triplet radical pair and, in the second step, the radical pair undergoes crossover to the singlet surface and recombines to give the formal H_2 insertion product. The hydrogenation reaction via triplet surface is estimated to be energetically more favorable compared to that at the singlet surface.

The activation barrier for the hydrogen abstraction reaction is predicted to be $2.6 \text{ kcal mol}^{-1}$ for **T-8**, which is lower than that for **T-7** and **T-25** ($\sim 7 \text{ kcal mol}^{-1}$). Still, these barriers are too high for the reactions to occur at 3 or 30 K, which indicates that the hydrogen abstraction reactions proceed via QMT. The hydrogen tunneling for **7**, **8**, and **25** are expected to produce the corresponding triplet radical pairs **55**, **56**, and **57**, respectively. The formation of **56** is calculated to be exothermic by $-8.5 \text{ kcal mol}^{-1}$, whereas the hydrogen abstraction reactions yielding **55** and **57** are slightly endothermic by $0.7 - 1.5 \text{ kcal mol}^{-1}$. The calculated endothermicities are marginal

enough to be considered beyond the accuracy of DFT calculations. The intersystem crossing of these radical pairs to singlet surface leads to exothermic and barrierless recombination, giving the corresponding hydrocarbons **52-54**.

Relative to **7** and **25**, the high reactivity of **8** towards H_2 and D_2 can be rationalized by the large exothermicity of **56** resulting in an early transition state $TS(T-8 \cdots H_2)$, and by lower and narrower activation barrier. The early transition state $TS(T-8 \cdots H_2)$ is formed at a larger intermolecular C–H distance (1.53 Å) and a shorter H–H distance (0.84 Å), which mimics the geometry of carbene more than that of radical pair **56**. Carbene **25** is estimated to have a slightly early transition state $TS(T-25 \cdots H_2)$ as compared to $TS(T-7 \cdots H_2)$ in **7**, which results in an almost thermoneutral reaction to form radical pair **57**, justifying the reactivity of **25** towards H_2 .

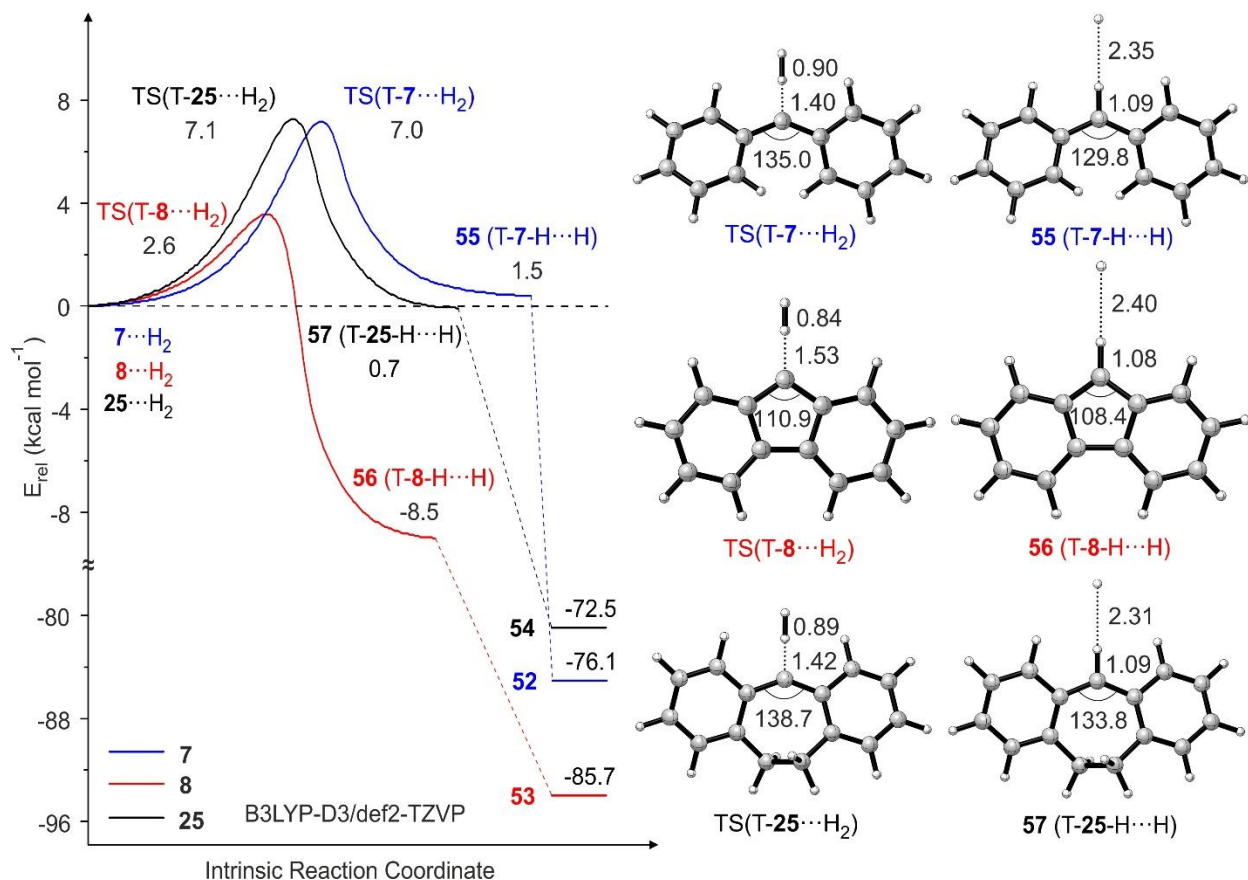


Figure 46. Hydrogenation of diphenylcarbene **7** (blue), fluorenylidene **8** (red), and dibenzocycloheptadienyldiene **25** (black) on the triplet potential energy surface along the intrinsic reaction path. Energy profiles were calculated at the B3LYP-D3/def2-TZVP level of theory. Energies are given in kcal mol⁻¹ and selected bond lengths and angles are given in Å and °, respectively.

It should be noted that the imbalance on the hydrogen abstraction enthalpies for carbenes **7**, **8** and **25** results from different carbene stabilities and not from different stabilities of the radical pairs. The five-membered ring in fluorenylidene **8** is predicted to have a carbene central bond angle of 112.1° in T-**8**, which is smaller than that of T-**7** (141.6°) and T-**25** (142.6°), hence destabilizes T-**8** relatively. The stability of radical pairs **55**, **56**, and **57** can be evaluated by comparing the C–H bond dissociation energies of the corresponding hydrocarbons **52**, **53**, and **34**. The BDEs of **52-54** are calculated to fall within a narrow range (73 – 77 kcal mol⁻¹) and thus stabilities of radical pairs **55-57** should be quite similar.

The global electrophilicity (ω) values of carbenes **7**, **8** and **25** were also computed to compare the reactivity of carbenes towards H₂ by the expression defined by Parr et al. (Eq. 3).^[174]

$$\omega = \frac{\mu^2}{2\eta} \quad (3)$$

Where μ is chemical potential and η is chemical hardness. These two parameters (μ and η) were calculated using two different methods. One of these methods proposed by Shakib et al. employs energies of HOMO and LUMO orbitals of carbenes (Eq. 4, Table 17).^[175]

$$\mu = (E_{\text{HOMO}} + E_{\text{LUMO}})/2 \quad \text{and} \quad \eta = (E_{\text{LUMO}} - E_{\text{HOMO}})/2 \quad (4)$$

Table 17. Global electrophilicity (ω) calculations using the method reported by Shakib et al.^[175]

Carbenes	HOMO ^[a] (a.u.)	LUMO ^[a] (a.u.)	μ (a.u.)	η (a.u.)	ω (a.u.)	(eV)
7	-0.1898	-0.1083	-0.1491	0.0814	0.1364	3.7
8	-0.2050	-0.1266	-0.1658	0.0784	0.1753	4.8
25	-0.1756	-0.1058	-0.1407	0.0698	0.1419	3.9

^[a]Calculated at the B3LYP-D3/def2-TZVP level of theory.

The second method reported by Proft et al. is mainly designed to calculate ω for radicals, in which μ and η are obtained from electron affinity (A) and ionization potential (I) values of triplet carbenes (Eq. 5, Table 18).^[176]

$$\mu = -\frac{I + A}{2\eta} \quad \text{and} \quad \eta = \frac{I - A}{2\eta} \quad (5)$$

Table 18. Global electrophilicity (ω) calculations using the method reported by Proft et al.^[176]

Carbenes	$I^{[a]}$ (a.u.)	$A^{[b]}$ (a.u.)	μ (a.u.)	η (a.u.)	ω (a.u.)	ω (eV)
7	0.2197	0.0523	-0.1360	0.0837	0.1106	3.0
8	0.2395	0.0693	-0.1544	0.0851	0.1401	3.8
25	0.2135	0.0588	-0.1361	0.0774	0.1198	3.3

^[a]Ionization potential (I) = $E_{(\text{radical cation})} - E_{(\text{triplet carbene})}$. ^[b]Electron affinity (A) = $E_{(\text{triplet carbene})} - E_{(\text{radical anion})}$. Calculated at the B3LYP-D3/def2-TZVP level of theory.

It can be seen that although the global electrophilicity values obtained from both approaches are different, trends in both approaches corroborate well; for example, **8** is predicted to have the largest global electrophilicity value among the three arylcarbenes, explaining its enhanced triplet reactivity towards H₂ and D₂ as observed in our experiments at cryogenic temperatures.

4.3. Conclusions

In analogy to **7** and **8**, dibenzocycloheptadienylidene **25** is found to be reactive towards molecular hydrogen under matrix isolation conditions despite of a considerable activation barrier of 7.1 kcal mol⁻¹ (B3LYP-D3/def2-TZVP level of theory), suggesting that the reaction proceeds via QMT. The triplet state of **25** undergoes hydrogenation reaction in two steps: a) first step is rate determining step where a H/D of H₂/D₂ molecule is abstracted by triplet carbene via QMT to form a radical pair, b) in second step, the radical pair recombines following intersystem crossing to produce the formal H₂ insertion product. The closed-shell singlet state S-**25** is predicted to lie 10 kcal mol⁻¹ above the triplet ground state, therefore H₂ activation reaction from thermally populated excited singlet state can be excluded under the experimental conditions. Also, the activation barrier calculated for the singlet state (17.8 kcal mol⁻¹) is higher than that for the triplet state (Figure A6).

Although arylcarbenes **7**, **8** and **25** have a similar framework and follow the same hydrogenation mechanism, carbene **25** shows intermediate reactivity towards molecular hydrogen as compared to **7** and **8**. Previous studies showed that **7** is stable in solid H₂, D₂, and argon matrices doped with D₂, and reacts only at higher temperature of 30 K in argon matrices doped with H₂, whereas **8** is found to be reactive in all of these matrices.^[51] Our experiments demonstrate that **25** reacts selectively in solid H₂ and argon doped H₂ matrices, while it does not exhibit any reactivity in D₂

matrices indicating a pronounced kinetic isotopic effect. These results suggest an increasing reactivity in the order **7** < **25** < **8**. The IRC calculations reveal that the higher reactivity of **8** results from the exothermicity associated to the hydrogen abstraction reaction having an early transition state with a lower and narrower barrier relative to **7** and **25**. The barrier for the reaction of **25** with H₂ is estimated to have a similar height and width as that of **7**, however their reaction energies are somewhat different. For **7**, the transition state is later, as a result, the reaction energy of **7** is slightly positive, whereas that of **25** is almost neutral. The products of the hydrogen abstraction reactions, radical pairs **55-57**, are calculated to have similar stabilities, which indicates that differences in reactivities of **7**, **8** and **25** towards molecular hydrogen is a consequence of intrinsic stabilities of carbenes, rather than the stabilities of the product radical pairs.

The comparison of global electrophilicity values of arylcarbenes **7**, **8** and **25** suggests the highest reactivity and electrophilicity for **8** and the least for **7**, which is reflected in the reactivity of carbenes (**7** < **25** < **8**) towards solid H₂ and D₂ under matrix isolation conditions.

Parts of chapter 4 were adapted with permission from Chem. Eur. J., **2018**, *24*, pp. 18801–18808.
Copyright 2018 WILEY-VCH.

5. Hydrogen and Halogen Bonding of Singlet Carbenes

5.1. Introduction

The hydrogen bond is one of the most important intermolecular interactions and it has been extensively investigated both experimentally and theoretically, owing to its significant role in chemistry and biology.^[177-185] On the other hand, there is a growing research in another type of intermolecular interaction, halogen bond,^[186] because of its great importance in molecular recognition,^[187-191] crystal engineering,^[187, 192-195] supramolecular chemistry,^[191, 194, 196-197] and biological systems.^[198-199] The halogen bonding is comparable to hydrogen bonding, because there exist an electron donor and an electron acceptor in both cases.^[190] The different electron acceptors in both cases make them noticeably different. An electropositive hydrogen atom is the electron acceptor in hydrogen bond D–H···A, whereas an electronegative halogen atom X = Cl, Br, or I is often considered as electron acceptor in halogen bond D–X···A.^[200] Politzer et al.^[201] and Clark et al.^[202] explained the halogen bond formation by interaction of an electron-rich region of A with a positive electrostatic potential region on the surface of the halogen, which lies *trans* to σ -orbital of D–X bond and is usually referred as σ -hole. The strength of halogen bond is dependent on the magnitudes of positive electrostatic potentials (σ -hole) on the halogens.^[203] The magnitude of the σ -hole is related to the polarizability of the halogen, thus the strength of halogen bond also follows the order of F < Cl < Br < I.^[201] It has also been demonstrated that halogen bonds exhibit similarities to hydrogen bonds in terms of directionality and strength; for example, the strength of halogen bonding increases in the order of C(sp³) < C(sp²) < C(sp) for C–X bond, similar to that for hydrogen bonding.^[204-206]

The compounds bearing lone pair, π electrons, an unpaired electron, σ electrons can potentially form hydrogen or halogen bonds.^[207] Legon and Millen pointed out that a lone pair is preferred for such intermolecular interactions, when there are multiple electron donating centers are competing with each other.^[208] The closed-shell singlet carbenes possess a lone pair of electrons in the sp² hybridized σ -orbital and an empty π -orbital, which make them suitable candidates for hydrogen and halogen bonding interactions. Due to presence of a lone pair, singlet carbenes can act as strong neutral bases,^[31] for example, singlet methylene **S-1** was determined to have a proton affinity (207 kcal mol⁻¹), similar to that of NH₃ (204 kcal mol⁻¹). Typical nucleophilic *N*-heterocyclic

carbenes (NHCs) are more basic and exhibit proton affinities between 250 – 260 kcal mol⁻¹.^[209] Consequently, singlet carbenes are excellent hydrogen and halogen bond acceptors. Arduengo et al. reported hydrogen and halogen-bonded complexes of NHCs, in which two NHCs are linked by a hydrogen or iodine atom resulting in strong C···(H/I)···C interactions.^[210-212] The X-ray structure analyses of these complexes show nearly linear geometries with a C–H–C hydrogen bond angle of 172.5° and a C–I–C halogen bond angle of 178.9°. There are also X-ray structure reports involving hydrogen bonding interactions of NHCs with 2,6-di-*tert*-butyl-4-methylphenol, methanol and diphenylamine.^[213-214]

As discussed in chapters 2 and 3, the closed-shell singlet states of arylcarbenes **7**, **8** and **25** are among the strongest neutral bases which are estimated to have proton affinities higher than 270 kcal mol⁻¹. Under the conditions of matrix isolation, carbenes **7** and **8** have been shown to form hydrogen-bonded complexes with proton donor solvents by switching their spin states from ground triplet to singlet states.^[1, 4, 105] However, such hydrogen-bonded complex was not observed between **25** and H₂O as the relative stabilization of S-**25** compared to that of T-**25** by hydrogen bonding is smaller than the S-T gap of the carbene.^[154]

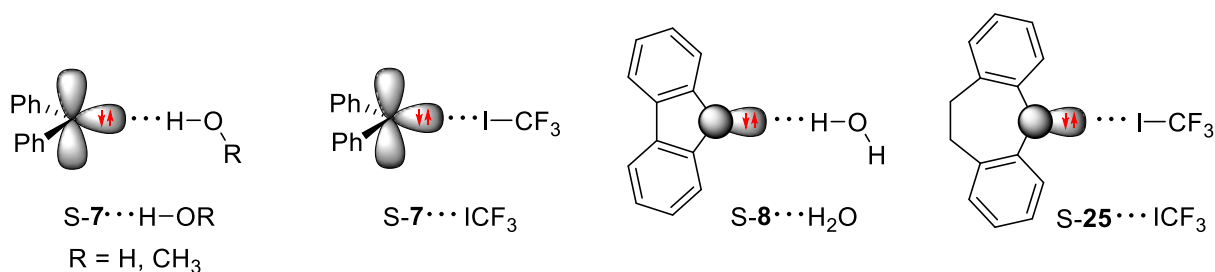
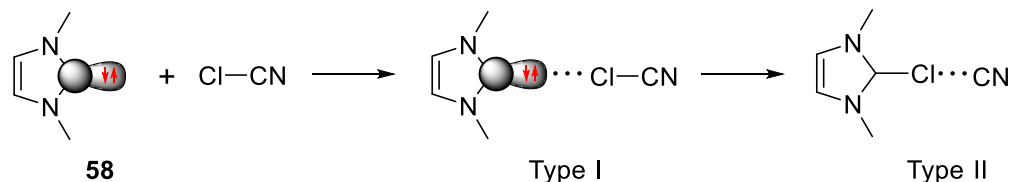


Chart 9. Closed-shell singlet states of triplet ground state arylcarbenes as hydrogen and halogen bond acceptors.

On the other hand, the reactions of **7** and **25** with halogen bond donor ICF₃ resulted in a formation of the corresponding halogen-bonded complexes, while carbene **8** forms an ylide in order to avoid antiaromatic destabilization in the central five-membered cyclopentadienylidene ring. Interestingly, both carbenes **7** and **25** on interaction with ICF₃ were found to produce two types of halogen-bonded complexes, classical (type I) halogen-bonded complex and unconventional (type II) ion pair complex.^[2, 154] Previously, a theoretical study was reported on such complexes between dimethyl-substituted NHC **58** and variety of halogen bond donors describing their different bonding scenarios.^[141] Type I complexes are described by long C–X distances and small binding energies, while the second type of complexes are predicted as ion-pair complexes between

D^- and XA^+ charged fragments, which are characterized by short C–X distances and large binding energies (Scheme 19).



Scheme 19. Classical (Type I) and ion-pair (Type II) halogen-bonded complexes between **58** and chlorocyanide.^[141]

For triplet ground state carbenes, the stabilization of the singlet state relative to triplet on complexation with hydrogen or halogen bond donor solvents should be higher than the S–T gap of the carbene in order to attain its singlet state reactivity. In contrast, singlet ground state carbenes can directly interact with hydrogen or halogen bond donors without the constraint of the S–T gap. In recent years, few spectroscopic studies have been reported on hydrogen bonding interactions of singlet ground state carbenes **3**, **58** and **59** under matrix isolation conditions.^[8, 133, 215] However, the halogen bonding interactions of singlet ground state carbenes are relatively less explored.

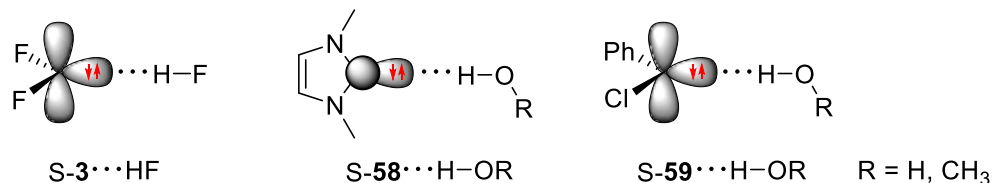


Chart 10. Closed-shell singlet states of singlet ground state carbenes as hydrogen bond acceptors.

In the present study, reactions of **59** with ICF_3 and di-*tert*-butyl-substituted NHC **60** with H_2O and ICF_3 were investigated to gain more insight on the following aspects: 1) comparison of hydrogen vs. halogen bonding interactions, and 2) halogen bonding and nature of halogen-bonded complexes (type I/type II).

5.2. Results and Discussion

5.2.1. Reaction of 1,3-di-*tert*-butyl-imidazole-2-ylidene with H_2O .

As we demonstrated previously, the reactions of dimethyl-substituted NHC **58** and phenylchlorocarbene **59** in argon matrices doped with 1% of H_2O (or MeOH) result in a formation of corresponding hydrogen-bonded complexes $S-58 \cdots H-OR$ and $S-59 \cdots H-OR$ ($R = H, Me$). The hydrogen-bonded complexes $S-59 \cdots H-OR$ were found to be stable under the conditions of matrix

isolation and photochemical excitation (254 nm) was required to induce O–H insertion,^[8] whereas the photochemistry of S-**58**···H–OR (R = H, Me) was not investigated.^[133] Also, the generation of **58** from its carboxylate precursor leads to deposition of CO₂ as side product in the matrix, which causes several complications such as recombination of **58** and CO₂ on annealing, combination bands of CO₂-H₂O in IR experiments with H₂O. To overcome these complications and assess the stability of NHC hydrogen-bonded complexes under photolysis conditions, reaction of a stable and highly nucleophilic NHC, 1,3-di-*tert*-butyl-imidazole-2-ylidene **60** with H₂O was studied under the similar conditions.

Carbene **60** was deposited in an argon matrix doped with 1% of H₂O at 3 K. The IR spectrum of the carbene is in good agreement with a calculated gas-phase spectrum of S-**60** (Figure 47). At 3 K the diffusion of H₂O in a solid argon is inhibited, whereas at higher temperatures between 25 and 30 K the diffusion is rapid, and bimolecular reactions with S-**60** can be directly monitored by IR spectroscopy. Warming up the matrix from 3 to 30 K results in a decrease of all IR bands of S-**60** and H₂O, and concurrently new IR signals appear at 708.9, 1102.1, 1135.9, 1213.3, 1373.2, 1401.1, and 3027.8 cm⁻¹ assigned to a hydrogen-bonded complex **61** between S-**60** and H₂O. The observed IR bands fit well with a DFT calculated spectrum of **61** (Figure 47c, Table 19). The signal appearing at 3027.8 cm⁻¹ is assigned to the bound O–H stretch in complex **61**, which amounts to a large red shift of 706.3 cm⁻¹ from the asymmetric stretch of matrix isolated H₂O, in a reasonably good agreement with computed red shift of 745.9 cm⁻¹ (Figure 48). The observed large shift is clearly an indicative of a very strongly hydrogen-bonded complex between S-**60** and H₂O. Such large shifts in hydrogen-bonded complexes have been observed in some strongly bonded systems such as **58**-H₂O/MeOH,^[133] **7**-MeOH,^[2] trimethylphosphite-HCl.^[216] The unbound O–H stretch in **61** is predicted to occur at 3847.9 cm⁻¹ with an intensity of nearly 20 times lower than that of the bound O–H stretch. The vibration corresponding to the unbound O–H stretch was not observed experimentally. Unlike S-**59**···H₂O, complex **61** is found to be stable under the conditions of matrix isolation, but also upon high energy irradiation such as 254 nm, suggesting a greater stability of **61** (S-**60**···H–OH) with respect to S-**59**···H–OH. At no instance, a formal O–H insertion product **62** is observed in our experiments (Scheme 20). This can be rationalized by DFT calculations, which predict **61** to be thermodynamically more stable than **62** by 2.3 kcal mol⁻¹ at the B3LYP-D3/def2-TZVP level of theory.

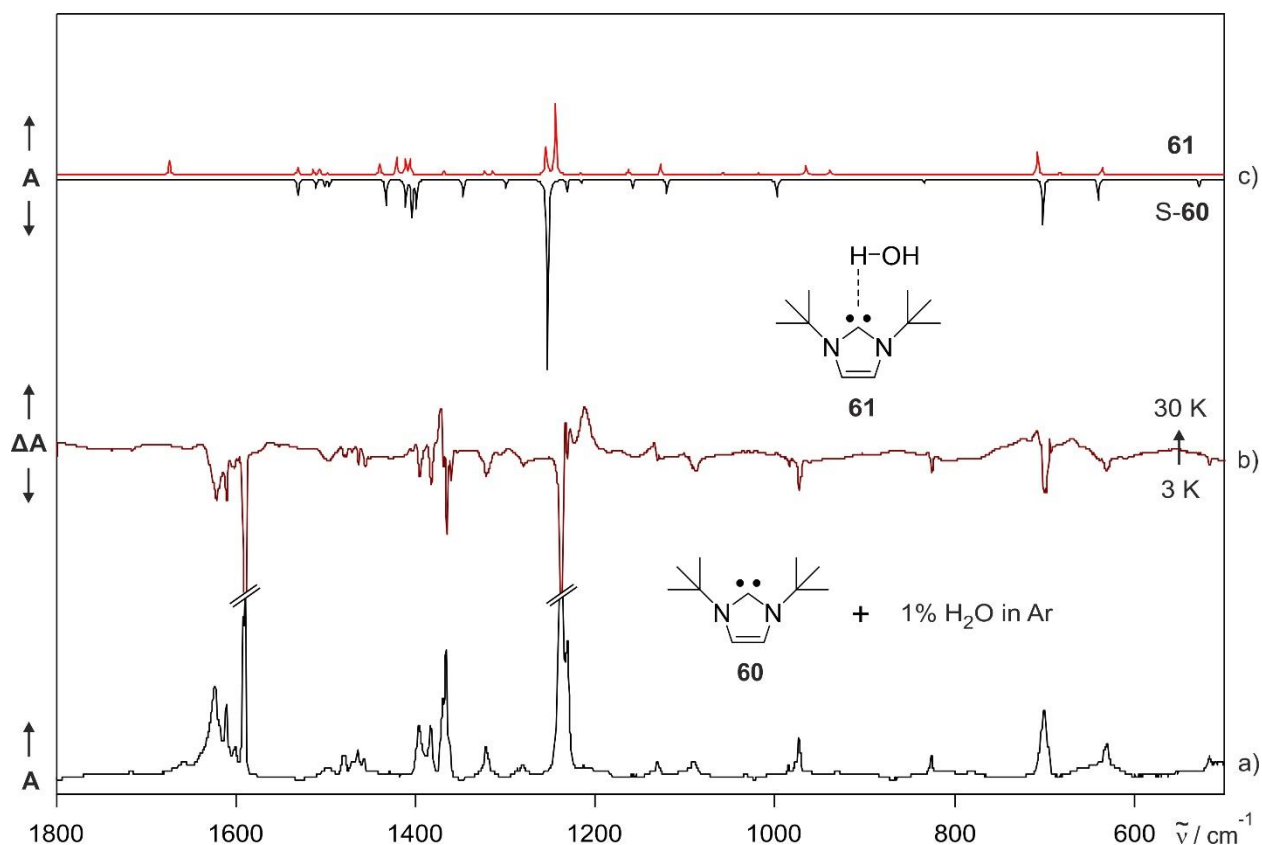


Figure 47. IR spectra showing the reaction between S-**60** and H₂O. a) IR spectrum of S-**60** in an argon matrix doped with 1% of H₂O at 3 K. b) Difference IR spectrum of the same matrix showing changes after annealing at 30 K. Bands pointing downwards assigned to S-**60** and H₂O are disappearing, and bands pointing upwards assigned to **61** are appearing. c) Computed IR spectrum of S-**60** (multiplied by -1, peaks pointing downwards) and computed IR spectrum of **61** (peaks pointing upwards) at the B3LYP-D3/def2-TZVP level of theory.

Table 19. IR vibrational frequencies of hydrogen-bonded complex **61** between S-**60** and H₂O.

Mode	Sym	DFT ^[a]		Argon ^[b]		Assignment
		$\tilde{\nu} / \text{cm}^{-1}$	I_{rel}	$\tilde{\nu} / \text{cm}^{-1}$	I_{rel}	
32	A	719.0	34	708.9	37	C–H wagging
36	A	905.9	74	940.3	58	O–H bend
49	A	1126.1	13	1102.1	16	C–H bend
50	A	1160.0	14	1135.9	16	C–H bend
54	A	1252.0	100	1213.3	100	C–N str.
64	A	1424.9	30	1373.2	34	C–N–C asym. str.
65	A	1444.1	8	1401.1	6	C–F str.
99	A	3144.9	-	3027.8	-	bound O–H str.

^[a]Calculated at the B3LYP-D3/def2-TZVP level of theory. ^[b]Argon matrix at 3 K.

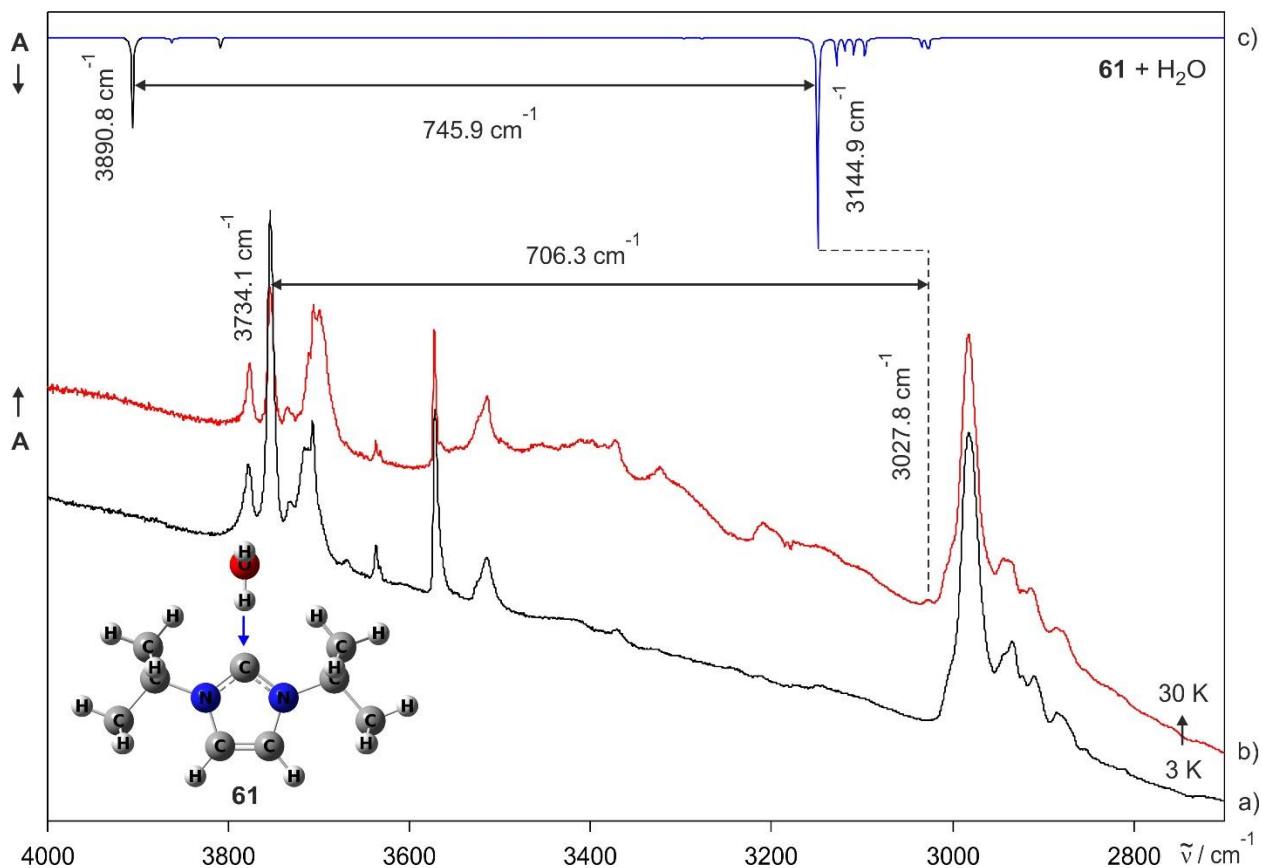
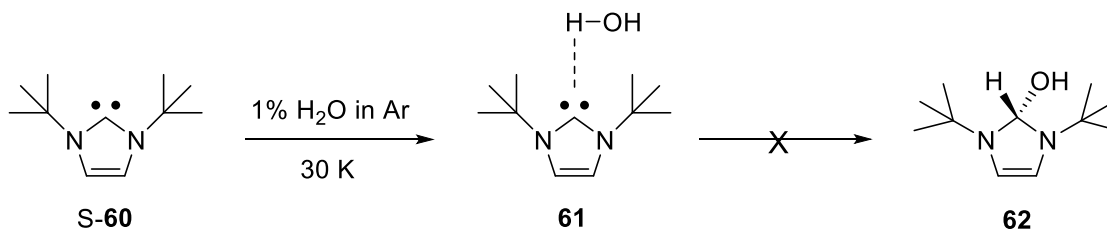


Figure 48. IR spectra showing the bound O–H stretching vibration in **61**. a) IR spectrum of **S-60** in an argon matrix doped with 1% of H₂O at 3 K. b) IR spectrum of the same matrix obtained after annealing at 30 K. Bands of **S-60** and H₂O are disappearing, and bands corresponding to bound O–H stretch in **61** (3027.8 cm⁻¹) and higher aggregates of H₂O are appearing. c) Superposition of computed IR spectra of **61**-blue line and H₂O-black line (multiplied by -1, peaks pointing downwards) at the B3LYP-D3/def2-TZVP level of theory. The computed IR bands of free H₂O have been introduced for the comparison.



Scheme 20. Reaction of 1,3-di-*tert*-butyl-imidazole-2-ylidene **60** with H₂O.

Computations. The experimental findings were corroborated by DFT calculations at the B3LYP-D3/def2-TZVP level of theory. Previously investigated system consisting of **59** and H₂O, showing a similar interaction, was also computed at the same level of theory for comparison. Carbene **60** is predicted to have a singlet ground state ($\Delta E_{S-T} = -79$ kcal mol⁻¹) and thus can react directly with H₂O to form hydrogen-bonded complex **61** between S-**60** and H₂O. The binding energy of S-**60**···H₂O is calculated to be 11.2 kcal mol⁻¹, which is larger than that of S-**59**···H₂O (8.3 kcal mol⁻¹). This can be rationalized by higher proton affinity of S-**60** (270 kcal mol⁻¹) as compared to that of S-**59** (252 kcal mol⁻¹). In addition, AIM and NBO analyses were also performed to describe a stronger hydrogen bonding interaction in S-**60**···H₂O relative to that in S-**59**···H₂O.

AIM analysis. Using the wavefunctions generated at the B3LYP-D3/def2-TZVP level of theory, bond critical points (3, -1) and ring critical points (3, +1) associated with the interactions in S-**59**···H₂O and S-**60**···H₂O were obtained (Figure 49). The values of electron density $\rho(r_c)$, eigenvalues of Hessian $\lambda_1, \lambda_2, \lambda_3$, the Laplacian of electron density ($\nabla^2\rho$), ellipticity ($|\lambda_1/\lambda_3|$), local electronic kinetic energy density $G(r_c)$, local electronic potential energy density V and hydrogen bond interaction energy E_{HB} for both complexes computed at bond critical points are given in Table 20.

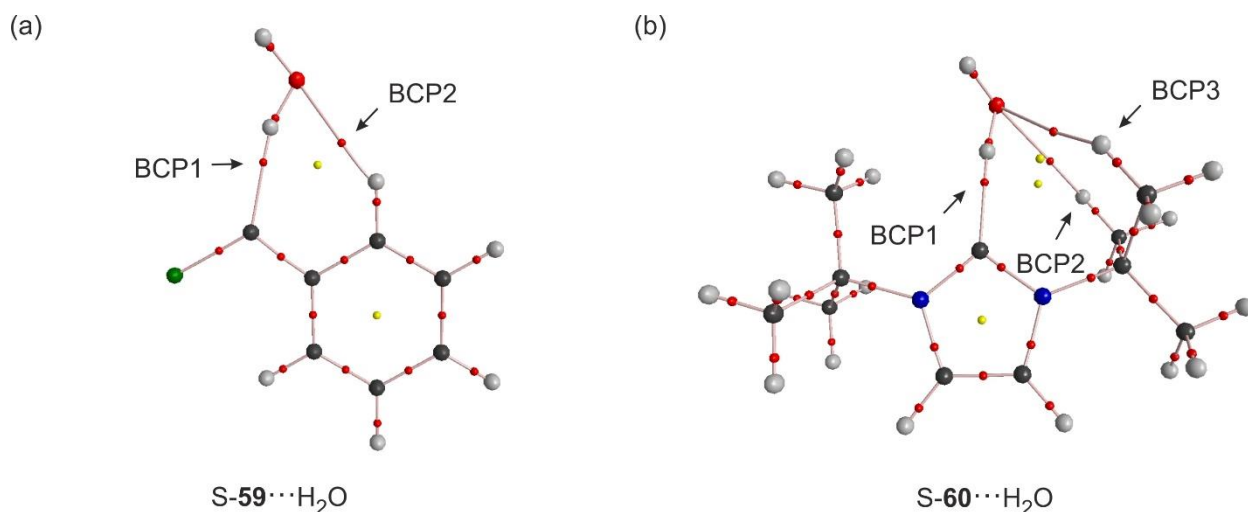


Figure 49. Structures of hydrogen-bonded complexes (a) S-**59**···H₂O and (b) S-**60**···H₂O showing the bond critical points computed at the B3LYP-D3/def2-TZVP level of theory.

Table 20. Summary of AIM calculations for the hydrogen-bonded complexes of carbenes **S-59** and **S-60** at the B3LYP-D3/def2-TZVP level of theory. All quantities, except E_{HB} , are expressed in a.u. E_{HB} is in kcal mol⁻¹.

Complexes	Bond critical point	$\rho(r_c)$	λ_1	λ_2	λ_3	$\nabla^2\rho(r_c)$	$ \lambda_1/\lambda_3 $	$G(r_c)$	$V(r_c)$	E_{HB}
S-59...H ₂ O	BCP1	0.0330	-0.0451	-0.0439	0.1549	-0.0165	0.2908	0.0207	-0.0250	7.8
	BCP2	0.0103	-0.0101	-0.0074	0.0587	-0.0103	0.1718	0.0083	-0.0043	1.9
S-60...H ₂ O	BCP1	0.0415	-0.0602	-0.0586	0.1844	-0.0164	0.3263	0.0252	-0.0340	10.6
	BCP2	0.0080	-0.0071	-0.0044	0.0395	-0.0070	0.1801	0.0056	-0.0042	1.3
	BCP3	0.0071	-0.0059	-0.0043	0.0398	-0.0074	0.1474	0.0057	-0.0040	1.2

The hydrogen-bonded complex between **S-59** and H₂O presents two interactions, a primary interaction (BCP1) between the carbene carbon and a hydrogen of H₂O, and a second interaction (BCP2) between a hydrogen of the aromatic ring of **S-59** and the oxygen of H₂O (Figure 49a). On the other hand, **S-60**...H₂O shows three interactions, a strong carbene carbon-hydrogen interaction (BCP1), and two relatively weak interactions (BCP2 and BCP3) between the hydrogen atoms of the tertiary butyl rings and the oxygen atom of water (Figure 49b). In both complexes at all BCPs, Laplacian $\nabla^2\rho(r_c)$ are less than zero, it implies that the charge is locally concentrated and the values of the ratio $|\lambda_1/\lambda_3|$ are less than 1, which is indicative of closed-shell interactions. It can be seen that the electron density $\rho(r_c)$ at the primary interaction between the carbene carbon and the hydrogen atom of water in **S-60**...H₂O is larger than that in **S-59**...H₂O, suggesting the stronger hydrogen bonding in the former interaction.

The values of $\rho(r_c)$ and $\nabla^2\rho(r_c)$ at the bond critical points in both complexes were used to evaluate their interaction energies, using the procedure described by Espinosa et al.^[217] This method involves the calculations of the local electronic kinetic energy density $G(r_c)$ by Eq. 6, followed by the evaluation of the local electronic potential energy density $V(r_c)$ by Eq. 7 and finally the interaction energy (E_{HB}) by Eq. 8.

$$G(r_c) = \frac{3}{10} (3\pi^2)^{2/3} \rho^{5/3}(r_c) + \frac{1}{6} \nabla^2\rho(r_c) \quad (6)$$

$$V(r_c) = \frac{\hbar^2}{4m} \nabla^2\rho(r_c) - 2G(r_c) \quad (7)$$

$$E_{\text{HB}} = \frac{1}{2} V(r_c) \quad (8)$$

Both hydrogen-bonded complexes exhibited secondary interactions in addition to the prominent C \cdots H–O interaction. Using the topological parameters corresponding to each of these (3, -1) critical points, the interaction energies of S-**59** \cdots H₂O at BCP1 and BCP2 are computed to be 7.8 and 1.9 kcal mol⁻¹, respectively. If these are assumed to be additive, the total interaction energy of the complex works out to be 9.7 kcal mol⁻¹, which is close to the value computed from the energies of the complex and monomers (8.3 kcal mol⁻¹). Likewise, the interaction energies derived from BCP1, BCP2 and BCP3 in S-**60** \cdots H₂O are 10.6, 1.3, and 1.2 kcal mol⁻¹, respectively, yielding a total interaction energy of 13.1 kcal mol⁻¹, again in good agreement with the computed value (11.3 kcal mol⁻¹). It must also be noted that the interaction energies calculated using the topological parameters also show the same trend; the interaction energy of S-**60** \cdots H₂O is larger than that of S-**59** \cdots H₂O.

NBO analysis. The major interaction in both hydrogen-bonded complexes is located between the lone pair of the carbene carbon C(n) and the σ^* orbital of the O–H bond of H₂O. The results obtained from NBO analysis are shown in Table 21. It can be seen that the electron occupancy in the σ^* acceptor orbital is larger in S-**60** \cdots H₂O compared to S-**59** \cdots H₂O. This large occupancy results from both a relatively smaller energy difference between donor and acceptor orbitals E(j)-E(i) and a larger overlap F(i, j). The increase of the electron occupancy in the σ^* acceptor orbital is also reflected in weakening of O–H bond. In S-**60** \cdots H₂O, the larger occupancy leads to elongation of O–H bond by 3.4%, whereas it is lengthened by 2.2% in S-**59** \cdots H₂O. Thus, *N*-heterocyclic carbene **60** exhibits stronger hydrogen bonding interaction than phenylchlorocarbene **59** by donating more electron density into the σ^* orbital of the O–H bond of H₂O.

Table 21. NBO Analysis for S-**59** \cdots H₂O and S-**60** \cdots H₂O complexes, performed at the B3LYP-D3/def2-TZVP level of theory. The symbolic representation C (n) and O–H (σ^*) indicates carbene carbon as donor and antibonding orbital of O–H bond as acceptor respectively. E is the second order perturbation energy in kcal mol⁻¹, E(j)-E(i) is the donor-acceptor energy difference in a. u., and F(i, j) is the overlap between the donor and acceptor orbitals in a. u.

Complexes	Orbitals involved		E	E(j) – E(i)	F (i, j)	Electron occupancy in O–H σ^*
	Donor	Acceptor				
S- 59 \cdots H ₂ O	C (n)	O–H (σ^*)	18.20	0.79	0.107	0.05293
S- 60 \cdots H ₂ O	C (n)	O–H (σ^*)	33.79	0.70	0.138	0.08973

5.2.2. Reactions of Phenylchlorocarbene and 1,3-di-*tert*-butyl-imidazole-2-ylidene with ICF₃.

Singlet carbenes should form halogen bonds in a similar fashion as hydrogen bonds. Hence, the reactions of carbenes **59** and **60** with ICF₃ as halogen bond donor were investigated.

Reaction of Phenylchlorocarbene 59 with ICF₃. Visible light photolysis (405 nm) of phenylchlorodiazirine **63** isolated in an argon matrix doped with 1% of ICF₃ at 3 K produces carbene **59** in its singlet state, in agreement with an IR spectrum reported in literature.^[8] Annealing at 30 K allows ICF₃ to diffuse in the matrix and results in a formation of new IR absorptions at 580.8, 668.5, 868.9, 1082.5, 1129.5, 1261.6 and 1310.4 cm⁻¹. These IR bands are assigned to a halogen-bonded complex **64** between *S*-**59** and ICF₃ by comparison with DFT calculation (Figure 50c, Table 22). Complex **64** exhibits conventional type I^[141] halogen bond with longer C...ICF₃ bond distance of 2.8 Å and C–I–C bond angle of 180°. IR spectrum of ICF₃ shows the characteristic A₁ symmetrical CF stretching vibration at 1064 cm⁻¹, and the degenerate E symmetrical vibration at 1175 cm⁻¹. In **64**, these vibrations are slightly blue and red-shifted to 1082.5 and 1129.5 cm⁻¹, respectively, indicating that the CF₃ fragment in **64** does not carry any charge similar to ICF₃ and further evidences the formation of the type I halogen-bonded complex.

Table 22. IR vibrational frequencies of classical halogen-bonded complex **64** between *S*-**59** and ICF₃.

Mode	Sym	DFT ^[a]		Argon ^[b]		Assignment
		$\tilde{\nu}$ / cm ⁻¹	I _{rel}	$\tilde{\nu}$ / cm ⁻¹	I _{rel}	
18	A	590.3	3	580.8	4	Ring def.
20	A	683.7	5	668.5	7	C–H wagging
25	A	873.9	8	869.1	10	Ring def.
31	A	1073.3	100	1082.5	100	F ₃ C–I str.
33	A	1140.8	34	1129.5	29	C–F str.
37	A	1277.9	36	1261.6	29	C–C str.
38	A	1335.4	5	1310.4	12	C–H bend
39	A	1363.6	2	1326.9	3	C–H bend
40	A	1471.7	5	1445.7	8	C–H bend
41	A	1510.0	2	1480.3	4	C–C str.

^[a]Calculated at the B3LYP-D3/def2-TZVP level of theory. ^[b]Argon matrix at 3 K.

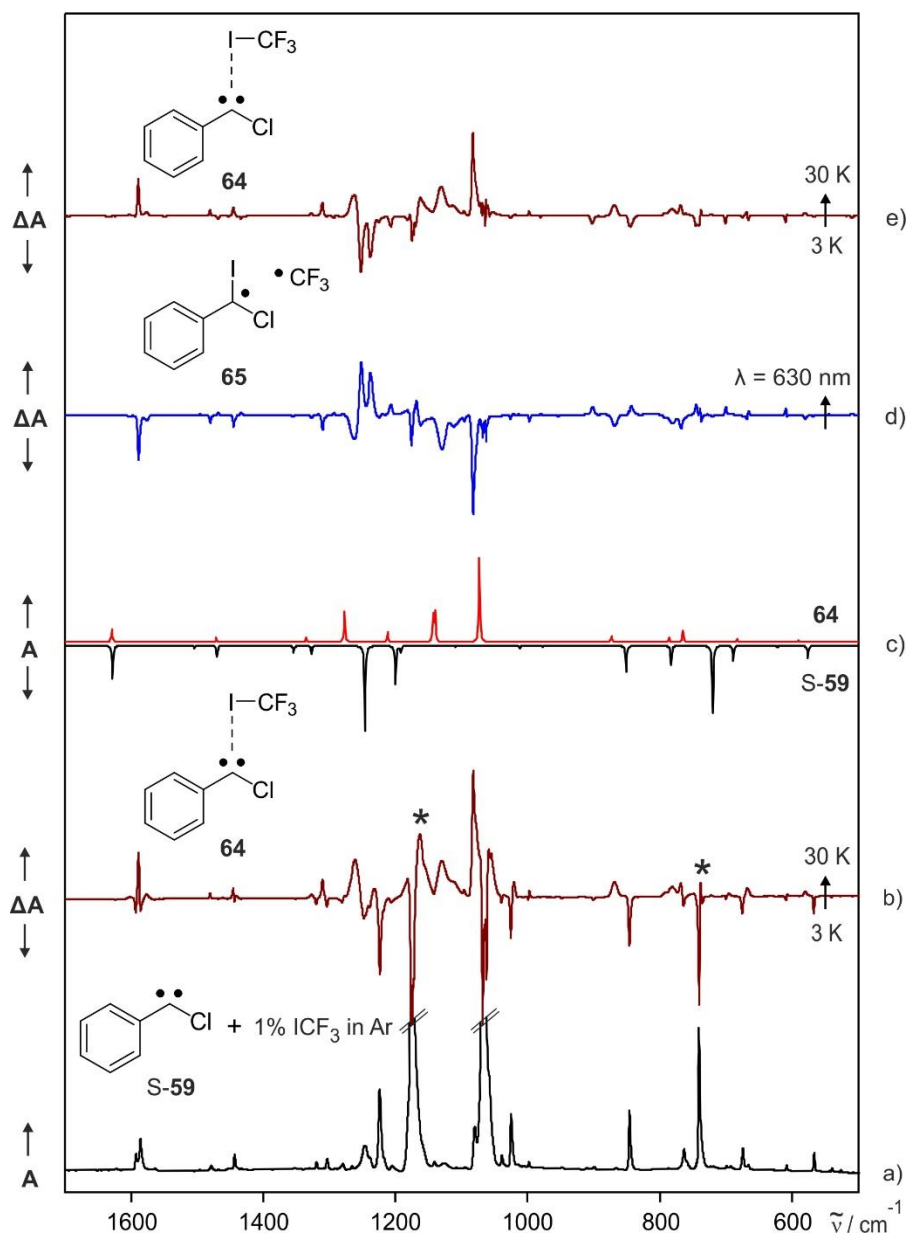


Figure 50. IR spectra showing the reaction between S-59 and ICF₃. a) IR spectrum of S-59 in an argon matrix doped with 1% of ICF₃ at 3 K. b) Difference IR spectrum showing changes after annealing at 30 K. Bands pointing downwards assigned to S-59 and ICF₃ are disappearing, and bands pointing upwards are assigned to halogen-bonded complex **64** are appearing. The bands marked with asterisks are assigned to higher aggregates of ICF₃. c) Computed IR spectrum of S-59 (multiplied by -1, peaks pointing downwards) and computed IR spectrum of **64** (peaks pointing upwards) at the B3LYP-D3/def2-TZVP level of theory. d) Difference IR spectrum of the same matrix showing the changes after 630 nm irradiation at 3 K. Bands pointing downwards assigned to complex **64** are disappearing, and bands pointing upwards assigned to radical pair **65** are appearing. e) Difference IR spectrum of the same matrix showing the changes after annealing at 30 K. Bands pointing downwards assigned to radical pair **65** are disappearing, and bands pointing upwards corresponding to complex **64** are appearing.

Subsequent irradiation with 630 nm leads to disappearance of all IR bands of **64**, and concurrently a new compound is formed. The strong IR vibrations at 1238.2 and 1252.0 cm^{-1} , assigned to CF_3 radical, and additional signals at 609.7, 665.8, 700.3, 744.9, 843.2 and 901.7 cm^{-1} altogether identify this compound as triplet radical pair **65** based on DFT calculations (Figure 51, Table 23). Furthermore, annealing of the same matrix restores the signals of the halogen-bonded complex **64**, accompanied by a decrease in the intensities of all IR bands assigned to **65** (Figure 50e). The interconversion between **64** and **65** is found to be reversible during multiple cycles of photolysis and annealing. The formal C–I insertion product **66** is not observed in spite of high exothermicity of 68 kcal mol^{-1} of reaction between S-**59** and ICF_3 (Scheme 21). This is probably due to matrix cage effects that inhibit the larger movements of the fragments in metastable species **64** and **65**.

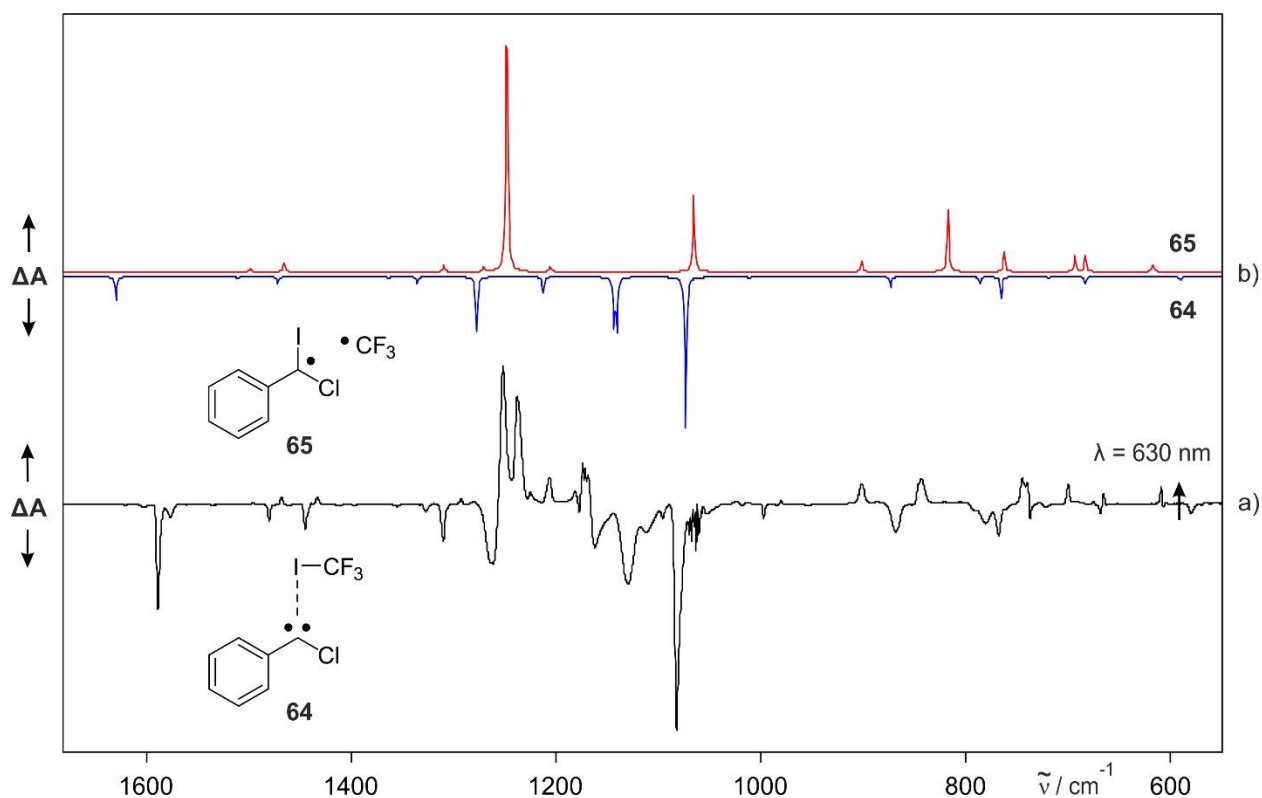
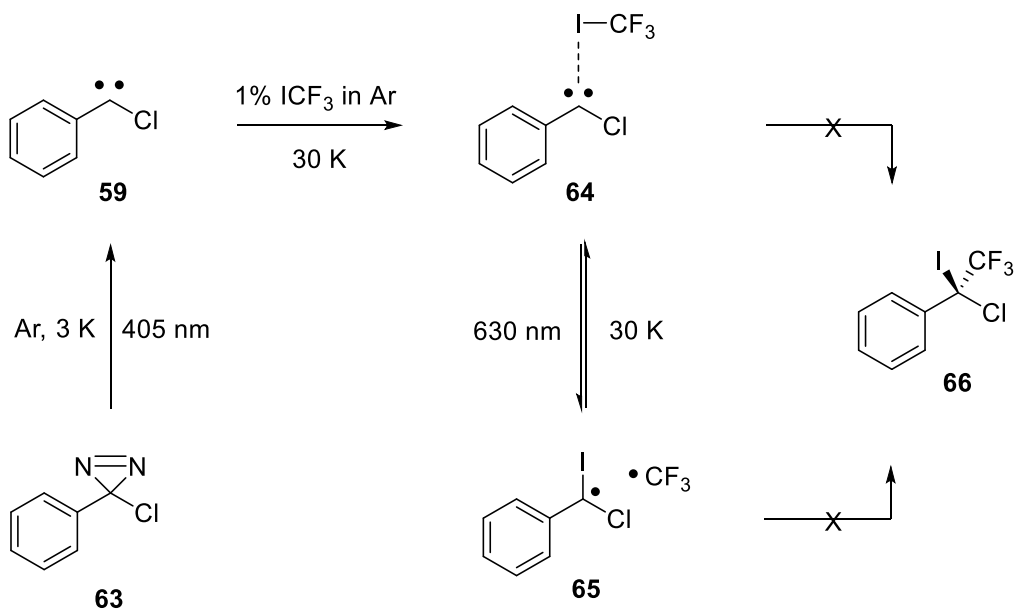


Figure 51. IR spectra showing the formation of radical pair **65** between **59** and ICF_3 . a) Difference IR spectrum of the halogen-bonded complex **64** showing the changes after 630 nm irradiation. Bands pointing downwards assigned to complex **64** are disappearing, and bands pointing upwards assigned to radical pair **65** are appearing. b) Computed IR spectrum of **64** (multiplied by -1, peaks pointing downwards) and computed IR spectrum of **65** (peaks pointing upwards) at the B3LYP-D3/ def2-TZVP level of theory.

Table 23. IR vibrational frequencies of triplet radical pair **65** between **59** and ICF₃.

Mode	Sym	DFT ^[a]		Argon ^[b]		Assignment
		$\tilde{\nu} / \text{cm}^{-1}$	I _{rel}	$\tilde{\nu} / \text{cm}^{-1}$	I _{rel}	
18	A	617.0	3	609.7	7	Ring def.
20	A	683.7	5	665.8	5	C-H wagging
21	A	693.3	6	700.3	7	Sym.CF ₃ str.
22	A	762.1	7	744.9	11	C-H wagging
23	A	817.8	20	843.2	10	C-I str.
25	A	901.7	4	901.7	7	Ring def.
35+36	A	1247.6+1248.4	100	1238.2 + 1252.0	100	C-F str.
38	A	1309.9	2	1292.6	3	C-C-C str.
40	A	1465.7	3	1433.6	3	C-H bend
41	A	1498.8	1	1468.2	3	C-H bend

^[a]Calculated at the B3LYP-D3/def2-TZVP level of theory. ^[b]Argon matrix at 3 K.

**Scheme 21.** Reaction of phenylchlorocarbene **59** with ICF₃.

Reaction of 1,3-di-*tert*-butyl-imidazole-2-ylidene **60 with ICF₃.** With ICF₃, nucleophilic carbene **60** is found to react in a similar fashion. Annealing of an argon matrix containing S-**60** and 1% of ICF₃ at 30 K gives rise to a new set of IR bands at 709.5, 721.5, 1082.8, 1124.5, 1225.3, 1278.4, 1372.9 and 1400.2 cm⁻¹ assigned to a halogen-bonded complex **67**. The IR spectrum correlates well with a DFT calculated spectrum of **67** (Figure 52, Table 24). Analogous to the halogen-bonded complex between S-**59** and ICF₃ (**64**), the complex **67** is predicted to have a long C...ICF₃ bond distance of 2.9 Å and linear geometry with C–I–C bond angle of 180°, indicating type I halogen bond structure.^[141]

A comparison of characteristic A₁ symmetrical (1082.8 cm⁻¹) and degenerate E symmetrical (1124.5 cm⁻¹) vibrations of CF₃ fragment in **67** with that of CF₃ anion,^[218] neutral ICF₃, and CF₃ cation^[218] reveals that CF₃ fragment in **67** does not carry any charge similar to that in complex **64**, signifying the formation of conventional type I halogen-bonded complex (Figure 53). It is important to note that the interactions of carbenes **59** and **60** with ICF₃ are found to be deficient in forming type II ion pair complexes, in contrast to S-**7**...ICF₃ and S-**25**...ICF₃ interactions (Chapter 2). The latter carbenes are relatively more basic and exhibit higher proton affinity values, as a result, more electron density is transferred from σ-orbitals of such carbenes into antibonding orbital of C–I bond of ICF₃ causing a dissociation of the C–I bond and the formation of type II complexes.

Table 24. IR vibrational frequencies of classical halogen bonded complex **67** between S-**60** and ICF₃.

Mode	Sym	DFT ^[a]		Argon ^[b]		Assignment
		$\tilde{\nu}$ / cm ⁻¹	I _{rel}	$\tilde{\nu}$ / cm ⁻¹	I _{rel}	
35	A	638.1	3	627.8	3	C–N str.
38	A	711.3	5	709.5	5	C–H wagging
39	A	720.3	2	721.0	4	Sym C–F str.
55	A	1072.5	100	1082.8	100	F ₃ C–I str.
57	A	1140.3	29	1124.5	33	C–F str.
63	A	1243.4	21	1225.3	33	Methyl C–H bend
66	A	1299.9	2	1278.4	2	Asym. N–C–N str.
68	A	1351.5	3	1337.9	3	Sym. N–C–N str.
73	A	1418.3	4	1372.9	17	C–H bend
74	A	1442.2	3	1400.2	7	Methyl C–H bend

^[a]Calculated at the B3LYP-D3/ def2-TZVP level of theory. ^[b]Argon matrix at 3 K.

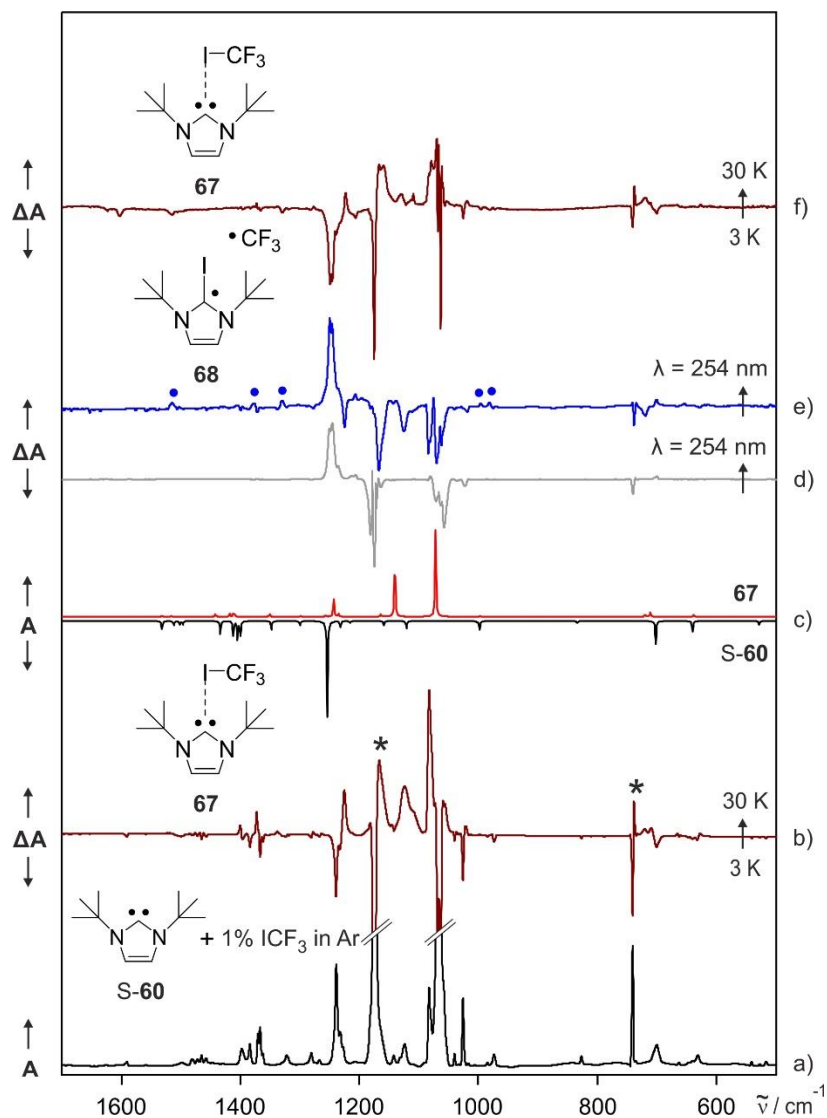


Figure 52. IR spectra showing the reaction between S-60 and ICF₃. a) IR spectrum of S-60 in argon doped with 1% of ICF₃ at 3 K. b) Difference IR spectrum showing the changes after annealing at 30 K. Bands pointing downwards assigned to S-60 and ICF₃ are disappearing, and bands pointing upwards assigned to halogen-bonded complex 67 are appearing. The bands marked with asterisks are assigned to higher aggregates of ICF₃. c) Computed IR spectrum of S-60 (multiplied by -1, peaks pointing downwards) and computed IR spectrum of 67 (peaks pointing upwards) at the B3LYP-D3/def2-TZVP level of theory. d) Difference IR spectrum obtained after 254 nm irradiation of annealed argon matrix containing 1% of ICF₃. Bands pointing downwards assigned to ICF₃ are disappearing, and the bands pointing upwards assigned to CF₃ radical are appearing. e) Difference IR spectrum of the annealed matrix (trace c) containing 67 showing the changes after 254 nm irradiation. Bands pointing downwards assigned to 67 and ICF₃ are disappearing, and bands pointing upwards assigned to triplet radical pair 68 (marked with blue dots) and CF₃ radical are appearing. f) Difference IR spectrum of the same matrix showing the changes after annealing at 30 K. Bands pointing downwards assigned to 68 and CF₃ radical are disappearing, and bands pointing upwards correspond to complex 67 and ICF₃ are appearing.

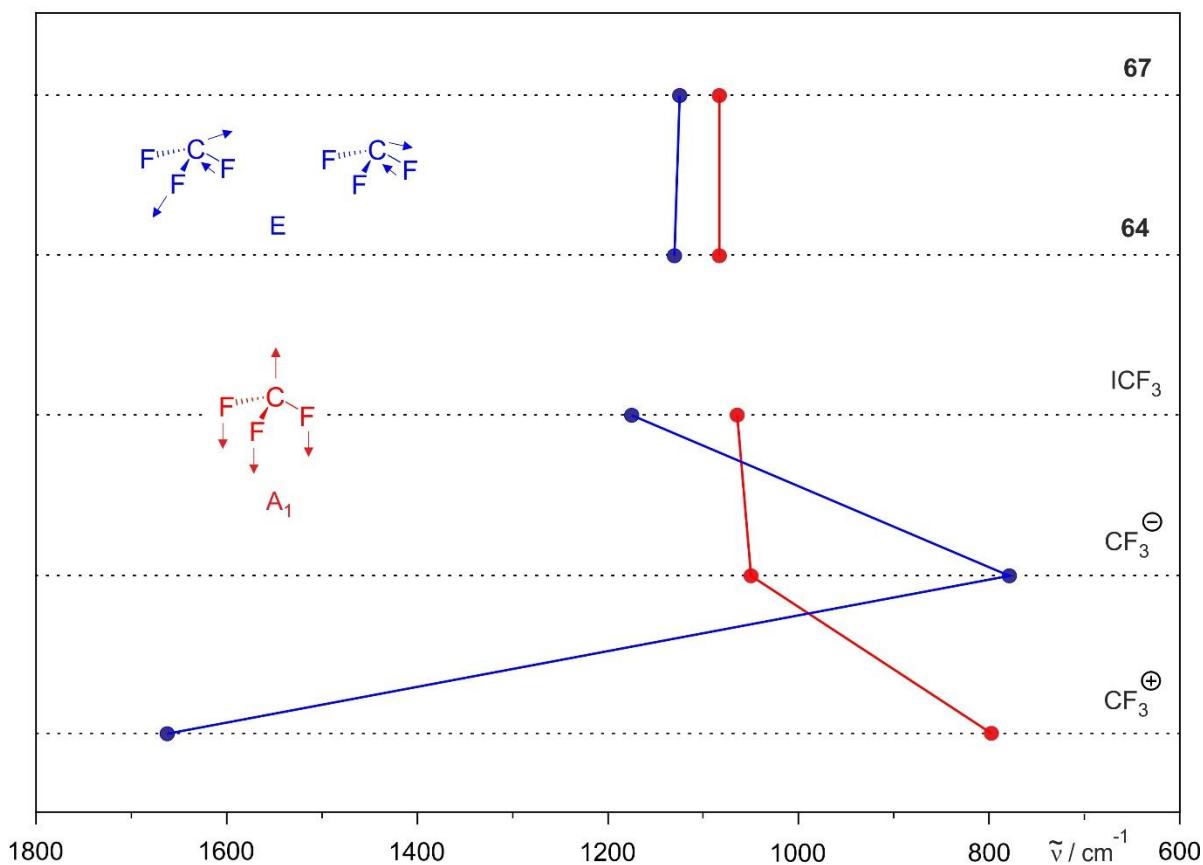


Figure 53. Characteristic IR vibrations of the CF_3 fragment. The experimental frequencies of the A_1 symmetrical (red) and degenerate E symmetrical CF stretching vibrations of the cation CF_3^+ ,^[218] of the anion CF_3^- ,^[218] and for the neutral ICF_3 are compared to those of **64** and **67** (two upper traces).

The matrix-isolated complex **67** is stable towards visible light irradiation, but upon UV irradiation (254 nm) produces two new species. Two strong bands at 1247.1 and 1251.7 cm^{-1} are assigned to CF_3 radicals by comparison with previous measurements from Clemitshaw and Sodeau^[139] and with a spectrum obtained upon 254 nm photolysis of an argon matrix containing 1% of ICF_3 (Figure 52d). The band at 1252 cm^{-1} was previously assigned to the free CF_3 radical, the band at 1247 cm^{-1} to the $\text{CF}_3\cdots\text{I}$ radical pair. Hence, these two signals of CF_3 radical are resultant of dissociation of unreacted ICF_3 molecules and do not correspond to photochemistry of complex **67**.

Remaining IR signals appearing at 654.2, 981.6, 996.3, 1330.2, 1376.2, 1395.3, and 1405.3 cm^{-1} are assigned to a triplet radical pair **68** (Figure 54, Table 25). Annealing of the same matrix leads to a recombination of radicals and forms back the halogen-bonded complex **67** and ICF_3 . The interconversion between **67** and **68** was reproducible in several irradiation/annealing cycles.

According to DFT calculations, the formation of a formal C–I insertion product **69** is calculated to be exothermic by 29 kcal mol⁻¹. However, compound **69** is not observed at any instances in our experiments (Scheme 22).

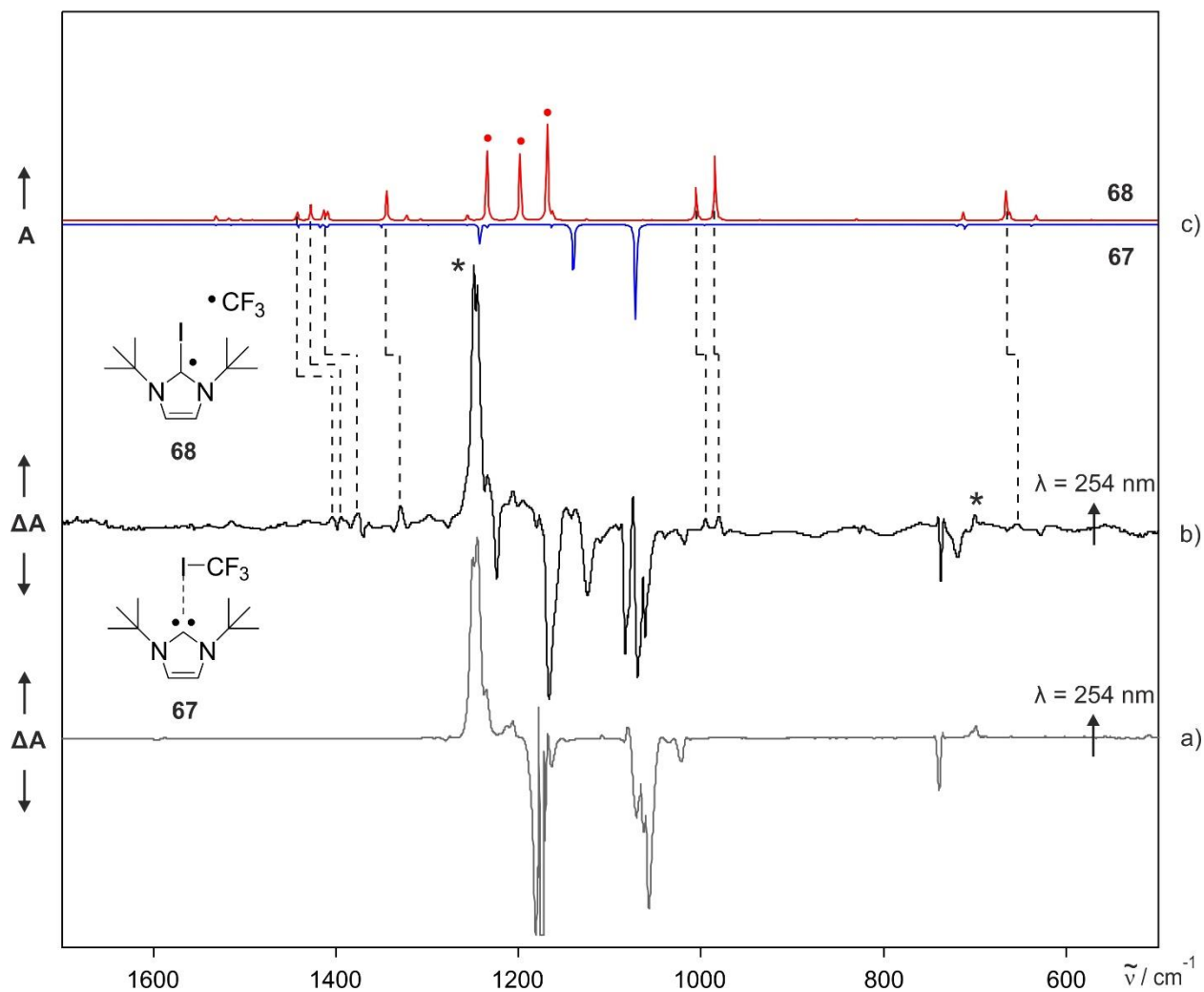
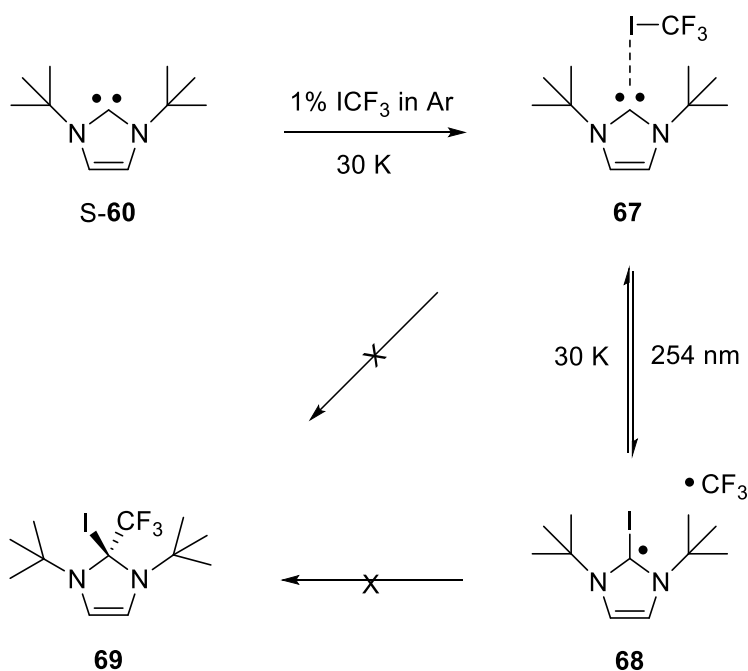


Figure 54. IR spectra showing the formation of radical pair **68**. a) Difference IR spectrum obtained after 254 nm irradiation of an annealed argon matrix containing 1% of ICF₃. Bands pointing downwards assigned to ICF₃ are disappearing, and bands pointing upwards assigned to CF₃ radical are appearing. b) Difference IR spectrum obtained after 254 nm irradiation of an annealed argon matrix containing **67** and 1% of ICF₃. Bands pointing downwards assigned to complex **67** and ICF₃ are disappearing, and bands pointing upwards assigned to triplet radical pair **68** and CF₃ radical (marked with asterisks) are appearing. c) Computed IR spectrum of **67** (multiplied by -1, peaks pointing downwards) and computed IR spectrum of **68** (peaks pointing upwards) at the B3LYP-D3/def2-TZVP level of theory. Bands marked with red dots are probably overlapping with broad vibrations of ICF₃ and **68** in the experiment.

Table 25. IR vibrational frequencies of triplet radical pair **68** between **60** and ICF₃.

Mode	Sym	DFT ^[a]		Argon ^[b]		Assignment
		$\tilde{\nu}$ / cm ⁻¹	I _{rel}	$\tilde{\nu}$ / cm ⁻¹	I _{rel}	
38	A	666.5	45	654.2	36	Ring def.
49	A	985.1	100	981.6	100	C–H wagging
51	A	1006.7	51	996.3	57	Sym.CF ₃ str.
68	A	1345.5	46	1330.2	95	C–H wagging
70 + 72	A	1410.9 + 1414.3	28	1376.2	51	C–I str.
73	A	1428.6	24	1395.3	44	Ring def.
74	A	1443.2	13	1405.3	39	C–F str.

^[a]Calculated at the B3LYP-D3/6-311G (d, p) level of theory. ^[b]Argon matrix at 3 K.

**Scheme 22.** Reaction of 1,3-di-*tert*-butyl-imidazole-2-ylidene **60** with ICF₃.

Computations. At the B3LYP-D3/def2-TZVP level of theory, interactions of ICF₃ with S-**59** and S-**60** are expected to form corresponding halogen-bonded complexes with binding energies of 10 and 11.4 kcal mol⁻¹, respectively. To understand the nature of halogen bonding interactions in S-**59**⋯ICF₃ and S-**60**⋯ICF₃, AIM and NBO analyses were performed at the same level of theory.

AIM analysis. The bond critical points (3, -1) associated with halogen bonding interactions in **S-59**···**ICF₃** (**64**) and **S-60**···**ICF₃** (**67**) complexes were generated using the wavefunctions at the B3LYP-D3/def2-TZVP level of theory (Figure 55). The values of electron density $\rho(r_c)$, eigenvalues of Hessian $\lambda_1, \lambda_2, \lambda_3$, the Laplacian of electron density ($\nabla^2\rho$) of electron density and ($|\lambda_1/\lambda_3|$) for both complexes computed at bond critical points are given in Table 26.

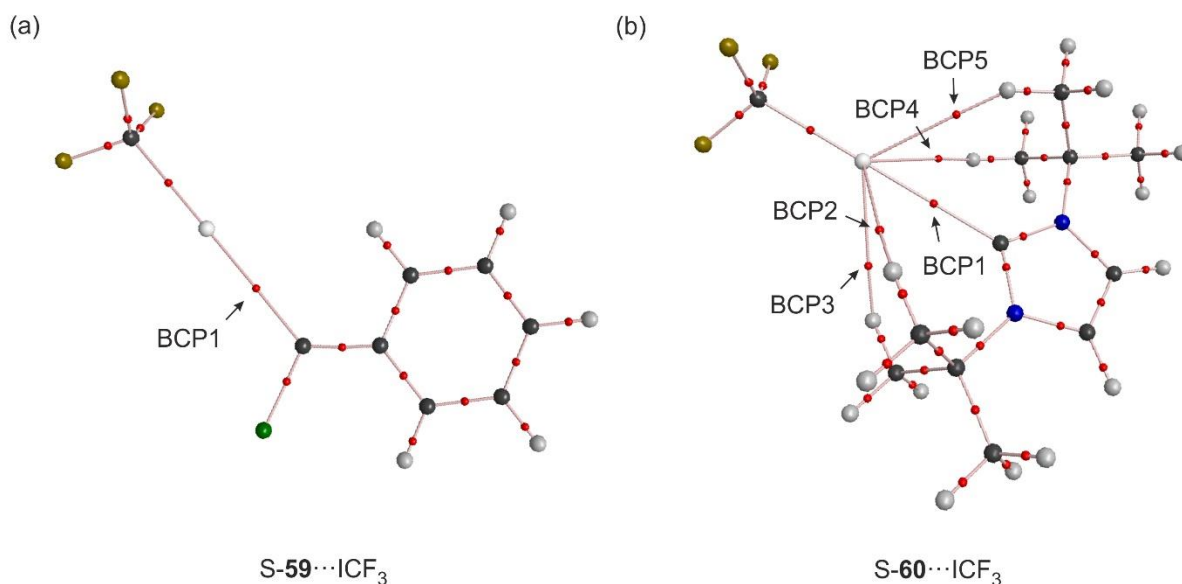


Figure 55. Structures of hydrogen-bonded complexes (a) **S-59**···**ICF₃** and (b) **S-60**···**ICF₃** showing the bond critical points computed at the B3LYP-D3/def2-TZVP level of theory.

Table 26. Summary of AIM calculation for the halogen-bonded complexes of **S-59** and **S-60** at the B3LYP-D3/def2-TZVP level of theory. All quantities are expressed in a.u.

Complexes	Bond critical point	$\rho(r_c)$	λ_1	λ_2	λ_3	$\nabla^2\rho(r_c)$	$ \lambda_1/\lambda_3 $
S-59 ··· ICF₃	BCP 1	0.0317	-0.0228	-0.0218	0.1050	-0.0151	0.2174
S-60 ··· ICF₃	BCP1	0.0263	-0.0181	-0.0172	0.0825	-0.0118	0.2189
	BCP2	0.0091	-0.0064	-0.0060	0.0364	-0.0060	0.1766
	BCP3	0.0089	-0.0063	-0.0058	0.0358	-0.0059	0.1756
	BCP4	0.0091	-0.0064	-0.0060	0.0365	-0.0060	0.1767
	BCP5	0.0089	-0.0063	-0.0058	0.0358	-0.0059	0.1757

Complex **S-59**···**ICF₃** presents only one interaction between carbene carbon of **S-59** and iodine of **ICF₃** (BCP1), whereas complex **S-60**···**ICF₃** shows five interactions: a strong carbene carbon-iodine interaction (BCP1), and four relatively weak interactions (BCP2, BCP3, BCP4 and BCP5)

between the iodine atom of ICF₃ and the hydrogen atoms of the tertiary butyl groups (Figure 55). The values of ratio $|\lambda_1/\lambda_3|$ at all BCPs are less than 1, which is an indication of closed-shell interactions. Also, Laplacian $\nabla^2\rho(r_c)$ at all BCPs are less than zero, which implies that the charge is locally concentrated in these interactions. It can be seen that the primary carbene carbon-iodine interaction in S-**59**···ICF₃ appears to be stronger than that in S-**60**···ICF₃, as revealed by the values of $\rho(r_c)$ and $(\nabla^2\rho)$ at corresponding BCPs. This can be explained by steric hindrance of *tert*-butyl groups in **60** which inhibits a facile approach of the iodine atom to the carbene carbon, but in turn leads to secondary interactions between iodine of ICF₃ and hydrogen of *tert*-butyl groups. As a result, both primary and secondary interactions overall contribute to the binding energy of the complex S-**60**···ICF₃.

NBO analysis. To discern the role of orbital interactions, NBO analysis was carried out for the halogen-bonded complexes S-**59**···ICF₃ and S-**60**···ICF₃. In both cases, there is a prominent interaction between the lone pair of carbene, serving as the electron donor to the σ^* orbital of C–I bond of ICF₃ which serves as the electron acceptor, as can be seen from the high values of second order perturbation energies (Table 27). The perturbation energy is directly proportional to orbital occupancy in the σ^* orbital of the C–I bond and the square of the overlap integral of donor and acceptor orbitals, $F(i, j)$ and inversely proportional to their energy difference $[E(j) - E(i)]$. It can be seen that although energy difference between donor and acceptor orbitals in S-**60**···ICF₃ is smaller than that in S-**59**···ICF₃, the overlap is somewhat less in the former complex due to bulky *tert*-butyl groups. Despite of which, S-**60**···ICF₃ has slightly more electron occupancy in the σ^* antibonding orbital of the C–I bond, since *tert*-butyl groups also act as σ -electron donors increasing basicity of S-**60** and causing more electron transfer from the carbene.

Table 27. NBO Analysis for S-**59**···ICF₃ and S-**60**···ICF₃ complexes, performed at the B3LYP-D3/def2-TZVP level of theory. The symbolic representation C (n) and C–I (σ^*) indicates carbene carbon as donor and antibonding orbital of C–I bond as acceptor respectively. E is the second order perturbation energy in kcal mol⁻¹, $E(j)-E(i)$ is the donor-acceptor energy difference in a. u., and $F(i, j)$ is the overlap between the donor and acceptor orbitals in a. u.

Complexes	Orbitals involved		E	E(j) – E(i)	F (i, j)	Electron occupancy in C–I σ^*
	Donor	Acceptor				
S- 59 ···ICF ₃	C (n)	C–I (σ^*)	24.63	0.34	0.082	0.24030
S- 60 ···ICF ₃	C (n)	C–I (σ^*)	25.95	0.27	0.074	0.24736

Hydrogen vs. Halogen Bonding. The work in this chapter allows us to compare the hydrogen and halogen bonding of carbenes. According to calculations at the B3LYP-D3/def2-TZVP level of theory, the singlet state of phenylchlorocarbene **S-59** is more stabilized by halogen bonding with ICF₃ (-10 kcal mol⁻¹) as compared to hydrogen bonding with H₂O (-8.3 kcal mol⁻¹), suggesting halogen bonding with ICF₃ to be stronger interaction than hydrogen bonding with H₂O. This interpretation was experimentally verified in case of dibenzocycloheptadienyliene **25** under matrix isolation conditions (Chapter 2), where triplet ground state carbene **T-25** is found to form a singlet complex with ICF₃, but not with H₂O as the stabilization of **S-25** by forming hydrogen-bonded complex is not large enough to overcome the S-T gap of the carbene. This is also supported by DFT calculations which predict larger stabilization of **S-25** by halogen bonding with ICF₃ (-14.6 kcal mol⁻¹) than hydrogen bonding with H₂O (-11.5 kcal mol⁻¹). In contrast to hydrogen bond, the halogen bond is accompanied by back-bonding interaction between lone pair of the halogen atom and the empty π -orbital of singlet carbene which strengthens the halogen bonding interactions comparatively. However, it is too early to generalize the notion of ‘halogen bonding > hydrogen bonding’ for all the carbenes.

The hydrogen-bonded complex of di-*tert*-butyl substituted NHC **60** with H₂O and the halogen-bonded complex of the same carbene with ICF₃ are predicted to have similar binding energies (~ 11 kcal mol⁻¹), anomalous to previous systems. The steric hindrance of the *tert*-butyl groups in **S-60**···ICF₃ limits the approach of the bulky iodine atom to the carbene carbon and thereby decreases the strength of halogen bond. On the other hand, the hydrogen of H₂O, due to its smaller size, can penetrate through the *tert*-butyl groups to form the hydrogen-bonded complex **S-60**···H₂O, and therefore steric hindrance in this case does not lead to weakening of hydrogen bond. It is tempting to compare the binding energies of hydrogen and halogen-bonded complexes of the NHC systems **58**, **60** and **70** having different extent of steric hindrances (Figure 56).

From this comparison, it can be deduced that systems involving less hindrance **58** and **70** follow a general trend; i.e., for a given carbene, interaction energies calculated for halogen-bonded complex with ICF₃ is larger than that for corresponding hydrogen-bonded complex with H₂O, since there is no considerable weakening effect on the strength of the halogen bond due to steric hindrance.

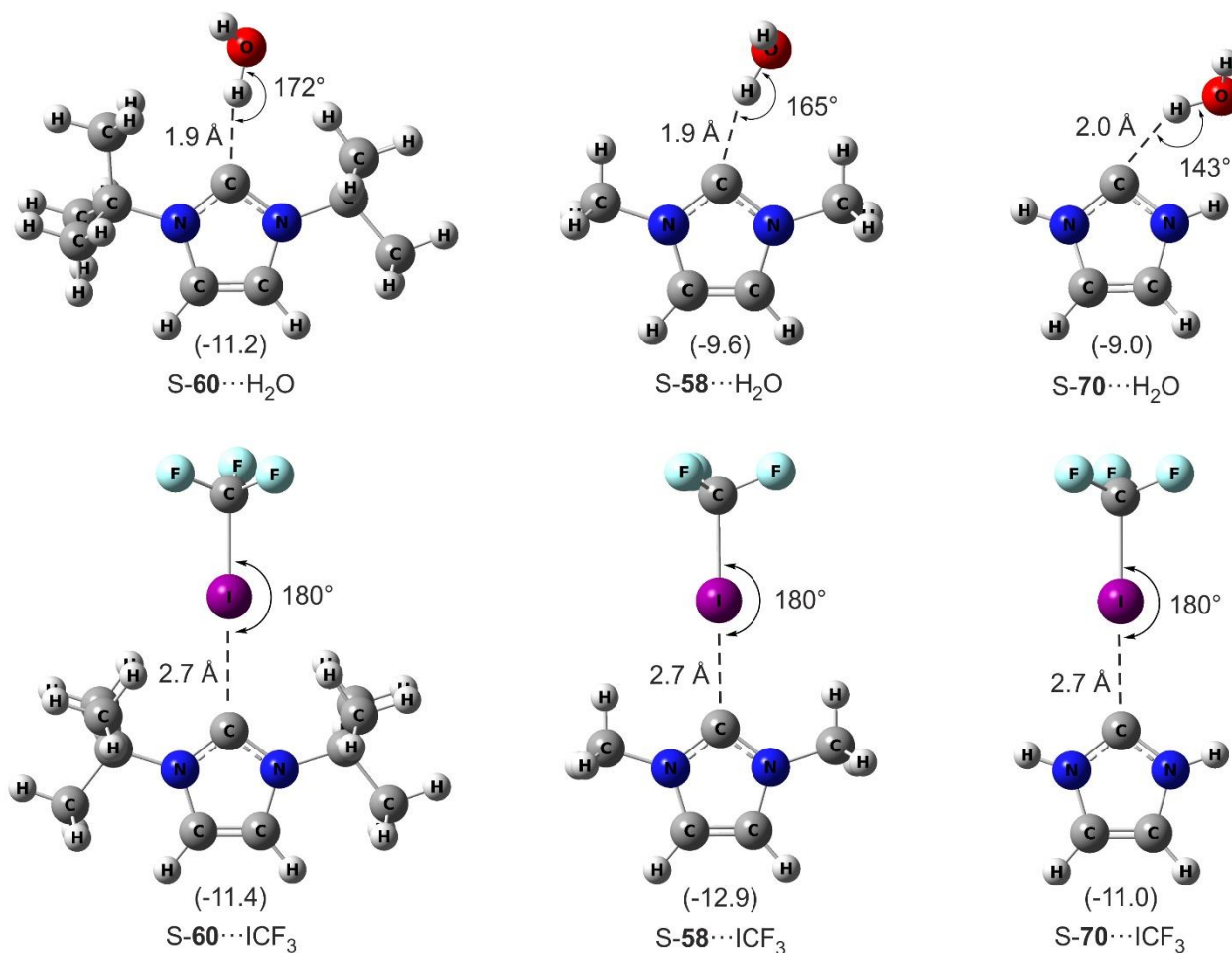


Figure 56. Optimized structures of hydrogen and halogen-bonded complexes of NHC systems **58**, **60** and **70** (shown in a descending order of steric hindrance from left to right), computed at the B3LYP-D3/def2-TZVP level of theory. Values in parenthesis correspond to binding energies of these complexes given in kcal mol⁻¹.

5.3. Conclusions

The singlet ground state carbenes **59** and **60** are strong bases and therefore act as excellent hydrogen and halogen bond acceptors. Consequently, these carbenes form strongly hydrogen and halogen-bonded complexes with H_2O and ICF_3 , respectively. Unlike previously investigated $\text{S-59}\cdots\text{H}_2\text{O}$ complex,^[8] the hydrogen-bonded complex **61** between **S-60** and H_2O is found to be stable even upon photochemical excitation (254 nm) and the formal O–H insertion product is not observed. This is also corroborated by DFT calculations (B3LYP-D3/def2-TZVP level of theory) which predict complex **61** ($\text{S-60}\cdots\text{H}_2\text{O}$) to be thermodynamically more stable than corresponding O–H insertion product by 2.3 kcal mol⁻¹. The highly nucleophilic NHC **S-60** is estimated to have higher proton affinity (270 kcal mol⁻¹) as compared to that of **S-59** (252 kcal mol⁻¹), thus the

binding energy of S-**60**···H₂O (11.2 kcal mol⁻¹) is calculated to be larger than that of S-**59**···H₂O (8.3 kcal mol⁻¹).

The halogen-bonded complexes **64** (S-**59**···ICF₃) and **67** (S-**60**···ICF₃) exhibit conventional type I halogen bonds, as revealed by long C···ICF₃ bond distances and do not carry any negative charge on CF₃ fragments as expected in type II ion pair complexes. The complexes **64** and **67** are stable at low temperatures, but rearrange photochemically to the corresponding triplet radical pairs **65** and **68**, respectively. At higher temperatures of 25 – 30 K, the radical pairs recombine followed by intersystem crossing to give back the complexes **64** and **67**. The recombination of radical pairs **65** and **68** to yield the respective C–I insertion products **66** and **69** is calculated to be highly exothermic by 65 and 55 kcal mol⁻¹, as compared to the formation of the halogen-bonded complexes by 7 and 32 kcal mol⁻¹, respectively. However, the formal C–I insertion products are not observed in our experiments probably due to matrix cage effects that inhibit the larger movements of the fragments in the radical pairs.

The comparison of binding energies of hydrogen and halogen-bonded complexes of S-**59** and S-**60** shows that the stabilization of the singlet carbenes by halogen bonding with ICF₃ is larger than the stabilization by hydrogen bonding with H₂O, provided that steric hindrance has no weakening effect on the strength of halogen bonds.

6. Ammonia Activation by 1,8-diazafluorenylidene

6.1. Introduction

The nature of substituents attached to a carbene carbon accounts for the chemical and physical properties of the carbene.^[219] It is well known that substituents affect singlet-triplet energy separations of carbenes by manipulating relative energies of σ and π orbitals of the carbene. In most of the diarylcarbenes, substituent effects are mainly transmitted through the π -system of the aryl rings to the π -orbital of the carbene, whereas the σ -orbital should respond less dramatically to the substituents.^[220] 1,8-diazafluorenylidene **71**, a derivative of fluorenylidene **8**, is a triplet ground state carbene, which presumably differs from this approach,^[6] where the σ orbitals containing the lone-pair electrons of ring nitrogen atoms of **71** are in appropriate orientation to interact with the σ -orbital of the carbene. This interaction, as a result, destabilizes the σ -orbital of the carbene and raises its energy relative to the π -orbital, which rationalizes a larger singlet-triplet energy separation in **71** compared to **8** despite of their similar structural frameworks (Chart 11).

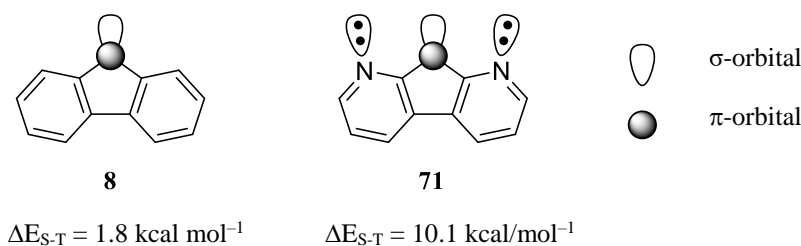


Chart 11. Structures of **8** and **71** showing the influence of orbital interactions of singlet-triplet energy separation (ΔE_{S-T}) of the carbenes, computed at the CCSD(T)/def2-TZVP//B3LYP-D3/def2-TZVP level of theory.

Li and Schuster suggested that the ring nitrogen atoms in **71** aid to modify the electronic properties of the singlet state so that major contribution is from π^2 configurations. Their EPR investigations on this system in frozen media at 77 K demonstrated that the ground state is triplet, however, **71** is also speculated to react from its upper singlet state.^[6] The reactivity of **71** in the π^2 electronic configurations derives mainly from the vacant and highly electrophilic σ -orbital. Reagents bearing lone-pairs such as ammonia can interact with this vacant σ -orbital of the carbene to form an ylide as one of the possible reaction products. Several examples of ylides between singlet carbene and ether, alcohol, pyridine and other reagents are reported in literature.^[221-225]

On the other hand, **71** can also react from its triplet ground state by abstracting hydrogen from ammonia, yielding either a radical pair or the formal N–H insertion product via subsequent recombination. It is rather difficult to probe the σ^2 reactivity of **71** with ammonia due to large S-T energy separation, which might prevent switching of the spin state from triplet to singlet on complexation. To examine the unusual and vibrant chemical behavior of **71**, its reaction with ammonia was investigated.

6.2. Results and Discussion

6.2.1. Matrix Isolation Spectroscopic Characterization of 1,8-diazafluorenylidene

IR spectroscopy. Diazo-1,8-diazafluorenylidene **72** deposited in an argon matrix at 20 K shows a strong absorption at 2095.7 cm^{-1} assigned to the characteristic asymmetric stretching vibration of the C=N=N group. The heterocyclic diazo compound **72** was reported to exhibit a remarkable thermal stability relative to the parent diazofluorene **29**; in diphenyl ether at 140°C , compound **72** was found to have a half-life of at least 2 days which is in striking contrast with the half-life of 30 minutes of **29** under similar conditions.^[6] This can be rationalized by a σ - π backbonding interaction of the ring nitrogen atoms with α -nitrogen of the diazo group (Chart 12), which in turn increase a barrier for the denitrogenation.^[6]

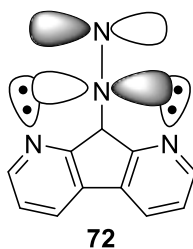


Chart 12. Schematic structure of diazo-1,8-diazafluorenylidene **72** showing the σ - π backbonding interaction.^[6]

Prolonged irradiation of **72** isolated in an argon matrix at 3 K with 450 nm for 24 hours produces 1,8-diazafluorenylidene in its triplet state T-**71**, in agreement with predictions from DFT calculations (Figure 57, Table 28). A less facile loss of nitrogen from **72** observed under the photochemical conditions could be a consequence of its enhanced stability. Annealing of the matrix containing T-**71** at 30 K does not show any significant changes. Also, no new features are observed after irradiation experiments with different wavelengths between 650 and 254 nm, suggesting the photostability of T-**71** in argon matrices.

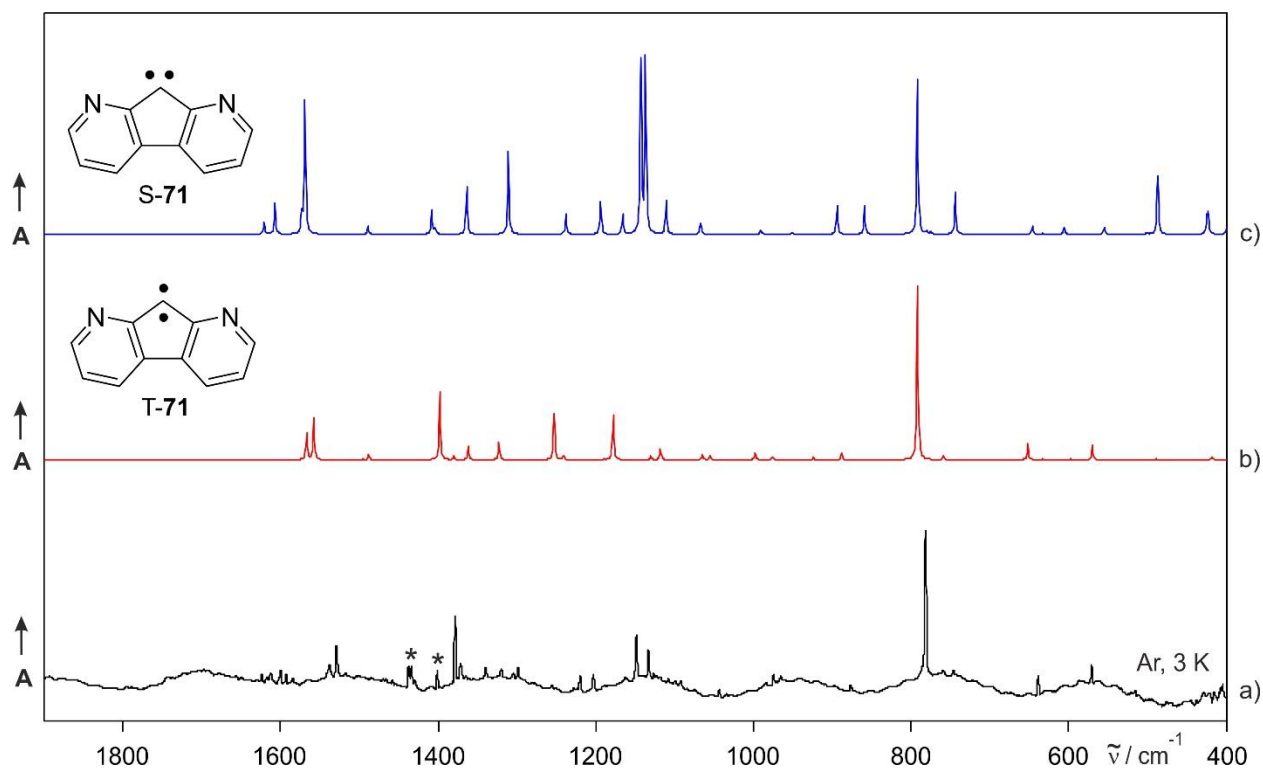


Figure 57. IR spectrum of carbene **71** in its triplet ground state. a) IR spectrum obtained after 450 nm irradiation of diazo-1,8-diazafluorenylidene **72** in an argon matrix at 3 K. Peaks marked with asterisks are assigned to remaining diazo precursor **72**. b) Computed IR spectrum of T-**71** at the B3LYP-D3/def2-TZVP level of theory. c) Computed IR spectrum of S-**72** (in σ^2 electronic configuration) at the B3LYP-D3/def2-TZVP level of theory.

Table 28. IR vibrational frequencies of triplet 1,8-diazafluorenylidene T-**71**.

Mode	Sym	DFT ^[a]		Argon ^[b]		Assignment
		$\tilde{\nu}/\text{cm}^{-1}$	I_{rel}	$\tilde{\nu}/\text{cm}^{-1}$	I_{rel}	
11	B1	588.4	12	570.7	18	C–H bend
14	A1	652.1	13	638.6	22	C–C–C bend
18	B1	799.5	100	780.9	100	C–H wagging
29	A1	1120.8	8	1133.0	17	C–H bend
31	B2	1177.8	40	1148.6	33	C–C–C asym. str.
34	B2	1253.4	34	1202.3 + 1219.1	22	C–N–C asym. str.
35	A1	1327.2	10	1298.1	9	C–H bend
37	A1	1367.1	9	1339.2	9	C–C–C bend
39	B2	1404.9	48	1378.1	53	C–H bend
42	B2	1561.1	32	1528.5	21	C=C str.
43	A1	1568.7	20	1537.8	11	C=C + C=N str.

^[a]Calculated at the B3LYP-D3/def2-TZVP level of theory. ^[b]Argon matrix at 3 K.

According to DFT calculations at the B3LYP-D3/def2-TZVP level of theory, carbene **71** is predicted to have a ground triplet state ($\sigma^1\pi^1$) lying 12.3 kcal mol⁻¹ below the closed-shell singlet state (σ^2), explaining the experimental findings. The possibility of a more reactive singlet state (π^2) is ruled out, since the IR results clearly show the formation of the triplet carbene at 3 K.

EPR spectroscopy. The assignment of triplet carbene T-**71** is confirmed by EPR experiments. Photolysis of diazo precursor **72** with 450 nm light in an argon matrix at 5 K produces the characteristic signals of triplet carbene T-**71**. The X-band EPR spectrum is simulated with zero field splitting (zfs) parameters of $|D/hc| = 0.435$ cm⁻¹ and $|E/hc| = 0.027$ cm⁻¹ (Figure 58), comparable to the values reported by Schuster et al. ($|D/hc| = 0.442$ cm⁻¹, $|E/hc| = 0.029$ cm⁻¹) in cryogenic matrices at 77 K.^[6]

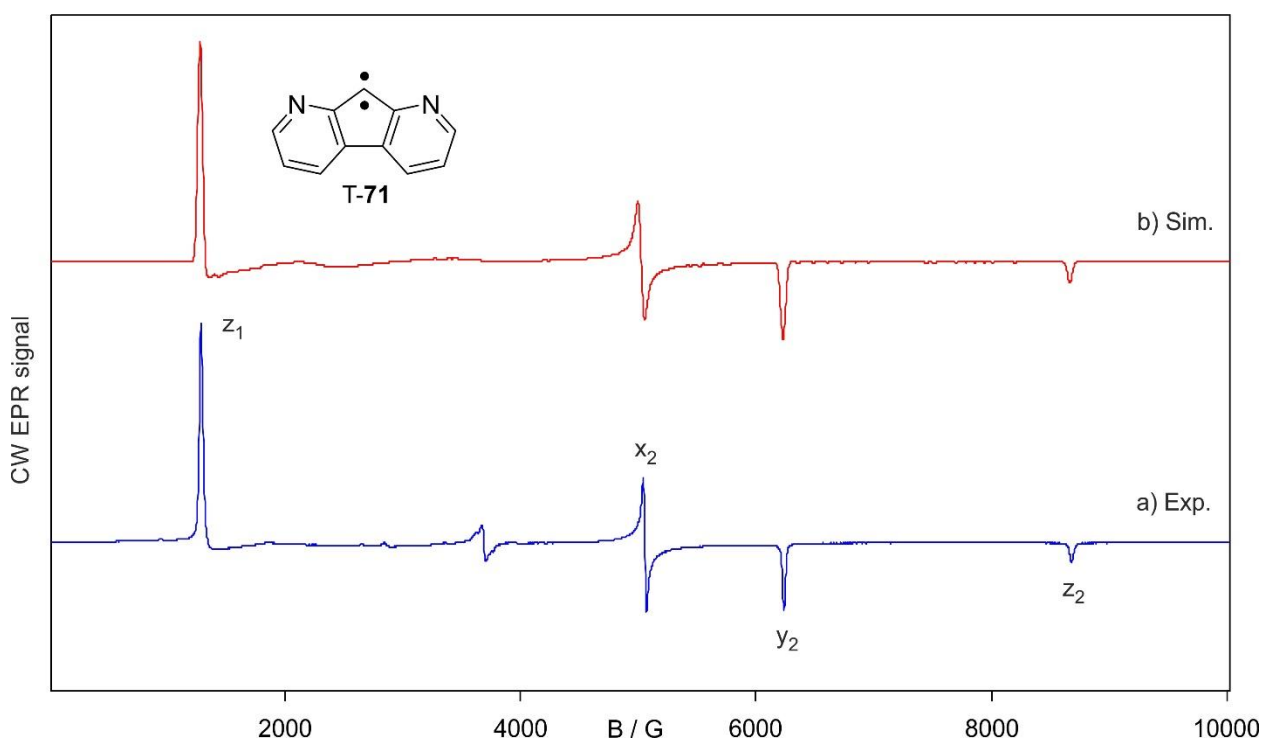


Figure 58. EPR spectrum of carbene **71** in its triplet ground state. a) X-band CW EPR spectrum of T-**71** in an argon matrix at 5 K. b) Simulated EPR spectrum of T-**71** with zfs parameters $|D/hc| = 0.435$ cm⁻¹ and $|E/hc| = 0.027$ cm⁻¹.

In addition to the formation of T-**71**, a weak signal at 283 mT is also observed upon irradiation of the diazo precursor **72** (Figure 59, marked with asterisk). This signal is assigned to a quintet state radical pair or quintet dicarbene **73** on the basis of similar quintet signal observed at 280 mT upon irradiation of bis(*p*-chlorophenyl)diazomethane in 2-MTHF glasses at 10 K.^[226] Such quintet state

radical pair can be formed through interaction of two adjacent triplet carbenes;^[227] the random molecular packing in the matrix cage could rationalize the presence of weak interaction between two carbenes in quintet state. In addition to the transition at 283 mT, several signals are observed, which matches reasonably well with a simulated spectrum with zfs parameters of $|D/hc| = 0.08 \text{ cm}^{-1}$ and $|E/hc| = 0.0048 \text{ cm}^{-1}$ (Figure 59, inset). The signals assigned to **73** grow with respect to an increase in sample concentration, providing further evidence for the formation of a quintet state radical pair.

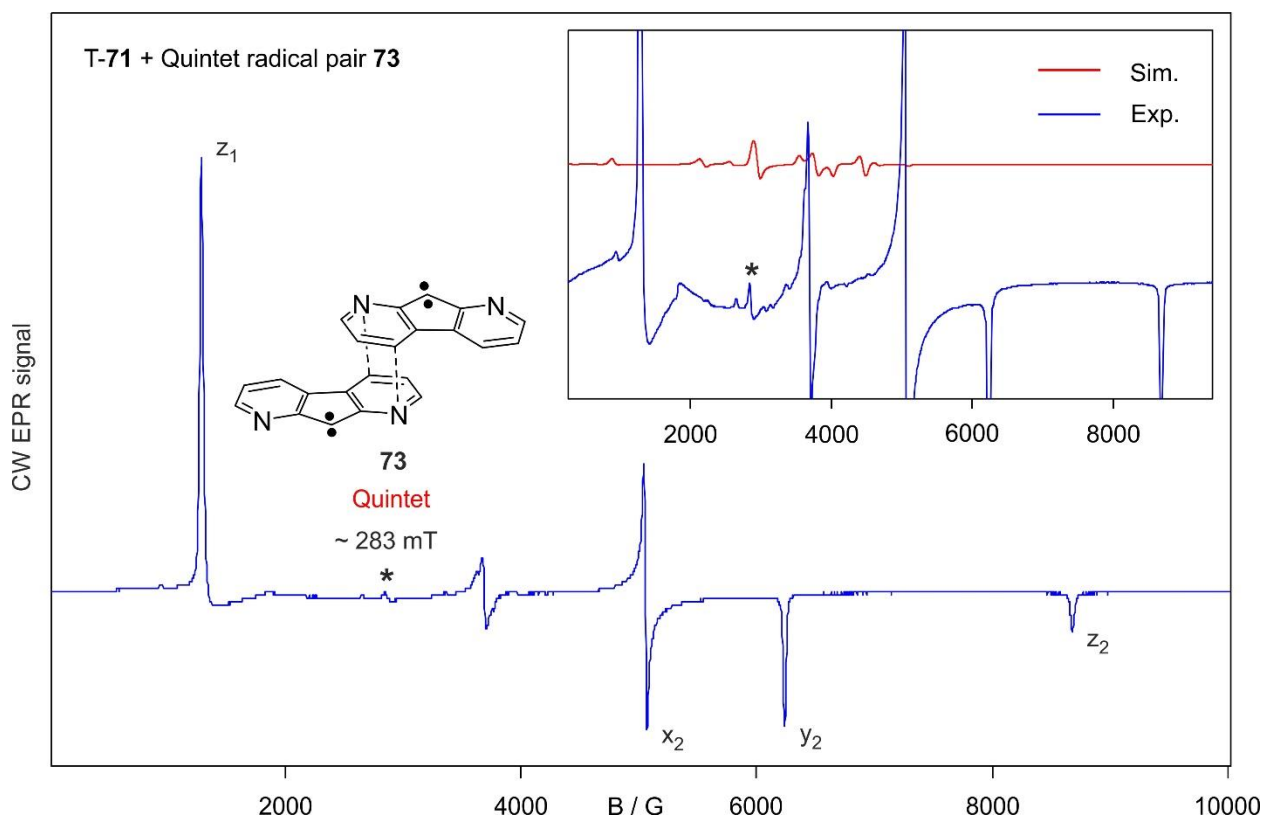


Figure 59. X-Band CW EPR experimental spectrum showing the formation of quintet state radical pair **73** in addition to T-**71** upon 450 nm irradiation of the diazo precursor **72** in an argon matrix at 5 K. The experimental EPR signals of **73** (blue line) and its simulated spectrum (red line) with the zfs parameters $|D/hc| = 0.08 \text{ cm}^{-1}$ and $|E/hc| = 0.0048 \text{ cm}^{-1}$ are shown in the inset.

UV-Vis spectroscopy. Carbene **71** was also examined using UV-Vis spectroscopy. In an argon matrix at 8 K, the diazo precursor **72** shows a series of UV absorptions, ranging from 200 to 350 nm, which decrease upon 450 nm photolysis. Concurrently, two strong UV absorptions at $\lambda_{\text{max}} = 251$ and 274 nm, and a weak UV absorption at $\lambda_{\text{max}} = 298$ nm are formed which are assigned to triplet carbene T-**71** (Figure 60). The electronic transitions from the π -orbital of carbene carbon

to the antibonding π -orbitals of the pyridine rings adjacent to the central five-membered ring are attributed to the UV bands of T-**71** (Figure A7), which are in good agreement with TD-DFT calculations ($\lambda = 240$ nm, $f = 0.2710$; $\lambda = 255$ nm, $f = 0.5076$ and $\lambda = 268$ nm, $f = 0.2070$).

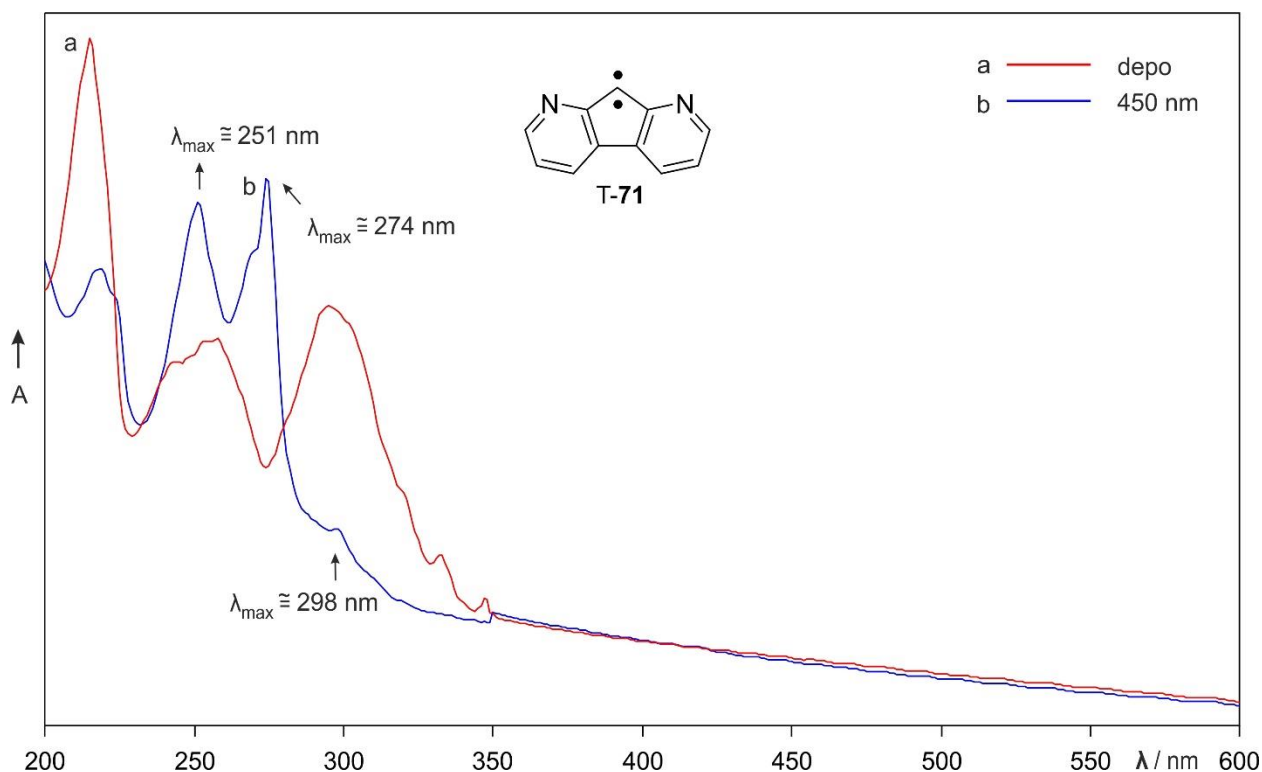


Figure 60. UV-Vis spectrum of carbene **71** in its triplet state. a) UV-Vis spectrum of the diazo precursor **72** isolated in an argon matrix at 8 K. b) UV-Vis spectrum of T-**71** ($\lambda_{\text{max}} = 251, 274,$ and 298 nm) generated upon 450 nm irradiation of the same matrix.

6.2.2. Reaction of 1,8-diazafluorenylidene with Ammonia

IR spectroscopy. To study the reaction of 1,8-diazafluorenylidene **71** and NH_3 , experiments were performed in argon matrices doped with 1% of NH_3 . As expected, 450 nm photolysis (~ 24 hrs) of the diazo precursor **72** in these matrices resulted in the formation of triplet carbene T-**71**. Warming up the matrix from 3 to 30 K allows the diffusion of NH_3 molecules, causing a decrease in IR bands of T-**71** and NH_3 , and concomitantly new signals are formed. Almost all of the newly observed bands are assigned to the reaction product of T-**71** with NH_3 , and NH_3 dimers or higher aggregates.^[228] However, two bands appearing at 1425.0 and 1429.5 cm^{-1} (marked with asterisks in Figure 61a) could not be assigned at first glance and overlap with signals appearing on annealing of the matrix containing the diazo precursor **72** and 1% of NH_3 (Figure 61b). These two bands

show very small shifts compared to IR band of the remaining diazo precursor **72** located at 1433.9 cm^{-1} , suggesting the possibility of formation of weak complexes between **72** and NH_3 .

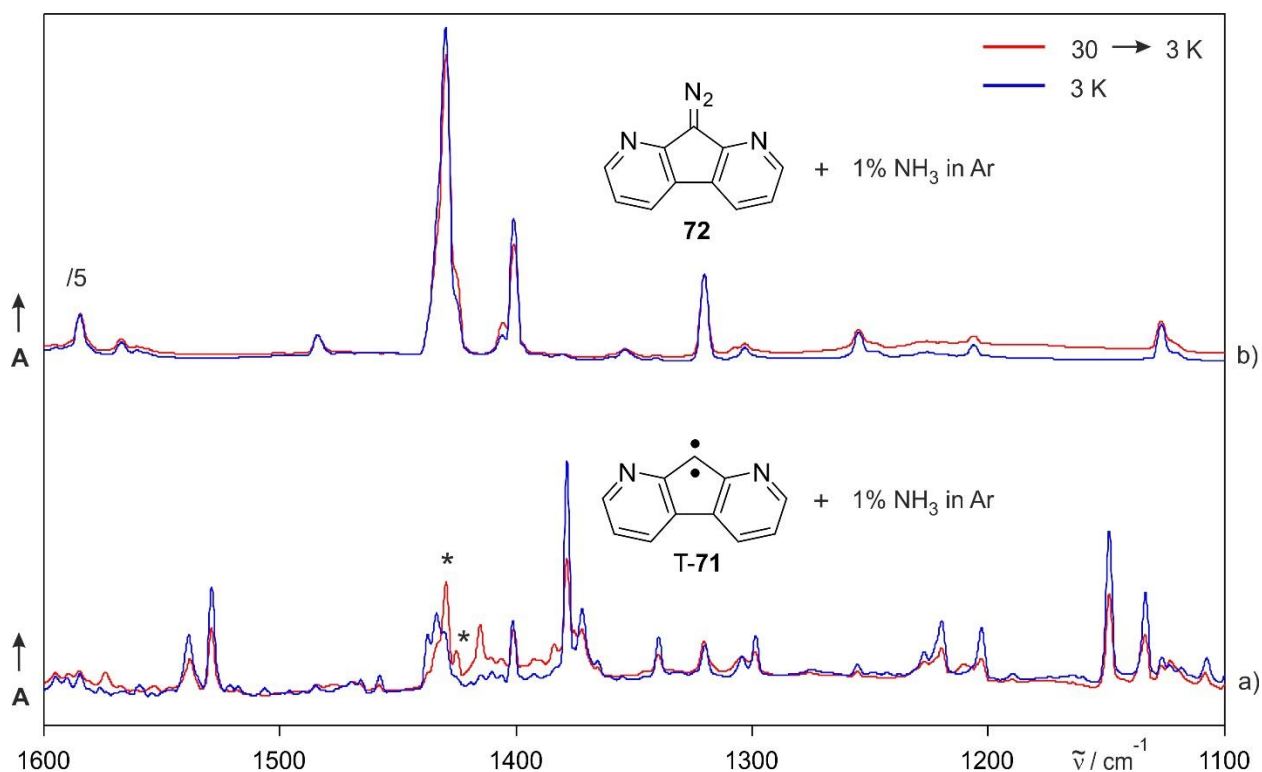


Figure 61. IR spectra showing the reaction products of diazo precursor **72** and NH_3 . a) IR spectra of an argon matrix containing T-71, 1% of NH_3 and remaining **72**, obtained before (blue line) and after (red line) annealing at 30 K. Bands marked with asterisks are tentatively assigned to weak complexes between **72** and NH_3 . b) IR spectra of an argon matrix containing **72** and 1% of NH_3 , obtained before (blue line) and after (red line) annealing at 30 K.

Additional experiments with longer irradiation (~ 50 hrs) were therefore carried out to remove diazo precursor **72** completely. Annealing of such matrices did not afford previously observed IR signals, and hence the signals are assigned to the chemistry between **72** and NH_3 (Figure 62). It should be noted that longer photolysis conditions result in disappearance of the IR bands of **72**, thereby preventing the formation of weak complexes between **72** and NH_3 in annealing experiments (bands marked with dotted lines in Figure 62). The signals of reaction product between T-71 and NH_3 appearing on annealing at 30 K are not altered due to change in the photolysis durations (bands marked with asterisk in Figure 62).

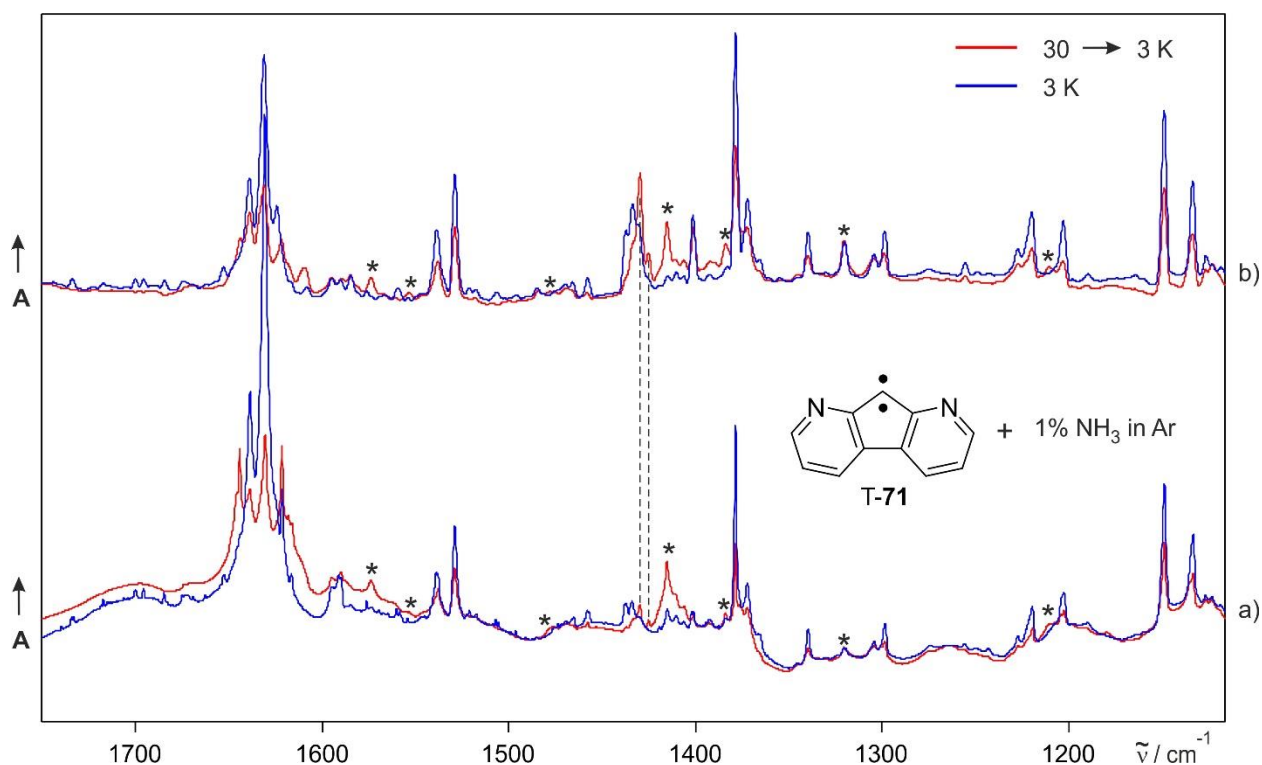


Figure 62. IR spectra showing the effect of photolysis duration on reaction of T-71 and NH₃. a) IR spectra of an argon matrix containing T-71 and 1% of NH₃, obtained upon prolonged 450 nm irradiation for 50 hrs (blue line) and after subsequent annealing (red line) at 30 K. b) IR spectra of an argon matrix containing T-71, 1% of NH₃ and remaining 72, obtained upon 450 nm irradiation for 30 hrs (blue line) and after subsequent annealing (red line) at 30 K. Bands marked with dotted lines assigned to reaction products of diazo precursor 72 and NH₃, almost disappear when 72 is photolyzed for longer duration, whereas bands marked with asterisk are assigned to reaction products of T-71 and NH₃.

Experiments onwards were performed with prolonged photolysis (450 nm, ~ 50 hrs, 3 K) to yield triplet carbene T-71 free of 72. Under these conditions, annealing of an argon matrix doped with 1% of NH₃ containing T-71 at 30 K yields a set of IR signals assigned at 723.8, 787.1, 817.4, 895.6, 1121.9, 1415.1, and 1573.8 cm⁻¹. These bands are assigned to 1,8-diazafluorenylamine 74, a formal N–H insertion product between 71 and NH₃ by comparison with IR spectrum of an authentic matrix-isolated sample of 74 (Figure 63).

When ND₃ was used, annealing at 30 K produced a set of IR bands at 512.2, 729.4, 932.7, 1048.1, 1121.0, 1414.0, 1476.4, and 1586.1 cm⁻¹ assigned to deuterated isotopomer of insertion product [D]-74. An IR spectrum obtained after annealing of argon matrix containing T-71 and 1% of ND₃ correlates well with a calculated spectrum of [D]-74 (Figure 64, Table 29).

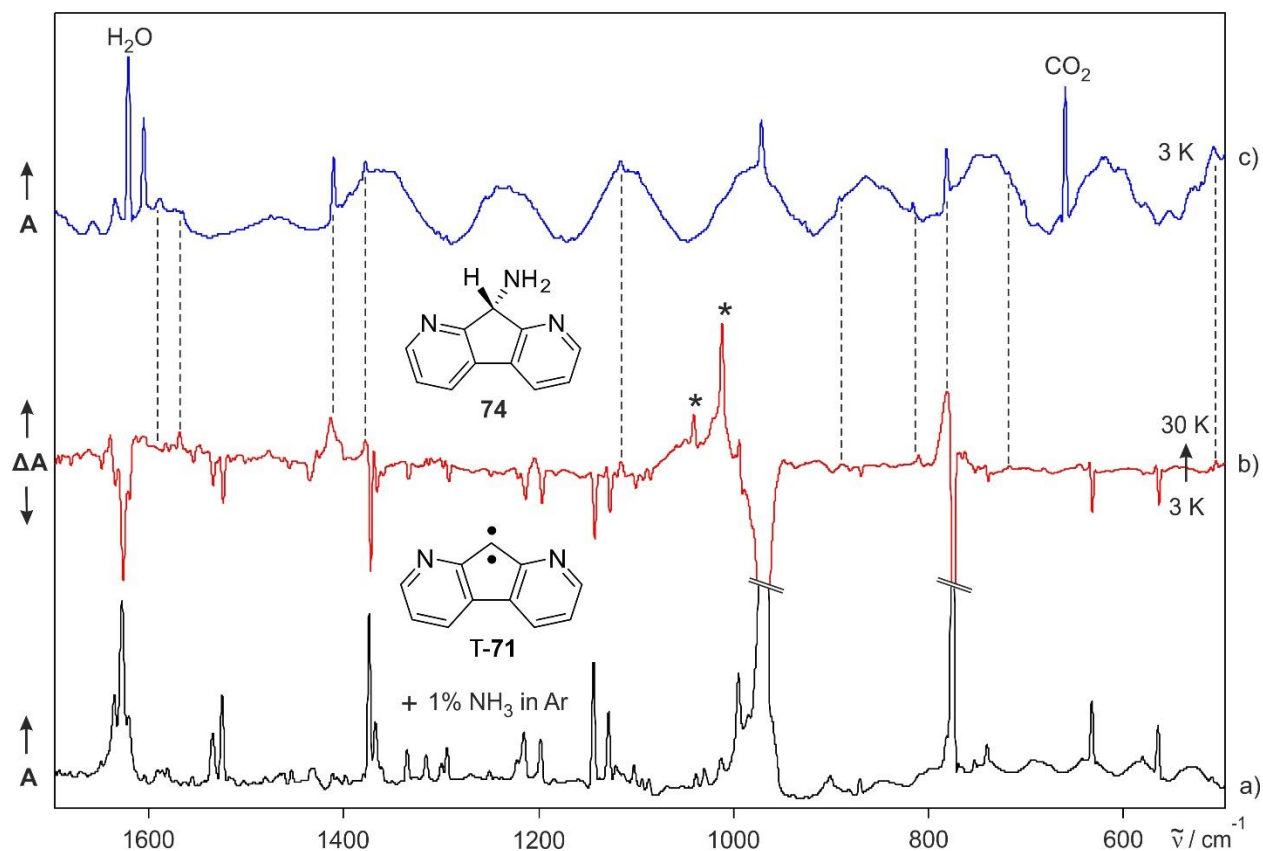


Figure 63. IR spectra showing the reaction between T-71 and NH₃. a) IR spectrum of T-71 in an argon matrix doped with 1% of NH₃ at 3 K. b) Difference IR spectrum of the same matrix showing the changes after annealing at 30 K. Bands pointing downwards assigned to T-71 and NH₃ are disappearing, and bands pointing upwards assigned to 74 and higher aggregates of NH₃ are appearing. Asterisks denote IR bands of NH₃ aggregates.^[228] c) IR spectrum of 74 isolated in an argon matrix at 3 K.

Table 29. IR vibrational frequencies of deuterated 1,8-diazafluorenylamine [D]-74.

Mode	Sym	DFT ^[a]		Argon ^[b]		Assignment
		$\tilde{\nu}/\text{cm}^{-1}$	I _{rel}	$\tilde{\nu}/\text{cm}^{-1}$	I _{rel}	
12	A''	519.3	12	512.2	23	C–C–C bend
19	A'	735.1	33	729.4	29	C–H wagging
27	A'	938.3	19	932.7	27	H ₂ N–C–H bend
35	A'	1089.7	33	1048.1	35	C–NH ₂ str.
38	A''	1156.3	37	1121.0	47	C–H def.
48	A''	1445.1	100	1414.0	100	C–H rocking
50	A''	1510.5	4	1476.4	6	C–H bend
51	A'	1611.6	35	1586.1	41	C=N str.

^[a]Calculated at the B3LYP-D3/def2-TZVP level of theory. ^[b]Argon matrix at 3 K.

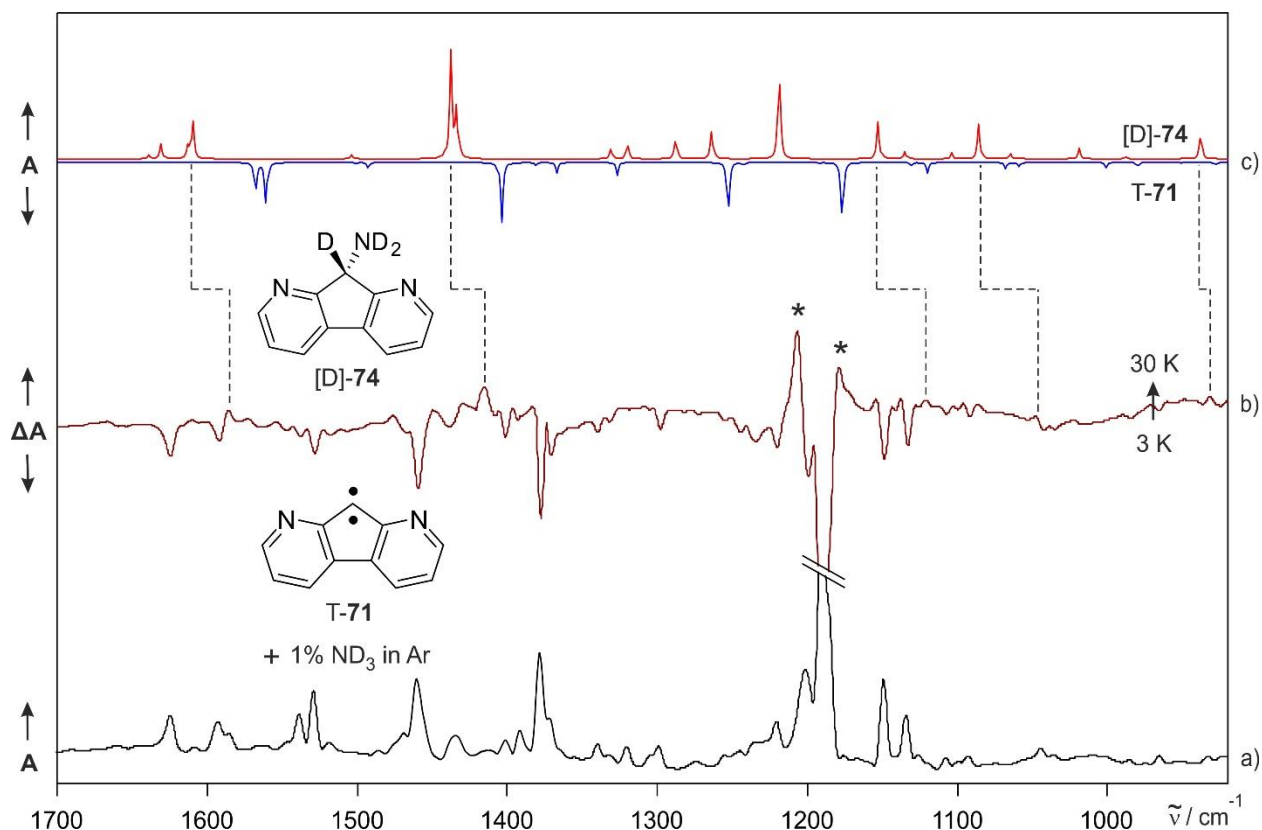


Figure 64. IR spectra showing the reaction between T-71 and ND₃. a) IR spectrum of T-71 in an argon matrix doped with 1% of ND₃ at 3 K. b) Difference IR spectrum of the same matrix showing the changes after annealing at 30 K. Bands pointing downwards assigned to T-71 and ND₃ are disappearing, and bands pointing upwards assigned to [D]-74 are appearing. Asterisks denote IR bands of ND₃ aggregates.^[228] c) Computed IR spectrum of T-71 (multiplied by -1, peaks pointing downwards) and computed IR spectrum of [D]-74 (peaks pointing upwards) at the B3LYP-D3/def2-TZVP level of theory.

The IR absorptions of [D]-74 looked very similar to those of 74 and showed no significant isotopic shifts. For example, the band at 1414.0 cm⁻¹, corresponding to C–H rocking vibration, shows negligible isotopic shift, which is also corroborated by computations (Figure 65).

From the analysis of the product isotope effects, an identical mechanism is expected for the formation of insertion products in NH₃ and ND₃ experiments. The direct insertion route indicates characteristic reaction of singlet carbene in σ² or π² configuration. Otherwise, the possibility of the insertion product arising from the abstraction-recombination route is characteristic of triplet carbene.

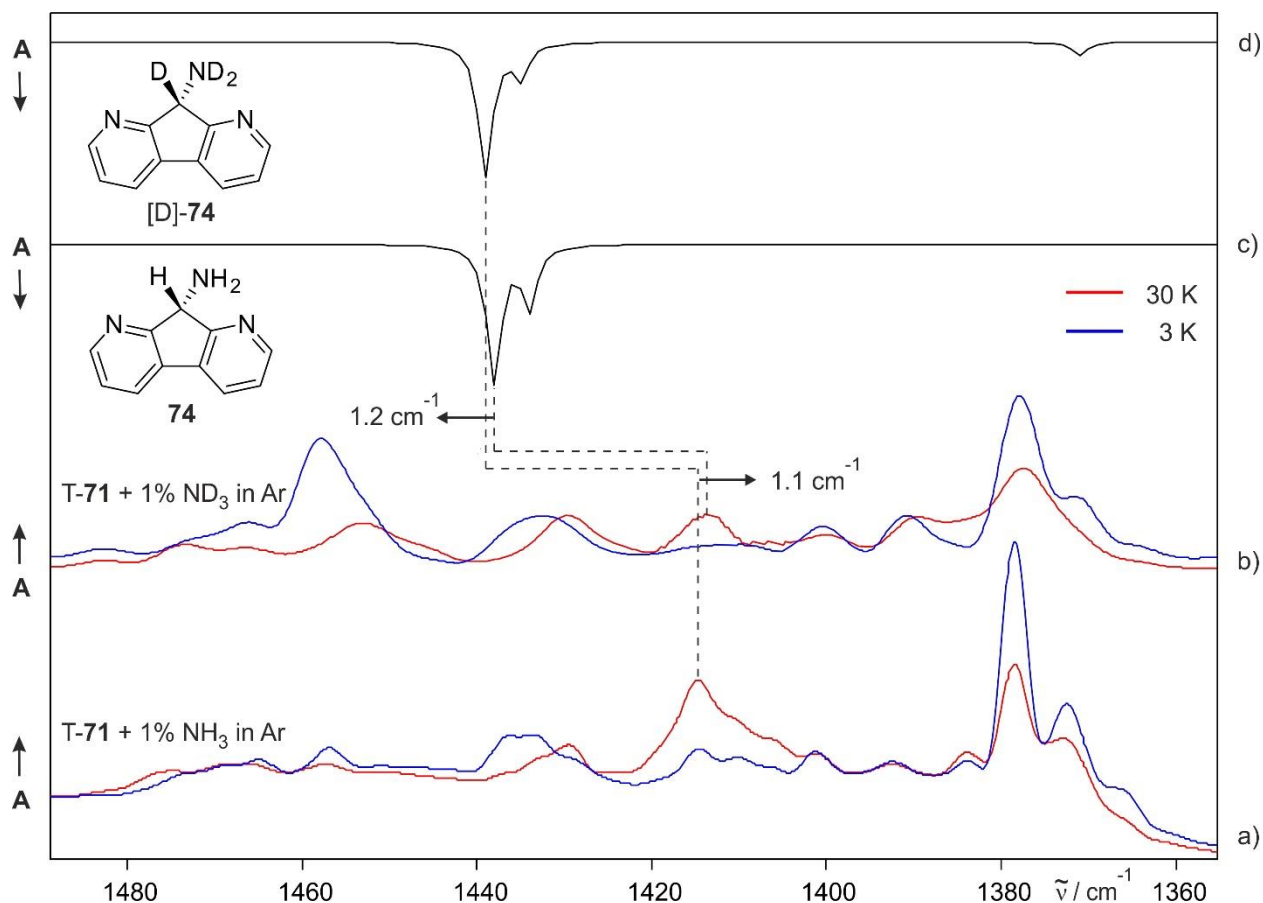


Figure 65. IR spectra showing the isotopic shift of C–H rocking vibrations of insertion product **74** and corresponding isotopomer [D]-**74**. a) IR spectra of an argon matrix containing T-**71** and 1% of NH₃, obtained before (blue line) and after (red line) annealing at 30 K. b) IR spectra of an argon matrix containing T-**71** and 1% of ND₃, obtained before (blue line) and after (red line) annealing at 30 K. c) Computed IR spectrum of [D]-**74** at the B3LYP-D3/def2-TZVP level of theory. d) Computed IR spectrum of **74** at the B3LYP-D3/def2-TZVP level of theory.

EPR experiments. To gain more insight into the mechanism of the N–H insertion reaction, the same type of experiments were performed using EPR spectroscopy. Photolysis with 450 nm of diazo precursor **72** in an argon matrix doped with 1% of NH₃ produces strong signals of T-**71**, weakly intense signals of quintet state radical pair **73** and new signals in the radical region. Annealing of the matrix at 25 K decreases the intensity of the signals of T-**71** attributed to the formation of the EPR silent N–H insertion product **74**, and simultaneously the signals present in the radical region around 3600 G increase in intensity (Figure 66).

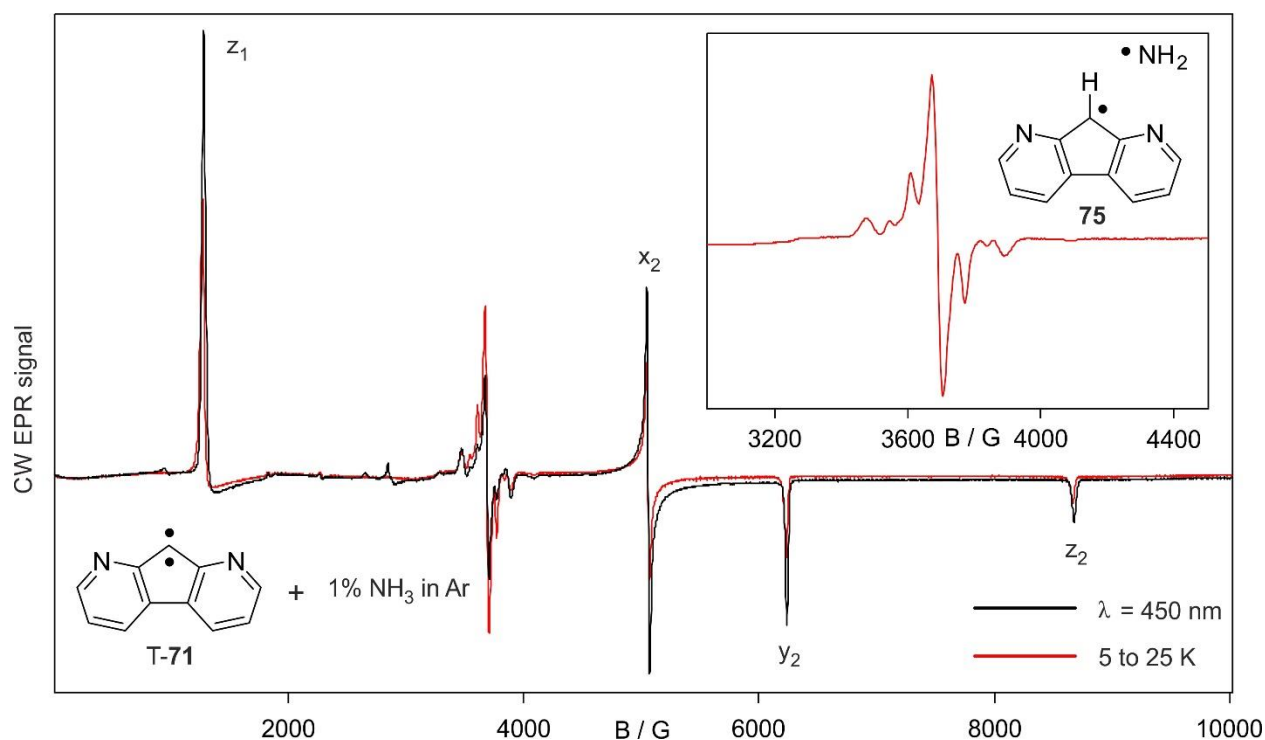


Figure 66. EPR spectra showing the reaction of T-71 with NH₃. Black line: spectrum of T-71 generated upon 450 nm photolysis of diazo precursor **72** in an argon matrix doped with 1% of NH₃ at 5 K. Red line: spectrum of the same matrix showing the changes after annealing at 25 K. The signals of T-71 decrease due to the formation of EPR silent insertion product **74**. The inset shows signals in radical region assigned to triplet radical pair **75** and NH₂ radical (see Figure 67).

The EPR signals of quintet state radical pair **73** which are assigned to an interaction of two adjacent triplet carbenes also disappear upon warming the matrix, probably due to conversion of **73** back to the triplet carbene.^[227] The increase of signals in the radical region upon annealing can be rationalized by the enhanced production of radical pairs **75** from T-71 and NH₃, and their partial conversion to give insertion product **74** via a radical-radical recombination mechanism. The intense radical signals are therefore assigned to radical pair **75**, resulting from abstraction of an ammonia hydrogen atom by triplet carbene T-71. In addition, the radical region exhibits a set of signals corresponding to the NH₂ radical on the basis of its hyperfine splitting and spectra reported in literature (Figure 67).^[229] The broad feature underlying NH₂ radical is tentatively assigned to C₁₁H₇N₂ radical. Experiments performed with ND₃ showed similar reactivity pattern in accordance with IR experiments and different hyperfine splitting due to deuterium atoms (Figure A8).

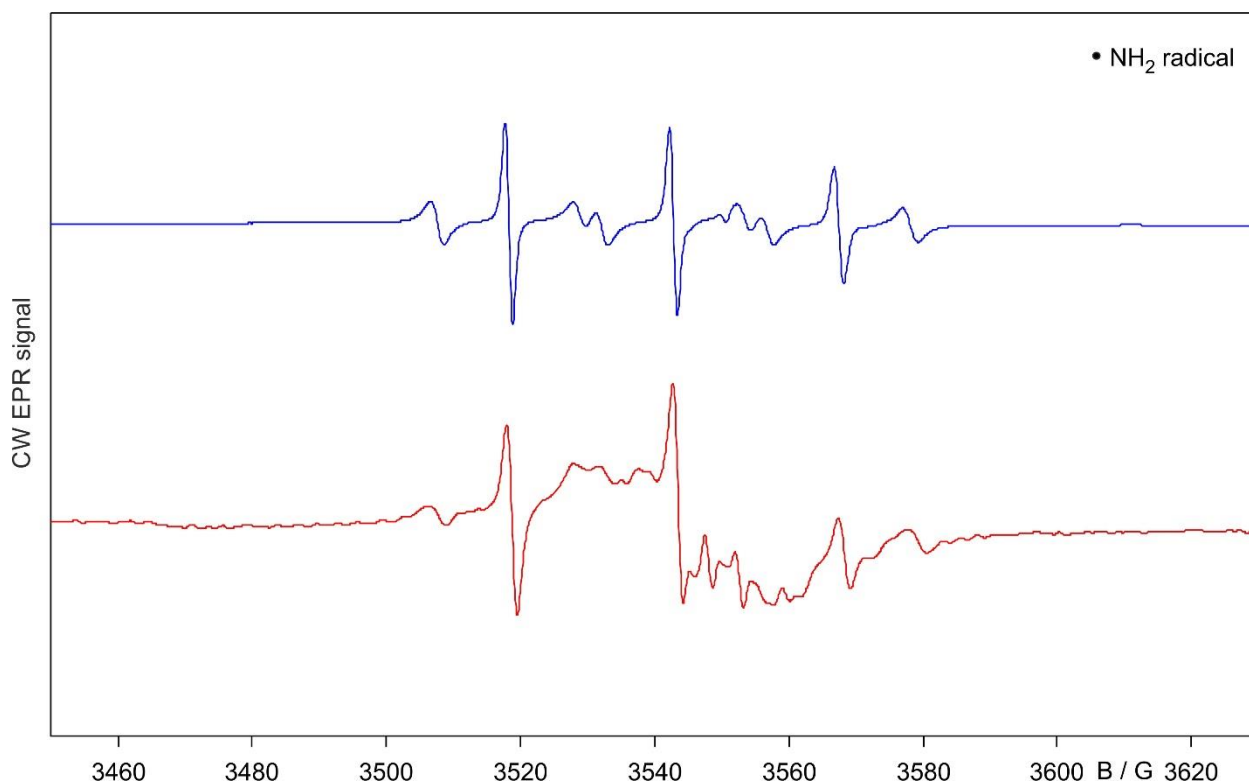


Figure 67. EPR spectra showing the hyperfine splitting of NH_2 radical observed (red line), which matches in reasonably good agreement with previously reported assignment of NH_2 radical (blue line).^[229]

UV-Vis experiments. The reaction between T-71 and NH_3 was also monitored by UV-Vis spectroscopy (Figure 68). Under the reaction conditions similar to the IR and EPR experiments as described above, photolysis of diazo precursor **72** in an argon matrix doped with 1% of NH_3 showed characteristic UV absorptions of T-71 ($\lambda_{\text{max}} = 251, 274, \text{ and } 298 \text{ nm}$) and additional signal at $\lambda_{\text{max}} = 308 \text{ nm}$. Annealing at 30 K results in a decrease of most of the bands assigned to T-71, accompanied by an increase in intensity of the signals at 298 and 308 nm, which are assigned to the formal N–H insertion product **74** by comparison with an UV-Vis spectrum of an authentic matrix-isolated sample. Coincidentally, the signal at 298 nm also corresponds to one of the UV absorptions of T-71; however, the assignment of this signal to **74** is confirmed by the reference spectrum.

Analogous to IR experiments, no significant shifts are observed in the bands assigned to the insertion product between T-71 and NH_3 , and the one obtained when T-71 is allowed to react with ND_3 at 30 K to give the corresponding isotopomer [D]-**74** (Figure A9). It suggests that the carbene center directly interacts with N–H/D bond of ammonia (Scheme 23).

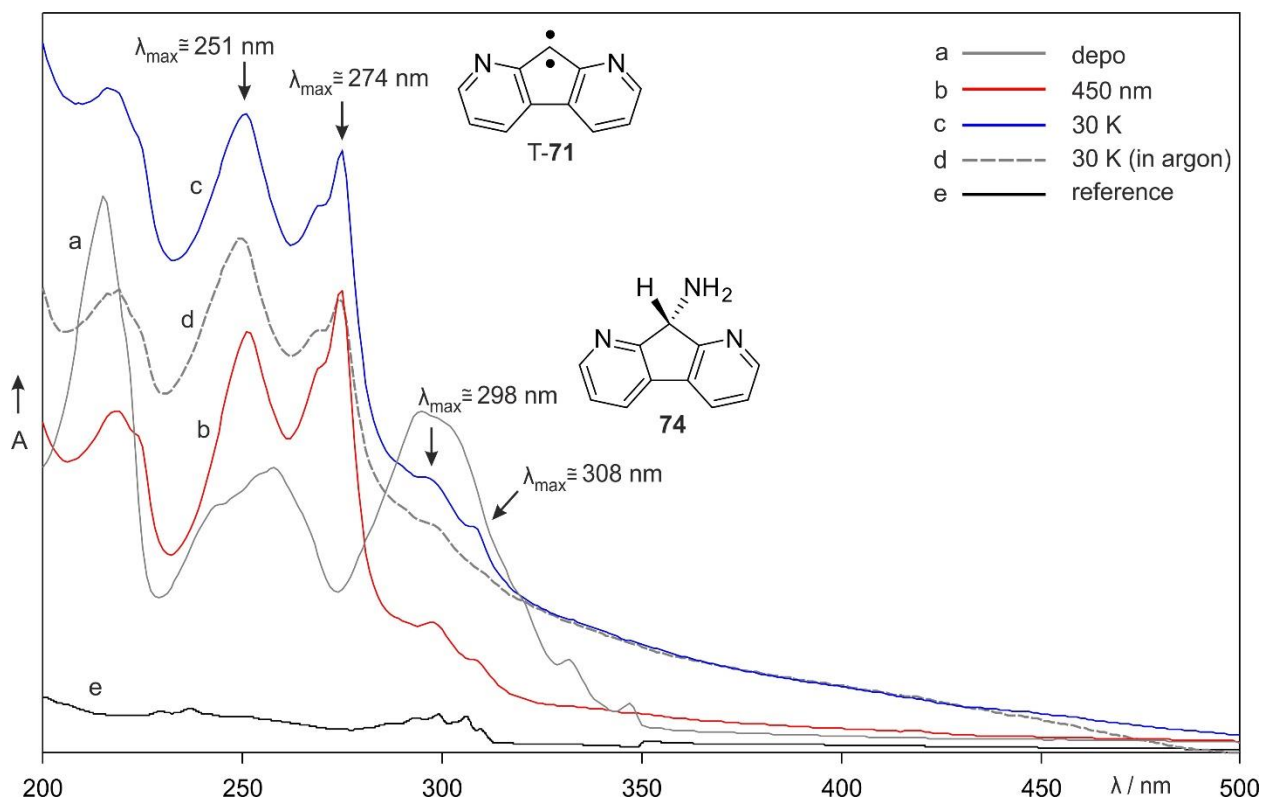
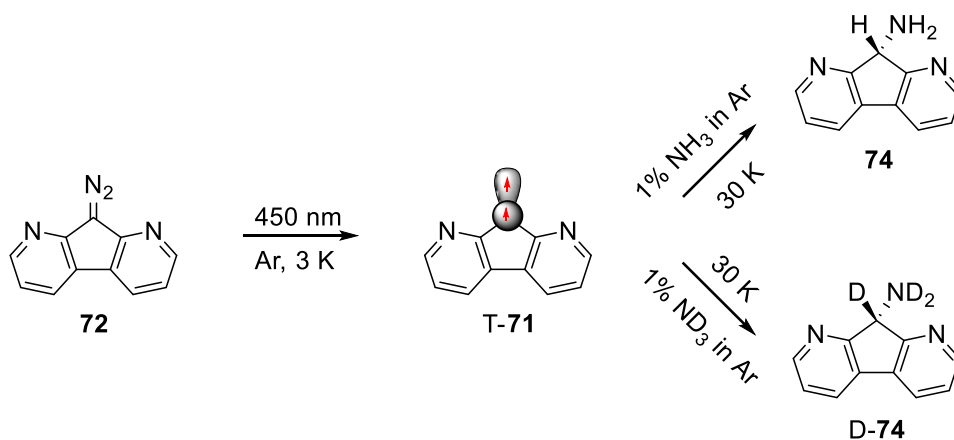


Figure 68. UV-Vis spectra showing the reaction of T-71 with NH₃ (except trace d). a) UV-Vis spectrum of diazo precursor **72** in an argon matrix doped with 1% of NH₃ at 8 K. b) UV-Vis spectrum of T-71 generated upon irradiation of the same matrix with 450 nm. c) UV-Vis spectrum of the same matrix obtained after annealing at 30 K. The bands at $\lambda_{\max} = 298$ and 308 nm are assigned to the formal N-H insertion product **74**. d) UV-Vis spectrum of T-71 in an argon showing the changes after annealing at 30 K. e) UV-Vis spectrum of authentic sample of **74** isolated in an argon matrix at 8 K.



Scheme 23. Reaction of 1,8-diazafluorenylidene **71** with NH₃ and ND₃.

Computations. At the B3LYP-D3/def2-TZVP level of theory, **71** is predicted to have a triplet ground state ($\sigma^1\pi^1$) lying 12.3 kcal mol⁻¹ below the singlet state (σ^2). Interaction of the lone pair electrons of the adjacent nitrogen atoms with two non-bonding electrons in σ -orbital of the singlet state (σ^2) results in a geometry in which the carbene carbon is lifted above the plane by 13°, leading to a non-planar geometry (Figure 69).

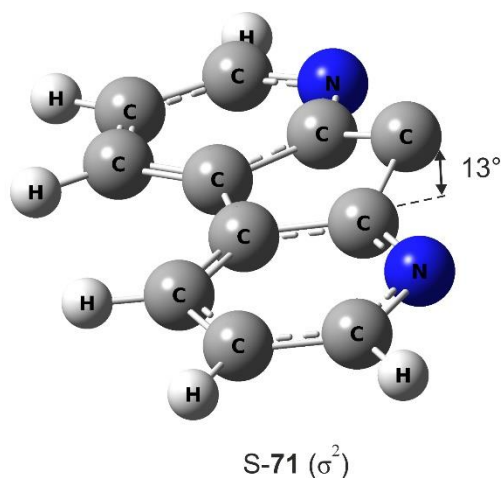


Figure 69. The structure of σ^2 configured singlet state S-**71** showing the non-planar geometry, computed at the B3LYP-D3/def2-TZVP level of theory.

In the π^2 electronic configuration, the singlet state is expected to have a planar configuration due to presence of empty σ -orbital. All attempts to computationally locate the planar π^2 configuration of **71** converged to the σ^2 configured singlet state. Thus, σ^2 configuration is assumed to be the lowest singlet state of carbene **71**.

Direct formation of the insertion product **74** indicates high reactivity of **71** towards ammonia even at temperatures as low as 25 – 30 K. Depending on the electronic configuration of carbene **71**, there are three possible routes for the formation of insertion product **74**: a) Hydrogen bonding interaction with ammonia may switch the spin state of **71** from triplet to singlet to yield the singlet complex in the σ^2 configuration followed by a rapid rearrangement to **74**. b) Similar to triplet carbenes which undergo insertion into C–H bonds,^[37] triplet carbene T-**71** can abstract a hydrogen atom from NH₃ to form triplet radical pair **75** and this radical pair could recombine to give **74**. c) The nitrogen lone pair of ammonia can interact with the highly electrophilic σ -orbital of a π^2 configured singlet carbene S-**71** forming an ylide which in turn rearranges to **74**.

At the B3LYP-D3/def2-TZVP level of theory, both singlet **S-71** (σ^2) and triplet **T-71** are predicted to form weak van der Waals complexes with stabilization energies of ~ 4 kcal mol $^{-1}$ (Figure 70). It is important to note that the triplet complex **T-71** \cdots NH $_3$ is calculated to be thermodynamically more stable than the singlet complex **S-71** \cdots NH $_3$ by 12.5 kcal mol $^{-1}$, which might explain why the chemistry between σ^2 singlet state **S-71** and NH $_3$ was not observed in our experiments.

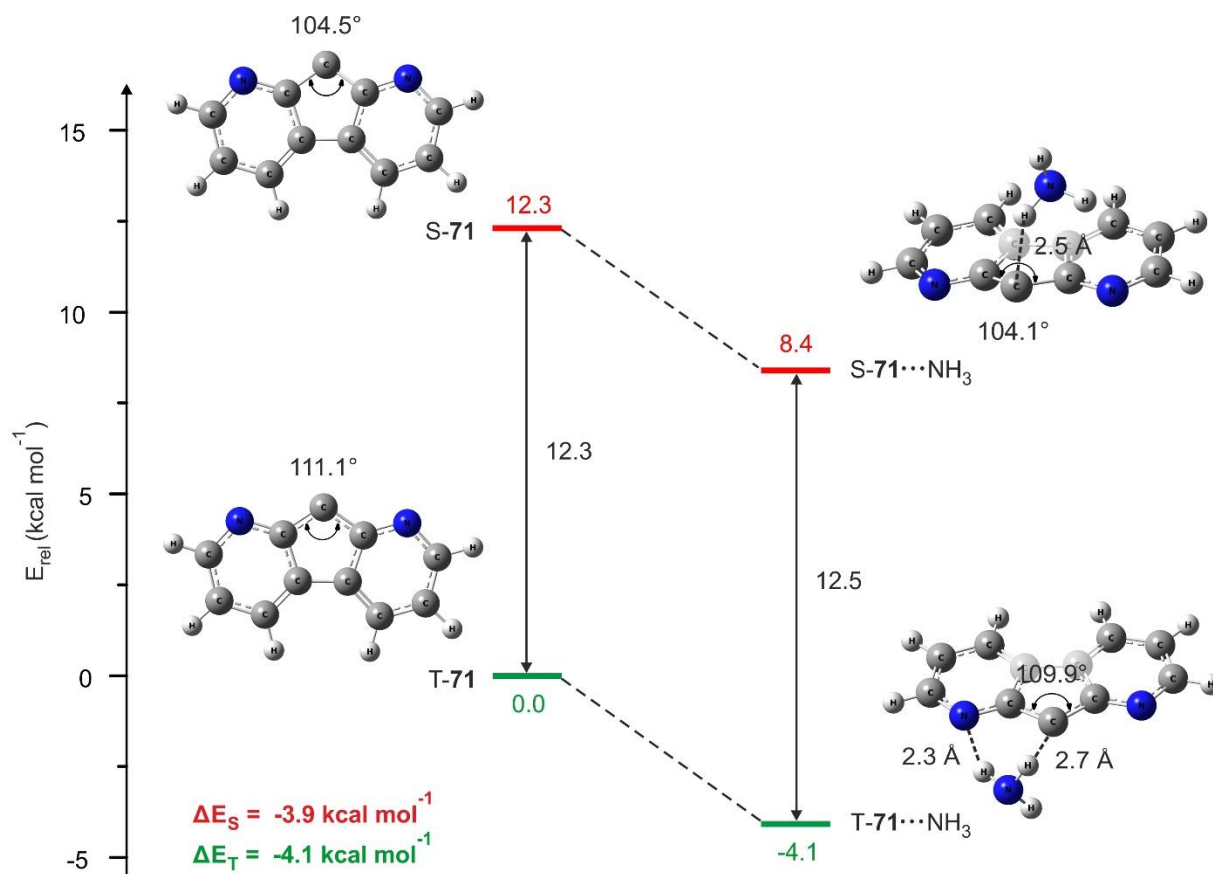


Figure 70. Relative energies of **T-71**, σ^2 configured **S-71**, and their most stable complexes with NH $_3$ computed at the B3LYP-D3/def2TZVP level of theory.

The experimentally observed insertion product **74** should be formed via thermodynamically favorable **T-71** \cdots NH $_3$ complex, even though it is not observed in our experiments (Figure 71). In a first step, abstraction of an ammonia hydrogen by **T-71** is expected to produce triplet radical pair **75** in an exothermic reaction (-10.7 kcal mol $^{-1}$). The activation barrier for hydrogen abstraction is calculated to be 3.1 kcal mol $^{-1}$, which is tentatively high for a reaction to occur at 30 K, indicating that the quantum mechanical tunneling (QMT) might contribute to the NH $_3$ activation by **T-71**. A second step involves intersystem crossing of **75** to the singlet surface, where radical recombination

is considered to be barrierless and highly exothermic by $-68.8 \text{ kcal mol}^{-1}$. The triplet reaction mechanism seems to be the most probable on the basis of finding from the IR, EPR experiments and the calculations.

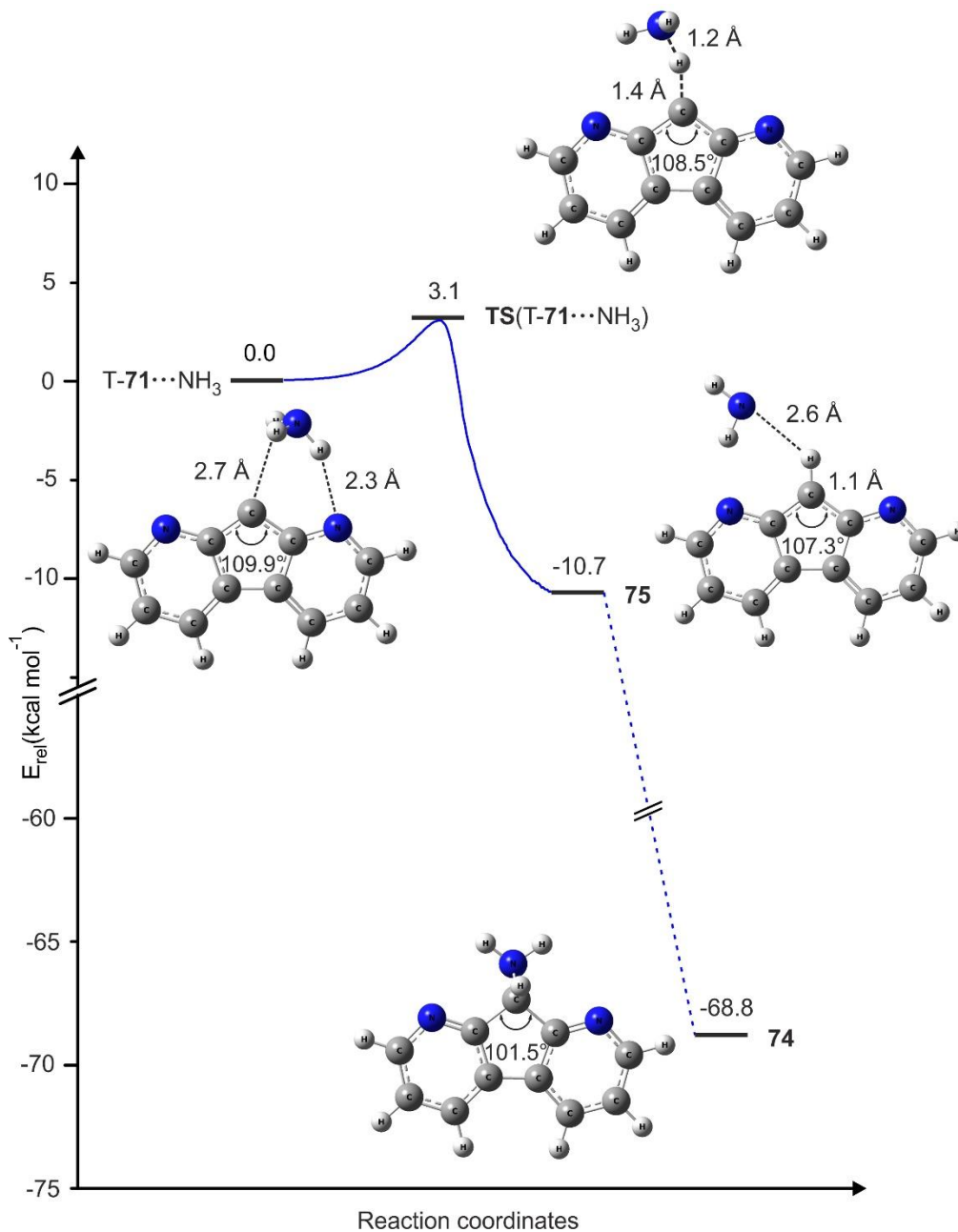


Figure 71. Potential energy surface showing the reaction of T-71 with NH₃ calculated at the B3LYP-D3/def2-TZVP level of theory. The geometries of weak triplet carbene complex T-71...NH₃, transition state TS(T-71...NH₃), triplet radical pair 75 and insertion product 74 are obtained from intrinsic reaction coordinate (IRC) calculation.

In the same manner, the formation of the deuterated insertion product [D]-74 via deuterium tunneling can be rationalized by IRC calculations (Figure 72) and it is also deduced from IR, UV-Vis and EPR experiments.

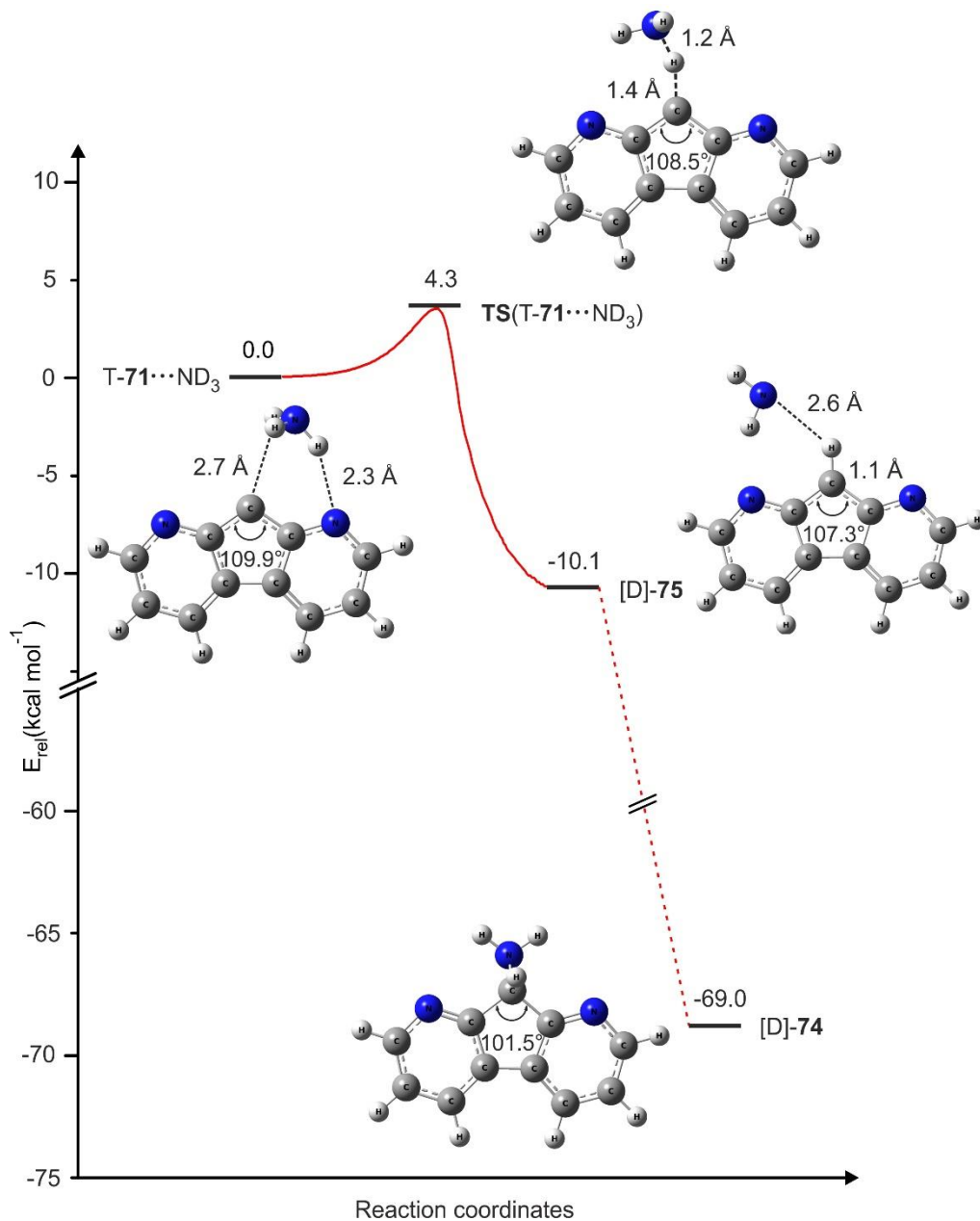


Figure 72. Potential energy surface showing the reaction of T-71 with ND₃ calculated at the B3LYP-D3/def2-TZVP level of theory. The geometries of weak triplet carbene complex T-71...ND₃, transition state TS(T-71...ND₃), triplet radical pair [D]-75 and insertion product [D]-74 are obtained from intrinsic reaction coordinate (IRC) calculation.

The participation of the singlet carbene in the π^2 electronic configuration is not expected, since carbene **71** has a triplet ground state using IR, UV-Vis and EPR spectroscopy. However, the possible route of ylide formation via the π^2 configured singlet carbene, followed by its rearrangement to insertion product **74** cannot be ignored and needs further investigation.

Conclusions

The reaction of 1,8-diazafluorenylidene **71** with ammonia demonstrated triplet ground state reactivity of the carbene. Triplet carbene T-**71** directly forms a formal N–H/D insertion product **74/D-74** on interaction with ammonia. The absence of kinetic isotopic effect indicates that the carbene center directly interacts with N–H/D bond of ammonia. Despite of considerable activation barrier for ammonia H/D abstraction by T-**71**, the reaction proceeds via QMT to produce triplet radical pair **75/D-75** as revealed by the radical signals in EPR experiments. The radical pair recombines at 25–30 K to form a formal N–H/D insertion product **74/D-74**, which is experimentally identified by comparison of its IR and UV-Vis spectra with that of an authentic matrix-isolated sample and DFT calculations. Upon complexation with ammonia, σ^2 configured singlet state was not observed experimentally. This is rationalized by a large singlet-triplet gap of **71**, which does not allow to stabilize σ^2 singlet state below the triplet state on complexation with ammonia. This is probably the first study of N–H/D activation by a triplet carbene observed at cryogenic temperatures of 25–30 K, which clearly highlights the unusual reactivity of 1,8-diazafluorenylidene **71**.

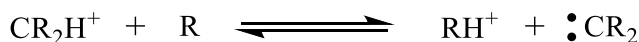
7. Proton Affinity Bracketing of 2,7-dinitrofluorenylidene

This project was carried out during Graduate School of Solvation internship in the group of Prof. Dr. Jeehiun K. Lee (Rutgers University, USA).

7.1. Introduction

The search for strongly basic compounds is an active field of chemical research. This can be supported by computational studies aiming to provide direction in synthesis of superbases where the molecular structure is designed to enhance the proton affinity (PA) of the compound.^[230-231] Few examples of a successful synergistic approach where experimental and theoretical methods were employed to synthesize strongly basic compounds, termed as ‘proton sponge’, have been reported by the groups of Sundermeyer and Maksic.^[232-233] Due to presence of lone pair, carbenes are considered as strong bases, possessing an even higher basicity than amines and imines. However, carbenes did not play an important role in acid-base chemistry until discovery of stable nucleophilic *N*-heterocyclic carbene (NHC) by Arduengo in 1991.^[234] NHCs became the focus of intensive investigations because transition metal complexes with NHC ligands are versatile catalysts for a variety of reactions.^[235-237] More basic carbenes should be more effective ligands^[238] and it is therefore of interest to determine the basicity of carbenes in terms of proton affinity.

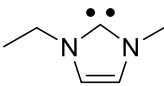
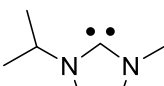
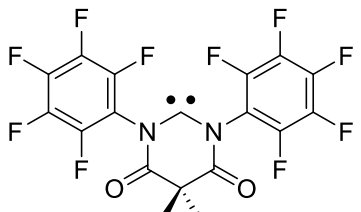
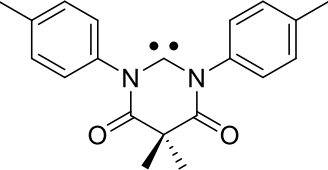
Several strategies have been developed to measure PAs of carbenes in solution phase, which mainly involve monitoring the exchange of isotopes in water^[239-242] or the reaction of the free carbene with hydrocarbon indicators in THF or DMSO,^[243-245] however, the resultant PAs are highly solvent dependent. The PAs are intrinsic to the chemical entity and can be measured in gas phase in which any interference of solution effects can be excluded. The gas phase PA of carbene is obtained experimentally by investigating the proton transfer equilibria between carbene :CR_2 and reference bases R_i whose PA have been established.

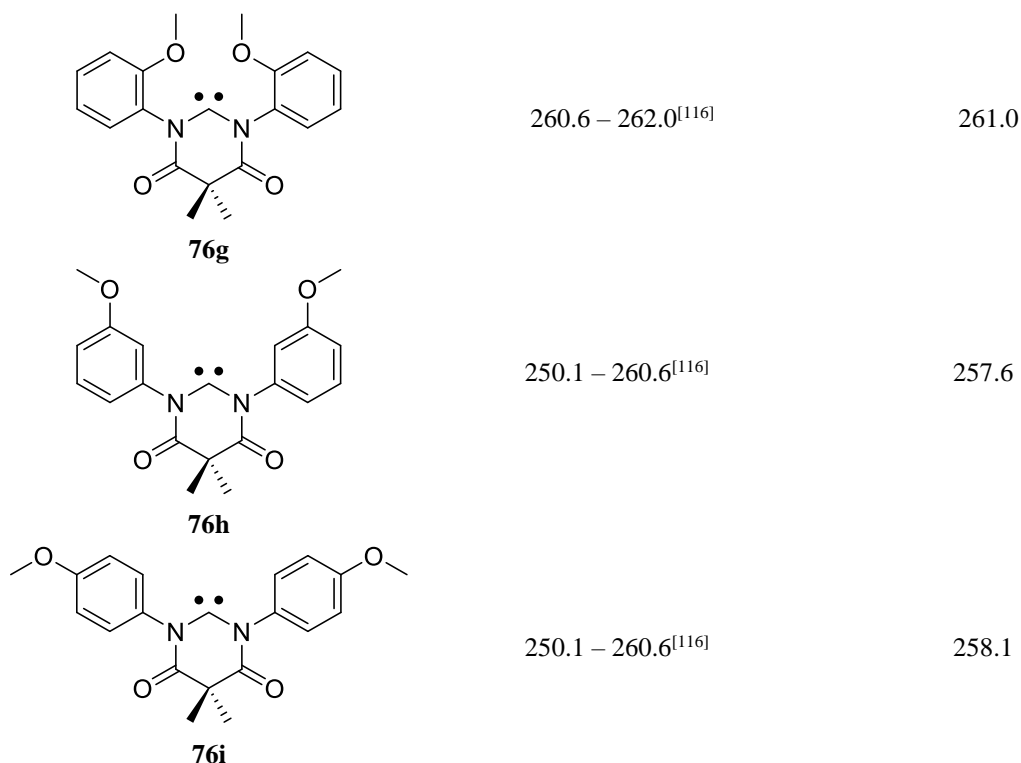


The ratio of the ions CR_2H^+ and RH^+ can be measured using ion cyclotron resonance (ICR) or house modified liquid chromatography quadrupole ion trap (LCQ) mass spectrometer.^[246-248] The upper and lower bounds of PA can be estimated through a technique known as bracketing. If proton transfer occurs from CR_2H^+ to R_1 , but does not occur from CR_2H^+ to R_2 , then PA of the carbene

:CR_2 is taken to be between the PAs of R_1 and R_2 . Previous PA measurements using bracketing technique were limited to very few carbenes such as difluorocarbene ($172 \pm 2 \text{ kcal mol}^{-1}$)^[249] and dichlorocarbene ($208 \pm 2 \text{ kcal mol}^{-1}$).^[250-251] Recently, Lee et al. bracketed PAs of a series of *N*-heterocyclic carbenes **76a-i**, which were found to be consistent with theoretical calculations (Table 30).^[116, 248, 252]

Table 30. Experimentally bracketed and computational gas phase proton affinities (PAs) of carbenes **76a-i** at 298 K.

Carbenes	PAs in kcal mol^{-1}	
	Experiment	B3LYP/6-31+G(d) calculations ^[116] for closed-shell singlet states
 76a	257.4 – 260.6 ^[248]	259.9
 76b	254.0 – 260.6 ^[248]	261.4
 76c	262.0 – 263.8 ^[116]	262.9
 76d	> 263.8 ^[116]	265.6
 76e	232.1 – 234.7 ^[116]	233.0
 76f	247.4 – 260.6 ^[116]	256.3



As discussed in chapter 3, the closed-shell singlet states of arylcarbenes **7**, **8** and **25** are estimated to have PAs > 270 kcal mol⁻¹. However, reference bases with PAs higher than 264 kcal mol⁻¹ are not feasible to implement in bracketing experiments due to their non-volatility. Arylcarbenes **7**, **8** and **25** with electron withdrawing substituents (-CF₃, -NO₂, -F) should be less basic relative to parent systems and the PAs of such substituted arylcarbenes can be adjusted within the range of PAs of the reference bases. Considering the experimental limitations, arylcarbenes **77-82** are maneuvered for bracketing experiments in the present work whose PAs in the singlet states are predicted to be lower than 264 kcal mol⁻¹ (Chart 13).

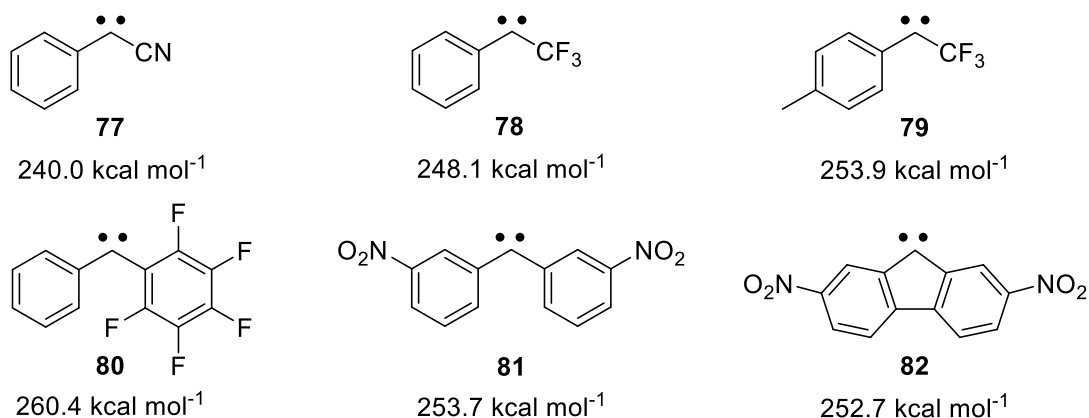


Chart 13. Computed PAs of selected arylcarbenes **77-82** in the singlet states at the B3LYP/6-31+G(d) level of theory.

7.2. Results and Discussion

The gas phase reactions of previously utilized reference bases^[248, 252] with cationic carbene precursors of **77-82** were carried out using LCQ-MS to bracket the PAs of the corresponding carbenes. Electrospray ionization of the formally hydrated products of **80-82** dissolved in fluoroboric acid were found to yield (**80-82**)H⁺ as the major signals, whereas remaining hydrated products of **77-79** could not afford signals of corresponding cationic carbenes under the similar conditions probably due to the instabilities of the cations. On the other hand, the reactions of **80** or **81** with reference bases resulted in the formation of ions with mass-to-charge ratios corresponding to clusters of **80H**⁺ or **81H**⁺ and the reference base. The proton transfer cannot be ascertained when such complexation occurs. The cation **82H**⁺ exhibited better yield and did not show considerable cluster formation, which led us to investigate the proton affinity of 2,7-dinitrofluorenylidene **82**.

According to DFT calculations at the B3LYP/6-31+G(d) level of theory, 2,7-dinitrofluorenylidene **82** is calculated to have PA of 252.7 kcal mol⁻¹ in its singlet state and 245.2 kcal mol⁻¹ in its ground triplet state. Five neutral reference bases with PAs close to calculated PA of **82** were chosen and allowed to react with **82H**⁺ for 0.03 – 1000 ms to assess the proton transfer reactions.

7.2.1. Reaction with *N,N,N',N'*-tetramethyl-1,3-propanediamine

Prior and after investigating the reaction of **82H**⁺ with *N,N,N',N'*-tetramethyl-1,3-propanediamine **83**, concentration of **83** (PA = 247.4 kcal mol⁻¹) was determined in terms of $P_{neutral}$ by control reaction where a weak protonated base reacts with **83**. *N,N*-dimethylcyclohexylamine **84** (PA = 235.1 kcal mol⁻¹) has lower PA than that of **83**, and hence was chosen as weak base. Since **83** is more basic than **84**, it was assumed that the reaction proceeds at the theoretical collision rate constant k'_{coll} ,^[253-254] which is obtained from the Average Dipole Orientation (ADO) method based on the dipole moment, polarizability, mass of neutral base and the mass of the protonated species (Eq. 9).

$$k'_{coll} = (2\pi q/\mu^{1/2})[\alpha^{1/2} + C\mu_D(2/\pi kT)^{1/2}] \quad (9)$$

Where μ_D is the dipole moment of the neutral reference base, μ is the reduced mass of protonated species, q is the charge of the ion, C is the dipole locking constant, and α is the polarizability of the neutral base.

By plotting the disappearance of protonated weak base **84H⁺** (m/z 128) vs. reaction time, $P_{neutral}$ was achieved (Eq. 10) by calculating the $slope'$ (Figure 73, Table 31).

$$P_{neutral} = -slope' / (k'_{coll} \times \phi) \quad (10)$$

Where ϕ is the conversion factor of 3.239×10^{16} molecules.cm⁻³.torr⁻¹.

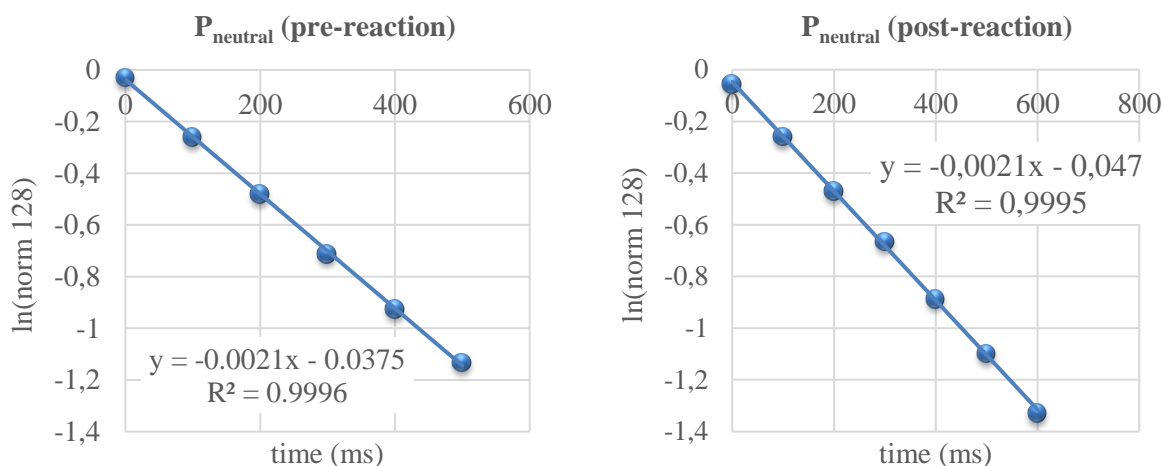


Figure 73. Plots showing the reaction of **84H⁺** (m/z 128) with **83** at different reaction times performed before and after the reaction of **82H⁺** and **83**. The decay of **84H⁺** indicates proton transfer from **84H⁺** to **83**. The resultant slopes are used to calculate concentration of **83** ($P_{neutral}$) using equation 10.

Table 31. Parameters used for the determination of $P_{neutral}$ of **83**. μ_D and α are the dipole moment and polarizability used for the calculation of theoretical collision rate constant k'_{coll} . ϕ is the conversion factor in molecules.cm³.torr⁻¹.

μ_D of 83	α of 83	$slope'$ (before)	$slope'$ (after)	k'_{coll} (84H⁺+83)	ϕ	$P_{neutral}$ of 83 (before)	$P_{neutral}$ of 83 (after)	$P_{neutral}$ of 83 (average)
0.7126	16.71	-2.1	-2.1	1.304E-09	3.239E+16	4.97E-08	4.97E-08	4.97E-08

When **82H⁺** was treated with reference base **83**, the relative intensity of **83H⁺** (m/z 131) increased with an increase in reaction time suggesting a proton transfer reaction from **82H⁺** to **83** (Figure 74, Scheme 24). Assuming pseudo-first order reaction, the rate of the reaction k_{exp} is estimated (Eq. 11) by monitoring the change in the concentration of **82H⁺** with respect to time ($slope$, Figure 75, Table 32) at given concentration of reference base **83** ($P_{neutral}$).

$$k_{exp} = -slope / (P_{neutral} \times \phi) \quad (11)$$

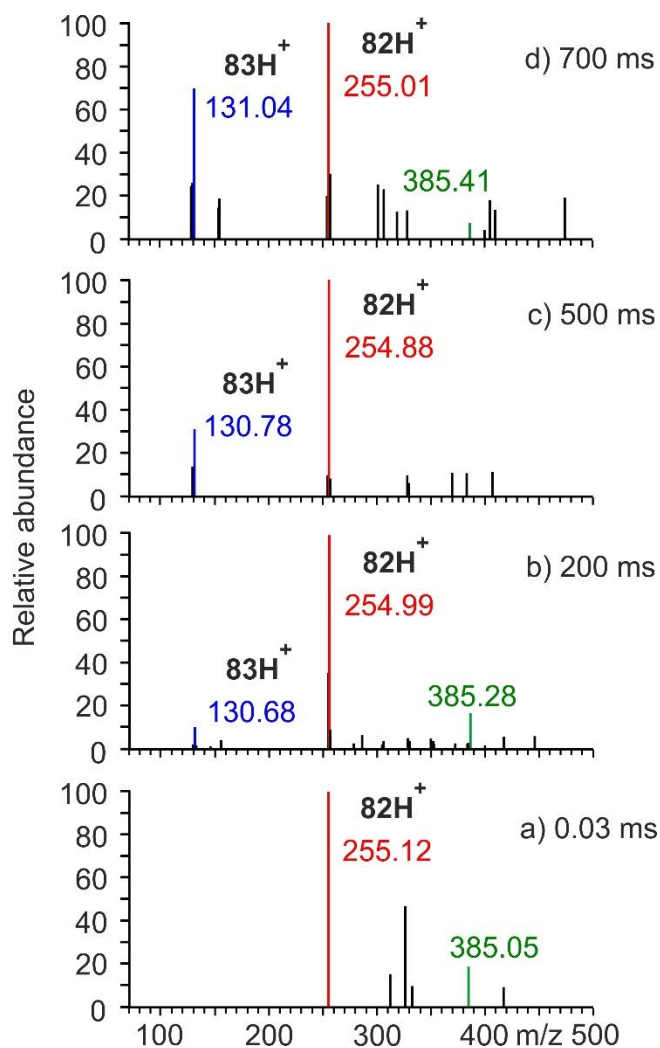
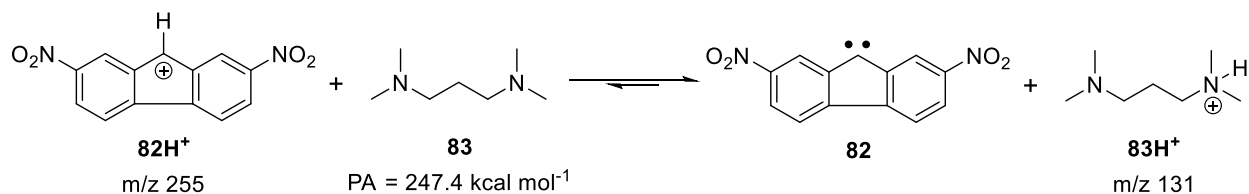


Figure 74. Kinetics of the reaction of 2,7-dinitrofluorenyl cation 82H^+ (m/z 255 – red bands) with N,N,N',N' -tetramethyl-1,3-propanediamine **83** at different reaction times a) 0.03, b) 200, c) 500, and d) 700 ms, showing the increase in relative intensity of 83H^+ (m/z 131 – blue bands) with time. Cluster formed between 82H^+ and **83** (or 83H^+ and **82**) is indicated by green bands (m/z 385). The remaining bands belonging to fragmentation ionic products are not assigned to highlight the reaction between 82H^+ and **83**.



Scheme 24. Reaction of 2,7-dinitrofluorenyl cation 82H^+ with N,N,N',N' -tetramethyl-1,3-propanediamine **83**.

To assess the occurrence or non-occurrence of the proton transfer reaction, reaction efficiency is calculated by Eq. 12.

$$efficiency = (k_{exp}/k_{coll}) \times 100\% \quad (12)$$

The cutoff is set to be 10%, meaning if the efficiency is higher than 10%, proton transfer occurs, otherwise it is assumed that there is no proton transfer reaction.^[246-247] The theoretical collision rate constant (k_{coll}) between $\mathbf{82H}^+$ and $\mathbf{83}$ is calculated by ADO method using Eq. 9. Based on the resultant values of k_{exp} and k_{coll} , $\mathbf{82H}^+$ shows the proton transfer to $\mathbf{83}$ with transfer efficiency of ~ 44% indicating lower PA of carbene $\mathbf{82}$ than reference base $\mathbf{83}$.

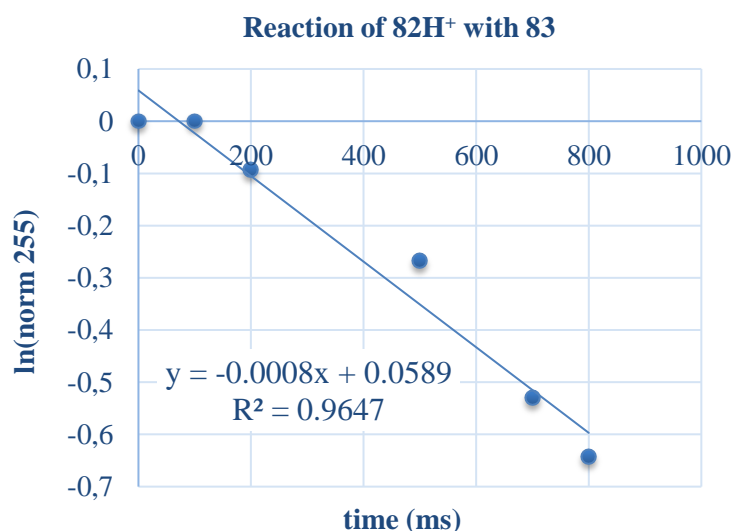


Figure 75. Plots showing the reaction of $\mathbf{82H}^+$ (m/z 255) with $\mathbf{83}$ at different reaction times. The decay of $\mathbf{82H}^+$ indicates proton transfer from $\mathbf{82H}^+$ to $\mathbf{83}$. The resultant slope is used to calculate rate of proton transfer reaction k_{coll} using equation 11.

Table 32. Experimental rate constant (K_{exp}) and the reaction efficiency of proton transfer reaction between $\mathbf{82H}^+$ and $\mathbf{83}$ derived from *slope*, concentration of $\mathbf{83}$ ($P_{neutral}$) and theoretical collision rate constant (k_{coll}). μ_D and α are the dipole moment and polarizability used for the calculation of k_{coll} . \emptyset is the conversion factor in molecules.cm³.torr⁻¹

μ_D of $\mathbf{83}$	α of $\mathbf{83}$	$P_{neutral}$ of $\mathbf{83}$ (average)	\emptyset	<i>slope</i>	k_{coll} ($\mathbf{82H}^+ + \mathbf{83}$)	K_{exp} ($\mathbf{82H}^+ + \mathbf{83}$)	<i>efficiency</i>
0.7126	16.71	4.97E-08	3.239E+16	-0.8	1.13E-09	4.97E-10	43.96%

7.2.2. Reaction of with N,N,N',N' -tetramethylethylenediamine

Since PA of carbene **82** is determined to be lower than $247.4 \text{ kcal mol}^{-1}$, further experiments were carried out in a similar manner using N,N,N',N' -tetramethylethylenediamine **85** as a reference base which has PA of $242.1 \text{ kcal mol}^{-1}$. The concentration of **85** was evaluated from control reaction between weak protonated base $\mathbf{84H}^+$ and **85** before and after the reaction of $\mathbf{82H}^+$ with **85** (Figure 76, Table 33).

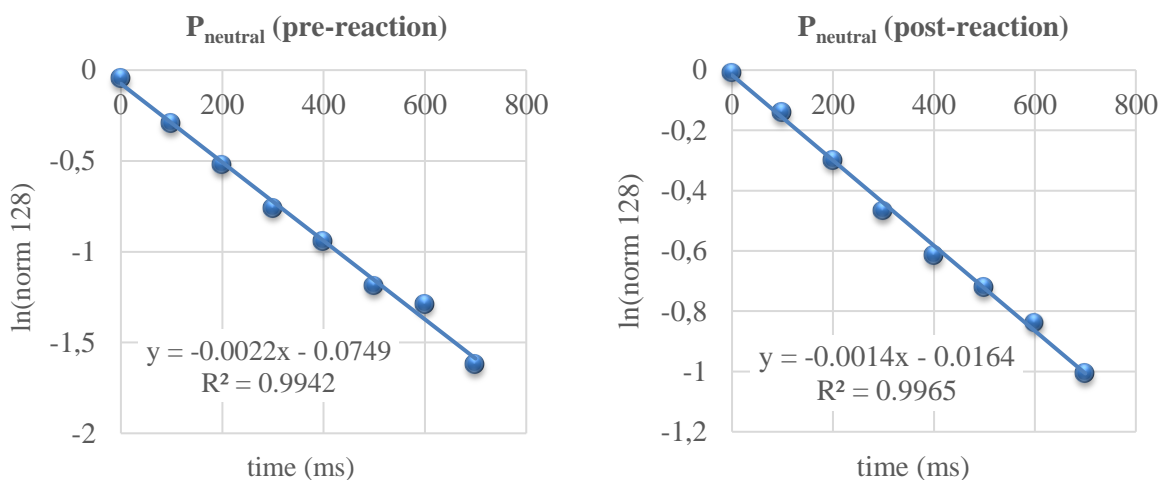


Figure 76. Plots showing the reaction of $\mathbf{84H}^+$ (m/z 128) with **85** at different reaction times performed before and after the reaction of $\mathbf{82H}^+$ and **85**. The decay of $\mathbf{84H}^+$ indicates proton transfer from $\mathbf{84H}^+$ to **85**. The resultant slopes are used to calculate concentration of **85** ($P_{neutral}$) using equation 10.

Table 33. Parameters used for the determination of $P_{neutral}$ of **85**. μ_D and α are the dipole moment and polarizability used for the calculation of theoretical collision rate constant k'_{coll} . \emptyset is the conversion factor in $\text{molecules.cm}^3.\text{torr}^{-1}$

μ_D of 85	α of 85	$slope'$ (before)	$slope'$ (after)	k'_{coll} ($\mathbf{84H}^+ + \mathbf{85}$)	\emptyset	$P_{neutral}$ of 85 (before)	$P_{neutral}$ of 85 (after)	$P_{neutral}$ of 85 (average)
0	14.86	-2.2	-1.4	1.16E-09	3.239E+16	5.86E-08	3.73E-08	4.81E-08

The reaction of $\mathbf{82H}^+$ with **85** resulted in an increase of relative intensity of the protonated base $\mathbf{85H}^+$ (m/z 117) with increase in reaction time (Figure 77, Scheme 25), suggesting proton transfer from $\mathbf{82H}^+$ to **85**. The kinetic data obtained from this reaction was employed to determine the rate of the reaction in the same manner as described for the reaction between $\mathbf{82H}^+$ with **83** (Figure 78, Table 34). The efficiency of the proton transfer reaction in this case is determined to be $\sim 38\%$, indicating $\text{PA of carbene } \mathbf{82} < \text{PA of } \mathbf{85}$ ($242.1 \text{ kcal mol}^{-1}$).

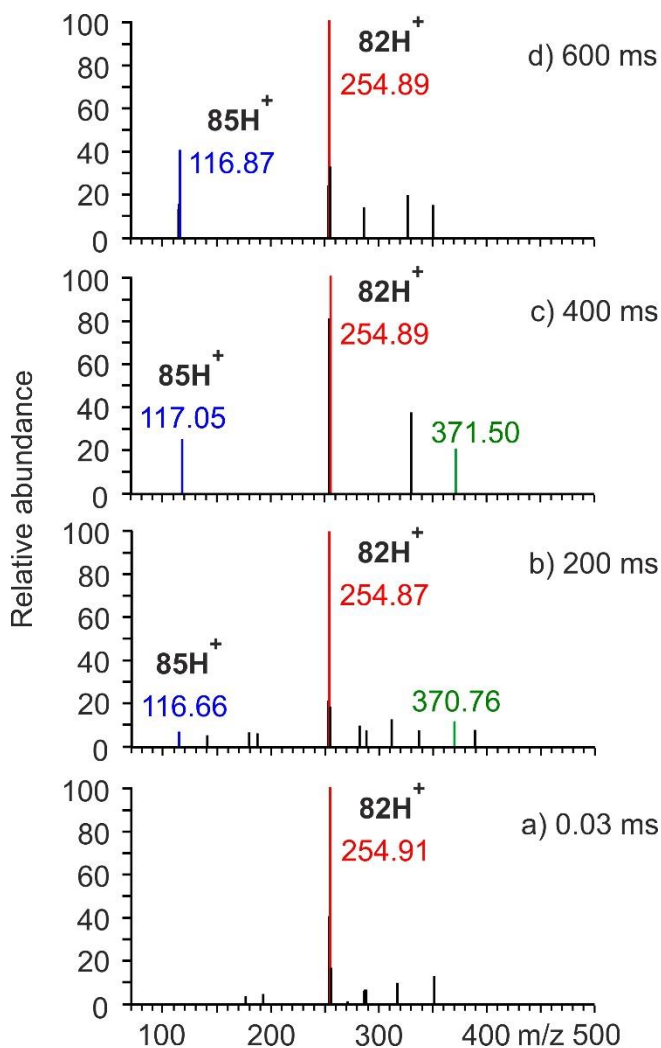
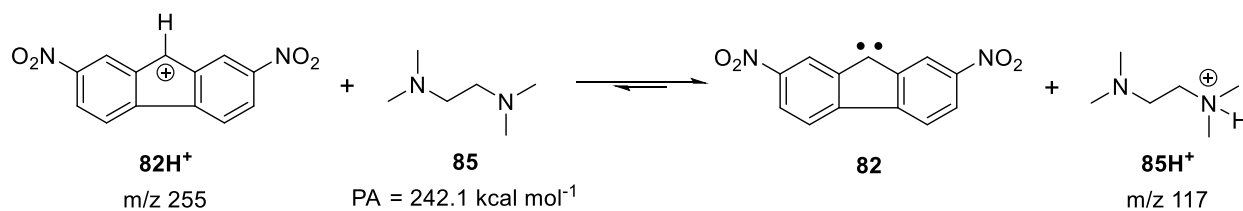


Figure 77. Kinetics of the reaction of 2,7-dinitrofluorenyl cation 82H^+ (m/z 255 – red bands) with N,N,N',N' -tetramethylethylenediamine **85** at different reaction times a) 0.03, b) 200, c) 400, and d) 600 ms, showing an increase in relative intensity of 85H^+ (m/z 117 – blue bands) with time. Cluster formed between 82H^+ and **85** (or 85H^+ and **82**) is indicated by green bands (m/z 371). The remaining bands belonging to fragmentation ionic products are not assigned to highlight the reaction between 82H^+ and **85**.



Scheme 25. Reaction of 2,7-dinitrofluorenyl cation 82H^+ with N,N,N',N' -tetramethylethylenediamine **85**.

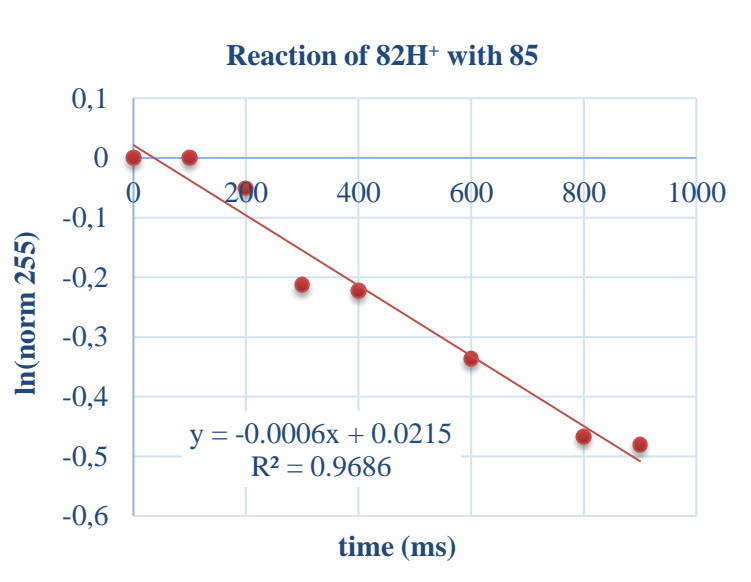


Figure 78. Plots showing the reaction of 82H^+ (m/z 255) with **85** at different reaction times. The decay of 82H^+ indicates proton transfer from 82H^+ to **85**. The resultant slope is used to calculate rate of proton transfer reaction k_{coll} using equation 11.

Table 34. Experimental rate constant (K_{exp}) and the reaction efficiency of proton transfer reaction between 82H^+ and **85** derived from *slope*, concentration of **85** ($P_{neutral}$) and theoretical collision rate constant (k_{coll}). μ_D and α are the dipole moment and polarizability used for the calculation of k_{coll} . ϕ is the conversion factor in molecules. cm^3 . torr^{-1}

μ_D of 85	α of 85	$P_{neutral}$ of 85 (average)	ϕ	<i>slope</i>	k_{coll} ($82\text{H}^+ + 85$)	K_{exp} ($82\text{H}^+ + 85$)	<i>efficiency</i>
0	14.86	4.81E-08	3.239E+16	-0.6	1.01E-09	3.85E-10	38.08%

7.2.3. Reaction with Tributylamine

Considering lower PA of carbene **82** relative to reference bases **83** and **85**, further efforts were directed towards reaction of 82H^+ with tributylamine **86** having lower PA (238.9 kcal mol⁻¹) relative to **83** and **85**. Before and after investigating the reaction between protonated carbene species 82H^+ and reference base **86**, 3-picoline **87** (PA = 225.5 kcal mol⁻¹) was used as weak base to determine the concentration of **86** ($P_{neutral}$) in the controlled kinetic experiments (Figure 79, Table 35). Analogous to reactions of **83** and **85** with 82H^+ , deprotonation of 82H^+ was observed when **86** was used as reference base with proton transfer efficiency of ~ 24% (Figure 80, Table 36), indicating carbene **82** to have PA even lower than that of **86** (238.9 kcal mol⁻¹). The disappearance of 82H^+ (m/z 255) accompanied by appearance of protonated base 86H^+ (m/z 94) confirms the proton transfer from 82H^+ to **86** (Figure 81, Scheme 26).

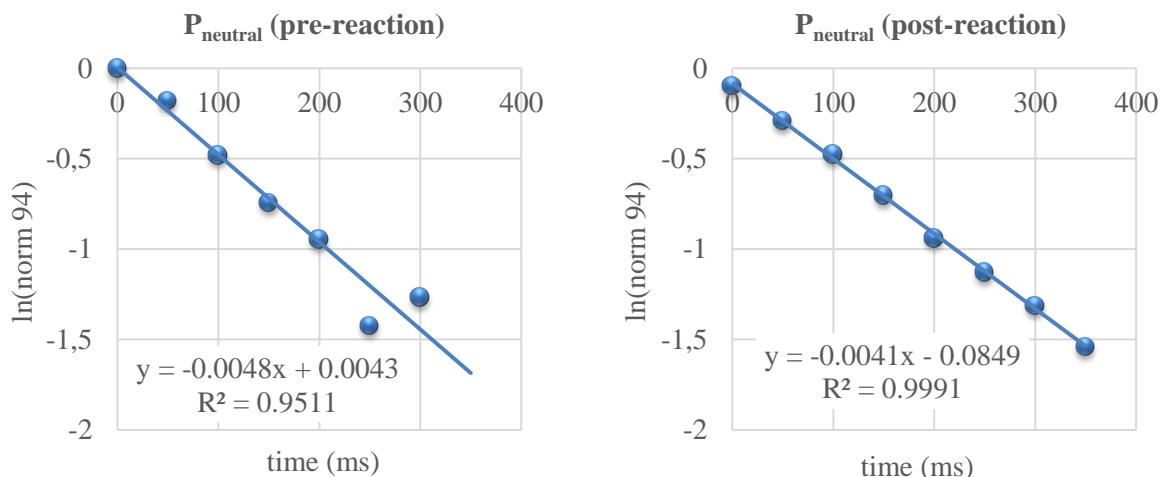


Figure 79. Plots showing the reaction of 87H^+ (m/z 94) with **86** at different reaction times performed before and after the reaction of 82H^+ and **86**. The decay of 87H^+ indicates proton transfer from 87H^+ to **86**. The resultant slopes are used to calculate concentration of **86** (P_{neutral}) using equation 10.

Table 35. Parameters used for the determination of P_{neutral} of **86**. μ_D and α are the dipole moment and polarizability used for the calculation of theoretical collision rate constant k'_{coll} . ϕ is the conversion factor in $\text{molecules}\cdot\text{cm}^3\cdot\text{torr}^{-1}$

μ_D of 86	α of 86	slope' (before)	slope' (after)	k'_{coll} ($87\text{H}^+ + \text{86}$)	ϕ	P_{neutral} of 86 (before)	P_{neutral} of 86 (after)	P_{neutral} of 86 (average)
0.5419	24.42	-4.8	-4.1	1.54E-09	3.239E+16	9.62E-08	8.22E-08	8.92E-08

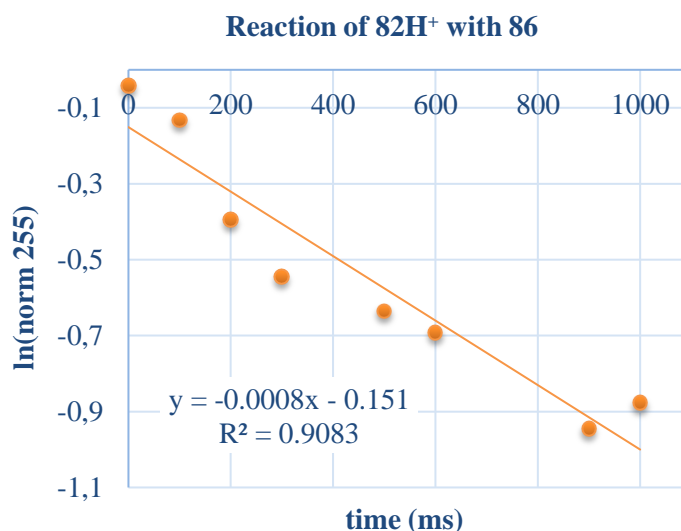


Figure 80. Plots showing the reaction of 82H^+ (m/z 255) with **86** at different reaction times. The decay of 82H^+ indicates proton transfer from 82H^+ to **86**. The resultant slope is used to calculate rate of proton transfer reaction k_{coll} using equation 11.

Table 36. Experimental rate constant (K_{exp}) and the reaction efficiency of proton transfer reaction between $82H^+$ and **86** derived from *slope*, concentration of **86** ($P_{neutral}$) and theoretical collision rate constant (k_{coll}). μ_D and α are the dipole moment and polarizability used for the calculation of k_{coll} . \emptyset is the conversion factor in molecules.cm³.torr⁻¹

μ_D of 86	α of 86	$P_{neutral}$ of 86 (average)	\emptyset	<i>slope</i>	k_{coll} ($82H^+ + 86$)	K_{exp} ($82H^+ + 86$)	<i>efficiency</i>
0.5419	24.42	8.92E-08	3.239E+16	-0.8	1.17E-09	2.77E-10	23.58%

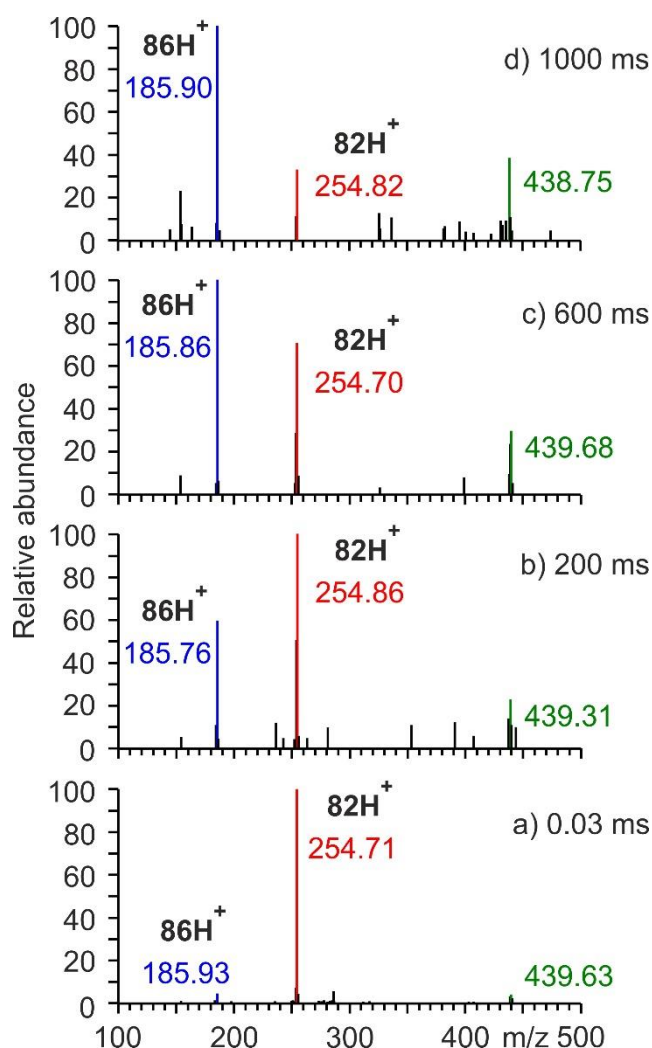
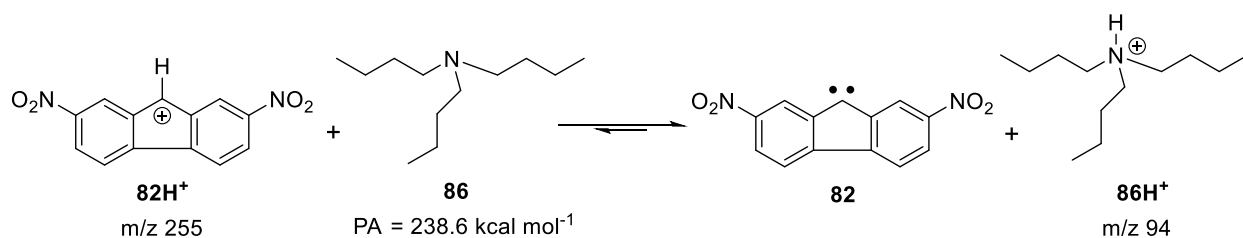


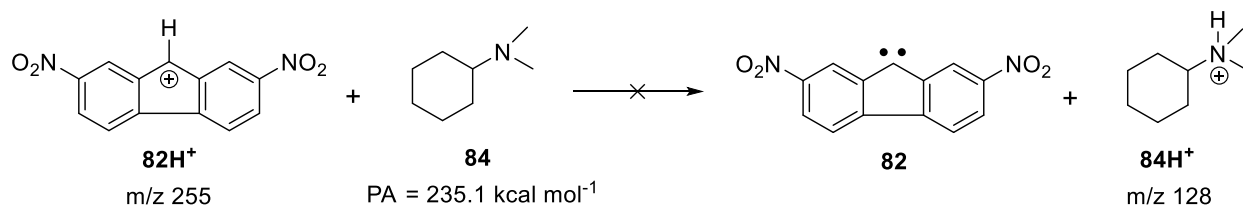
Figure 81. Kinetics of the reaction of 2,7-dinitrofluorenyl cation $82H^+$ (m/z 255 – red bands) with tributylamine **86** at different reaction times a) 0.03, b) 200, c) 600, and d) 1000 ms, showing the increase in relative intensity of $86H^+$ (m/z 186 – blue bands) with time, accompanied by decrease in relative intensity of $82H^+$. Cluster formed between $82H^+$ and **86** (or $86H^+$ and **82**) is indicated by green bands (m/z 439). The remaining bands belonging to fragmentation ionic products are not assigned to highlight the reaction between $82H^+$ and **86**.



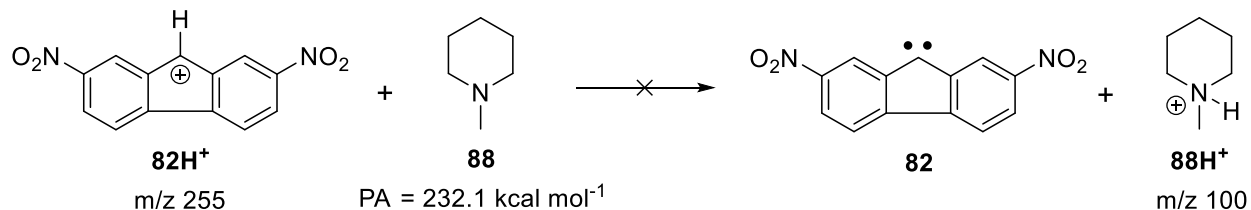
Scheme 26. Reaction of 2,7-dinitrofluorenyl cation 82H^+ with tributylamine **86**.

7.2.4. Reaction with *N,N*-dimethylcyclohexylamine and *N*-methylpiperidine

Building upon the aforementioned PA results obtained for **82**, less basic reference bases such as *N,N*-dimethylcyclohexylamine **84** (PA = 235.1 kcal mol⁻¹) and *N*-methylpiperidine **88** (PA = 232.1 kcal mol⁻¹) were used to bracket the PA of carbene **82**. Proton transfer from protonated derivative of **82** was not observed with **84** and **88** even at longer reaction times (Schemes 27 and 28), indicating **82** to have higher PA than these reference bases. Thus, the experimental PA of carbene **82** is bracketed between 235.1 kcal mol⁻¹ (PA of **84**) and 238.6 kcal mol⁻¹ (PA of **86**).



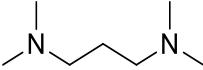
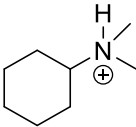
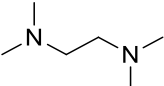
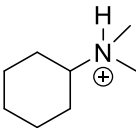
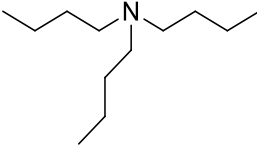
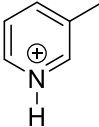
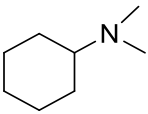
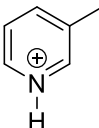
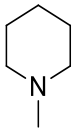
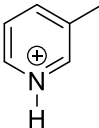
Scheme 27. Reaction of 2,7-dinitrofluorenyl cation 82H^+ with *N,N*-dimethylcyclohexylamine **84**.



Scheme 28. Reaction of 2,7-dinitrofluorenyl cation 82H^+ with *N*-methylpiperidine **88**.

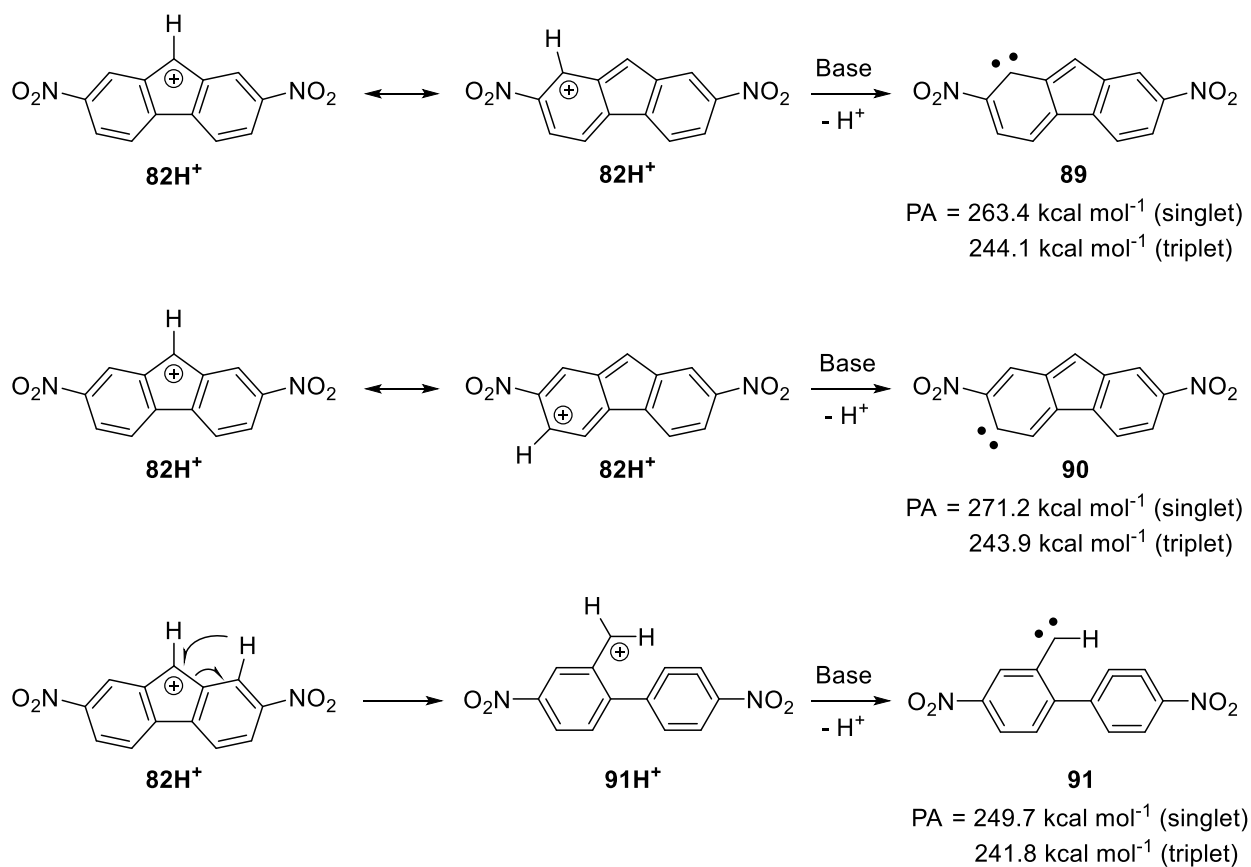
The PA bracketing results obtained from the reactions of 2,7-dinitrofluorenyl cation 82H^+ with five reference bases **83**, **84**, **85**, **86**, and **88** were found to be reproducible. The overall summary of PA bracketing of 2,7-dinitrofluorenylidene **82** is given in Table 37.

Table 37. Summary of proton affinity (PA) bracketing for 2,7-dinitrofluorenylidene **82**.

Reference Base	PA (kcal mol ⁻¹)	Charged species in kinetic experiment PA (kcal mol ⁻¹)	Proton Transfer efficiency
 83 <i>N,N,N',N'</i> - tetramethyl-1,3-propanediamine MW = 130.15 g/mol	247.4	 84H⁺ <i>N,N</i> -dimethylcyclohexylamine 235.1	(+) 42.94% (+) 43.96%
 85 <i>N,N,N',N'</i> - tetramethylethylenediamine MW = 116.2 g/mol	242.1	 84H⁺ <i>N,N</i> -dimethylcyclohexylamine 235.1	(+) 38.08% (+) 35.12%
 86 Tributylamine MW = 185.35 g/mol	238.6	 87H⁺ 3-picoline 225.5	(+) 23.58% (+) 25.25%
 84 <i>N,N</i> -dimethylcyclohexylamine MW = 127.23 g/mol		235.1	 87H⁺ 3-picoline 225.5
 88 N-methylpiperidine MW = 99.17 g/mol	232.1		 87H⁺ 3-picoline 225.5

(+) symbol indicates occurrence of proton transfer and (-) symbol indicates no proton transfer reactions.

Computations. At the B3LYP/6-31+G(d) level of theory, carbene **82** is predicted to have PA of 252.7 or 245.2 kcal mol⁻¹ depending on the deprotonation either to the singlet or the triplet state, which is substantially higher than the experimental PA value bracketed between 235.1 and 238.6 kcal mol⁻¹. This discrepancy in experimental and calculated PA of **82** could be due to high reactivity of destabilized antiaromatic cation **82H⁺** (NICS(0) = 25.6). The DFT calculations performed by Gaussian usually consider antiaromaticity and should not miscalculate energy of **82H⁺**, otherwise NICS calculations would be unjustifiable. Another possibility could be that the unstable cation **82H⁺** rearranges to other relatively stable cationic geometries maintaining the mass-to-charge ratio constant and then deprotonation take place upon reaction with suitable base. For that reason, possible cationic geometries with m/z = 255 and subsequent deprotonated carbenes were computed (Scheme 29). However, expected PA could not be achieved with these possibilities.

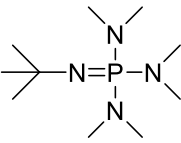
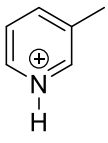


Scheme 29. Deprotonation pathways of possible cationic systems with m/z 255 on reaction with reference base.

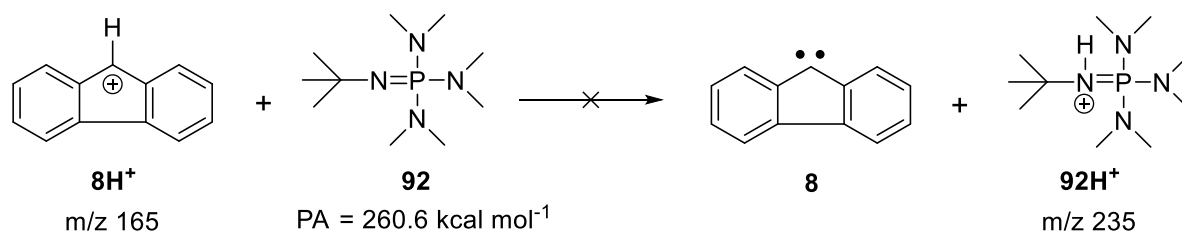
To verify the assumption of high reactivity of antiaromatic cation **82H**⁺ leading to the lower experimental PA of the corresponding carbene, bracketing experiments were carried out with parent system fluorenylidene **8**, as its cation **8H**⁺ is also antiaromatic (mentioned as **8H**⁺ in this chapter to maintain consistency with other protonated systems, otherwise it is mentioned as **40** in Chapter 3 or elsewhere in this dissertation). Cation **8H**⁺ (m/z 165) was produced by electrospray ionization of corresponding hydrate precursor dissolved in fluoroboric acid solution. DFT calculations at B3LYP/6-31+G(d) level of theory predicts PAs of 271.8 and 268.0 kcal mol⁻¹ for singlet and triplet states of **8**, respectively. Considering the lower experimental PA of **82** relative to computationally predicted PA values, *tert*-butylimino-tris-(dimethylamino)phosphorane **92** with PA of 260.6 kcal mol⁻¹ was chosen as reference base to estimate the PA of **8**. Experiments performed in similar manner as that of dinitro-substituted fluorenylidene system showed a proton transfer from **8H**⁺ to **92** with transfer efficiency of ~ 17 % suggesting PA of carbene **8** with PA lower than 260.6 kcal mol⁻¹ (Table 38, Scheme 30).

To bracket the PA of **8**, additional experiments need to be performed with relatively less basic reference bases such as iminotris-(dimethylamino)phosphorane (PA = 257.4 kcal mol⁻¹) and *tert*-octyliminotris-(dimethylamino)phosphorene (PA = 262.0 kcal mol⁻¹). The present results demonstrate PA of **8** lower than 260.6 kcal mol⁻¹, which is far away from calculated values of 271.8 and 268.0 kcal mol⁻¹ depending upon the deprotonation either to singlet and triplet state, respectively. Although DFT calculations seem to consider the destabilization of antiaromatic systems, it is poorly reflected in the experiments where such systems turn out to be more reactive.

Table 38. Summary of proton affinity (PA) bracketing for fluorenylidene **8**.

Reference Base	PA (kcal mol ⁻¹)	Charged species in kinetic experiment PA (kcal mol ⁻¹)	Proton Transfer efficiency
 92 <i>t</i> BuP1dma MW = 234.32 g/mol	260.6	 87H ⁺ 3-picoline 225.5	(+) 17.07% (+) 16.25%

(+) symbol indicates occurrence of proton transfer and (-) symbol indicates no proton transfer reactions.



Scheme 30. Reaction of fluorenyl cation **8H⁺** or **40** with *tert*-butylimino-tris-(dimethylamino)phosphorane **75**.

7.3. Conclusions

The gas-phase reactions of 2,7-dinitrofluorenyl cation **82H⁺** with different reference bases were carried to bracket the PA of 2,7-dinitrofluorenylidene **82**. From the experiments, the PA of carbene **82** is bracketed between 235.1 – 238.6 kcal mol⁻¹. However, DFT calculations at the B3LYP-D3/6-31+G (d) level of theory predict higher PAs (252.7 and 245.2 kcal mol⁻¹ for singlet and triplet states of **82**, respectively). The parent carbene fluorenylidene **8** also follows a similar trend as that of dinitro-substituted derivative, exhibiting experimental PA lower than computed values. This discrepancy in experimental and computational PA of **8** and **82** is intriguing, considering the high reactivity of corresponding antiaromatic cations and needs further investigation.

Experimental Section

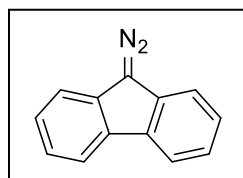
Materials

All chemicals and solvents were used as received without further purification. Fluorenone (98%) dibenzosuberone (97%), *p*-toluenesulfonyl hydrazide (98%), 2,7-dinitrofluorenone (98%) and benzamidine hydrochloride (97%) were purchased from ABCR. Sodium hydride (60% dispersion in mineral oil), 1,8-diazafluorenone (99%), tetrafluoroboric acid (48% wt. in H₂O), hydroxylamine hydrochloride (reagent grade 99%), hydrazine hydrate (reagent grade, 50-60%), sodium borohydride (96%) and zinc dust (98%) were purchased from Sigma Aldrich. Iodine (99%) and 3,3'-dinitrobenzophenone were purchased from Alfa Aesar. Yellow mercuric oxide (99%) and Hydrazine hydrate (80%, hydrazine 51%) and were purchased from Acros Organics. Sodium hypochlorite (14% active chlorine) was purchased from VWR chemicals. Deuterated water (99% D) was purchased from Deutero GmbH. Deuterated sodium hydroxide (99%) and deuterated lithium aluminum hydride (98%) were purchased from Merck.

Synthesis

Thin layer chromatography (TLC) analyses were carried out using Polygram G/UV254 silica gel pre-coated plates and the spots were analyzed using a CAMAG UV lamp. ICN silica 32-63 (60 Å) was used for column chromatography. The NMR spectra were recorded (0-16 ppm region) with DPX 200, 250 and DRX 400 Bruker instruments. NMR shifts are reported in parts per million (ppm) downfield from tetramethylsilane and referenced with respect to the solvent signal. Signal multiplicities are reported according to standard assignments. Mass spectra were recorded on a Varian MAT-CH5 spectrometer at 70 eV with electron impact as ion source. HR-MS-EI spectra were recorded on a Joel AccuTOF GCv JMST100GCV apparatus. Elemental analyses were carried out using varioMICRO V4.0.8.

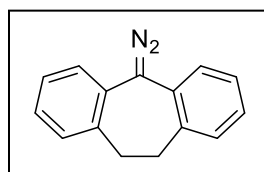
Diazo fluorene (29). The diazo compound was synthesized according to literature procedure.^[255]



A suspension of fluorenone and *p*-toluenesulfonyl hydrazide of 1.2 eq. in acetonitrile was refluxed for 30 min. and the crystals obtained upon cooling were filtered. These crystals were purified by column chromatography using CH₂Cl₂/hexane (2:1) as eluent to obtain pure yellow crystals of fluorenone *p*-

tosylhydrazone. A dioxane solution of fluorenone *p*-tosylhydrazone and 50% aqueous NaOH was stirred at 50°C for 24 hrs under argon. The reaction mixture was diluted with H₂O and extracted with ethyl acetate. The combined organic extracts were washed with H₂O, dried over MgSO₄ and concentrated under reduced pressure. Flash chromatography using CH₂Cl₂/hexane (2:1) as eluent gave red crystals of desired product. IR (Ar, 3 K): $\tilde{\nu}$ = 2061 (vs), 1608 (m), 1448 (s), 1443 (s), 1378 (m), 1331 (m), 1310 (m), 1225 (m), 1220 (m), 1155 (m), 752 (s), 725 (s), 653 (m) cm⁻¹. ¹H-NMR (200 MHz, DMSO-*d*₆): δ = 8.08 (d, *J* = 7.8 Hz, 2 H), 7.71 (d, *J* = 7.6 Hz, 2 H), 7.45–7.29 (m, 4 H) ppm. ¹³C-NMR (50 MHz, DMSO-*d*₆): δ = 126.97, 126.46, 124.75, 124.54, 121.16, 120.97, 119.71 ppm.

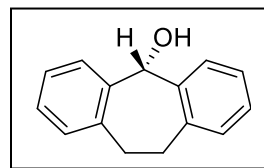
Diazodibenzocycloheptadienyldene (26). The diazo compound was obtained by the thermal



decomposition of sodium salt of dibenzosuberone *p*-tosylhydrazone at 55°C under reduced pressure. IR (argon, 3K): $\tilde{\nu}$ = 2045 (vs), 1604 (m), 1600 (m), 1580 (m), 1572 (m), 1496 (s), 1449 (m), 1332 (m), 1309 (m), 1245 (m), 910.2 (m), 756 (s), 749 (m), 745 (m), 638 (m) cm⁻¹. The sodium salt was

prepared by deprotonation of its tosylhydrazone. Under argon atmosphere, 1.2 eq. of sodium hydride (60% dispersion in mineral oil) was washed with dry pentane 3-4 times. The dibenzosuberone *p*-tosylhydrazone, synthesized from dibenzosuberone according to a literature procedure,^[256] was dissolved in dichloromethane and added in one portion to the washed sodium hydride. The solution was stirred for 3 hrs at room temperature. The solvent was removed in high vacuum to obtain pink salt and it was stored under inert atmosphere at -20°C. ¹H-NMR (200 MHz, D₂O): δ = 7.68 (d, *J* = 7.9 Hz, 2H), 6.88-7.27 (m, 7H), 6.41-6.86 (m, 2H), 2.67 (t, *J* = 12.5 Hz, 4H), 1.90 (s, 3H) ppm. ¹³C-NMR (50 MHz, D₂O): δ = 152.97, 141.73, 140.14, 138.71, 137.93, 137.70, 137.18, 130.17, 129.16, 128.46, 128.40, 128.15, 127.98, 127.69, 126.55, 125.49, 33.32, 31.17, 20.44 ppm. MS (EI): *m/z* found for ¹²C₂₂¹H₁₉¹⁴N₂²³Na₁¹⁶O₂³²S₁ ([M]⁺): 398.1607, calculated: 398.1065.

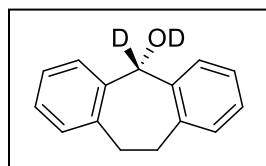
Dihydrodibenzotropylium alcohol (42). The compound was synthesized according to literature procedure.^[257] Dibenzosuberone and NaBH₄ (2 eq.) were combined in a



round bottom flask with stir bar. MeOH was added, and the reaction was stirred at room temperature. After 24 hrs, the reaction was diluted with H₂O to give a precipitate. This was filtered, and rinsed with additional H₂O and

dried to give product as a white solid. IR (LDA water ice, 8 K) $\tilde{\nu}$ = 1276 (m), 1220 (m), 1106 (m), 1045 (s), 946 (m), 746 (m), 722 (m), 709 (m), 626 (m) cm^{-1} . ^1H NMR (200 MHz, CDCl_3): δ = 7.46 (dd, J = 6.3, 2.0 Hz, 2H), 7.19 (m, 6H), 5.96 (d, J = 1.7 Hz, 1H), 3.43 (m, 2H), 3.12 (m, 2H), 2.29 (d, J = 2.5 Hz, 1H) ppm. ^{13}C NMR (100 MHz, CDCl_3): δ = 140.6, 139.0, 130.3, 128.1, 127.2, 126.3, 76.6, 32.5 ppm. MS (EI) m/z found for $^{12}\text{C}_{15}^1\text{H}_{14}^{16}\text{O}_1$ ($[\text{M}]^+$) 210.1033, calculated: 210.1039.

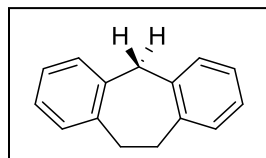
Deuterated dihydrodibenzotropylium alcohol (d_2 -42). The compound was synthesized by



following literature procedure.^[258] A solution of dibenzosuberone and LiAlD_4 (1.0 eq.) in dry ether was refluxed for 2.5 hrs. After cooling to room temperature, 40 % NaOD in D_2O was added to reaction mixture and filtered.

The reaction mixture was washed with D_2O and the combined organic phases were evaporated to obtain required alcohol ($[\text{D}]$ -8). IR (LDA water ice, 8 K) $\tilde{\nu}$ = 1207 (s), 1047 (m), 1024 (m), 950 (m), 838 (m), 825 (m), 777 (s), 764 (s), 721 (m) cm^{-1} . ^1H NMR (200 MHz, CDCl_3): δ = 7.55-7.45 (m, 2H), 7.33-7.18 (m, 6H), 3.60-3.07 (m, 4H) ppm. MS (EI): m/z found for $^{12}\text{C}_{15}^1\text{H}_{12}^2\text{H}_2^{16}\text{O}_1$ ($[\text{M}]^+$): 212.0918, calculated: 212.1170.

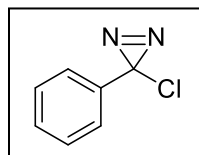
Dibenzosuberane (54). The compound was synthesized by following a literature procedure.^[259]



Iodine (0.33 eq.) and acetic acid were stirred together under N_2 in a flask fitted with a condenser and a dropping funnel. Hypophosphorous acid (50% aq.) of 1.6 eq. was added and the mixture was heated to reflux. A solution of dibenzosuberone in acetic acid was added over a period of 1–2 hrs. The

mixture was then stirred and refluxed for an additional 24 hrs, cooled, diluted with H_2O and extracted with hexane. The hexane solution is then dried over MgSO_4 . The hexane was concentrated and purified by flash chromatography to afford dibenzosuberane as white solid. IR (Ar, 3 K): $\tilde{\nu}$ = 1499 (m), 1293 (m), 950 (m), 762 (s), 739 (s), 711 (s), 701 (m), 625 (m), and 586 (m) cm^{-1} . ^1H -NMR (200 MHz, CDCl_3): δ = 7.24–7.00 (m, 8 H), 4.13 (s, 2 H), 3.19 (s, 1 H) ppm. ^{13}C -NMR (50 MHz, CDCl_3): δ = 139.28, 138.99, 129.57, 129.00, 126.60, 126.05, 41.02, 32.54 ppm. MS (EI): m/z found for $^{12}\text{C}_{15}^1\text{H}_{14}$ ($[\text{M}]^+$): 194.2040, calculated: 194.1096.

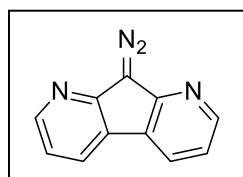
Phenylchlorodiazirine (63). The compound was synthesized according to Graham diazirine synthesis procedure.^[260] To a solution of Lithium chloride (3.1 eq.) in DMSO,



benzamidinium hydrochloride dissolved in pentane was added and the mixture was submerged into an ice-salt bath. Meanwhile, NaCl (3.5 eq.) dissolved in sodium hypochloride (14% active chlorine) was dripped in reaction flask within 15 min.

and the reaction mixture was stirred for an additional 45 min. The aqueous DMSO layer was extracted with pentane, the combined organic extracts were washed with water and dried with saturated aqueous NaCl solution. The pentane was concentrated and purified by column chromatography using pentane as eluent to yield the desired product as yellow oil. IR (Ar, 3 K): $\tilde{\nu} = 1574$ (s), 1498 (m), 1451 (m), 1040 (m), 1015 (m), 913 (vs), 757 (m), 692 (m), 667 (m) cm^{-1} . $^1\text{H-NMR}$ (200 MHz, CDCl_3): $\delta = 7.46\text{--}7.36$ (m, 3 H), 7.17–7.09 (m, 2 H) ppm. $^{13}\text{C-NMR}$ (50 MHz, CDCl_3): $\delta = 135.71, 129.32, 128.55, 126.00, 47.13$ ppm.

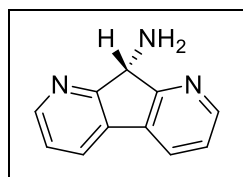
Diazo-1,8-diazafluorenylidene (72). The compound was synthesized in two steps. In the first



step, 1,8-diazafluorenone hydrazone was synthesized from the reaction of 1,8-diazafluorenone with hydrazine hydrate (80%) according to literature procedure.^[261] In second step, the hydrazone obtained was oxidized to obtained diazo compound by following literature procedure.^[262] Under argon

atmosphere, a mixture of dried hydrazine, mercuric oxide (2 eq.) and anhydrous sodium sulfate (1.8 eq.) in dry Et_2O was stirred at room temperature. After 1 hr., a freshly prepared, concentrated solution of KOH in ethanol was added (10 drops). The color of the solution changed from yellow to grey-black and the reaction was stirred for additional 4 hrs. The resulting solution was filtered, washed with Et_2O and combined organic fractions were concentrated to obtain diazo-1,8-diazafluorenylidene as orange crystals. IR (Ar, 3 K): $\tilde{\nu} = 2096$ (vs), 1585 (m), 1429 (s), 1401 (s), 1320 (m), 1254 (m), 1126 (m), 781 (m), 516 (m) cm^{-1} . $^1\text{H-NMR}$ (200 MHz, CDCl_3): $\delta = 8.59$ (dd, $J = 5$ Hz, 1.5 Hz, 2H), 8.22 (d, $J = 7.8$ Hz, 2 H), 7.33 (m, 2H) ppm.

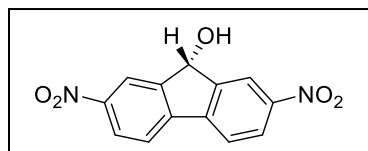
1,8-diazafluorenylamine (74). The compound was prepared from 1,8-diazafluorenone oxime by following the literature procedure.^[263] The synthesis of the oxime was carried



out from 1,8-diazafluorenone and hydroxylamine hydrochloride according to literature procedure^[264] and used without further purification. To a 110 °C solution of 1,8-diazafluorenone oxime in glacial acetic acid and water (9 eq.),

zinc dust (6 eq.) was added in small portions. After 1 hr., the solution was filtered, concentrated and the residue was treated with 5 N HCl. The mixture was cooled down to 0°C for 10 hrs and filtered to obtain 1,8-diazafluorenone oxime hydrochloride, which was basified with ammonia to afford the amine as red-brown solid. IR (Ar, 3K): 1591 (m), 1576 (m), 1414 (vs), 11520 (m), 895 (m), 820 (m), 785 (s), 650 (m), 512 (m) cm^{-1} . $^1\text{H-NMR}$ (200 MHz, $\text{DMSO-}d_6$): $\delta = 8.69$ (s, 2H), 8.27 (s, 1H), 7.68 (m, 4H), 7.00 (s, 1H), 6.63 (s, 1H) ppm.

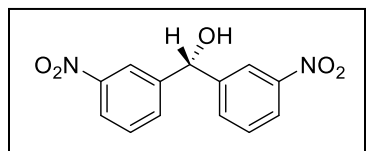
2,7-dinitrofluorenol (93). The compound was prepared from diazo-2,7-dinitrofluorenylidene according to literature procedure.^[265] The diazo precursor was



synthesized from 2,7-dinitrofluorenone was used without further purification. To a heated solution (70-75°C) of 45% aqueous tetrafluoroboric acid (3.3 eq.), H_2O (37 eq.) in acetonitrile, diazo-

2,7-dinitrofluorenylidene was added and the mixture was heated for 5 minutes. The hot solution was then filtered and kept for 4-5 hours at -25°C to obtain crude product, which was then recrystallized in nitromethane to afford the desired product. $^1\text{H-NMR}$ (200 MHz, $\text{DMSO-}d_6$): $\delta = 8.23$ -8.42 (m, 6H), 6.48 (d, $J = 6.7$ Hz, 1H), 5.7 (d, $J = 6.4$ Hz, 1H) ppm. $^{13}\text{C-NMR}$ (50 MHz, $\text{DMSO-}d_6$): $\delta = 149.65$, 147.99, 143.43, 124.83, 122.80, 120.24, 72.96 ppm. Elemental analysis found for $\text{C}_{13}\text{H}_8\text{N}_2\text{O}_5$ (%): C 55.04, H 3.09, N 10.31, O 31.56, calculated (%): C 57.36, H 2.96, N 10.29, O 29.39.

3,3'-dinitrobenzhydrol (94). The compound was synthesized according to literature procedure.^[266] A solution of 3,3'-dinitrobenzophenone and NaBH_4



(2 eq.) in ethanol was refluxed for 30 min. The resultant reaction mixture was then extracted with ethyl acetate/ H_2O and organic extracts were concentrated to obtain yellow colored product. ^1H

NMR (200 MHz, CDCl_3 -*d*): $\delta = 8.27$ – 7.92 (m, 4H), 7.64 (dd, $J = 7.7$, 1.6 Hz, 2H), 7.48 (d, $J = 7.9$ Hz, 2H), 5.97 (s, 1H), 2.70 (s, 1H) ppm. ^{13}C NMR (50 MHz, CDCl_3) $\delta = 148.46$, 144.73, 132.57, 129.90, 123.11, 121.42, 74.34 ppm. MS (EI): m/z found for $^{12}\text{C}_{13}^{1}\text{H}_{10}^{14}\text{N}_2^{16}\text{O}_5$ ($[\text{M}]^+$): 274.1085, calculated: 274.0590.

Matrix Isolation

Matrix isolation experiments were performed by standard techniques as reported in literature^[1, 3] using Sumitomo Heavy industries two-staged closed cycle helium cryostat (cooling power 1 W at 4 K) to obtain temperatures around 3 K. High vacuum (10^{-5} to 10^{-7}) is reached through an oil diffusion pump in combination with a rotary pump for IR and UV-Vis experiments, while turbo pump connected with a rotary pump is used for X-band EPR experiments. Cesium iodide, sapphire and an oxygen-free high-conductivity copper were used as materials for the IR, UV-vis and EPR spectroscopic windows, respectively. The temperature of the windows is controlled by resistance heater connected through a silicon diode to an Oxford ITC4 temperature controller. For the matrix isolation experiments, Ar (Messer-Griesheim; 99.9999%) was used as inert host material, while H₂ (Air Liquide, 99.999%), D₂ (Merck Schuchardt, 99.5%), H₂O, and D₂O were utilized as reactive hosts and also to generate doped argon gas mixtures. ICF₃ (Fluorochem, 99%), BF₃ ($\geq 96.5\%$), NH₃, and ND₃ (Sigma Aldrich, 99%) were used to generate doped argon gas mixtures. The gas mixture of 1% of H₂O (or ICF₃ or BF₃ or NH₃ or ND₃) or 5% of H₂ (or D₂) in excess of argon was prepared in mixing chamber using gas filling station. H₂O or D₂O was degassed several times before preparing the doped argon mixture. The matrices were generated by co-deposition of appropriate precursor or stable compound (**26** at 57°C; **29** at 45°C; **42** at 68°C; **54** at 75°C; **60** at 0°C; **63** at -30°C; **72** at 65°C; **74** at 170°C) with argon or doped argon gas mixture on cold spectroscopic windows at the lowest possible temperatures (3–8 K for IR and UV-Vis, and 5 K for EPR). A typical flow rate of approximately of 1.80 sccm, controlled by a MKS mass flow controller, was used for the deposition of argon or gas mixture. Deposition times varied between 30 min and 2 hrs. The experiments in doped argon matrices were carried out as described in literature.^[154]

For the preparation of low density amorphous ice (LDA), vapours of degassed ultrapure water held at room temperature were allowed to co-deposit together with diazo precursor **26** in high vacuum system on spectroscopic window maintained at 50 K. After finishing the co-deposition, the matrices generated were cooled at the lowest temperature possible. The deposition rate of the water vapours was controlled by a fine metering valve. The experiments in LDA water ice were performed as described in literature.^[1, 4] Solid H₂ and D₂ matrices were generated by depositing **26** in excess of H₂ or D₂ on spectroscopic window maintained at 3 K. Due to high volatility of H₂,

temperatures below 4 K are necessary to prevent sublimation of H₂, whereas D₂ matrices are stable up to 6 K under matrix isolation conditions. The experiments in solid H₂ and D₂ matrices were carried out as described in literature.^[5]

Photolysis of the matrices were performed by custom-made LEDs with $\lambda = 630, 530, 450, 405,$ and 365 nm (max. power of 5 W). For broadband IR irradiation in the range between $\lambda = 730 - 2500$ nm, a lamp-pumped OPO laser (InnoLas Laser model SpitLight 600 midband) was used. A low pressure mercury lamp with $\lambda = 254$ nm (Grüntzel) was used for narrowband irradiation. FTIR spectra were recorded in the range between 400 and 4000 cm⁻¹ using Bruker IFS66 and IFS66s spectrometers with a resolution of 0.5 cm⁻¹. The IR spectrometers were purged by dry air for avoiding CO₂ and water from atmosphere. UV-Vis spectra were recorded in the range between 200 and 800 nm using a Varian Cary 5000 spectrometer with a resolution of 0.2 nm. X-band continuous wave (CW) EPR spectra were recorded using a Bruker Elexsys X-band spectrometer.

Calculations

Computations were carried out using the Gaussian-09 suite of programs.^[267] In all the chapters, except chapter 6, the gas phase geometry optimizations, vibrational frequencies and IRC profiles were calculated at B3LYP functional^[268-270] including D3 dispersion corrections^[271] using def2-TZVP^[272] basis set. In Chapter 6, the geometry optimization and frequency calculations were performed at B3LYP functional without the dispersion corrections using 6-31+G(d)^[268, 273-276] basis set to corroborate calculated proton affinity values with that of previously reported computational methods.^[116] Tight convergence criteria were used throughout. For the continuum solvation model, argon was used as solvent via keywords SCRF = (IEFPCM, solvent = argon). The CCSD(T) single-point calculations were performed using the Molpro software.^[277] Atoms-in-molecules analysis, implemented through AIM 2000^[148] was performed to understand bonding characteristics in the complexes. NBO analysis was also performed using the NBO version 3.1 program^[278] to estimate natural charges on monomers in the complexes and to understand the nature of bonding in noncovalent interactions. Experimental EPR spectra were analyzed using the *Easyspin* program packet.^[279] Computed vibrational spectra were simulated using a Lorentzian line shape and a full width at half-maximum (fwhm) of 1.0 cm⁻¹.

References

- [1] P. Costa, M. Fernandez-Oliva, E. Sanchez-Garcia, W. Sander, *J. Am. Chem. Soc.* **2014**, *136*, 15625-15630.
- [2] S. Henkel, P. Costa, L. Klute, P. Sokkar, M. Fernandez-Oliva, W. Thiel, E. Sanchez-Garcia, W. Sander, *J. Am. Chem. Soc.* **2016**, *138*, 1689-1697.
- [3] P. Costa, J. Mieres-Perez, N. Ozkan, W. Sander, *Angew. Chem. Int. Ed.* **2017**, *56*, 1760-1764.
- [4] P. Costa, I. Trosien, M. Fernandez-Oliva, E. Sanchez-Garcia, W. Sander, *Angew. Chem. Int. Ed.* **2015**, *54*, 2656-2660.
- [5] E. Mendez-Vega, M. Maehara, A. H. Raut, J. Mieres-Perez, M. Tsuge, Y. P. Lee, W. Sander, *Chem. Eur. J.* **2018**, *24*, 18801-18808.
- [6] Y. Z. Li, G. B. Schuster, *J. Org. Chem.* **1986**, *51*, 3804-3811.
- [7] G. D. Frey, V. Lavallo, B. Donnadiou, W. W. Schoeller, G. Bertrand, *Science* **2007**, *316*, 439-441.
- [8] G. Richter, E. Mendez-Vega, W. Sander, *J. Phys. Chem. A* **2016**, *120*, 3524-3532.
- [9] E. V. Anslyn, D. A. Dougherty, *Modern physical organic chemistry*, University Science, Sausalito, CA, **2006**.
- [10] D. Bourissou, O. Guerret, F. P. Gabbai, G. Bertrand, *Chem. Rev.* **2000**, *100*, 39-92.
- [11] N. C. Baird, K. F. Taylor, *J. Am. Chem. Soc.* **1978**, *100*, 1333-1338.
- [12] R. Hoffmann, G. D. Zeiss, G. W. Vandine, *J. Am. Chem. Soc.* **1968**, *90*, 1485-&.
- [13] A. R. W. McKellar, P. R. Bunker, T. J. Sears, K. M. Evenson, R. J. Saykally, S. R. Langhoff, *J. Chem. Phys.* **1983**, *79*, 5251-5264.
- [14] K. K. Murray, D. G. Leopold, T. M. Miller, W. C. Lineberger, *J. Chem. Phys.* **1988**, *89*, 5442-5453.
- [15] S. Koda, *Chem. Phys. Lett.* **1978**, *55*, 353-357.
- [16] C. W. Bauschlicher, H. F. Schaefer, P. S. Bagus, *J. Am. Chem. Soc.* **1977**, *99*, 7106-7110.
- [17] D. Feller, W. T. Borden, E. R. Davidson, *Chem. Phys. Lett.* **1980**, *71*, 22-26.
- [18] J. F. Harrison, *J. Am. Chem. Soc.* **1971**, *93*, 4112-4119.
- [19] J. F. Harrison, R. C. Liedtke, J. F. Liebman, *J. Am. Chem. Soc.* **1979**, *101*, 7162-7168.
- [20] K. K. Irikura, W. A. Goddard, J. L. Beauchamp, *J. Am. Chem. Soc.* **1992**, *114*, 48-51.
- [21] R. Hoffmann, G. D. Zeiss, G. W. Vandine, *J. Am. Chem. Soc.* **1968**, *90*, 1485-1499.
- [22] L. Pauling, *J. Chem. Soc., Chem. Comm.* **1980**, 688-689.
- [23] W. W. Schoeller, *J. Chem. Soc., Chem. Comm.* **1980**, 124-125.
- [24] B. C. Gilbert, D. Griller, A. S. Nazran, *J. Org. Chem.* **1985**, *50*, 4738-4742.
- [25] D. A. Modarelli, S. Morgan, M. S. Platz, *J. Am. Chem. Soc.* **1992**, *114*, 7034-7041.
- [26] C. A. Richards, S. J. Kim, Y. Yamaguchi, H. F. Schaefer, *J. Am. Chem. Soc.* **1995**, *117*, 10104-10107.
- [27] J. E. Gano, R. H. Wettach, M. S. Platz, V. P. Senthilnathan, *J. Am. Chem. Soc.* **1982**, *104*, 2326-2327.
- [28] D. R. Myers, V. P. Senthilnathan, M. S. Platz, M. J. Jones, *J. Am. Chem. Soc.* **1986**, *108*, 4232-4233.
- [29] G. B. Schuster, in *Adv. Phys. Org. Chem.*, Vol. 22 (Eds.: V. Gold, D. Bethell), Academic Press, **1986**, pp. 311-361.
- [30] W. Kirmse, in *Advances in carbene chemistry, Vol. 1* (Ed.: U. H. Brinker), Jai Press, Greenwich, Conn., **1994**, pp. 1 - 57.
- [31] W. Kirmse, in *Advances in Carbene Chemistry, Vol. 3* (Ed.: U. H. Brinker), Elsevier Science B.V., **2001**, pp. 1-51.
- [32] W. Kirmse, J. Kilian, S. Steenken, *J. Am. Chem. Soc.* **1990**, *112*, 6399-6400.
- [33] M. S. Platz, V. P. Senthilnathan, B. B. Wright, C. W. Mccurdy, *J. Am. Chem. Soc.* **1982**, *104*, 6494-6501.
- [34] H. Tomioka, Y. Izawa, *J. Am. Chem. Soc.* **1977**, *99*, 6128-6129.
- [35] H. Tomioka, S. Suzuki, Y. Izawa, *J. Am. Chem. Soc.* **1982**, *104*, 3156-3162.

- [36] B. B. Wright, M. S. Platz, *J. Am. Chem. Soc.* **1984**, *106*, 4175-4180.
- [37] L. M. Hadel, M. S. Platz, J. C. Scaiano, *J. Am. Chem. Soc.* **1984**, *106*, 283-287.
- [38] P. S. Skell, R. C. Woodworth, *J. Am. Chem. Soc.* **1956**, *78*, 4496-4497.
- [39] W. Kirmse, *Carbene Chemistry*, Academic Press, New York, London, **1971**.
- [40] J. E. Baldwin, A. H. Andrist, *J. Chem. Soc. D. Chem. Comm.* **1971**, *0*, 1512-1513.
- [41] D. Bethell, K. McDonald, *J. Chem. Soc., Perkin Trans. 2* **1977**, 671-677.
- [42] G. L. Closs, A. D. Trifunac, *J. Am. Chem. Soc.* **1970**, *92*, 7227-7229.
- [43] T. G. Savino, V. P. Senthilnathan, M. S. Platz, *Tetrahedron* **1986**, *42*, 2167-2180.
- [44] M. Jones, Jr., R. A. Moss, *Reactive Intermediate Chemistry* **2004**, 273-328.
- [45] R. A. Moss, M. S. Platz, M. Jones, Jr., Eds., *Reactive Intermediate Chemistry*, **2004**.
- [46] J. Wang, J. Kubicki, H. Peng, M. S. Platz, *J. Am. Chem. Soc.* **2008**, *130*, 6604-6609.
- [47] J. G. Langan, E. V. Sitzmann, K. B. Eisenthal, *Chem. Phys. Lett.* **1984**, *110*, 521-527.
- [48] J. G. Langan, E. V. Sitzmann, K. B. Eisenthal, *Chem. Phys. Lett.* **1986**, *124*, 59-62.
- [49] E. V. Sitzmann, J. Langan, K. B. Eisenthal, *J. Am. Chem. Soc.* **1984**, *106*, 1868-1869.
- [50] E. V. Sitzmann, J. G. Langan, D. Griller, K. B. Eisenthal, *Chem. Phys. Lett.* **1989**, *161*, 353-360.
- [51] G. W. Robinson, R. P. Frosch, *J. Chem. Phys.* **1962**, *37*, 1962-1973.
- [52] G. W. Robinson, R. P. Frosch, *J. Chem. Phys.* **1963**, *38*, 1187-1203.
- [53] J. Wang, J. Kubicki, E. F. Hilinski, S. L. Mecklenburg, T. L. Gustafson, M. S. Platz, *J. Am. Chem. Soc.* **2007**, *129*, 13683-13690.
- [54] M. S. Singh, *Reactive Intermediates in Organic Chemistry: Structure and Mechanism*, Wiley-VCH Verlag, **2014**.
- [55] G. A. Olah, *Angew. Chem. Int. Ed.* **1973**, *12*, 173-212.
- [56] G. A. Olah, G. K. Suryaprakash, J. Sommer, *Science* **1979**, *206*, 13-20.
- [57] G. A. Olah, Y. K. Mo, *J. Org. Chem.* **1973**, *38*, 3221-3223.
- [58] G. A. Olah, D. J. Donovan, *J. Am. Chem. Soc.* **1977**, *99*, 5026-5039.
- [59] G. A. Olah, G. Klopman, R. H. Schlosberg, *J. Am. Chem. Soc.* **1969**, *91*, 3261-3268.
- [60] G. A. Olah, R. H. Schlosberg, *J. Am. Chem. Soc.* **1968**, *90*, 2726-2727.
- [61] R. A. McClelland, *Tetrahedron* **1996**, *52*, 6823-6858.
- [62] W. Kirmse, *Liebigs Ann. Chem.* **1963**, *666*, 9-16.
- [63] P. K. Das, *Chem. Rev.* **1993**, *93*, 119-144.
- [64] G. N. Lewis, *Valence and the structure of atoms and molecules*, The Chemical catalog company, inc., New York, **1923**.
- [65] J. N. Brønsted, *Recl. Trav. Chim. Pays-Bas Belg.* **1923**, *42*, 718-728.
- [66] R. G. Pearson, *J. Am. Chem. Soc.* **1963**, *85*, 3533-3539.
- [67] R. G. Pearson, *Science* **1966**, *151*, 172-&.
- [68] R. G. Pearson, *Chem. Br.* **1967**, *3*, 103-107.
- [69] R. G. Pearson, *J. Chem. Educ.* **1968**, *45*, 581-587.
- [70] R. G. Pearson, *J. Chem. Educ.* **1968**, *45*, 643-648.
- [71] H. Yamamoto, Oxford University Press, New York, **1999**.
- [72] R. S. Mulliken, *J. Am. Chem. Soc.* **1952**, *74*, 811-824.
- [73] C. Laurence, J.-F. Gal, in *Lewis Basicity and Affinity Scales*, John Wiley & Sons, Ltd., Wiltshire, United Kingdom, **2010**, pp. 111-227.
- [74] A. D. Buckingham, *The hydrogen bond: An electrostatic interaction?*, John Wiley & Sons, Inc., New York, **1997**.
- [75] A. E. Reed, L. A. Curtiss, F. Weinhold, *Chem. Rev.* **1988**, *88*, 899-926.
- [76] C. Laurence, J.-F. Gal, *Lewis Basicity and Affinity Measurement: Definitions and Context* John Wiley & Sons, Inc., New York, **2010**.
- [77] M. Berkowitz, S. K. Ghosh, R. G. Parr, *J. Am. Chem. Soc.* **1985**, *107*, 6811-6814.
- [78] R. G. Parr, R. G. Pearson, *J. Am. Chem. Soc.* **1983**, *105*, 7512-7516.
- [79] F. E. Hahn, M. C. Jahnke, *Angew. Chem. Int. Ed.* **2008**, *47*, 3122-3172.
- [80] O. Back, B. Donnadiou, P. Parameswaran, G. Frenking, G. Bertrand, *Nat. Chem.* **2010**, *2*, 369-373.

- [81] A. J. I. Arduengo, *Acc. Chem. Res.* **1999**, *32*, 913-921.
- [82] A. J. I. Arduengo, R. Krafczyk, *Chem. unserer Zeit* **1998**, *32*, 6-14.
- [83] W. A. Herrmann, C. Kocher, *Angew. Chem. Int. Ed.* **1997**, *36*, 2162-2187.
- [84] A. J. I. Arduengo, F. Davidson, R. Krafczyk, W. J. Marshall, R. Schmutzler, *Monatsh. Chem.* **2000**, *131*, 251-265.
- [85] H. Li, C. Risko, J. H. Seo, C. Campbell, G. Wu, J. L. Bredas, G. C. Bazan, *J. Am. Chem. Soc.* **2011**, *133*, 12410-12413.
- [86] C. M. Bax, A. R. Katritzky, L. E. Sutton, *J. Chem. Soc.* **1958**, *0*, 1258-1263.
- [87] H. C. Brown, R. R. Holmes, *J. Am. Chem. Soc.* **1956**, *78*, 2173-2176.
- [88] M. F. Lappert, *J. Chem. Soc.* **1962**, *0*, 542-548.
- [89] M. A. Beckett, G. C. Strickland, J. R. Holland, K. S. Varma, *Polymer* **1996**, *37*, 4629-4631.
- [90] D. G. Brown, R. S. Drago, T. F. Bolles, *J. Am. Chem. Soc.* **1968**, *90*, 5706-5712.
- [91] Y. L. Yang, Y. Kou, *Chem. Comm.* **2004**, *0*, 226-227.
- [92] U. Mayer, V. Gutmann, W. Gerger, *Monatsh. Chem.* **1975**, *106*, 1235-1257.
- [93] A. H. Zewail, *Pure Appl. Chem.* **2000**, *72*, 2219-2231.
- [94] T. Bally, in *Reactive Intermediate Chemistry*, Vol. 263 (Ed.: R. A. Moss, Platz, M. S., Jones, M. Jr.), John Wiley & Sons, Inc., Hoboken, New Jersey, **2005**, pp. 795-845.
- [95] E. Whittle, D. A. Dows, G. C. Pimentel, *J. Chem. Phys.* **1954**, *22*, 1943.
- [96] I. Norman, G. Porter, *Nature* **1954**, *174*, 508-509.
- [97] I. R. Dunkin, *Chem. Soc. Rev.* **1980**, *9*, 1-23.
- [98] H. E. Hallam, *Vibrational spectroscopy of trapped species: infrared and Raman studies of matrix-isolated molecules, radicals and ions*, J. Wiley, London, **1973**.
- [99] C. Wenstrup, *Angew. Chem. Int. Ed.* **2018**, *57*, 11508-11521.
- [100] A. Marduykov, R. Crespo-Otero, E. Sanchez-Garcia, W. Sander, *Chem. Eur. J.* **2010**, *16*, 8679-8689.
- [101] X. Zhang, A. V. Friderichsen, S. Nandi, G. B. Ellison, D. E. David, J. T. McKinnon, T. G. Lindeman, D. C. Dayton, M. R. Nimlos, *Rev. Sci. Instrum.* **2003**, *74*, 3077-3086.
- [102] V. E. Bondybey, A. M. Smith, J. Agreiter, *Chem. Rev.* **1996**, *96*, 2113-2134.
- [103] T. Enyo, A. Nicolaides, H. Tomioka, *J. Org. Chem.* **2002**, *67*, 5578-5587.
- [104] S. Radhakrishnan, J. Mieres-Perez, M. S. Gudipati, W. Sander, *J. Phys. Chem. A* **2017**, *121*, 6405-6412.
- [105] P. Costa, W. Sander, *Angew. Chem. Int. Ed.* **2014**, *53*, 5122-5125.
- [106] P. Costa, W. Sander, *J. Phys. Org. Chem.* **2015**, *28*, 71-74.
- [107] J. B. Fenn, M. Mann, C. K. Meng, S. F. Wong, C. M. Whitehouse, *Science* **1989**, *246*, 64-71.
- [108] M. Yamashita, J. B. Fenn, *J. Phys. Chem.* **1984**, *88*, 4451-4459.
- [109] M. Yamashita, J. B. Fenn, *J. Phys. Chem.* **1984**, *88*, 4671-4675.
- [110] P. Kebarle, L. Tang, *Anal. Chem.* **1993**, *65*, 972A-986A.
- [111] G. Taylor, *Proc. Royal Soc. Lond.* **1964**, *280*, 383-397.
- [112] R. E. March, in *Encyclopedia of Analytical Chemistry* (Ed.: R. A. Meyers), John Wiley & Sons, Ltd., Chichester, **2000**, pp. 11848-11872.
- [113] W. Paul, *Angew. Chem.* **1990**, *102*, 780-789.
- [114] M. Liu, Rutgers, The State University of New Jersey **2011**.
- [115] M. Liu, T. T. Li, F. S. Amegayibor, D. S. Cardoso, Y. L. Fu, J. K. Lee, *J. Org. Chem.* **2008**, *73*, 9283-9291.
- [116] M. Chen, J. P. Moerdyk, G. A. Blake, C. W. Bielawski, J. K. Lee, *J. Org. Chem.* **2013**, *78*, 10452-10458.
- [117] K. Wang, M. Chen, Q. Y. Wang, X. D. Shi, J. K. Lee, *J. Org. Chem.* **2013**, *78*, 7249-7258.
- [118] R. G. Cooks, T. L. Kruger, *J. Am. Chem. Soc.* **1977**, *99*, 1279-1281.
- [119] S. A. McLuckey, D. Cameron, R. G. Cooks, *J. Am. Chem. Soc.* **1981**, *103*, 1313-1317.
- [120] S. Gronert, W. Y. Feng, F. Chew, W. M. Wu, *Int. J. Mass spectrom.* **2000**, *195*, 251-258.
- [121] K. B. Eisenthal, R. A. Moss, N. J. Turro, *Science* **1984**, *225*, 1439-1445.

- [122] S. Gronert, J. R. Keeffe, R. A. More O'Ferrall, *J. Am. Chem. Soc.* **2011**, *133*, 3381-3389.
- [123] R. A. Moss, *Acc. Chem. Res.* **1989**, *22*, 15-21.
- [124] M. S. Platz, V. M. Maloney, in *Kinetics and Spectroscopy of Carbenes and Biradicals* (Ed.: M. S. Platz), Springer US, Boston, MA, **1990**, pp. 239-352.
- [125] M. S. Platz, *The chemistry, kinetics, and mechanisms of triplet carbene processes in low-temperature glasses and solids*, Plenum: New York, N. Y., **1990**.
- [126] W. Sander, G. Bucher, S. Wierlacher, *Chem. Rev.* **1993**, *93*, 1583-1621.
- [127] J. Wang, Y. L. Zhang, J. Kubicki, M. S. Platz, *Photoch Photobio Sci* **2008**, *7*, 552-557.
- [128] K. B. Eisenthal, N. J. Turro, E. V. Sitzmann, I. R. Gould, G. Hefferon, J. Langan, Y. Cha, *Tetrahedron* **1985**, *41*, 1543-1554.
- [129] P. B. Grasse, B. E. Brauer, J. J. Zupancic, K. J. Kaufmann, G. B. Schuster, *J. Am. Chem. Soc.* **1983**, *105*, 6833-6845.
- [130] B. B. Wright, M. S. Platz, *J. Am. Chem. Soc.* **1984**, *106*, 4175-4180.
- [131] J. R. Keeffe, R. A. M. O'Ferrall, *Arkivoc* **2008**, 183-U149.
- [132] J. R. Pliego, W. B. DeAlmeida, *J Chem Soc Faraday T* **1997**, *93*, 1881-1883.
- [133] A. H. Raut, G. Karir, K. S. Viswanathan, *J. Phys. Chem. A* **2016**, *120*, 9390-9400.
- [134] I. M. Moritani, S.; Nishino, M.; Yamamoto, Y.; Itoh, K.; Mataga, N., *J. Am. Chem. Soc.* **1967**, *89*, 1259-1260.
- [135] E. Wasserman, W. A. Yager, A. M. Trozzolo, R. W. Murray, *J. Chem. Phys.* **1964**, *40*, 2408-2410.
- [136] H. L. Woodcock, D. Moran, B. R. Brooks, P. v. R. Schleyer, H. F. Schaefer, III, *J. Am. Chem. Soc.* **2007**, *129*, 3763-3770.
- [137] I. Moritani, S. I. Murahashi, H. Ashitaka, K. Kimura, H. Tsubomura, *J. Am. Chem. Soc.* **1968**, *90*, 5918-5919.
- [138] L. M. Hadel, M. S. Platz, B. B. Wright, J. C. Scaiano, *Chem. Phys. Lett.* **1984**, *105*, 539-543.
- [139] K. C. Clemitshaw, J. R. Sodeau, *J. Phys. Chem.* **1988**, *92*, 5491-5497.
- [140] S. Henkel, I. Trosien, J. Mieres-Perez, T. Lohmiller, A. Savitsky, E. Sanchez-Garcia, W. Sander, *J. Org. Chem.* **2018**, *83*, 7586-7592.
- [141] O. Donoso-Tauda, P. Jaque, J. Elguero, I. Alkorta, *J. Phys. Chem. A* **2014**, *118*, 9552-9560.
- [142] O. Edlund, A. Lund, M. Shiotani, J. Sohma, K. A. Thuomas, *Mol. Phys.* **1976**, *32*, 49-69.
- [143] J. M. Bassler, P. L. Timms, J. L. Margrave, *J. Chem. Phys.* **1966**, *45*, 2704-&.
- [144] M. E. Jacox, W. E. Thompson, *J. Chem. Phys.* **2011**, *134*.
- [145] M. E. Jacox, W. E. Thompson, *J. Chem. Phys.* **1995**, *102*, 4747-4756.
- [146] L. A. Montero, A. M. Esteva, J. Molina, A. Zapardiel, L. Hernandez, H. Marquez, A. Acosta, *J. Am. Chem. Soc.* **1998**, *120*, 12023-12033.
- [147] P. Costa, I. Trosien, J. Mieres-Perez, W. Sander, *J. Am. Chem. Soc.* **2017**, *139*, 13024-13030.
- [148] R. F. W. Bader, *Atoms in molecules : a quantum theory*, Clarendon Press, Oxford, U. K., **1994**.
- [149] E. V. Sitzmann, J. G. Langan, D. Griller, K. B. Eisenthal, *Chem. Phys. Lett.* **1989**, *161*, 353-360.
- [150] P. B. Grasse, B. E. Brauer, J. J. Zupancic, K. J. Kaufmann, G. B. Schuster, *J. Am. Chem. Soc.* **1983**, *105*, 6833-6845.
- [151] J. Peon, D. Polshakov, B. Kohler, *J. Am. Chem. Soc.* **2002**, *124*, 6428-6438.
- [152] M. C. Courtney, A. C. MacCormack, R. A. M. O'Ferrall, *J. Phys. Org. Chem.* **2002**, *15*, 529-539.
- [153] J. J. Looker, *J. Org. Chem.* **1968**, *33*, 1304-1306.
- [154] A. H. Raut, P. Costa, W. Sander, *Chem. Eur. J.* **2018**, *24*, 18043-18051.
- [155] C. G. Salzmann, P. G. Radaelli, E. Mayer, J. L. Finney, *Phys. Rev. Lett.* **2009**, *103*.
- [156] O. Mishima, L. D. Calvert, E. Whalley, *Nature* **1984**, *310*, 393-395.
- [157] C. A. Tulk, C. J. Benmore, J. Urquidi, D. D. Klug, J. Neufeind, B. Tomberli, P. A. Egelstaff, *Science* **2002**, *297*, 1320-1323.
- [158] A. Shalit, F. Perakis, P. Hamm, *J. Phys. Chem. B* **2013**, *117*, 15512-15518.
- [159] F. Low, K. Amann-Winkel, T. Loerting, F. Fujara, B. Geil, *Phys. Chem. Chem. Phys.* **2013**, *15*, 9308-9314.
- [160] H. R. Zelsmann, *J. Mol. Struct.* **1995**, *350*, 95-114.

- [161] M. S. Gudipati, *J. Phys. Chem. A* **2004**, *108*, 4412-4419.
- [162] M. S. Gudipati, L. J. Allamandola, *Astrophys. J.* **2004**, *615*, L177-L180.
- [163] M. S. Gudipati, L. J. Allamandola, *J. Phys. Chem. A* **2006**, *110*, 9020-9024.
- [164] M. S. Gudipati, L. J. Allamandola, *Astrophys. J.* **2006**, *638*, 286-292.
- [165] L. M. Hadel, M. S. Platz, B. B. Wright, J. C. Scaiano, *Chem. Phys. Lett.* **1984**, *105*, 539-543.
- [166] H. Tomioka, in *Reactive Intermediate Chemistry* (Eds.: R. A. Moss, M. S. Platz, M. S. Jones), John Wiley & Sons, Inc., Hoboken, NJ, **2004**, pp. 375-462.
- [167] R. L. Barcus, B. B. Wright, E. Leyva, M. S. Platz, *J. Phys. Chem.* **1987**, *91*, 6677-6683.
- [168] S. Henkel, M. Ertelt, W. Sander, *Chem. Eur. J.* **2014**, *20*, 7585-7588.
- [169] S. Henkel, W. Sander, *Angew. Chem. Int. Ed.* **2015**, *54*, 4603-4607.
- [170] W. Sander, R. Hubert, E. Kraka, J. Grafenstein, D. Cremer, *Chem. Eur. J.* **2000**, *6*, 4567-4579.
- [171] P. S. Zuev, R. S. Sheridan, *J. Am. Chem. Soc.* **2001**, *123*, 12434-12435.
- [172] C. Kötting, W. Sander, *J. Am. Chem. Soc.* **1999**, *121*, 8891-8897.
- [173] W. Siebrand, T. A. Wildman, *Acc. Chem. Res.* **1986**, *19*, 238-243.
- [174] R. G. Parr, L. Von Szentpaly, S. B. Liu, *J. Am. Chem. Soc.* **1999**, *121*, 1922-1924.
- [175] F. Naderi, M. R. Momeni, F. A. Shakib, *A Density Functional Theory Study on the Stability and Ligand Properties of the Different Substituted Phenyl Carbenes*, Vol. 7, **2012**.
- [176] F. De Vleeschouwer, V. Van Speybroeck, M. Waroquier, P. Geerlings, F. De Proft, *Org. Lett.* **2007**, *9*, 2721-2724.
- [177] D. Braga, F. Grepioni, G. R. Desiraju, *Chem. Rev.* **1998**, *98*, 1375-1406.
- [178] G. R. Desiraju, *Acc. Chem. Res.* **2002**, *35*, 565-573.
- [179] G. R. Desiraju, T. Steiner, *The weak hydrogen bond in structural chemistry and biology*, Oxford University Press, Oxford ; New York, **1999**.
- [180] J. A. Gerlt, M. M. Kreevoy, W. W. Cleland, P. A. Frey, *Chem. Biol.* **1997**, *4*, 259-267.
- [181] S. J. Grabowski, *Hydrogen Bonding—New Insights*, Springer, **2006**.
- [182] G. A. Jeffrey, *An introduction to hydrogen bonding*, Oxford University Press, New York, **1997**.
- [183] C. L. Perrin, J. B. Nielson, *Annu. Rev. Phys. Chem.* **1997**, *48*, 511-544.
- [184] S. Scheiner, *Hydrogen bonding : a theoretical perspective*, Oxford University Press, New York, **1997**.
- [185] L. Sobczyk, S. J. Grabowski, T. M. Krygowski, *Chem. Rev.* **2005**, *105*, 3513-3560.
- [186] M. Fourmigue, *Curr. Opin. Solid State Mater. Sci.* **2009**, *13*, 36-45.
- [187] C. B. Aakeroy, M. Fasulo, N. Schultheiss, J. Desper, C. Moore, *J. Am. Chem. Soc.* **2007**, *129*, 13772-13773.
- [188] E. Corradi, S. V. Meille, M. T. Messina, P. Metrangolo, G. Resnati, *Angew. Chem. Int. Ed.* **2000**, *39*, 1782-1786.
- [189] D. B. Fox, R. Liantonio, P. Metrangolo, T. Pilati, G. Resnati, *J. Fluorine Chem.* **2004**, *125*, 271-281.
- [190] P. Metrangolo, H. Neukirch, T. Pilati, G. Resnati, *Acc. Chem. Res.* **2005**, *38*, 386-395.
- [191] P. Metrangolo, G. Resnati, *Chem. Eur. J.* **2001**, *7*, 2511-2519.
- [192] D. Cincic, T. Friscic, W. Jones, *Chem. Eur. J.* **2008**, *14*, 747-753.
- [193] D. Cincic, T. Friscic, W. Jones, *J. Am. Chem. Soc.* **2008**, *130*, 7524-7525.
- [194] P. Metrangolo, F. Meyer, T. Pilati, G. Resnati, G. Terraneo, *Angew. Chem. Int. Ed.* **2008**, *47*, 6114-6127.
- [195] P. Metrangolo, G. Resnati, T. Pilati, R. Liantonio, F. Meyer, *J. Polym. Sci., Part A: Polym. Chem.* **2007**, *45*, 1-15.
- [196] S. Derossi, L. Brammer, C. A. Hunter, M. D. Ward, *Inorg. Chem.* **2009**, *48*, 1666-1677.
- [197] T. Shirman, T. Arad, M. E. van der Boom, *Angew. Chem. Int. Ed.* **2010**, *49*, 926-929.
- [198] P. Auffinger, F. A. Hays, E. Westhof, P. S. Ho, *Proc. Natl. Acad. Sci. USA* **2004**, *101*, 16789-16794.
- [199] A. R. Voth, F. A. Hays, P. S. Ho, *Proc. Natl. Acad. Sci. USA* **2007**, *104*, 6188-6193.
- [200] P. P. Zhou, W. Y. Qiu, S. Liu, N. Z. Jin, *Phys. Chem. Chem. Phys.* **2011**, *13*, 7408-7418.

- [201] P. Politzer, P. Lane, M. C. Concha, Y. G. Ma, J. S. Murray, *J. Mol. Model.* **2007**, *13*, 305-311.
- [202] T. Clark, M. Hennemann, J. S. Murray, P. Politzer, *J. Mol. Model.* **2007**, *13*, 291-296.
- [203] P. Politzer, J. S. Murray, *Chemphyschem* **2013**, *14*, 278-294.
- [204] E. Bilewicz, A. J. Rybarczyk-Pirek, A. T. Dubis, S. J. Grabowski, *J. Mol. Struct.* **2007**, *829*, 208-211.
- [205] A. C. Legon, *Angew. Chem. Int. Ed.* **1999**, *38*, 2687-2714.
- [206] A. C. Legon, *Phys. Chem. Chem. Phys.* **2010**, *12*, 7736-7747.
- [207] B. Raghavendra, E. Arunan, *J. Phys. Chem. A* **2007**, *111*, 9699-9706.
- [208] A. C. Legon, D. J. Millen, *Chem. Soc. Rev.* **1987**, *16*, 467-498.
- [209] H. Chen, D. R. Justes, R. G. Cooks, *Org. Lett.* **2005**, *7*, 3949-3952.
- [210] A. J. Arduengo, III, S. F. Gamper, M. Tamm, J. C. Calabrese, F. Davidson, H. A. Craig, *J. Am. Chem. Soc.* **1995**, *117*, 572-573.
- [211] A. J. Arduengo, III, M. Kline, J. C. Calabrese, F. Davidson, *J. Am. Chem. Soc.* **1991**, *113*, 9704-9705.
- [212] A. J. Arduengo, III, M. Tamm, J. C. Calabrese, *J. Am. Chem. Soc.* **1994**, *116*, 3625-3626.
- [213] J. A. Cowan, J. A. C. Clyburne, M. G. Davidson, R. L. W. Harris, J. A. K. Howard, P. Kupper, M. A. Leech, S. P. Richards, *Angew. Chem. Int. Ed.* **2002**, *41*, 1432-1434.
- [214] M. Movassaghi, M. A. Schmidt, *Org. Lett.* **2005**, *7*, 2453-2456.
- [215] I. S. Sosulin, E. S. Shiryayeva, D. A. Tyurin, V. I. Feldman, *J. Chem. Phys.* **2017**, *147*, 131102.
- [216] N. Ramanathan, B. P. Kar, K. Sundararajan, K. S. Viswanathan, *J. Phys. Chem. A* **2012**, *116*, 12014-12023.
- [217] E. Espinosa, E. Molins, C. Lecomte, *Chem. Phys. Lett.* **1998**, *285*, 170-173.
- [218] D. Forney, M. E. Jacox, K. K. Irikura, *J. Chem. Phys.* **1994**, *101*, 8290-8296.
- [219] R. A. Moss, M. J. Jones, *React. Intermed. (Wiley)* **1985**, *3*, 45-108.
- [220] P. H. Mueller, N. G. Rondan, K. N. Houk, J. F. Harrison, D. Hooper, B. H. Willen, J. F. Liebman, *J. Am. Chem. Soc.* **1981**, *103*, 5049-5052.
- [221] A. Admasu, A. D. Gudmundsdottir, M. S. Platz, *J. Phys. Chem. A* **1997**, *101*, 3832-3840.
- [222] P. A. Hoijemberg, R. A. Moss, K. Krogh-Jespersen, *J. Phys. Chem. A* **2012**, *116*, 358-363.
- [223] M. B. Jones, M. S. Platz, *J. Org. Chem.* **1991**, *56*, 1694-1695.
- [224] R. A. Moss, L. Wang, C. M. Odorisio, M. Zhang, K. Krogh-Jespersen, *J. Phys. Chem. A* **2010**, *114*, 209-217.
- [225] J. Xue, H. L. Luk, M. S. Platz, *J. Am. Chem. Soc.* **2011**, *133*, 1763-1765.
- [226] H. Iwamura, *Pure Appl. Chem.* **1987**, *59*, 1595-1604.
- [227] H. Murai, M. Torres, O. P. Strausz, *J. Am. Chem. Soc.* **1980**, *102*, 7390-7391.
- [228] S. Suzer, L. Andrews, *J. Chem. Phys.* **1987**, *87*, 5131-5140.
- [229] Y. A. Tsegaw, Ruhr Universität Bochum (Bochum), **2018**.
- [230] I. Despotovic, Z. B. Maksic, R. Vianello, *New J. Chem.* **2007**, *31*, 52-62.
- [231] R. Vianello, H. Maskill, Z. B. Maksic, *Eur. J. Org. Chem.* **2006**, 2581-2589.
- [232] V. Raab, E. Gauchenova, A. Merkoulov, K. Harms, J. Sundermeyer, B. Kovacevic, Z. B. Maksic, *J. Am. Chem. Soc.* **2005**, *127*, 15738-15743.
- [233] V. Raab, J. Kipke, R. M. Gschwind, J. Sundermeyer, *Chem. Eur. J.* **2002**, *8*, 1682-1693.
- [234] A. J. I. Arduengo, R. L. Harlow, M. Kline, *J. Am. Chem. Soc.* **1991**, *113*, 361-363.
- [235] F. Glorius, *N-Heterocyclic Carbenes in Transition Metal Catalysis, Vol. 21*, Springer, Heidelberg, **2007**.
- [236] W. A. Herrmann, *Angew. Chem. Int. Ed.* **2002**, *41*, 1290-1309.
- [237] S. P. Nolan, *N-Heterocyclic carbenes in synthesis*, Wiley, New York, **2006**.
- [238] A. M. Magill, K. J. Cavell, B. F. Yates, *J. Am. Chem. Soc.* **2004**, *126*, 8717-8724.
- [239] T. L. Amyes, S. T. Diver, J. P. Richard, F. M. Rivas, K. Toth, *J. Am. Chem. Soc.* **2004**, *126*, 4366-4374.
- [240] E. M. Higgins, J. A. Sherwood, A. G. Lindsay, J. Armstrong, R. S. Massey, R. W. Alder, A. C. O'Donoghue, *Chem. Commun.* **2011**, *47*, 1559-1561.

- [241] R. S. Massey, C. J. Collett, A. G. Lindsay, A. D. Smith, A. C. O'Donoghue, *J. Am. Chem. Soc.* **2012**, *134*, 20421-20432.
- [242] M. W. Washabaugh, W. P. Jencks, *Biochemistry-Us* **1988**, *27*, 5044-5053.
- [243] R. W. Alder, P. R. Allen, S. J. Williams, *J. Chem. Soc., Chem. Commun.* **1995**, *0*, 1267-1268.
- [244] Y. Chu, H. Deng, J. P. Cheng, *J. Org. Chem.* **2007**, *72*, 7790-7793.
- [245] Y. J. Kim, A. Streitwieser, *J. Am. Chem. Soc.* **2002**, *124*, 5757-5761.
- [246] K. M. Ervin, *Chem. Rev.* **2001**, *101*, 391-444.
- [247] S. Gronert, *Chem. Rev.* **2001**, *101*, 329-360.
- [248] M. Liu, M. Chen, S. S. Zhang, I. Yang, B. Buckley, J. K. Lee, *J. Phys. Org. Chem.* **2011**, *24*, 929-936.
- [249] J. Vogt, J. L. Beauchamp, *J. Am. Chem. Soc.* **1975**, *97*, 6682-6685.
- [250] P. Ausloos, S. G. Lias, *J. Am. Chem. Soc.* **1978**, *100*, 4594-4595.
- [251] B. A. Levi, R. W. Taft, W. J. Hehre, *J. Am. Chem. Soc.* **1977**, *99*, 8454-8455.
- [252] M. Liu, I. Yang, B. Buckley, J. K. Lee, *Org. Lett.* **2010**, *12*, 4764-4767.
- [253] K. J. Miller, J. A. Savchik, *J. Am. Chem. Soc.* **1979**, *101*, 7206-7213.
- [254] T. Su, W. J. Chesnavich, *J. Chem. Phys.* **1982**, *76*, 5183-5185.
- [255] W. Zeng, T. E. Ballard, A. G. Tkachenko, V. A. Burns, D. L. Feldheim, C. Melander, *Bioorg. Med. Chem. Lett.* **2006**, *16*, 5148-5151.
- [256] T. Yang, Z. Q. Jiang, X. D. Huang, H. X. Wei, J. Y. Yuan, W. Yue, Y. Y. Li, W. L. Ma, *Org. Electron.* **2013**, *14*, 2184-2191.
- [257] M. C. Young, A. M. Johnson, R. J. Hooley, *Chem. Commun.* **2014**, *50*, 1378-1380.
- [258] A. L. J. Beckwith, C. J. Easton, *J. Am. Chem. Soc.* **1981**, *103*, 615-619.
- [259] L. D. Hicks, J. K. Han, A. J. Fry, *Tetrahedron Lett.* **2000**, *41*, 7817-7820.
- [260] W. H. Graham, *J. Am. Chem. Soc.* **1965**, *87*, 4396-4397.
- [261] A. Schonberg, K. Junghans, *Chem. Ber. Recl.* **1962**, *95*, 2137-2143.
- [262] A. Levy, S. Cohen, I. Agranat, *Org. Biomol. Chem.* **2003**, *1*, 2755-2763.
- [263] W. Z. Yan, J. Qing, H. B. Mei, J. X. Nong, J. Huang, J. Zhu, H. L. Jiang, L. Liu, L. Q. Zhang, J. Li, *Bioorg. Med. Chem. Lett.* **2015**, *25*, 5682-5686.
- [264] K. Kloc, J. Mlochowski, Z. Szulc, *J. Prakt. Chem.* **1977**, *319*, 959-967.
- [265] F. F. Guzik, A. K. Colter, *Can. J. Chem.* **1965**, *43*, 1441-1447.
- [266] M. Jereb, D. Vrazic, *Org. Biomol. Chem.* **2013**, *11*, 1978-1999.
- [267] M. J. Frisch, G. W. Trucks, H. B. Schlegel, G. E. Scuseria, M. A. Robb, J. R. Cheeseman, G. Scalmani, V. Barone, B. Mennucci, G. A. Petersson, H. Nakatsuji, M. Caricato, X. Li, H. P. Hratchian, A. F. Izmaylov, J. Bloino, G. Zheng, J. L. Sonnenberg, M. Hada, M. Ehara, K. Toyota, R. Fukuda, J. Hasegawa, M. Ishida, T. Nakajima, Y. Honda, O. Kitao, H. Nakai, T. Vreven, J. Montgomery, J. A., J. E. Peralta, F. Ogliaro, M. Bearpark, J. J. Heyd, E. Brothers, K. N. Kudin, V. N. Staroverov, R. Kobayashi, J. Normand, K. Raghavachari, A. Rendell, J. C. Burant, S. S. Iyengar, J. Tomasi, M. Cossi, N. Rega, N. J. Millam, M. Klene, J. E. Knox, J. B. Cross, V. Bakken, C. Adamo, J. Jaramillo, R. Gomperts, R. E. Stratmann, O. Yazyev, A. J. Austin, R. Cammi, C. Pomelli, J. W. Ochterski, R. L. Martin, K. Morokuma, V. G. Zakrzewski, G. A. Voth, P. Salvador, J. J. Dannenberg, S. Dapprich, A. D. Daniels, Ö. Farkas, J. B. Foresman, J. V. Ortiz, J. Cioslowski, D. J. Fox, Revision B.01 ed., Gaussian, Inc., Wallingford CT, **2010**.
- [268] C. T. Lee, W. T. Yang, R. G. Parr, *Phys. Rev. B* **1988**, *37*, 785-789.
- [269] B. Miehlich, H. Stoll, A. Savin, *Mol. Phys.* **1997**, *91*, 527-536.
- [270] S. H. Vosko, L. Wilk, M. Nusair, *Can. J. Phys.* **1980**, *58*, 1200-1211.
- [271] S. Grimme, J. Antony, S. Ehrlich, H. Krieg, *J. Chem. Phys.* **2010**, *132*, 154104.
- [272] F. Weigend, M. Haser, H. Patzelt, R. Ahlrichs, *Chem. Phys. Lett.* **1998**, *294*, 143-152.
- [273] A. D. Becke, *J. Chem. Phys.* **1993**, *98*, 1372-1377.
- [274] A. D. Becke, *J. Chem. Phys.* **1993**, *98*, 5648-5652.
- [275] W. Kohn, A. D. Becke, R. G. Parr, *J. Phys. Chem.* **1996**, *100*, 12974-12980.

- [276] P. J. Stephens, F. J. Devlin, C. F. Chabalowski, M. J. Frisch, *J. Phys. Chem.* **1994**, *98*, 11623-11627.
- [277] H. J. Werner, P. J. Knowles, G. Knizia, F. R. Manby, M. Schutz, *Wiley Interdiscip. Rev. Comput. Mol. Sci.* **2012**, *2*, 242-253.
- [278] E. D. Glendening, A. E. Reed, J. E. Carpenter, F. Weinhold.
- [279] S. Stoll, A. Schweiger, *J. Magn. Reson.* **2006**, *178*, 42-55.

Acknowledgements

I would like to express my sincere gratitude to Prof. Dr. Wolfram Sander for providing me an opportunity to conduct my doctoral studies in his research group. His guidance, generous contribution of knowledge and experience, valuable comments and motivation is what made this work possible. I have really enjoyed my tenure under his guidance.

I am also grateful to Prof. Dr. Nürnberger for being the second supervisor and several insightful scientific discussions. I would like to thank Prof. Jeehiun Lee for hosting me for a two-month research internship in her group at Rutgers University, New Jersey (USA). It was always a great pleasure to discuss with her about different research topics, especially in the field of mass spectroscopy. I also extend my thanks to her group members Allison, Jiahui, Lanxing and Ning for teaching me ion cyclotron resonance and liquid quadrupole resonance mass spectroscopy and for providing me a nice atmosphere during my stay.

My sincere gratitude goes to Herr Torsten Haenschke for his generous help with compute related problems and installing required software required for this work. I want to thank Dr. Dirk Grote for his help with EPR simulations. I would like to express my appreciation to Catharina Fulde for unreserved technical assistance throughout the work and explaining me technical details of various instruments. I wish to thank Herr Klaus Gomann and Robin Giebmanns for their help in synthesis laboratory. Special thanks to Herr Klaus for being my Deutsch Lehrer and showing a great patience in listening to my ultraslow German. I am very grateful to administrative help received by Frau Sabine Weiss and Frau Jacinta Essling. I thank Frau Gundula Talbot, the coordination office of Graduate School of Chemistry and Biochemistry, for her advices for completion of the doctoral program requirements.

I am extremely thankful to all the former and present lab members, namely, Adam, Adrián, Ankit, Arun, Christian, Corina, Enrique, Geneviève, Iris, Joel, Julien, Karoline, Liang, Linda, Melania, Mika, Mohamed, Nesli, Nora, Paolo, Pritam, Soumya, Stefan, Sujan, Tim, Tino, Tobias, and Yetsedaw for all the help and kindness. This group is really amazing! I doubt that I will have such a good time in any other group in the future. I would like to extend my thanks to my in-depth and summer internship students Max, Sebastian, Shivangi (IISER Mohali) and Vikas (IIT Mumbai) for their sincere efforts in synthesizing various compounds. A million thanks to Paolo and Stefan

for everything you have taught me and I want to know how much I value your support. I am grateful to Joel and Enrique for helping me with the calculations and introducing Cuban way of life. I also wish to convey my deepest thanks to Stefan, Enrique, Iris and Yetsedaw proofreading some of the sections of my dissertation, and helping with the synthesis, measurement and data analysis. Thanks a lot to Corina, Nora, Stefan, and Melania for a special outdoor group activity 'Escape Room' and Pritam for Marathi talks which gave me homely feeling.

Time flew by in the company of good friends Nitish, Gaurav, Devendra, Vivek, Vaibhav, Dipali, Tarun, Swati, Anirban, Vishal, Pragati, Sagar, Kaushik, Mona, Ujas, Shiva, Swati, Mrunmay, Sandeepan, Swapnil whom created 'Indian' atmosphere during my stay in Germany. Another special rounds of thanks to friends away from here, Sayali, Banny, Aniket, Aru, Tejas, Nikhil, Nayan, Manas, TC, Yogesh, Bapu, Piyush and other who are not mentioned by name for having a laugh whenever possible. My heartiest gratitude are also to Prof. K. S. Viswanathan at IISER Mohali for introducing to Matrix Isolation and motivating me to pursue my career in research.

Last but not least, I wish to acknowledge my family for all the support, encouragement and wishes from a distance. I cannot thank them enough. Thank you for your everlasting love from thousands of miles away. This is for you!

Appendix

Figures

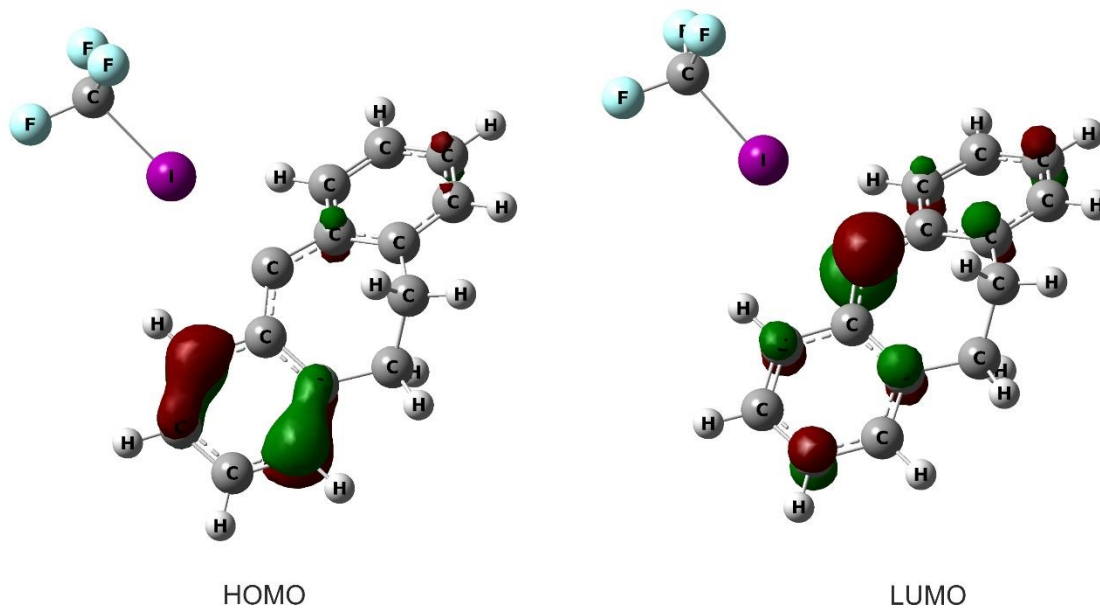


Figure A1. Molecular orbitals involved in electronic transition ($\lambda = 346$ nm) assigned to conventional halogen-bonded complex **33a** between singlet dibenzocycloheptadienylidene **S-25** and ICF₃, computed at the B3LYP-D3/def2-TZVP level of theory.

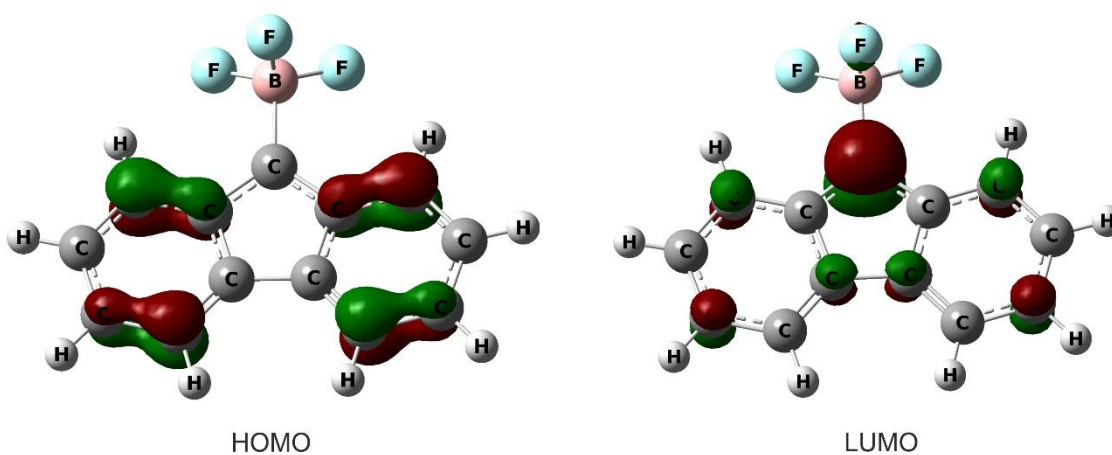


Figure A2. Molecular orbitals involved in electronic transition ($\lambda = 405$ nm) assigned to conventional Lewis adduct **36** between singlet fluorenylidene **S-8** and BF₃, computed at the B3LYP-D3/def2-TZVP level of theory.

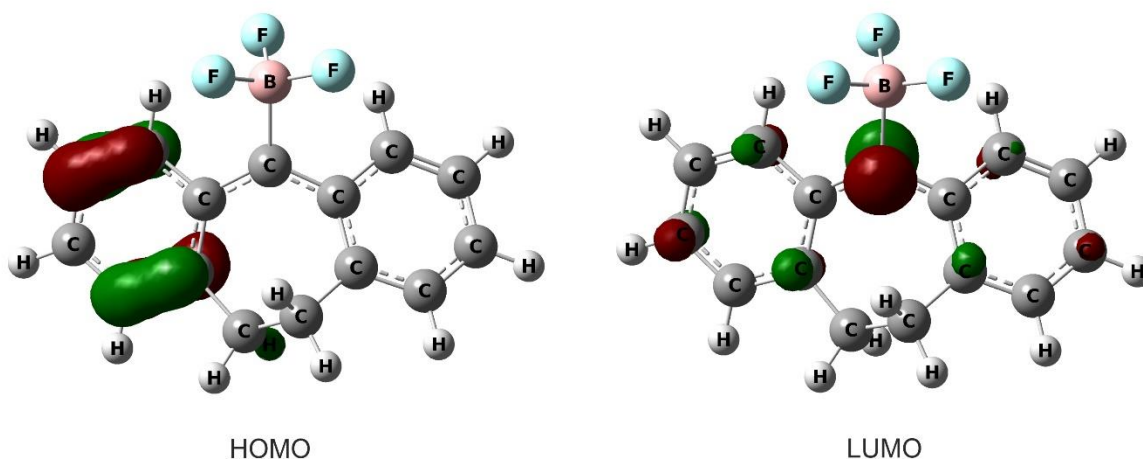


Figure A3. Molecular orbitals involved in electronic transition ($\lambda = 372$ nm) assigned to conventional Lewis adduct **38a** between singlet dibenzocycloheptadienylidene **S-25** and BF_3 , computed at the B3LYP-D3/def2-TZVP level of theory.

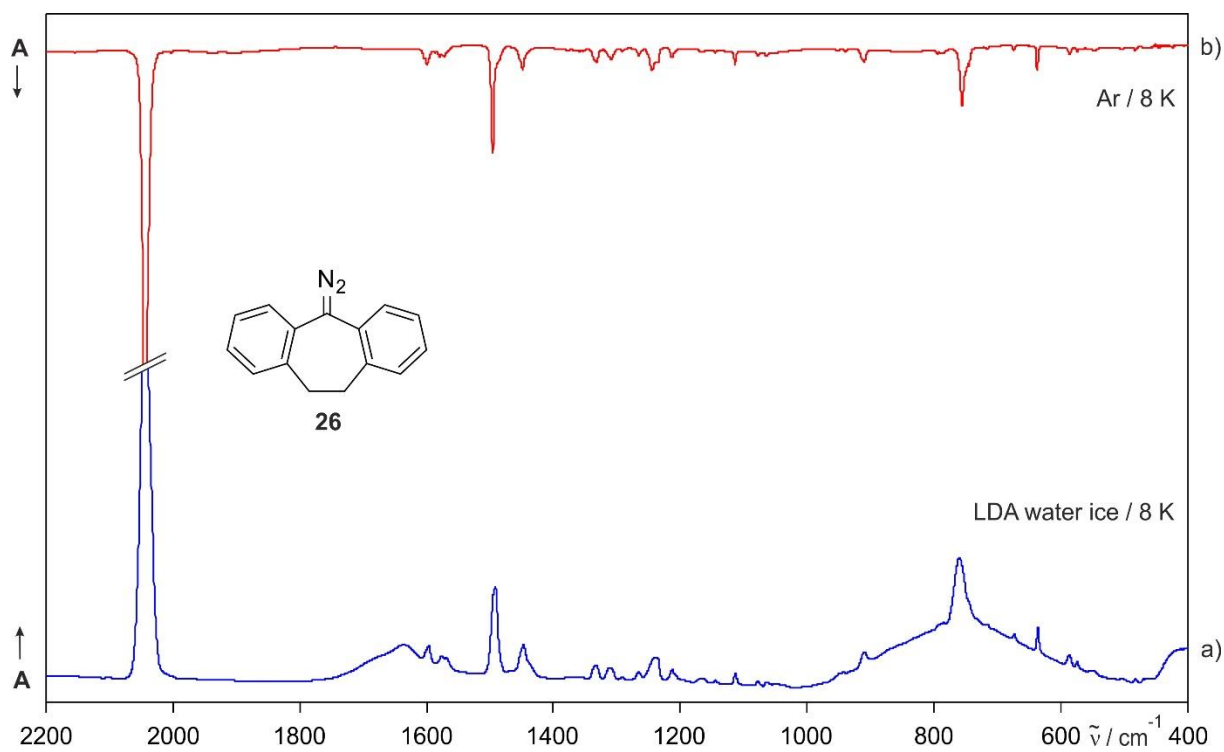


Figure A4. a) IR spectrum of diazodibenzocycloheptadienylidene **26** trapped in LDA water ice at 8 K. The line broadening is attributed to inhomogeneity of the matrix cages in LDA water ice. b) IR spectrum of **26** trapped in a solid argon matrix at 8 K.

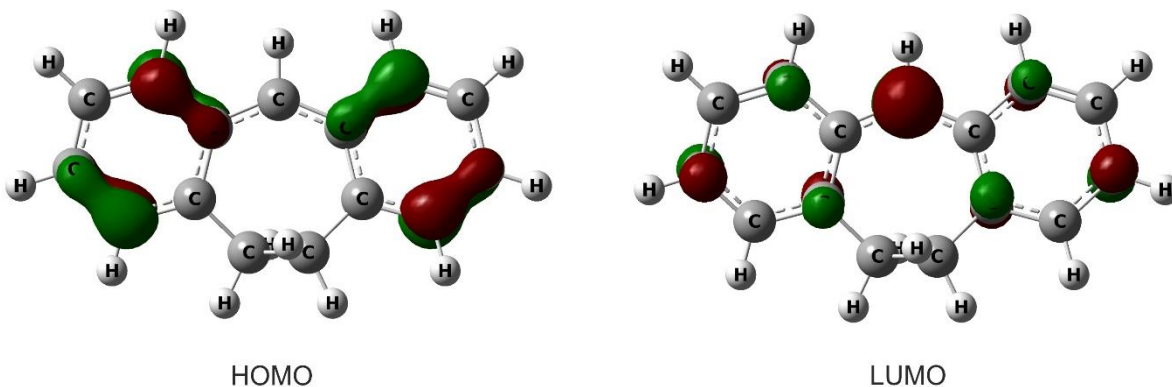


Figure A5. Molecular orbitals involved in electronic transition ($\lambda = 346$ nm) assigned to dihydrodibenzotropylium cation **41**, computed at the B3LYP-D3/def2-TZVP level of theory.

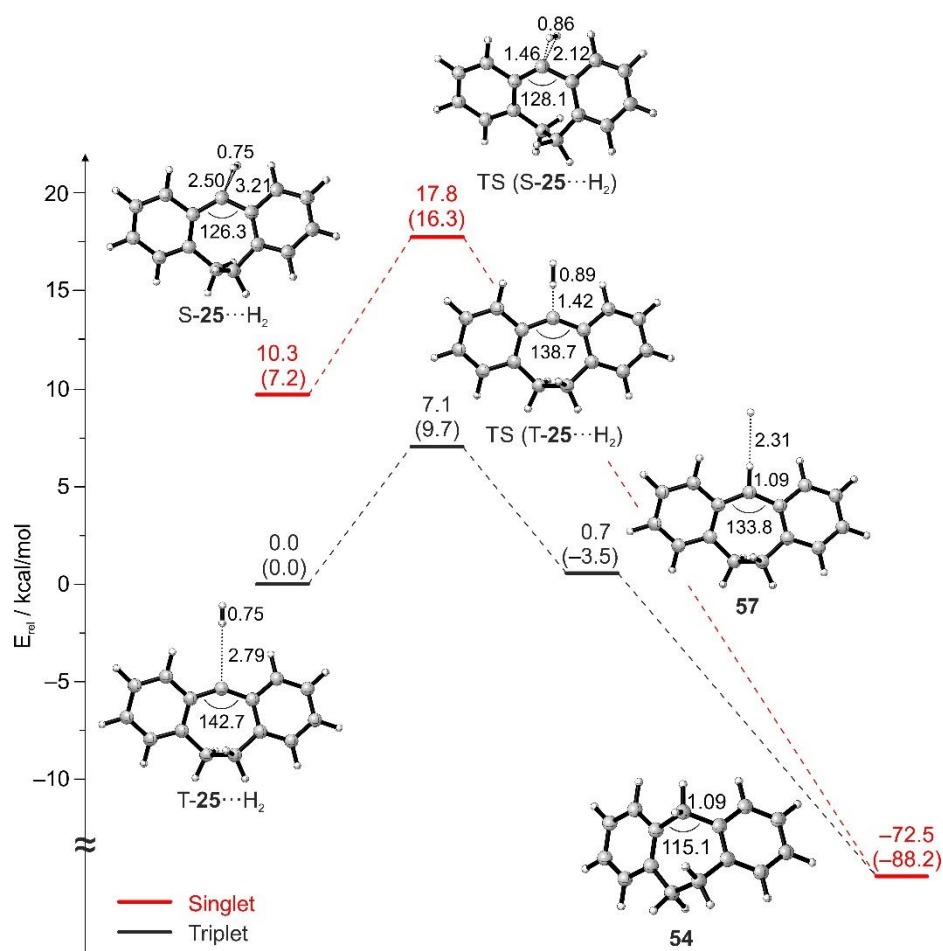


Figure A6. Hydrogenation of dibenzocycloheptadienylidene **25** on the singlet (red) and triplet (black) potential energy surfaces calculated at the ZPE-corrected B3LYP-D3/def2-TZVP level of theory. Values in parentheses correspond to CCSD(T)/cc-PVDZ//B3LYP-D3/def2-TZVP energies. Energies are given in kcal/mol and selected bond lengths and angles are given in Å and °, respectively.

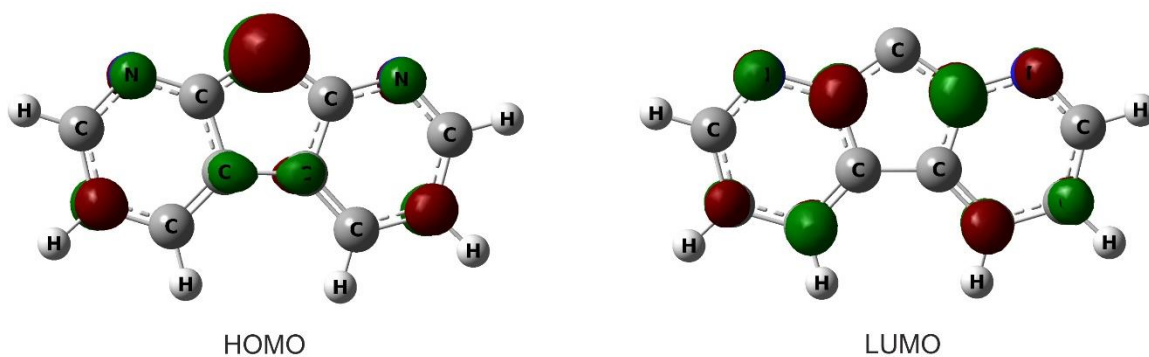


Figure A7. Molecular orbitals involved in electronic transition ($\lambda = 255$ nm) assigned to 1,8-diazafluorenylidene **71**, computed at the B3LYP-D3/def2-TZVP level of theory.

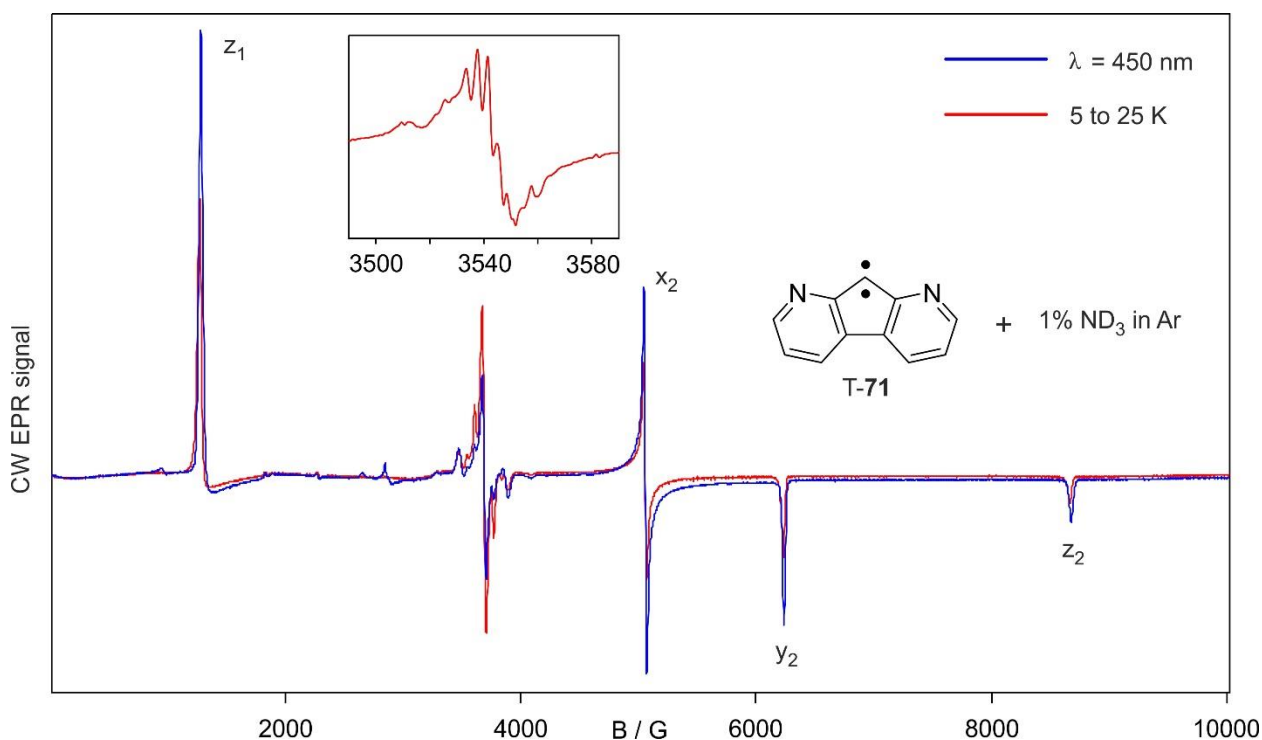


Figure A8. EPR spectra showing the reaction of T-**71** with ND₃. Blue line: spectrum of T-**71** generated upon 450 nm photolysis of diazo precursor **72** in an argon matrix doped with 1% of ND₃ at 5 K. Red line: spectrum of the same matrix showing the changes after annealing at 25 K. The signals of T-**71** decrease due to the formation of EPR silent deuterated insertion product [D]-**74**. The inset shows the hyperfine splitting which is roughly assigned to ND₂ radical. However, this radical assignment is tentative due to the broad and complex radical area arising probably from the interaction of the radical electron with multiple surrounding nuclei. The splitting observed in the signals of ND₂ radical differ from that of NH₂ radical (Figure 67), which implies that this splitting of radical signals arises mainly due to hydrogen or deuterium atoms rather than nitrogen atom.

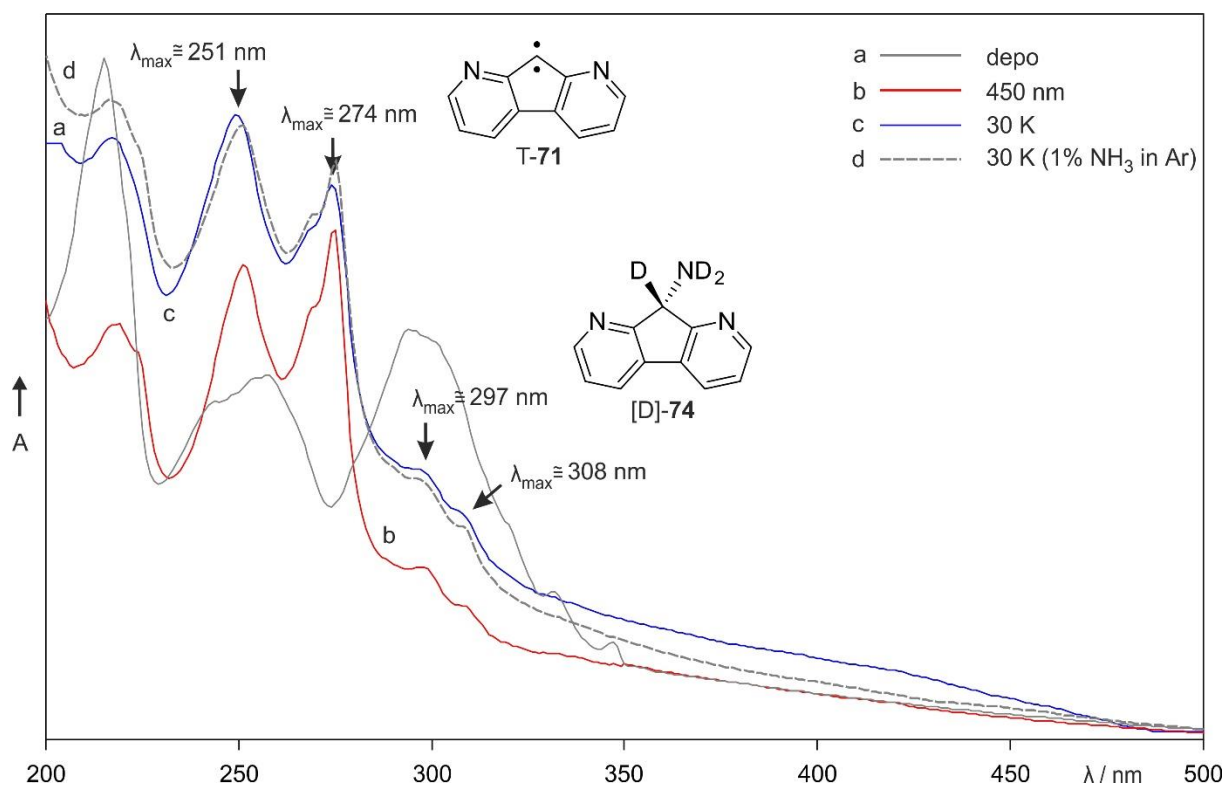


Figure A9. UV-Vis spectra showing the reaction of T-71 with ND₃ (except trace d). a) UV-Vis spectrum of diazo precursor **72** in an argon matrix doped with 1% of ND₃ at 8 K. b) UV-Vis spectrum of T-71 generated upon irradiation of the same matrix with 450 nm. c) UV-Vis spectrum of the same matrix obtained after annealing at 30 K. The bands at $\lambda_{\max} = 297$ and 308 nm are assigned to the formal N–D insertion product [D]-74. d) UV-Vis spectrum of T-71 in an argon matrix doped with 1% of NH₃ showing the changes after annealing at 30 K. The newly formed bands at $\lambda_{\max} = 298$ and 308 nm are assigned to the formal N–H insertion product **74**, indicating no isotopic shift with respect to deuterated product.

Tables

Table A1. Vibrational frequencies of diazodibenzocycloheptadienyldiene **26**.

Mode	DFT ^[a]		LDA water ^[b]		Argon ^[c]		Assignment
	$\tilde{\nu}$ / cm ⁻¹	I _{abs}	$\tilde{\nu}$ / cm ⁻¹	I _{abs}	$\tilde{\nu}$ / cm ⁻¹	I _{abs}	
20	595.7	1	586.2	1	586.3	2	CH ₂ bend
22	653.5	2	637.6	3	636.0	6	C=N ₂ bend
25, 26, 27	759.6, 764.6, 772.5	15	755.7	12	759.8	18	C-H wagging
32	928.2	3	910.2	2	910.9	4	Ring def.
51	1276.9	7	1244.8	3	1241.2	6	Sym. C-C-C str.
55	1345.2	4	1332.3	3	1333.2	6	C=C str.
62	1494.6	5	1448.6	3	1447.6	8	C-H bend
63	1524.3	12	1495.9	15	1491.9	23	C=C str.
65	1606.2	3	1572.5	1	1569.3	3	C=C str.
67	1638.3	3	1599.7	2	1596.8	4	C=C str.
69	2152.6	100	2045.3	100	2044.4	100	Asym. C=N ₂ str.

^[a]Calculated at the B3LYP-D3/def2-TZVP level of theory. ^[b]Argon matrix at 8 K. ^[c]LDA water ice at 8 K.

Optimized Geometries

Calculated at B3LYP-D3/def2-TZVP level of theory

Table A2. Cartesian coordinates of S-7.

Atom	X	Y	Z
C	3.72842400	-0.70766900	-0.13845400
C	2.64014000	-1.25634700	-0.81345600
C	1.39928500	-0.64565000	-0.74135800
C	1.23024300	0.57676900	-0.04314600
C	2.36771300	1.14116000	0.58194700
C	3.58391500	0.48379700	0.57412800
H	4.69299000	-1.19814100	-0.18042900
H	2.76122500	-2.17198000	-1.37914300
H	0.55004200	-1.07920300	-1.25271100
H	2.25186000	2.09505200	1.07973400
H	4.43532600	0.91216000	1.08791800
C	0.00000000	1.29658500	0.00000000
C	-1.23024300	0.57676900	0.04314600
C	-1.39928500	-0.64565000	0.74135800
C	-2.36771300	1.14116000	-0.58194700
C	-2.64014000	-1.25634700	0.81345600
H	-0.55004200	-1.07920300	1.25271100
C	-3.58391500	0.48379700	-0.57412800
H	-2.25186000	2.09505200	-1.07973400
C	-3.72842400	-0.70766900	0.13845400
H	-2.76122500	-2.17198000	1.37914300
H	-4.43532600	0.91216000	-1.08791800
H	-4.69299000	-1.19814100	0.18042900

E = -501.49342503, ZPE = 0.1843713

Table A3. Cartesian coordinates of T-7.

Atom	X	Y	Z
C	3.98519600	-0.49841900	-0.07987700
C	2.95793400	-1.29712700	-0.58431900
C	1.64851100	-0.85629300	-0.56289300
C	1.31830900	0.41491900	-0.01553200
C	2.38050900	1.21269700	0.48315600
C	3.68473200	0.75767200	0.44919100
H	5.00876000	-0.84914100	-0.10307600
H	3.18681800	-2.26958900	-1.00296300
H	0.85763500	-1.47225000	-0.97023800
H	2.14987100	2.18630700	0.89565500
H	4.47897100	1.38219800	0.83902100
C	0.00000000	0.87392500	0.00000000
C	-1.31830900	0.41491900	0.01553300
C	-1.64851100	-0.85629300	0.56289400
C	-2.38050900	1.21269700	-0.48315600
C	-2.95793400	-1.29712700	0.58431900
H	-0.85763500	-1.47225000	0.97023800
C	-3.68473200	0.75767200	-0.44919100
H	-2.14987100	2.18630700	-0.89565500
C	-3.98519600	-0.49841900	0.07987600
H	-3.18681900	-2.26958900	1.00296300
H	-4.47897100	1.38219800	-0.83902200
H	-5.00876000	-0.84914100	0.10307500

E = -501.50152284, ZPE = 0.183402

Table A4. Cartesian coordinates of S-7...H₂O.

Atom	X	Y	Z
C	-3.86507200	-0.88688400	0.15138200
C	-2.80458600	-1.51166200	0.80533800
C	-1.52700700	-0.98789300	0.71011800
C	-1.28714000	0.21363400	-0.00218300
C	-2.39437800	0.85968200	-0.60083500
C	-3.65498200	0.29295100	-0.56272700
H	-4.86066700	-1.30807600	0.21570300
H	-2.97981300	-2.41298800	1.37932200
H	-0.70341200	-1.47170600	1.21786400
H	-2.22247900	1.80463100	-1.09935900
H	-4.48598600	0.78308300	-1.05368500
C	-0.01316900	0.84904900	-0.08936600
C	1.18535400	0.07557300	-0.09023300
C	1.29513700	-1.21827500	-0.65913100
C	2.35421900	0.66712000	0.44868500
C	2.50924900	-1.88163800	-0.67892100
H	0.42435600	-1.66699200	-1.11834400
C	3.54647600	-0.03317000	0.48797300
H	2.28210300	1.67571700	0.83629600
C	3.63000200	-1.30155200	-0.08609600
H	2.58778800	-2.85622800	-1.14436300
H	4.42435000	0.41711000	0.93361700
H	4.57457100	-1.83137700	-0.08835400
O	0.70465600	3.67299400	0.18935200
H	1.12780700	3.90329000	-0.64377700
H	0.34951500	2.75798400	0.04624300

E = -577.97448692, ZPE = 0.2087585

Table A5. Cartesian coordinates of T-7...H₂O.

Atom	X	Y	Z
C	4.01246200	-0.84160800	-0.04339700
C	3.00132500	-1.68846500	-0.49976000
C	1.68663000	-1.26484300	-0.52239600
C	1.33665000	0.03609300	-0.06481200
C	2.38195400	0.88420600	0.38517400
C	3.69178800	0.44474500	0.39240700
H	5.04069700	-1.17898000	-0.03366000
H	3.24719500	-2.68436600	-0.84730800
H	0.90749800	-1.91726300	-0.89378400
H	2.13712200	1.88397800	0.72020600
H	4.47439300	1.10681400	0.74108300
C	0.01019700	0.47220700	-0.09041100
C	-1.30421800	0.00542300	-0.03781700
C	-1.61638800	-1.23106600	0.59421200
C	-2.37758800	0.76076100	-0.57914600
C	-2.92051100	-1.68288700	0.65197800
H	-0.81606900	-1.81112500	1.03421000
C	-3.67638400	0.29560100	-0.50384100
H	-2.16319400	1.71092800	-1.05107300
C	-3.95935400	-0.92763300	0.10559100
H	-3.13632400	-2.62912700	1.13277800
H	-4.47975700	0.88627000	-0.92601000
H	-4.97887300	-1.28661200	0.15856700
O	-0.14110800	3.53255300	0.07105800
H	-0.69573100	3.47788700	0.85690100
H	-0.00746800	2.60596800	-0.18705900

E = -577.97309732, ZPE = 0.2066486

Table A6. Cartesian coordinates of S-7...ICF₃.

Atom	X	Y	Z
C	3.72288000	2.63258700	-0.78470700
C	3.10877300	1.39541100	-0.70836900
C	1.87442200	1.23876000	-0.02839600
C	1.29652800	2.38349600	0.57078600
C	1.94918200	3.60128300	0.54393400
C	3.15556400	3.73233100	-0.14400100
H	4.64846100	2.74455500	-1.33493400
H	3.54480400	0.54219700	-1.20988400
H	0.34341100	2.28064500	1.07044600
H	1.50946100	4.46064800	1.03330300
H	3.64649200	4.69624800	-0.19226800
C	1.17038900	-0.00004800	0.00141300
C	1.87194000	-1.24029900	0.02941100
C	1.29087400	-2.38364400	-0.56940600
C	3.10703500	-1.39968400	0.70739900
C	1.94123900	-3.60268900	-0.54411900
H	0.33727600	-2.27886800	-1.06774300
C	3.71878900	-2.63811900	0.78232600
H	3.54553000	-0.54754500	1.20859600
C	3.14836700	-3.73646000	0.14198900
H	1.49912200	-4.46092600	-1.03331400
H	4.64496700	-2.75213100	1.33112600
H	3.63748100	-4.70135700	0.18905700
C	-3.73764100	0.00110800	-0.00105200
I	-1.48093700	0.00222400	0.00118900
F	-4.24649600	1.16195200	-0.46881100
F	-4.24038500	-0.98638500	-0.77463500
F	-4.24394200	-0.17618500	1.23893100

E = -1137.10072605, ZPE = 0.1993443

Table A7. Cartesian coordinates of T-7...ICF₃.

Atom	X	Y	Z
C	-2.40675100	-1.03223100	-0.31019300
C	-3.77496000	-0.97491100	0.07865600
C	-1.80956500	-2.31302600	-0.43522900
C	-4.48160000	-2.13194200	0.34346200
H	-4.25676500	-0.00939600	0.15801700
C	-2.53390100	-3.45909300	-0.17038600
H	-0.77337600	-2.37911200	-0.73761500
C	-3.87041900	-3.38078700	0.22342500
H	-5.52077500	-2.06572300	0.64149600
H	-2.05631900	-4.42598900	-0.26794800
H	-4.43108800	-4.28302200	0.43012200
C	-1.70475700	1.50804700	-0.30383400
C	-2.17981400	1.99246100	0.94581800
C	-1.19256100	2.45296600	-1.22940700
C	-2.16006500	3.34430800	1.22969200
H	-2.55029900	1.28424200	1.67501000
C	-1.17322900	3.80028600	-0.92543300
H	-0.81451500	2.09855000	-2.17928600
C	-1.65803900	4.25708400	0.30089500
H	-2.52943700	3.69487600	2.18548100
H	-0.77909700	4.50559100	-1.64617400
H	-1.63954000	5.31385700	0.53328100
C	-1.70112900	0.13893500	-0.59094800
C	3.59515700	-0.57308800	0.19479800
I	1.47403200	-0.14133600	-0.07006800
F	3.83071100	-1.88424300	0.08088300
F	4.32760600	0.06174600	-0.72580700
F	4.01249400	-0.17940300	1.40196000

E = -1137.09296179, ZPE = 0.1975109

Table A8. Cartesian coordinates of S-7...BF₃.

Atom	X	Y	Z
C	-3.75673200	-1.53550800	0.13568200
C	-2.66774000	-2.05376700	0.83366100
C	-1.43798300	-1.42856700	0.75236400
C	-1.27745500	-0.23717500	0.00303300
C	-2.40906200	0.29602600	-0.65647700
C	-3.62053600	-0.36968300	-0.61477300
H	-4.71689900	-2.03337600	0.18936000
H	-2.78362100	-2.94242600	1.44026900
H	-0.59931200	-1.81566300	1.31365500
H	-2.30559100	1.21487000	-1.21075600
H	-4.47086500	0.03153900	-1.15038100
C	-0.01328400	0.44059300	-0.05191900
C	1.19904800	-0.32548700	-0.06301200
C	1.24802900	-1.62377000	-0.62872900
C	2.40428000	0.23460600	0.42760100
C	2.43538000	-2.32864100	-0.68672800
H	0.35589200	-2.04193900	-1.07259800
C	3.57578600	-0.49650400	0.40502900
H	2.38525700	1.22586300	0.85271000
C	3.59723200	-1.77274400	-0.15594300
H	2.46259500	-3.30624400	-1.14994900
H	4.48344600	-0.06789400	0.80898800
H	4.52560200	-2.32914400	-0.19362700
B	0.11113100	2.12413600	0.01347100
F	0.43386500	2.34855900	1.36591400
F	1.14302200	2.52940100	-0.83025800
F	-1.08288000	2.74953600	-0.32385000

E = -826.26987861, ZPE = 0.2005739

Table A9. Cartesian coordinates of T-7...BF₃.

Atom	X	Y	Z
C	-4.36054200	-0.76110000	-0.09881500
C	-3.48169600	-1.84511100	-0.07788300
C	-2.13007000	-1.65046900	0.13010200
C	-1.60429200	-0.34040100	0.31528600
C	-2.51753600	0.74553800	0.29827000
C	-3.86680100	0.52993500	0.09351800
H	-5.41870400	-0.92151600	-0.25929800
H	-3.86030100	-2.84998400	-0.21971200
H	-1.45414100	-2.49481500	0.16112600
H	-2.13915800	1.74805000	0.44076900
H	-4.54527300	1.37382800	0.08015400
C	-0.24023600	-0.14942100	0.54219400
C	0.99494800	-0.76572600	0.31960400
C	1.21202800	-1.57057300	-0.83292100
C	2.08310300	-0.57773000	1.20992800
C	2.43879000	-2.16465900	-1.05594100
H	0.40191700	-1.70429500	-1.53746900
C	3.30567400	-1.17307500	0.96640000
H	1.93998700	0.04593800	2.08200000
C	3.49334100	-1.97195100	-0.16217100
H	2.58343100	-2.77700300	-1.93746200
H	4.12309800	-1.01792800	1.65933800
H	4.45380000	-2.43513900	-0.34713700
B	0.99121100	2.51269100	-0.30704200
F	1.60070100	2.61597900	0.85696000
F	1.61684700	1.98960000	-1.33964500
F	-0.21765600	3.02085100	-0.45870600

E = -826.22324383, ZPE = 0.1964589

Table A10. Cartesian coordinates of S-8.

Atom	X	Y	Z
C	-0.62502700	-3.16792600	0.00000000
C	0.38309700	-2.18449600	0.00000000
C	0.00000000	-0.86502800	0.00000000
C	-1.37261700	-0.49697300	0.00000000
C	-2.35264000	-1.47885800	0.00000000
C	-1.96957400	-2.82645200	0.00000000
C	-0.19216000	1.44710100	0.00000000
C	0.76754300	0.39899800	0.00000000
C	2.11498900	0.66767100	0.00000000
H	2.85520800	-0.12341500	0.00000000
C	2.52255800	2.01574700	0.00000000
C	1.59939700	3.05120500	0.00000000
C	0.22700900	2.76953200	0.00000000
H	-0.34175200	-4.21344300	0.00000000
H	1.42642000	-2.47641500	0.00000000
H	-3.39636500	-1.19072700	0.00000000
H	-2.72103600	-3.60528500	0.00000000
H	3.58087800	2.24664300	0.00000000
H	1.94383900	4.07718600	0.00000000
H	-0.51005000	3.56270600	0.00000000
C	-1.57543200	0.95660400	0.00000000

E = -500.28015895, ZPE = 0.1625641

Table A11. Cartesian coordinates of T-8.

Atom	X	Y	Z
C	0.00000000	3.02184400	-1.12693900
C	0.00000000	1.65959800	-1.44103000
C	0.00000000	0.73259800	-0.41622500
C	0.00000000	1.17547800	0.94887900
C	0.00000000	2.53881500	1.24852000
C	0.00000000	3.45319900	0.20143900
C	0.00000000	-1.17547800	0.94887900
C	0.00000000	-0.73259800	-0.41622500
C	0.00000000	-1.65959800	-1.44103000
H	0.00000000	-1.33920300	-2.47600900
C	0.00000000	-3.02184400	-1.12693900
C	0.00000000	-3.45319900	0.20143900
C	0.00000000	-2.53881500	1.24852000
H	0.00000000	3.75303600	-1.92513600
H	0.00000000	1.33920300	-2.47600900
H	0.00000000	2.87389700	2.27758700
H	0.00000000	4.51391700	0.41718100
H	0.00000000	-3.75303600	-1.92513600
H	0.00000000	-4.51391700	0.41718100
H	0.00000000	-2.87389700	2.27758700
C	0.00000000	0.00000000	1.73950300

E = -500.28796986, ZPE = 0.1626441

Table A12. Cartesian coordinates of S-8···H₂O.

Atom	X	Y	Z
C	-2.42547800	-2.21982100	-0.00342300
C	-1.01518800	-2.23178200	-0.00741400
C	-0.36057400	-1.02575700	0.00219000
C	-1.08296600	0.19867900	0.01574500
C	-2.47278900	0.19774100	0.01953400
C	-3.14286300	-1.03296800	0.00950100
C	1.12534900	0.75937000	0.01208100
C	1.07344800	-0.66161000	0.00072300
C	2.22344900	-1.41207900	-0.01087100
H	2.19805600	-2.49491800	-0.02074100
C	3.45894200	-0.73487600	-0.01053200
C	3.52644500	0.65053400	0.00040900
C	2.35024500	1.41102100	0.01146100
H	-2.95846500	-3.16284000	-0.01109800
H	-0.48025300	-3.17363800	-0.01837900
H	-3.00539400	1.14149500	0.02964000
H	-4.22464100	-1.06031900	0.01099500
H	4.37569900	-1.31162700	-0.01971400
H	4.49087200	1.14125600	-0.00060500
H	2.38190500	2.49324200	0.01800700
C	-0.20505500	1.36251300	0.02105100
O	-2.20649400	3.46766100	-0.10027400
H	-2.06251700	4.19748100	0.50929500
H	-1.38109400	2.92279500	-0.05793300

E = -576.76230413, ZPE = 0.1869368

Table A13. Cartesian coordinates of T-8···H₂O.

Atom	X	Y	Z
C	2.37093600	-2.26991600	-0.00000500
C	0.97326000	-2.22505800	-0.00000800
C	0.34008200	-0.99717900	0.00000000
C	1.12060900	0.20741500	0.00001200
C	2.51601600	0.15114000	0.00001600
C	3.12878100	-1.09688100	0.00000700
C	-1.15517700	0.81227900	0.00001000
C	-1.07630000	-0.62099300	-0.00000100
C	-2.23533700	-1.37316400	-0.00001100
H	-2.19108600	-2.45563300	-0.00001900
C	-3.47154700	-0.72015000	-0.00000900
C	-3.54821000	0.67418900	0.00000200
C	-2.39574700	1.45169700	0.00001100
H	2.87261300	-3.22914500	-0.00001200
H	0.39842800	-3.14339800	-0.00001800
H	3.09501700	1.06555200	0.00002500
H	4.20928200	-1.16082200	0.00000900
H	-4.38284300	-1.30426800	-0.00001600
H	-4.51801000	1.15478800	0.00000300
H	-2.45660700	2.53232000	0.00002000
C	0.18499500	1.27120700	0.00001700
O	2.35526100	3.54174000	-0.00002100
H	1.80849300	3.30958500	-0.75943800
H	1.80845800	3.30958300	0.75937100

E = -576.75808280, ZPE = 0.185517

Table A14. Cartesian coordinates of S-8-I··CF₃ (30).

Atom	X	Y	Z
C	3.21585100	-3.00918400	0.46450700
C	3.50554000	-1.65014800	0.54098600
C	2.52120200	-0.72920700	0.20822700
C	1.24419900	-1.17602900	-0.22384200
C	0.96240500	-2.53817600	-0.29209000
C	1.95319100	-3.44743100	0.05532800
C	1.24420100	1.17602800	-0.22384100
C	2.52120300	0.72920400	0.20822800
C	3.50554300	1.65014400	0.54098700
H	4.48485500	1.31673500	0.86170600
C	3.21585600	3.00918000	0.46450800
C	1.95319700	3.44742900	0.05532900
C	0.96240900	2.53817600	-0.29208800
H	3.97381300	-3.73556300	0.72829500
H	4.48485200	-1.31674200	0.86170600
H	-0.01545800	-2.88559400	-0.60305700
H	1.74442900	-4.50861100	0.01016600
H	3.97382000	3.73555800	0.72829600
H	1.74443800	4.50861000	0.01016700
H	-0.01545300	2.88559600	-0.60305600
C	0.46885300	0.00000100	-0.56324400
I	-1.48785900	0.00000200	-0.97015800
C	-2.96976200	0.00000000	1.01350500
F	-3.75510900	1.08713100	1.04291300
F	-2.19444000	-0.00001600	2.10143200
F	-3.75512900	-1.08711700	1.04289600

E = -1135.90017854, ZPE = 0.1775512

Table A15. Cartesian coordinates of T-8··ICF₃.

Atom	X	Y	Z
C	-1.28868000	3.11290400	-1.09483800
C	-1.66162900	1.80493100	-1.41773100
C	-2.01712300	0.93543000	-0.40170000
C	-1.99967600	1.38428600	0.96306100
C	-1.62569200	2.69327000	1.26948500
C	-1.27181500	3.54819100	0.23181000
C	-2.65652300	-0.87232600	0.94945100
C	-2.42733700	-0.47139100	-0.40914000
C	-2.59186700	-1.38191100	-1.43507900
H	-2.41616200	-1.09321100	-2.46430400
C	-2.98450900	-2.68765100	-1.12789100
C	-3.20915600	-3.07876800	0.19405600
C	-3.04816000	-2.18006900	1.24188400
H	-1.00458500	3.79605400	-1.88460200
H	-1.66531900	1.47811700	-2.45048500
H	-1.60700700	3.03126500	2.29721300
H	-0.97475100	4.56473500	0.45458700
H	-3.11417000	-3.40693700	-1.92620800
H	-3.51079500	-4.09678600	0.40408700
H	-3.21929200	-2.48493700	2.26596000
C	-2.39290700	0.26954300	1.74400800
I	1.32917200	0.11123200	-0.13657700
C	3.34062400	-0.65516900	0.14132900
F	3.75150900	-1.31468900	-0.94611700
F	4.20066500	0.34145100	0.37208900
F	3.38923400	-1.49467800	1.17959100

E = -1135.87920419, ZPE = 0.1767447

Table A16. Cartesian coordinates of C–I insertion product **31** between **8** and ICF₃.

Atom	X	Y	Z
C	2.66961700	-3.00171800	-0.42725800
C	2.94710200	-1.64122300	-0.52164900
C	1.93426700	-0.73172000	-0.24644000
C	0.65697600	-1.18563600	0.11425000
C	0.37934800	-2.53842600	0.20781200
C	1.39964200	-3.44701900	-0.06386800
C	0.65697900	1.18563600	0.11425200
C	1.93426900	0.73171700	-0.24643900
C	2.94710600	1.64121800	-0.52164700
H	3.93591500	1.30006200	-0.80070200
C	2.66962400	3.00171400	-0.42725500
C	1.39965000	3.44701700	-0.06386500
C	0.37935400	2.53842600	0.20781500
H	3.44844200	-3.72326100	-0.63896700
H	3.93591200	-1.30006900	-0.80070400
H	-0.61014700	-2.88250400	0.47490900
H	1.20185200	-4.50885600	0.00332300
H	3.44845000	3.72325400	-0.63896300
H	1.20186200	4.50885400	0.00332700
H	-0.61014000	2.88250600	0.47491100
C	-0.24671000	0.00000000	0.35676500
I	-1.90455800	0.00000300	-1.12371300
C	-0.86376100	-0.00000100	1.76116200
F	-1.62477500	1.08428500	1.99148500
F	-1.62474700	-1.08430500	1.99149500
F	0.11715000	0.00001500	2.68567000

E = -1136.01424133, ZPE = 0.1815605

Table A17. Cartesian coordinates of radical pair **32** between **8** and ICF₃.

Atom	X	Y	Z
C	-3.00297300	-1.49438800	1.76321400
C	-2.88632700	-0.15721400	1.37491800
C	-1.65332500	0.31917000	0.97029900
C	-0.52125200	-0.54941800	0.95276200
C	-0.64922800	-1.88306800	1.34218300
C	-1.89589400	-2.34547400	1.74596100
C	0.17725200	1.54917800	0.20723000
C	-1.21584800	1.63282200	0.50380400
C	-1.89407800	2.82310200	0.31924800
H	-2.95194100	2.89731000	0.53974200
C	-1.19535400	3.93498500	-0.15898400
C	0.16825000	3.85426900	-0.44981000
C	0.86495600	2.66503300	-0.27040200
H	-3.96516400	-1.87673300	2.07901000
H	-3.75299500	0.49222800	1.38880500
H	0.20874600	-2.54284600	1.32246900
H	-2.01174800	-3.37826400	2.04823800
H	-1.71816300	4.87127900	-0.30678600
H	0.68779400	4.72873200	-0.81988600
H	1.92163700	2.60066600	-0.49704600
C	0.59850000	0.20986600	0.48496300
I	2.51765000	-0.52052900	0.22863000
C	-1.37113000	-1.39355600	-2.44584700
F	-1.15431700	-0.09198700	-2.38983100
F	-0.30155200	-2.07903300	-2.08133300
F	-2.43245400	-1.73966500	-1.74096900

E = -1135.90859188, ZPE = 0.1769597

Table A18. Cartesian coordinates of S-8...BF₃ (36).

Atom	X	Y	Z
C	3.03645600	-2.12252700	0.01387300
C	1.67102100	-2.48024300	0.02326300
C	0.74047800	-1.47468100	-0.00775100
C	1.15048600	-0.11427600	-0.04846600
C	2.49740800	0.23167500	-0.05995000
C	3.44452700	-0.79730800	-0.02653500
C	-1.15047200	-0.11433300	-0.04848200
C	-0.74039900	-1.47471700	-0.00775700
C	-1.67089600	-2.48032200	0.02327800
H	-1.38320000	-3.52341800	0.05503600
C	-3.03634600	-2.12266900	0.01389000
C	-3.44448300	-0.79746700	-0.02653500
C	-2.49741400	0.23155700	-0.05996500
H	3.78300500	-2.90664900	0.03835600
H	1.38337500	-3.52335400	0.05500300
H	2.78105900	1.27437600	-0.09923900
H	4.49978900	-0.56011400	-0.03340700
H	-3.78286000	-2.90682300	0.03838700
H	-4.49975600	-0.56032800	-0.03340900
H	-2.78109900	1.27424900	-0.09927100
C	-0.00002100	0.75072700	-0.07219800
B	-0.00005100	2.40165200	0.00735500
F	-1.15413000	2.90127400	-0.59918300
F	1.15399000	2.90136600	-0.59912600
F	-0.00009800	2.64306200	1.39184100

E = -825.06514426, ZPE = 0.1782677

Table A19. Cartesian coordinate of T-8...BF₃.

Atom	X	Y	Z
C	3.02274000	-2.02571900	0.37171500
C	1.66050100	-2.30564500	0.51893500
C	0.73299600	-1.41695900	0.01103300
C	1.17739500	-0.22975900	-0.66079600
C	2.53911300	0.04142500	-0.79730100
C	3.45387000	-0.86664100	-0.27653100
C	-1.17740100	-0.22974000	-0.66079400
C	-0.73302000	-1.41694700	0.01103300
C	-1.66053800	-2.30562000	0.51893400
H	-1.34145500	-3.20753200	1.02718200
C	-3.02277300	-2.02567400	0.37171500
C	-3.45388600	-0.86658800	-0.27652900
C	-2.53911500	0.04146500	-0.79729900
H	3.75424100	-2.71755800	0.76913300
H	1.34140500	-3.20755100	1.02718400
H	2.87016400	0.94470400	-1.29214800
H	4.51427600	-0.67239200	-0.37219900
H	-3.75428500	-2.71750200	0.76913200
H	-4.51428900	-0.67232300	-0.37219700
H	-2.87015400	0.94474900	-1.29214500
C	0.00000200	0.45336000	-1.05450400
B	0.00002400	2.79050400	0.48629300
F	-1.14164600	3.16730600	-0.05881200
F	1.14171600	3.16727800	-0.05878900
F	0.00000500	2.13998700	1.63170300

E = -825.00920614, ZPE = 0.1754499

Table A20. Cartesian coordinate of B–F insertion product **37** between **8** and BF₃.

Atom	X	Y	Z
C	-3.00792400	-1.94949600	0.16940700
C	-1.64918700	-2.22894700	0.29848800
C	-0.73329400	-1.21507300	0.05119500
C	-1.18104200	0.06600000	-0.30243300
C	-2.52859500	0.34591000	-0.43105400
C	-3.44602200	-0.67935300	-0.19938900
C	1.18105000	0.06606100	-0.30243400
C	0.73336900	-1.21503600	0.05119400
C	1.64931300	-2.22886300	0.29848600
H	1.31769700	-3.22072300	0.57869500
C	3.00803500	-1.94934300	0.16940300
C	3.44606800	-0.67917800	-0.19939400
C	2.52858900	0.34603900	-0.43105700
H	-3.73405300	-2.73116300	0.35348500
H	-1.31752100	-3.22079000	0.57869600
H	-2.86572300	1.33423300	-0.71857200
H	-4.50580300	-0.48616400	-0.30363300
H	3.73420400	-2.73097300	0.35348000
H	4.50583900	-0.48593500	-0.30363900
H	2.86566800	1.33437800	-0.71857500
C	-0.00001900	1.00337400	-0.47485500
B	-0.00006800	2.13032900	0.64707800
F	-0.00003600	1.61930500	-1.74120100
F	-0.00018900	3.41307800	0.34444500
F	0.00000000	1.79683100	1.92557200

E = -825.06071927, ZPE = 0.1788894

Table A21. Cartesian coordinate of S-25.

Atom	X	Y	Z
C	-3.96885900	0.17770800	0.04790100
C	-2.94044400	1.06220600	0.36182400
C	-1.28252700	-0.67604800	-0.02141600
C	-2.35916400	-1.54886500	-0.31821900
C	-3.67776600	-1.13227200	-0.31772300
C	0.00000000	-1.32817000	0.00001900
C	1.28252800	-0.67604500	0.02143100
C	2.94044100	1.06220800	-0.36183300
H	3.18503500	2.08432400	-0.62795800
C	3.96885900	0.17771000	-0.04792400
C	3.67777100	-1.13227000	0.31770400
C	2.35916900	-1.54886100	0.31822200
H	-4.99690300	0.51739500	0.08665600
H	-3.18504200	2.08432100	0.62794700
H	-2.09790200	-2.57567500	-0.53625700
H	-4.47350100	-1.82317800	-0.56481500
H	4.99690300	0.51739600	-0.08669300
H	4.47351000	-1.82317600	0.56478600
H	2.09790900	-2.57567000	0.53627000
C	1.60654300	0.67622300	-0.30278900
C	-1.60654600	0.67622100	0.30279700
C	0.53588900	1.70232400	-0.54856700
H	0.05608600	1.52514000	-1.51770200
H	0.99916500	2.68882100	-0.60687600
C	-0.53589400	1.70232200	0.54858000
H	-0.99917200	2.68881800	0.60689000
H	-0.05609100	1.52513700	1.51771500

E = -578.94636186, ZPE = 0.2203915

Table A22. Cartesian coordinate of T-25.

Atom	X	Y	Z
C	-4.01224000	0.15184000	0.01148200
C	-2.99031000	1.07026500	0.24669900
C	-1.32356500	-0.67196200	-0.00040700
C	-2.37760900	-1.59082100	-0.23791300
C	-3.69693500	-1.18451700	-0.23019600
C	0.00000200	-1.11948500	0.00001300
C	1.32356800	-0.67196700	0.00041200
C	2.99030400	1.07027000	-0.24669900
H	3.24199300	2.10880100	-0.43029200
C	4.01223900	0.15184800	-0.01148100
C	3.69694000	-1.18451200	0.23019000
C	2.37761600	-1.59082400	0.23790900
H	-5.04410400	0.47851700	0.01513500
H	-3.24200200	2.10879600	0.43029100
H	-2.12428500	-2.62595300	-0.42709800
H	-4.48385800	-1.90476500	-0.41519200
H	5.04410100	0.47853000	-0.01512800
H	4.48386800	-1.90475500	0.41518000
H	2.12429800	-2.62595700	0.42709000
C	1.65507100	0.69519200	-0.25521200
C	-1.65507400	0.69519400	0.25521700
C	0.57293900	1.70779900	-0.51972500
H	0.14221000	1.53465800	-1.51201900
H	1.02589400	2.70032100	-0.54797900
C	-0.57294500	1.70780900	0.51972000
H	-1.02590100	2.70033200	0.54794700
H	-0.14222400	1.53469200	1.51202100

E = -578.96205637, ZPE = 0.2198326

Table A23. Cartesian coordinate of S-25...H₂O (27).

Atom	X	Y	Z
C	-3.97069100	-0.54506400	-0.08733600
C	-2.93789300	-1.45004500	-0.32147400
C	-1.28765400	0.30177200	0.01434100
C	-2.36760800	1.19695200	0.23228900
C	-3.68690300	0.78376300	0.20569600
C	-0.00310800	0.94047700	0.01242300
C	1.28460000	0.30902700	-0.02142700
C	2.95377100	-1.42088600	0.32952900
H	3.20920600	-2.43936500	0.59837700
C	3.97003000	-0.53482600	-0.02033900
C	3.66633600	0.77372400	-0.37932900
C	2.34804900	1.19007300	-0.34659100
H	-4.99834900	-0.88502200	-0.13369200
H	-3.18039300	-2.48388500	-0.53866700
H	-2.11859300	2.23560000	0.40715300
H	-4.48679100	1.49019200	0.38509700
H	4.99942800	-0.87225400	-0.01137400
H	4.45306500	1.46535600	-0.65127800
H	2.08783400	2.21772300	-0.56529500
C	1.61878400	-1.03882200	0.30784800
C	-1.60544500	-1.06463900	-0.25643200
C	0.55614000	-2.05611000	0.61453200
H	0.09655900	-1.84177800	1.58579800
H	1.02229500	-3.03888900	0.70134600
C	-0.53640000	-2.10166700	-0.45989000
H	-1.00134300	-3.08896900	-0.46507300
H	-0.07476700	-1.97089900	-1.44536100
O	-0.03544900	3.82627500	0.03190500
H	0.27697300	4.07638800	0.90722600
H	-0.01360300	2.82323900	0.02746200

E = -655.43091547, ZPE = 0.244807

Table A24. Cartesian coordinate of T-25...H₂O (28a).

Atom	X	Y	Z
C	4.00596600	-0.54427900	0.02028600
C	2.97585100	-1.45007700	0.26679700
C	1.32343900	0.30040000	-0.01887000
C	2.38628600	1.20700500	-0.27055600
C	3.70175100	0.78911600	-0.24821200
C	-0.00048900	0.74998200	-0.02862000
C	-1.32890200	0.31298200	-0.01483600
C	-2.99865800	-1.42940400	-0.23841400
H	-3.25215400	-2.46914400	-0.41165400
C	-4.01780900	-0.50766500	-0.00544400
C	-3.69946200	0.82968900	0.22421600
C	-2.38025800	1.23614100	0.22305600
H	5.03513700	-0.87885400	0.03463100
H	3.21805700	-2.48728900	0.46900600
H	2.14990900	2.24193900	-0.48139600
H	4.49419100	1.50005400	-0.44461000
H	-5.05011800	-0.83279600	-0.00195000
H	-4.48387000	1.55312500	0.40644000
H	-2.13186600	2.27458000	0.40045200
C	-1.66331700	-1.05625900	-0.25811000
C	1.64353400	-1.06539200	0.26239000
C	-0.58407900	-2.07343300	-0.51331600
H	-0.14750800	-1.90739100	-1.50414800
H	-1.03980500	-3.06456400	-0.53777200
C	0.55468600	-2.06846000	0.53375100
H	1.00233200	-3.06267900	0.57655400
H	0.11886500	-1.88160100	1.52129500
O	0.03502700	3.86134600	-0.02681700
H	-0.04453800	2.93483300	-0.30264500
H	0.33992300	3.80694600	0.88562800

E = -655.43359880, ZPE = 0.243263

Table A25. Cartesian coordinate of T-25...H₂O (28b).

Atom	X	Y	Z
C	-3.82529400	0.01359000	-0.51265400
C	-2.80265800	-0.87912200	-0.83606700
C	-1.12982400	0.78181200	-0.27154400
C	-2.18406000	1.67823300	0.04218700
C	-3.50653900	1.29903300	-0.07599800
C	0.19728300	1.18799300	-0.11400400
C	1.50790200	0.70518100	-0.07153300
C	3.11556000	-1.10018400	0.07596800
H	3.33336000	-2.16032700	0.13814900
C	4.16859000	-0.18739700	0.05460500
C	3.89940800	1.17784200	-0.03104700
C	2.59288400	1.61831000	-0.09437000
H	-4.85913500	-0.29344000	-0.60187300
H	-3.05704000	-1.87801500	-1.17180300
H	-1.92880100	2.67213800	0.38654000
H	-4.29281100	1.99834200	0.17776800
H	5.19050300	-0.54089100	0.10193400
H	4.71165100	1.89330500	-0.05038300
H	2.37380000	2.67606800	-0.16218900
C	1.79043800	-0.69355500	0.02208300
C	-1.46365000	-0.52977500	-0.73509000
C	0.67386900	-1.70241500	0.05284400
H	0.16295700	-1.66336800	1.02077400
H	1.10671300	-2.70056600	-0.03083600
C	-0.38009000	-1.51972800	-1.06606300
H	-0.84405200	-2.48442900	-1.27719400
H	0.13059100	-1.21135100	-1.98472700
O	-1.77734800	-0.81799900	2.57079000
H	-1.34153900	0.02841600	2.42248500
H	-2.39032700	-0.89079200	1.82913200

E = -655.43523401, ZPE = 0.2432841

Table A26. Cartesian coordinate of S-25···ICF₃ (33a).

Atom	X	Y	Z
C	3.06457400	-3.74086600	-0.27031500
C	3.76271900	-2.59740700	0.10420300
C	1.77509200	-1.23550300	-0.20911200
C	1.09088100	-2.43122000	-0.55513200
C	1.71651700	-3.66075700	-0.59960600
C	0.99018600	-0.04591800	-0.37028400
C	1.46391900	1.30585400	-0.31224400
C	2.74310700	3.16582700	0.57250800
H	3.49213300	3.54775900	1.25610500
C	2.09089100	4.04496500	-0.28769600
C	1.12298400	3.57061300	-1.16651200
C	0.78441900	2.23077000	-1.14110200
H	3.57532600	-4.69591700	-0.29069500
H	4.80693100	-2.68485600	0.38070000
H	0.04518200	-2.34981400	-0.81180300
H	1.16340700	-4.54661600	-0.88203000
H	2.33598000	5.09949300	-0.26446600
H	0.60852800	4.24886500	-1.83445500
H	-0.00961300	1.85777200	-1.77232300
C	2.47717800	1.80334100	0.55238500
C	3.15726300	-1.34736400	0.14718700
C	3.26029400	0.86797200	1.42652000
H	2.60441000	0.36675700	2.14517800
H	3.98469400	1.44051900	2.00713100
C	3.99837400	-0.17955700	0.58964600
H	4.84653900	-0.56617900	1.15807700
H	4.42396200	0.30826200	-0.29610600
I	-1.70625600	-0.14066200	-0.10284800
C	-3.91143600	-0.15196000	0.33683300
F	-4.46808700	-1.35958500	0.10082200
F	-4.16979700	0.15386500	1.62607600
F	-4.58074800	0.74309000	-0.42112800

E = -1214.55388818, ZPE = 0.2353166

Table A27. Cartesian coordinate of T-25···ICF₃.

Atom	X	Y	Z
C	-1.70459600	-4.12236300	0.09391400
C	-1.91948500	-3.11997800	1.03825700
C	-1.72549000	-1.42233700	-0.67796000
C	-1.51094500	-2.45602500	-1.62454900
C	-1.49907700	-3.78198300	-1.24245000
C	-1.69376200	-0.08635900	-1.09157400
C	-1.99202300	1.21439600	-0.67382600
C	-2.99904300	2.78207300	0.87285500
H	-3.55842300	2.97700400	1.78079000
C	-2.55733700	3.85446500	0.10002600
C	-1.83013500	3.61440100	-1.06500200
C	-1.55016400	2.31814700	-1.44635700
H	-1.69858300	-5.16034600	0.40030900
H	-2.08031000	-3.39272500	2.07502200
H	-1.35002100	-2.18133500	-2.65885600
H	-1.33159600	-4.55478600	-1.98173400
H	-2.77624000	4.86855100	0.40833100
H	-1.47972500	4.44167200	-1.66884200
H	-0.97987800	2.12204800	-2.34489400
C	-2.74243100	1.46662600	0.51589600
C	-1.92789500	-1.77742700	0.69172900
C	-3.23040200	0.32729400	1.37041600
H	-4.05168400	-0.18893100	0.86152600
H	-3.64739600	0.73879100	2.29097600
C	-2.14394700	-0.71251300	1.73279100
H	-2.41442000	-1.19582300	2.67289500
H	-1.20136400	-0.18485400	1.91571900
I	1.52897000	0.06223900	-0.20478500
C	3.61756100	0.26205700	0.36829200
F	3.93151500	-0.61178400	1.33000100
F	4.42018000	0.03636400	-0.67638200
F	3.86933400	1.49199600	0.82722900

E = -1214.55402530, ZPE = 0.2338405

Table A28. Cartesian coordinate of radical pair **34** between **25** and ICF₃.

Atom	X	Y	Z
C	-4.49916200	1.14210400	0.45764200
C	-3.40399500	1.77733500	1.02710900
C	-1.88493200	0.32572500	-0.17124600
C	-3.00455800	-0.31154900	-0.73449400
C	-4.29308400	0.09434700	-0.43380800
C	-0.53282000	-0.12201900	-0.50428900
C	0.59088300	0.67284100	-0.94303700
C	1.82866500	2.74743600	-1.20843000
H	1.93841200	3.80042900	-0.97540700
C	2.78502400	2.13303000	-2.00114300
C	2.66343500	0.77175800	-2.26117200
C	1.59942500	0.06857500	-1.74013200
H	-5.50325600	1.45917600	0.70893700
H	-3.55862200	2.58923900	1.72824300
H	-2.85239100	-1.13056500	-1.42433600
H	-5.13496100	-0.40822500	-0.89254000
H	3.61710900	2.70221200	-2.39460700
H	3.39491700	0.25914600	-2.87271500
H	1.51595600	-0.98280400	-1.97000600
C	0.73863500	2.06749000	-0.66689400
C	-2.10073200	1.38886300	0.72694100
C	-0.17049800	2.88657300	0.22337200
H	-0.89887500	3.42246800	-0.39595000
H	0.44385000	3.65563900	0.69709600
C	-0.92959100	2.11902800	1.31029600
H	-1.27855800	2.82462400	2.06577000
H	-0.25183600	1.42264200	1.81130800
I	-0.26993100	-2.23075400	-0.29649100
C	2.43744400	-0.27111200	1.58124800
F	1.62551800	-0.16936100	2.62457900
F	3.19249800	-1.35219200	1.66724500
F	3.17417900	0.81860400	1.44778200

E = -1214.55022755, ZPE = 0.2345104

Table A29. Cartesian coordinate of C–I insertion product **35** between **25** and ICF₃.

Atom	X	Y	Z
C	3.78130000	1.97066500	-0.41366600
C	2.60124500	2.57030400	-0.80633600
C	1.27032400	0.72211100	0.02320300
C	2.48923800	0.13717600	0.42098500
C	3.71604500	0.73960600	0.22286400
C	-0.01281400	-0.10864200	0.25790000
C	-1.43200600	0.36580400	-0.15020000
C	-3.20084000	2.01759700	-0.27668800
H	-3.49926200	3.05742300	-0.22364200
C	-4.15052400	1.04986600	-0.55222800
C	-3.74521500	-0.27278600	-0.63034500
C	-2.41489600	-0.59566800	-0.42409300
H	4.73148800	2.45672500	-0.59442000
H	2.63440700	3.54146400	-1.28487000
H	2.49057900	-0.83989600	0.87090700
H	4.61542300	0.23496100	0.55087100
H	-5.18551700	1.32602500	-0.70861600
H	-4.45608100	-1.06004100	-0.84484400
H	-2.14264600	-1.63707000	-0.46584900
C	-1.85398000	1.70688700	-0.07113400
C	1.34547300	1.98574400	-0.59503700
C	-0.90608600	2.85202600	0.11791000
H	-0.42563300	2.81893200	1.09812300
H	-1.46705300	3.78554200	0.07133700
C	0.15978500	2.82636000	-0.98088900
H	0.51215700	3.83904400	-1.17902300
H	-0.29089100	2.46795500	-1.91120100
I	0.43939600	-2.07082300	-0.83494100
C	-0.15255400	-0.47689300	1.77594900
F	0.89898700	-1.10569900	2.32300000
F	-1.21842200	-1.25230600	2.02422400
F	-0.32188700	0.67151700	2.47099200

E = -1214.639987, ZPE = 0.2394189

Table A30. Cartesian coordinate of S-25...BF₃ (38a).

Atom	X	Y	Z
C	-3.84618500	-1.13012300	-0.62639100
C	-2.80460600	-1.98853800	-0.29576600
C	-1.28916200	-0.11283100	-0.01375200
C	-2.39329400	0.73913600	-0.31202700
C	-3.63830400	0.24342800	-0.63451800
C	-0.02607100	0.56223000	0.08302700
C	1.25729600	-0.06645400	-0.10676800
C	2.91265100	-1.80165700	0.19348000
H	3.21145200	-2.74589400	0.63228300
C	3.81482900	-1.09234500	-0.59410800
C	3.45355200	0.13645300	-1.13467100
C	2.20758000	0.66565200	-0.85601800
H	-4.82178000	-1.53767800	-0.86154500
H	-2.99231100	-3.05513400	-0.26099900
H	-2.23463600	1.80362100	-0.32826600
H	-4.44273900	0.92286600	-0.88171000
H	4.80369400	-1.49577100	-0.77296400
H	4.15319100	0.69614600	-1.74089200
H	1.93399000	1.63746400	-1.23809900
C	1.63059800	-1.32423000	0.42357700
C	-1.53102700	-1.52508000	0.00791300
C	0.65444200	-2.11531800	1.24094300
H	0.28307400	-1.52314500	2.08208400
H	1.15424700	-2.98813400	1.66254700
C	-0.51466200	-2.57673700	0.37748400
H	-1.04268800	-3.38315100	0.89171100
H	-0.12383400	-3.01850700	-0.54795000
B	0.01801800	2.23671700	0.39602600
F	-0.23016000	2.89954100	-0.81806700
F	-0.96475600	2.51563400	1.34924700
F	1.27296300	2.56507100	0.89873700

E = -903.72263139, ZPE = 0.2364018

Table A31. Cartesian coordinate of T-25...BF₃.

Atom	X	Y	Z
C	3.89300000	-1.10700900	-0.20007500
C	2.85529200	-1.57536000	0.60400000
C	1.23797400	-0.35353700	-0.72187400
C	2.30715500	0.11048300	-1.52991600
C	3.61071800	-0.25941300	-1.27053900
C	-0.06854100	0.06387500	-0.99392600
C	-1.40673300	-0.20347300	-0.68866300
C	-3.13749000	-1.58220300	0.29644400
H	-3.43097300	-2.46525300	0.85273200
C	-4.11752800	-0.68878800	-0.13221400
C	-3.74897000	0.45333400	-0.84140200
C	-2.41789600	0.69466500	-1.11454100
H	4.91302600	-1.40317300	0.00797400
H	3.08231400	-2.23696000	1.43226400
H	2.07845300	0.77105900	-2.35598300
H	4.41108900	0.10870500	-1.89961300
H	-5.15904200	-0.88220800	0.08986900
H	-4.50304700	1.15497200	-1.17455900
H	-2.12199700	1.58382200	-1.65474000
C	-1.79148500	-1.37577300	0.03326000
C	1.53490200	-1.21646000	0.37878200
C	-0.75621800	-2.36139000	0.50615100
H	-0.36488700	-2.92221100	-0.34973700
H	-1.24398500	-3.09023000	1.15556500
C	0.43296600	-1.72853300	1.26655200
H	0.85295000	-2.47043500	1.94771800
H	0.05613400	-0.91060500	1.88884700
B	0.33871800	2.46556500	0.81218200
F	0.04107000	1.69541200	1.84073400
F	1.59783800	2.67734500	0.49133600
F	-0.61963000	3.09526400	0.16198700

E = -903.68449794, ZPE = 0.2328258

Table A32. Cartesian coordinate of B–F insertion product **39** between **25** and BF_3 .

Atom	X	Y	Z
C	-3.92707000	-1.01973700	-0.50958700
C	-2.84141000	-1.81445900	-0.18643000
C	-1.33944800	0.06028400	-0.31702800
C	-2.45331600	0.86119300	-0.62033100
C	-3.72982000	0.33794600	-0.72370900
C	-0.01820600	0.84453300	-0.23975000
C	1.33994000	0.14779300	-0.35231800
C	2.98079800	-1.49213900	0.29582400
H	3.23634900	-2.38311200	0.85704900
C	3.94586000	-0.87973800	-0.49130000
C	3.60716800	0.25111500	-1.21860300
C	2.31823000	0.76143100	-1.14135800
H	-4.91624900	-1.45348600	-0.58295500
H	-2.99619700	-2.87184400	-0.00592900
H	-2.30413300	1.91693900	-0.79847600
H	-4.56102200	0.98725100	-0.96644700
H	4.94835000	-1.28587000	-0.53709100
H	4.34070800	0.74361600	-1.84397800
H	2.06648400	1.64734700	-1.70327100
C	1.67886300	-0.99893400	0.38251400
C	-1.53963700	-1.30847400	-0.07758100
C	0.66168600	-1.76407200	1.18315500
H	0.23644100	-1.15139200	1.97937000
H	1.16007400	-2.60376900	1.66955100
C	-0.46351400	-2.30333700	0.29445900
H	-0.94910900	-3.13583900	0.80744600
H	-0.02257400	-2.72295600	-0.61581300
B	-0.03069000	1.71314100	1.10231600
F	-0.07907800	1.79006000	-1.29702200
F	-0.12226600	3.02697700	1.06512100
F	0.04507500	1.14373900	2.29425700

E = -903.71173738, ZPE = 0.2372973

Table A33. Cartesian coordinate of benzhydryl cation **15**.

Atom	X	Y	Z
C	0.09773200	3.88638300	-0.58189200
C	-0.31885500	2.83723900	-1.40865800
C	-0.36790800	1.55150900	-0.91948600
C	0.00000000	1.28491000	0.42630800
C	0.36163100	2.37720100	1.26089800
C	0.43385800	3.65621400	0.75298500
H	0.13437100	4.89378500	-0.97667400
H	-0.62083500	3.04171800	-2.42683500
H	-0.75174200	0.75686500	-1.54152500
H	0.61161600	2.19025500	2.29778200
H	0.73459800	4.47874300	1.38726500
C	0.00000000	0.00000000	1.01013900
C	0.00000000	-1.28491000	0.42630800
C	0.36790800	-1.55150900	-0.91948600
C	-0.36163100	-2.37720100	1.26089800
C	0.31885500	-2.83723900	-1.40865800
H	0.75174200	-0.75686500	-1.54152500
C	-0.43385800	-3.65621400	0.75298500
H	-0.61161600	-2.19025500	2.29778200
C	-0.09773200	-3.88638300	-0.58189200
H	0.62083500	-3.04171800	-2.42683500
H	-0.73459800	-4.47874300	1.38726500
H	-0.13437100	-4.89378500	-0.97667400
H	0.00000000	0.00000000	2.09728600

E = -501.9450149, ZPE = 0.1992132

Table A34. Cartesian coordinates of fluorenyl cation **40**.

Atom	X	Y	Z
C	2.61410500	-1.92186900	0.00000000
C	2.16423100	-0.57726700	0.00000000
C	0.81765000	-0.34858900	0.00000000
C	-0.09370400	-1.44806300	0.00000000
C	0.35798800	-2.77053200	0.00000000
C	1.73395700	-2.99649100	0.00000000
C	-1.36881800	0.48172900	0.00000000
C	0.00000000	0.88885500	0.00000000
C	0.31779600	2.21723300	0.00000000
H	1.34328000	2.56192100	0.00000000
C	-0.74262100	3.15841600	0.00000000
C	-2.07633300	2.77026600	0.00000000
C	-2.40816500	1.41591700	0.00000000
H	3.67968800	-2.11302600	0.00000000
H	2.88350600	0.23086600	0.00000000
H	-0.34185900	-3.59644000	0.00000000
H	2.11802900	-4.00691500	0.00000000
H	-0.50054500	4.21359700	0.00000000
H	-2.85516400	3.51986200	0.00000000
H	-3.44238500	1.09607200	0.00000000
C	-1.41105200	-0.93234600	0.00000000
H	-2.31475100	-1.52948800	0.00000000

E = -500.7289384, ZPE = 0.1765736

Table A35. Cartesian coordinate of dihydrodibenzotropylium cation **41**.

Atom	X	Y	Z
C	3.97552600	-0.15913000	0.00272000
C	2.96567700	-1.09509600	0.22452300
C	1.30018900	0.63600600	-0.00903700
C	2.35430400	1.57565300	-0.20269500
C	3.67168600	1.18531400	-0.21385800
C	0.00000000	1.18250000	0.00000000
C	-1.30018900	0.63600600	0.00903800
C	-2.96567700	-1.09509600	-0.22452300
H	-3.23544600	-2.12780800	-0.40361400
C	-3.97552600	-0.15913000	-0.00272100
C	-3.67168600	1.18531400	0.21385700
C	-2.35430400	1.57565300	0.20269500
H	5.00858300	-0.48336700	0.00541300
H	3.23544600	-2.12780800	0.40361300
H	2.10057400	2.61697800	-0.35663600
H	4.45930000	1.90747700	-0.37762000
H	-5.00858300	-0.48336700	-0.00541400
H	-4.45930000	1.90747700	0.37761900
H	-2.10057400	2.61697800	0.35663600
C	-1.62810800	-0.73721100	-0.21832700
C	1.62810800	-0.73721100	0.21832800
C	-0.58045000	-1.77428100	-0.49903200
H	-0.19296200	-1.62624900	-1.51410800
H	-1.05254400	-2.75634300	-0.49607400
C	0.58045000	-1.77428000	0.49903200
H	1.05254400	-2.75634300	0.49607500
H	0.19296200	-1.62624800	1.51410900
H	0.00000000	2.26856100	0.00000100

E = -579.4128242, ZPE = 0.235367

Table A36. Cartesian coordinate of deuterated dihydrodibenzotropylium cation [D]-41.

Atom	X	Y	Z
C	3.97552600	-0.15913000	0.00272000
C	2.96567700	-1.09509600	0.22452300
C	1.30018900	0.63600600	-0.00903700
C	2.35430400	1.57565300	-0.20269500
C	3.67168600	1.18531400	-0.21385800
C	0.00000000	1.18250000	0.00000000
C	-1.30018900	0.63600600	0.00903800
C	-2.96567700	-1.09509600	-0.22452300
H	-3.23544600	-2.12780800	-0.40361400
C	-3.97552600	-0.15913000	-0.00272100
C	-3.67168600	1.18531400	0.21385700
C	-2.35430400	1.57565300	0.20269500
H	5.00858300	-0.48336700	0.00541300
H	3.23544600	-2.12780800	0.40361300
H	2.10057400	2.61697800	-0.35663600
H	4.45930000	1.90747700	-0.37762000
H	-5.00858300	-0.48336700	-0.00541400
H	-4.45930000	1.90747700	0.37761900
H	-2.10057400	2.61697800	0.35663600
C	-1.62810800	-0.73721100	-0.21832700
C	1.62810800	-0.73721100	0.21832800
C	-0.58045000	-1.77428100	-0.49903200
H	-0.19296200	-1.62624900	-1.51410800
H	-1.05254400	-2.75634300	-0.49607400
C	0.58045000	-1.77428000	0.49903200
H	1.05254400	-2.75634300	0.49607500
H	0.19296200	-1.62624800	1.51410900
D	0.00000000	2.26856100	0.00000100

E = -579.4128242, ZPE = 0.2320157

Table A37. Cartesian coordinate of dihydrodibenzotropylium radical 43.

Atom	X	Y	Z
C	4.00648800	-0.19879300	-0.00289200
C	2.97004800	-1.10180300	0.21578700
C	1.31266900	0.65674600	0.00399200
C	2.38961500	1.55935500	-0.19671300
C	3.70578900	1.14636400	-0.20591200
C	0.00000000	1.21780600	0.00000100
C	-1.31266900	0.65674600	-0.00399200
C	-2.97004800	-1.10180300	-0.21578800
H	-3.20648900	-2.14595600	-0.38610300
C	-4.00648800	-0.19879300	0.00289100
C	-3.70578900	1.14636400	0.20591200
C	-2.38961500	1.55935500	0.19671400
H	5.03337200	-0.54085600	-0.00896100
H	3.20649000	-2.14595600	0.38610200
H	2.15914000	2.60616700	-0.35589300
H	4.49775000	1.86605500	-0.37051500
H	-5.03337200	-0.54085600	0.00895900
H	-4.49775000	1.86605500	0.37051400
H	-2.15914000	2.60616700	0.35589300
C	-1.63692200	-0.71068500	-0.23268300
C	1.63692200	-0.71068500	0.23268300
C	-0.57309300	-1.73470100	-0.51298700
C	0.57309300	-1.73470100	0.51298800
H	-0.15145300	-1.56684500	-1.51014200
H	-1.03689900	-2.72245100	-0.53572700
H	0.15145300	-1.56684400	1.51014300
H	1.03689900	-2.72245100	0.53572900
H	0.00000000	2.30314000	0.00000100

E = -579.6400469, ZPE = 0.232518

Table A38. Cartesian coordinate of T-7...H₂ complex.

Atom	X	Y	Z
C	0.00000000	0.00000000	0.81024289
C	-0.02146341	1.31589997	0.34213889
C	0.45437508	2.38991909	1.13724189
C	-0.54672183	1.62791621	-0.94286511
C	0.42611568	3.68785884	0.66366389
H	0.84633654	2.17455281	2.12257589
C	-0.56037308	2.93056482	-1.40293411
H	-0.94233880	0.82879195	-1.55545811
C	-0.07398974	3.96954426	-0.60844211
H	0.79897003	4.49180251	1.28610089
H	-0.95941413	3.14480549	-2.38689211
H	-0.09026392	4.98796129	-0.97420011
C	0.02146341	-1.31589997	0.34213889
C	-0.45437508	-2.38991909	1.13724189
C	0.54672183	-1.62791621	-0.94286511
C	-0.42611568	-3.68785884	0.66366389
H	-0.84633654	-2.17455281	2.12257589
C	0.56037308	-2.93056482	-1.40293411
H	0.94233880	-0.82879195	-1.55545811
C	0.07398974	-3.96954426	-0.60844211
H	-0.79897003	-4.49180251	1.28610089
H	0.95941413	-3.14480549	-2.38689211
H	0.09026392	-4.98796129	-0.97420011
H	0.00000000	0.00000000	3.57140289
H	0.00000000	0.00000000	4.31724689

E = -502.6825581, ZPE = 0.1951031

Table A39. Cartesian coordinate of TS(T-7...H₂).

Atom	X	Y	Z
C	0.00000000	0.00000000	0.94517207
C	0.02047317	-1.30584992	0.40401001
C	-0.41548883	-2.41045496	1.17563895
C	0.51147419	-1.57162385	-0.90026200
C	-0.39177080	-3.69331194	0.66145589
H	-0.77789184	-2.23619801	2.18030895
C	0.53041022	-2.86024783	-1.40200506
H	0.89633419	-0.75548782	-1.49603396
C	0.07510522	-3.92942187	-0.63143511
H	-0.73814080	-4.51960597	1.26972085
H	0.91236223	-3.03798978	-2.39985306
H	0.09341724	-4.93553985	-1.02980816
C	-0.02047317	1.30584992	0.40401001
C	0.41548883	2.41045496	1.17563895
C	-0.51147419	1.57162385	-0.90026200
C	0.39177080	3.69331194	0.66145589
H	0.77789184	2.23619801	2.18030895
C	-0.53041022	2.86024783	-1.40200506
H	-0.89633419	0.75548782	-1.49603396
C	-0.07510522	3.92942187	-0.63143511
H	0.73814080	4.51960597	1.26972085
H	-0.91236223	3.03798978	-2.39985306
H	-0.09341724	4.93553985	-1.02980816
H	0.00000000	0.00000000	2.34539407
H	0.00000000	0.00000000	3.24590307

E = -502.6710948, ZPE = 0.1947638

Table A40. Cartesian coordinate of T-7-H···H triplet radical pair (**55**).

Atom	X	Y	Z
C	0.00000000	0.00000000	1.00825800
C	-0.01962266	1.29454029	0.40159400
C	0.34749170	2.41756137	1.18165600
C	-0.44104633	1.54349767	-0.92583900
C	0.33702250	3.69650360	0.65727400
H	0.65692031	2.26026208	2.20826800
C	-0.46093470	2.82844983	-1.44007000
H	-0.79977195	0.72531575	-1.53341400
C	-0.06259446	3.91324979	-0.66113600
H	0.63661283	4.53299435	1.27646600
H	-0.80194434	2.99032799	-2.45528800
H	-0.07705508	4.91501068	-1.07064400
C	0.01962266	-1.29454029	0.40159400
C	-0.34749170	-2.41756137	1.18165600
C	0.44104633	-1.54349767	-0.92583900
C	-0.33702250	-3.69650360	0.65727400
H	-0.65692031	-2.26026208	2.20826800
C	0.46093470	-2.82844983	-1.44007000
H	0.79977195	-0.72531575	-1.53341400
C	0.06259446	-3.91324979	-0.66113600
H	-0.63661283	-4.53299435	1.27646600
H	0.80194434	-2.99032799	-2.45528800
H	0.07705508	-4.91501068	-1.07064400
H	0.00000000	0.00000000	2.09432100
H	0.00000000	0.00000000	4.44360700

E = -502.6819489, ZPE = 0.1967489

Table A41. Cartesian coordinate of insertion product between **7** and H₂ (**52**).

Atom	X	Y	Z
C	0.00000000	0.00000000	1.47868203
H	-0.04357027	-0.87392347	2.13422447
H	0.04357027	0.87392347	2.13422447
C	-1.26604115	0.05878253	0.64954999
C	-1.46915106	1.10531212	-0.25282135
C	-2.24910919	-0.92184251	0.76140330
C	-2.62579501	1.17167965	-1.01699137
H	-0.70582302	1.86684016	-0.36205281
C	-3.41017114	-0.86116397	-0.00463973
H	-2.10655426	-1.74250796	1.45515078
C	-3.60243505	0.18647761	-0.89572607
H	-2.76635093	1.99136310	-1.71075686
H	-4.16209918	-1.63408101	0.09600373
H	-4.50394401	0.23632102	-1.49321009
C	1.26604115	-0.05878253	0.64954999
C	2.24910919	0.92184251	0.76140330
C	1.46915106	-1.10531212	-0.25282135
C	3.41017114	0.86116397	-0.00463973
H	2.10655426	1.74250796	1.45515078
C	2.62579501	-1.17167965	-1.01699137
H	0.70582302	-1.86684016	-0.36205281
C	3.60243505	-0.18647761	-0.89572607
H	4.16209918	1.63408101	0.09600373
H	2.76635093	-1.99136310	-1.71075686
H	4.50394401	-0.23632102	-1.49321009

E = -502.8179984, ZPE = 0.2091584

Table A42. Cartesian coordinate of T-8···H₂ complex.

Atom	X	Y	Z
C	0.00000000	1.66053400	-1.55025416
C	0.00000000	0.73276100	-0.52619416
C	0.00000000	1.17562200	0.83899084
C	0.00000000	2.53852900	1.14002084
C	0.00000000	3.45346400	0.09346884
C	0.00000000	3.02264600	-1.23508216
H	0.00000000	1.34101700	-2.58549916
H	0.00000000	2.87241800	2.16944384
H	0.00000000	4.51406600	0.30969884
H	0.00000000	3.75425800	-2.03288816
C	0.00000000	-1.66053400	-1.55025416
C	0.00000000	-3.02264600	-1.23508216
C	0.00000000	-3.45346400	0.09346884
C	0.00000000	-2.53852900	1.14002084
C	0.00000000	-1.17562200	0.83899084
C	0.00000000	-0.73276100	-0.52619416
H	0.00000000	-1.34101700	-2.58549916
H	0.00000000	-3.75425800	-2.03288816
H	0.00000000	-4.51406600	0.30969884
H	0.00000000	-2.87241800	2.16944384
C	0.00000000	0.00000000	1.62843984
H	0.00000000	0.00000000	4.31532584
H	0.00000000	0.00000000	5.06112384

E = -501.4685996, ZPE = 0.1739616

Table A43. Cartesian coordinate of TS(T-8···H₂).

Atom	X	Y	Z
C	0.00000000	-1.66069187	-1.52732420
C	0.00000000	-0.73242397	-0.50375211
C	0.00000000	-1.17003911	0.86052385
C	0.00000000	-2.53257914	1.16397571
C	0.00000000	-3.45062303	0.11968762
C	0.00000000	-3.02249090	-1.20957434
H	0.00000000	-1.34327876	-2.56318917
H	0.00000000	-2.86534624	2.19406168
H	0.00000000	-4.51079506	0.33815351
H	0.00000000	-3.75577282	-2.00591141
C	0.00000000	1.66069187	-1.52732420
C	0.00000000	3.02249090	-1.20957434
C	0.00000000	3.45062303	0.11968762
C	0.00000000	2.53257914	1.16397571
C	0.00000000	1.17003911	0.86052385
C	0.00000000	0.73242397	-0.50375211
H	0.00000000	1.34327876	-2.56318917
H	0.00000000	3.75577282	-2.00591141
H	0.00000000	4.51079506	0.33815351
H	0.00000000	2.86534624	2.19406168
C	0.00000000	0.00000000	1.66625997
H	0.00000000	0.00000000	3.19535297
H	0.00000000	0.00000000	4.03841497

E = -501.4628936, ZPE = 0.1724626

Table A44. Cartesian coordinate of T-8-H···H triplet radical pair (**56**).

Atom	X	Y	Z
C	0.00000000	1.66183300	-1.53917911
C	0.00000000	0.73151300	-0.51798811
C	0.00000000	1.15694300	0.84578589
C	0.00000000	2.52006100	1.15414689
C	0.00000000	3.44494100	0.11568289
C	0.00000000	3.02311100	-1.21567211
H	0.00000000	1.34943600	-2.57646011
H	0.00000000	2.85051200	2.18574089
H	0.00000000	4.50415300	0.33933189
H	0.00000000	3.76014300	-2.00867611
C	0.00000000	-1.66183300	-1.53917911
C	0.00000000	-3.02311100	-1.21567211
C	0.00000000	-3.44494100	0.11568289
C	0.00000000	-2.52006100	1.15414689
C	0.00000000	-1.15694300	0.84578589
C	0.00000000	-0.73151300	-0.51798811
H	0.00000000	-1.34943600	-2.57646011
H	0.00000000	-3.76014300	-2.00867611
H	0.00000000	-4.50415300	0.33933189
H	0.00000000	-2.85051200	2.18574089
C	0.00000000	0.00000000	1.68051989
H	0.00000000	0.00000000	2.76136689
H	0.00000000	0.00000000	5.16232489

E = -501.4830737, ZPE = 0.1749467

Table A45. Cartesian coordinate of insertion product between **8** and H₂ (**53**).

Atom	X	Y	Z
C	1.64381600	0.00000000	1.49898690
C	0.73204100	0.00000000	0.44819690
C	1.18008300	0.00000000	-0.88338310
C	2.53496400	0.00000000	-1.16844810
C	3.44769900	0.00000000	-0.11434010
C	3.00398500	0.00000000	1.20760490
H	1.30342200	0.00000000	2.52717790
H	2.88536700	0.00000000	-2.19394410
H	4.51008800	0.00000000	-0.32313610
H	3.72634600	0.00000000	2.01425390
C	-1.64381600	0.00000000	1.49898690
C	-3.00398500	0.00000000	1.20760490
C	-3.44769900	0.00000000	-0.11434010
C	-2.53496400	0.00000000	-1.16844810
C	-1.18008300	0.00000000	-0.88338310
C	-0.73204100	0.00000000	0.44819690
H	-1.30342200	0.00000000	2.52717790
H	-3.72634600	0.00000000	2.01425390
H	-4.51008800	0.00000000	-0.32313610
H	-2.88536700	0.00000000	-2.19394410
C	0.00000000	0.00000000	-1.82570410
H	0.00000000	-0.87815363	-2.47891905
H	0.00000000	0.87815363	-2.47891905

E = -501.6184352, ZPE = 0.1873412

Table A46. Cartesian coordinate of T-25...H₂ complex.

Atom	X	Y	Z
C	0.00387900	4.01145100	-0.22325000
C	0.24779900	2.98847700	-1.13812400
C	-0.00443600	1.32389600	0.60614900
C	-0.25215500	2.37911800	1.52106600
C	-0.24639700	3.69756900	1.11175100
C	0.00000000	0.00000000	1.05365000
C	0.00443600	-1.32389600	0.60614900
C	-0.24779900	-2.98847700	-1.13812400
H	-0.43629900	-3.23837800	-2.17618900
C	-0.00387900	-4.01145100	-0.22325000
C	0.24639700	-3.69756900	1.11175100
C	0.25215500	-2.37911800	1.52106600
H	0.00659800	5.04272700	-0.55177100
H	0.43629900	3.23837800	-2.17618900
H	-0.44752900	2.12952300	2.55548900
H	-0.43938600	4.48504900	1.82928200
H	-0.00659800	-5.04272700	-0.55177100
H	0.43938600	-4.48504900	1.82928200
H	0.44752900	-2.12952300	2.55548900
C	-0.25724100	-1.65413400	-0.76038300
C	0.25724100	1.65413400	-0.76038300
C	-0.52273600	-0.57033300	-1.77051800
H	-1.51231000	-0.13528100	-1.59299900
H	-0.55643700	-1.02163800	-2.76356500
C	0.52273600	0.57033300	-1.77051800
H	0.55643700	1.02163800	-2.76356500
H	1.51231000	0.13528100	-1.59299900
H	0.00000000	0.00000000	3.83969300
H	0.00000000	0.00000000	4.58554500

E = -580.1430723, ZPE = 0.2316683

Table A47. Cartesian coordinate of TS(T-25...H₂).

Atom	X	Y	Z
C	0.01371716	4.00901453	-0.23549092
C	0.25552387	2.97331611	-1.13409792
C	-0.00041303	1.32190315	0.62605908
C	-0.24035969	2.39502442	1.52323508
C	-0.23477253	3.70908400	1.10199008
C	0.00000000	0.00000000	1.12438408
C	0.00041303	-1.32190315	0.62605908
C	-0.25552387	-2.97331611	-1.13409792
H	-0.44708340	-3.20841706	-2.17491992
C	-0.01371716	-4.00901453	-0.23549092
C	0.23477253	-3.70908400	1.10199008
C	0.24035969	-2.39502442	1.52323508
H	0.01878933	5.03607319	-0.57692492
H	0.44708340	3.20841706	-2.17491992
H	-0.43293028	2.16809099	2.56281408
H	-0.42472303	4.50275957	1.81348008
H	-0.01878933	-5.03607319	-0.57692492
H	0.42472303	-4.50275957	1.81348008
H	0.43293028	-2.16809099	2.56281408
C	-0.26141192	-1.64205718	-0.74118892
C	0.26141192	1.64205718	-0.74118892
C	-0.52799662	-0.56247172	-1.75288692
H	-1.51292572	-0.11832713	-1.57259592
H	-0.56956329	-1.01677416	-2.74417992
C	0.52799662	0.56247172	-1.75288692
H	0.56956329	1.01677416	-2.74417992
H	1.51292572	0.11832713	-1.57259592
H	0.00000000	0.00000000	2.54716208
H	0.00000000	0.00000000	3.43975208

E = -580.1314622, ZPE = 0.2312542

Table A48. Cartesian coordinate of T-25-H···H triplet radical pair (57).

Atom	X	Y	Z
C	-0.00809800	4.00561800	-0.23692400
C	0.22170200	2.96993700	-1.13813100
C	-0.00365500	1.31254300	0.61834300
C	-0.21904800	2.38813000	1.51891400
C	-0.22820200	3.70420200	1.10546000
C	0.00000000	0.00000000	1.17877700
C	0.00365500	-1.31254300	0.61834300
C	-0.22170200	-2.96993700	-1.13813100
H	-0.40216000	-3.20690400	-2.18046400
C	0.00809800	-4.00561800	-0.23692400
C	0.22820200	-3.70420200	1.10546000
C	0.21904800	-2.38813000	1.51891400
H	-0.01126100	5.03267800	-0.57851100
H	0.40216000	3.20690400	-2.18046400
H	-0.38835700	2.15652000	2.56396700
H	-0.40435600	4.49576800	1.82285500
H	0.01126100	-5.03267800	-0.57851100
H	0.40435600	-4.49576800	1.82285500
H	0.38835700	-2.15652000	2.56396700
C	-0.23455100	-1.63680500	-0.74730200
C	0.23455100	1.63680500	-0.74730200
C	-0.51582700	-0.57095400	-1.76890800
H	-1.51049400	-0.14524300	-1.59684900
H	-0.54370400	-1.03304200	-2.75730500
C	0.51582700	0.57095400	-1.76890800
H	0.54370400	1.03304200	-2.75730500
H	1.51049400	0.14524300	-1.59684900
H	0.00000000	0.00000000	2.26476500
H	0.00000000	0.00000000	4.57810500

E = -580.1432253, ZPE = 0.2328913

Table A49. Cartesian coordinate of insertion product between 8 and H₂ (54).

Atom	X	Y	Z
C	-3.65547895	0.00311308	-0.84652007
C	-2.85397195	1.00914506	-0.31705003
C	-1.27064303	-0.63205499	0.46452503
C	-2.07748504	-1.63369597	-0.06767001
C	-3.26479600	-1.32361393	-0.72257206
C	0.01689993	-0.96273004	1.17799908
C	1.28293397	-0.52466107	0.45854314
C	2.72471407	1.05523089	-0.64603279
H	2.89939311	2.06077389	-1.01369778
C	3.70812605	0.09411787	-0.81577576
C	3.48442999	-1.19471013	-0.34877177
C	2.28293295	-1.48632710	0.27776017
H	-4.57930593	0.25581711	-1.35160311
H	-3.15845291	2.04524007	-0.41331303
H	-1.77278607	-2.66931598	0.03080200
H	-3.88050601	-2.11509791	-1.13101709
H	4.63796908	0.34879684	-1.30860672
H	4.23514897	-1.96510615	-0.47168275
H	2.10686491	-2.49242209	0.64053516
C	1.50602103	0.77871493	-0.01600885
C	-1.66273698	0.70734602	0.33781702
C	0.52933606	1.94443096	0.06213912
H	0.25025812	2.21103997	-0.96312489
H	1.07556807	2.80750994	0.45496915
C	-0.76325697	1.78762799	0.87390306
H	-1.28960095	2.74420300	0.85677405
H	-0.51663602	1.59221697	1.92187607
H	0.06961389	-2.04010004	1.33660908
H	0.00032090	-0.51515704	2.17776808

E = -580.2727993, ZPE = 0.2458453

Table A50. Cartesian coordinate of S-25...H₂ complex.

Atom	X	Y	Z
C	3.97017017	0.23493448	-0.20415612
C	2.93087465	1.14882110	-0.35077772
C	1.28715677	-0.61150155	-0.01308074
C	2.37549149	-1.50756555	0.13978741
C	3.69470513	-1.10066860	0.06900986
C	0.00683621	-1.27140423	-0.03153867
C	-1.27974874	-0.63131752	-0.05825607
C	-2.95233070	1.09690390	0.29830048
H	-3.21014529	2.10600764	0.59910236
C	-3.95952631	0.23816635	-0.13587287
C	-3.65118780	-1.06149946	-0.52246932
C	-2.33737074	-1.48861386	-0.45077682
H	4.99560228	0.57289199	-0.29441630
H	3.16662143	2.19021823	-0.53871365
H	2.12040339	-2.54685291	0.29635729
H	4.49917522	-1.81362849	0.19522020
H	-4.98499673	0.58643451	-0.16287080
H	-4.43189983	-1.73741953	-0.84690422
H	-2.06774193	-2.50751820	-0.69410433
C	-1.62184870	0.69837296	0.32750716
C	1.59964657	0.76558467	-0.22909103
C	-0.56262625	1.67875089	0.74396042
H	-0.10978726	1.36696737	1.69120178
H	-1.02653968	2.65014784	0.92325984
C	0.53518205	1.82540766	-0.31514209
H	1.00974768	2.80318795	-0.21268899
H	0.07510492	1.80930047	-1.31031037
H	-0.11135969	-2.70067267	2.00948164
H	-0.13672728	-2.86529150	2.74096231

E = -580.1278955, ZPE = 0.2327655

Table A51. Cartesian coordinate of TS(S-25...H₂).

Atom	X	Y	Z
C	3.97848903	0.24212085	-0.23004708
C	2.92467306	1.12514089	-0.40073801
C	1.30832201	-0.62507607	0.07069596
C	2.40951398	-1.50345311	0.22613789
C	3.71627999	-1.08622415	0.10777087
C	0.01110799	-1.27246902	0.04586296
C	-1.30469799	-0.64816597	0.01507503
C	-2.96397793	1.10595708	0.22462515
H	-3.21517488	2.13566707	0.45141520
C	-3.97120297	0.22426413	-0.15104586
C	-3.66384402	-1.10007787	-0.44544093
C	-2.34875603	-1.52000792	-0.35693098
H	4.99795404	0.58577882	-0.35355109
H	3.13632609	2.15864390	-0.64994397
H	2.19083095	-2.54199512	0.43906785
H	4.52888097	-1.78790819	0.24637382
H	-4.99465496	0.57349917	-0.21441282
H	-4.44224205	-1.79215683	-0.73971394
H	-2.08108908	-2.54549492	-0.57663703
C	-1.63741494	0.69437902	0.31789009
C	1.59516105	0.73488893	-0.22165099
C	-0.57736889	1.68154897	0.70985911
H	-0.13086488	1.38994591	1.66620308
H	-1.03730885	2.65970798	0.86013816
C	0.52885508	1.79159998	-0.34661992
H	1.00704112	2.76925996	-0.26385189
H	0.07585805	1.75747304	-1.34419191
H	-0.02247502	-2.26885807	1.11614492
H	-0.04391799	-2.16011710	1.97029993

E = -580.1162798, ZPE = 0.2332368

Table A52. Cartesian coordinate of S-59.

Atom	X	Y	Z
C	-1.57637900	-1.39712100	0.00000000
C	-0.25304200	-1.00402100	-0.00000300
C	0.08651800	0.36669300	0.00000200
C	-0.95518100	1.31674600	-0.00000100
C	-2.28341800	0.91949700	-0.00000100
C	-2.59170100	-0.43645100	0.00000200
H	-1.83151400	-2.44925100	0.00000100
H	0.53504700	-1.74459400	-0.00000300
H	-0.68149700	2.36371600	-0.00000100
H	-3.07450300	1.65791900	-0.00000100
H	-3.62760700	-0.75313900	0.00000200
C	1.40699100	0.96591200	0.00000100
Cl	2.68690300	-0.20365700	0.00000000

E = -729.9824167, ZPE = 0.0945631

Table A53. Cartesian coordinate of T-59.

Atom	X	Y	Z
C	-1.67465200	1.37392300	0.00000000
C	-0.33651200	1.03098800	0.00000000
C	0.05399100	-0.33573500	0.00000000
C	-0.96571800	-1.32374700	0.00000000
C	-2.29648300	-0.95698400	0.00000000
C	-2.66442900	0.39026200	0.00000000
H	-1.95437100	2.42027100	0.00000000
H	0.42708600	1.79718600	0.00000000
H	-0.68349800	-2.36831200	0.00000000
H	-3.06029200	-1.72452200	0.00000000
H	-3.70974900	0.66965000	0.00000000
C	1.39621500	-0.72541800	0.00000000
Cl	2.81802100	0.14623500	0.00000000

E = -729.9747091, ZPE = 0.0941166

Table A54. Cartesian coordinate of protonated cation of 59 (59H⁺).

Atom	X	Y	Z
C	-1.65155300	-1.40656800	0.00000000
C	-0.32443300	-1.06437600	-0.00000300
C	0.04678700	0.31396900	-0.00000400
C	-0.96894000	1.32062900	0.00000000
C	-2.29382200	0.95707300	0.00000200
C	-2.63260200	-0.40060300	0.00000200
H	-1.94819700	-2.44637500	0.00000000
H	0.44273600	-1.82649200	-0.00000600
H	-0.68451200	2.36540700	0.00000000
H	-3.06955100	1.71018600	0.00000500
H	-3.67791300	-0.68457000	0.00000500
C	1.36148600	0.74931700	-0.00000700
Cl	2.71381500	-0.22042600	0.00000300
H	1.58104300	1.81244100	0.00000300

E = -730.397342, ZPE = 0.1084017

Table A55. Cartesian coordinate of S-59...H₂O.

Atom	X	Y	Z
C	-2.35112000	-1.08935600	0.02126400
C	-0.98065800	-1.23919700	0.01743800
C	-0.13665000	-0.10448200	-0.00674100
C	-0.72599000	1.18071000	-0.02693400
C	-2.10514900	1.32210700	-0.02483600
C	-2.91355200	0.19138600	-0.00044000
H	-2.99444200	-1.95966300	0.04134400
H	-0.54085000	-2.22693300	0.03478400
H	-0.07599300	2.04686500	-0.04582000
H	-2.54919500	2.30869900	-0.04054400
H	-3.99131800	0.30058500	0.00255700
C	1.30194400	-0.08324200	-0.00873000
Cl	2.04798900	-1.63688000	-0.00886600
O	2.21395200	2.70553600	0.09266000
H	2.96902700	2.92023400	-0.46291600
H	2.12239900	1.72533500	0.05391300

E = -806.4617889, ZPE = 0.1188265

Table A56. Cartesian coordinate of S-**59**...ICF₃ (**64**).

Atom	X	Y	Z
C	4.97343200	-0.46876100	0.00092800
C	3.95748200	0.46354800	0.00070000
C	2.60515700	0.04815500	-0.00015000
C	2.32298400	-1.33638600	-0.00079900
C	3.34768400	-2.26740900	-0.00062600
C	4.66945500	-1.83355300	0.00026100
H	6.00679000	-0.14709900	0.00162400
H	4.18849500	1.51970400	0.00120800
H	1.28852800	-1.65148700	-0.00143900
H	3.12137600	-3.32532300	-0.00116000
H	5.47325800	-2.55948700	0.00044900
C	1.44557000	0.89447500	-0.00036100
Cl	1.75310100	2.57870300	-0.00026100
C	-3.37387300	-0.44379000	0.00022000
F	-4.18059800	0.61169000	-0.21403500
F	-3.73693100	-0.99189800	1.17551300
F	-3.63888800	-1.35014700	-0.96032600
I	-1.23699600	0.14266500	-0.00014400

E = -1365.5822975, ZPE = 0.1091823

Table A57. Cartesian coordinate of radical pair **65** between **59** and ICF₃.

Atom	X	Y	Z
C	-4.64867100	-0.92145400	-0.00000100
C	-3.71927100	0.10071400	-0.00000100
C	-2.32698500	-0.17748500	0.00000000
C	-1.93960600	-1.54128900	0.00000100
C	-2.88213400	-2.55108400	0.00000100
C	-4.24428500	-2.25526200	0.00000000
H	-5.70328400	-0.67591600	-0.00000200
H	-4.05750200	1.12603200	-0.00000200
H	-0.89022700	-1.79839600	0.00000200
H	-2.55191000	-3.58219300	0.00000100
H	-4.97792200	-3.05062200	0.00000000
C	-1.36888900	0.87653100	0.00000000
Cl	-1.84711000	2.53019800	-0.00000100
C	3.91174200	-0.68801100	-0.00000100
F	4.77942900	0.30768700	0.00008000
F	4.01695000	-1.42261700	-1.09136800
F	4.01689600	-1.42274700	1.09128400
I	0.70888400	0.58020500	0.00000100

E = -1365.5701039, ZPE = 0.1080613

Table A58. Cartesian coordinate of C–I insertion product **66** between **59** and ICF₃.

Atom	X	Y	Z
C	-3.94266600	-0.90695700	-0.14442700
C	-3.58491000	-0.12170200	0.94138800
C	-2.27407800	0.31679500	1.09258700
C	-1.29798300	-0.02883500	0.15844400
C	-1.66742400	-0.82590300	-0.93226300
C	-2.97608000	-1.25540300	-1.08235200
H	-4.96300900	-1.24953200	-0.25930300
H	-4.32464600	0.15693800	1.68074000
H	-2.01958300	0.93214400	1.94115900
H	-0.92875300	-1.12033400	-1.66258100
H	-3.23828100	-1.87169500	-1.93254600
C	0.12916800	0.47881700	0.26882100
Cl	0.47223000	1.32220800	1.81227300
I	1.58246500	-1.19680000	0.10710500
C	0.45451500	1.49899200	-0.86293100
F	0.32410200	0.94191600	-2.07808200
F	-0.40343100	2.53094500	-0.80125700
F	1.69404700	1.99053300	-0.77491200

E = -1365.6787014, ZPE = 0.1128674

Table A59. Cartesian coordinate of S-**60**.

Atom	X	Y	Z
C	0.00000000	0.55349700	-0.00000100
C	-0.67577900	-1.62207100	0.00000200
C	0.67577900	-1.62207100	-0.00000300
H	-1.35407400	-2.45405700	0.00000500
H	1.35407400	-2.45405600	-0.00000500
N	-1.06620200	-0.28982200	0.00000300
N	1.06620200	-0.28982200	-0.00000300
C	-2.46419200	0.22138200	0.00000000
C	2.46419100	0.22138200	0.00000000
C	2.66719900	1.07311900	1.25904200
H	3.67994600	1.48058000	1.27804900
H	1.95179100	1.89363300	1.27450700
H	2.51872200	0.47028900	2.15710800
C	3.45598400	-0.94338500	-0.00002500
H	3.34555100	-1.56854600	0.88773700
H	3.34553500	-1.56852000	-0.88780400
H	4.46992400	-0.54304100	-0.00002800
C	2.66718900	1.07316500	-1.25901200
H	2.51870700	0.47036700	-2.15709800
H	1.95178000	1.89367800	-1.27444300
H	3.67993600	1.48062700	-1.27801100
C	-2.66719900	1.07312100	-1.25904100
H	-1.95179100	1.89363500	-1.27450400
H	-2.51872200	0.47029300	-2.15710700
H	-3.67994600	1.48058200	-1.27804700
C	-2.66718900	1.07316300	1.25901400
H	-3.67993600	1.48062500	1.27801300
H	-2.51870700	0.47036400	2.15709900
H	-1.95178000	1.89367600	1.27444600
C	-3.45598400	-0.94338500	0.00002400
H	-3.34553500	-1.56852100	0.88780200
H	-4.46992400	-0.54304100	0.00002600
H	-3.34555000	-1.56854500	-0.88773900

E = -540.9177816, ZPE = 0.2951841

Table A60. Cartesian coordinate of T-60.

Atom	X	Y	Z
C	-0.00861200	0.43221600	0.67710000
C	-0.71040100	-1.61519800	0.27610500
C	0.57800400	-1.53352400	-0.12152500
H	-1.32452100	-2.49469100	0.36222600
H	1.24674900	-2.34002600	-0.37216000
N	-1.18727800	-0.32405500	0.61969000
N	1.00085500	-0.20504800	-0.10071000
C	-2.40780000	0.23393400	-0.05863200
C	2.41122500	0.21257900	-0.03128700
C	3.02704300	-0.18885600	1.31984300
H	4.05924300	0.15889900	1.39214900
H	2.44930900	0.24508500	2.13646300
H	3.02266400	-1.27412500	1.43859100
C	3.18118100	-0.44102800	-1.18386500
H	3.22050500	-1.52666900	-1.08414200
H	2.71934100	-0.19906500	-2.14206700
H	4.20957700	-0.07688500	-1.19085000
C	2.44226500	1.73530600	-0.19310700
H	1.99480900	2.02980600	-1.14368400
H	1.88869500	2.21959500	0.61288700
H	3.47216300	2.09395000	-0.16623000
C	-2.11050100	0.50001600	-1.54051200
H	-1.29091600	1.21330800	-1.64190900
H	-1.82448400	-0.42410500	-2.04590600
H	-2.98875100	0.91115600	-2.04279300
C	-2.76160700	1.53753400	0.65861300
H	-3.63971000	1.99515800	0.19957400
H	-2.97270400	1.35051200	1.71260400
H	-1.93385700	2.24644300	0.59698200
C	-3.55155300	-0.76914900	0.09137800
H	-3.69543800	-1.03274800	1.14071500
H	-4.47804100	-0.33235900	-0.28439500
H	-3.36513000	-1.68248400	-0.47558900

E = -540.7880723, ZPE = 0.291386

Table A61. Cartesian coordinate of protonated cation of 60 (60H⁺).

Atom	X	Y	Z
C	0.00000000	0.45700200	0.00000000
C	-0.67984800	-1.62646100	0.00000200
C	0.67984700	-1.62646100	-0.00000200
H	-1.36371700	-2.45271900	0.00000300
H	1.36371700	-2.45271900	-0.00000300
N	-1.09114400	-0.31180200	0.00000200
N	1.09114400	-0.31180200	-0.00000200
C	-2.50823300	0.21983500	0.00000000
C	2.50823300	0.21983500	0.00000000
C	2.69211600	1.06202100	1.26627900
H	3.71416300	1.43779500	1.30297000
H	2.02472800	1.92462100	1.28166500
H	2.51417700	0.46662000	2.16235500
C	3.48028600	-0.95746500	-0.00002100
H	3.36982600	-1.57782800	0.89018800
H	3.36981300	-1.57780600	-0.89024500
H	4.49530900	-0.56318400	-0.00002300
C	2.69210700	1.06205900	-1.26625400
H	2.51416000	0.46668500	-2.16234700
H	2.02472200	1.92466200	-1.28161000
H	3.71415500	1.43783100	-1.30294200
C	-2.69211600	1.06202300	-1.26627700
H	-2.02472800	1.92462300	-1.28166300
H	-2.51417600	0.46662400	-2.16235400
H	-3.71416300	1.43779700	-1.30296800
C	-2.69210800	1.06205700	1.26625600
H	-3.71415500	1.43783000	1.30294300
H	-2.51416000	0.46668200	2.16234700
H	-2.02472200	1.92466000	1.28161300
C	-3.48028600	-0.95746500	0.00001900
H	-3.36981400	-1.57780700	0.89024200
H	-4.49530900	-0.56318400	0.00002100
H	-3.36982600	-1.57782700	-0.89019100
H	0.00000000	1.52998500	0.00000000

E = -541.3615213, ZPE = 0.3093161

Table A62. Cartesian coordinate of S-**60**···H₂O (**61**).

Atom	X	Y	Z
C	-0.00880000	0.27980000	0.08060000
C	0.57353000	-1.90735000	-0.07981900
C	-0.77554500	-1.84895300	-0.08217500
H	1.21604900	-2.76499800	-0.13656200
H	-1.49690700	-2.64260600	-0.14479400
N	-1.11109600	-0.50592400	0.02018900
N	1.02488600	-0.60071100	0.02440000
C	2.45126700	-0.15920500	0.02437200
C	3.37230300	-1.38046600	0.07757600
H	3.26223700	-2.01335700	-0.80473600
H	4.40623200	-1.03757300	0.10818800
H	3.19370500	-1.98277300	0.97029900
C	2.69530900	0.71928700	1.25731900
H	3.74410500	1.02022700	1.28925900
H	2.08231600	1.61729100	1.22023400
H	2.46513400	0.16854100	2.17145100
C	2.71599300	0.63427700	-1.26167700
H	2.09466200	1.52703600	-1.30065400
H	3.76272800	0.94232100	-1.29741600
H	2.50775200	0.01915800	-2.13945500
C	-2.51363400	-0.01534600	0.01828500
C	-2.53949500	1.49581100	0.24557400
H	-2.00663700	2.03170000	-0.53722300
H	-3.57918700	1.82757900	0.25418200
H	-2.08313000	1.75551900	1.20049100
C	-3.28170000	-0.71506800	1.14831900
H	-3.32391700	-1.79546300	1.00523700
H	-2.80897300	-0.51512800	2.11095400
H	-4.30715200	-0.34482900	1.18293000
C	-3.14037300	-0.34356700	-1.34396700
H	-4.17217400	0.00951900	-1.37682100
H	-2.58156100	0.14316000	-2.14421100
H	-3.14546000	-1.41811400	-1.53317900
O	0.47932400	3.11152500	-0.17386700
H	0.00507700	3.59793200	0.50655400
H	0.24086300	2.15378400	-0.03236100

E = -617.4021267, ZPE = 0.3198212

Table A63. Cartesian coordinate of O–H insertion product between **60** and H₂O (**62**).

Atom	X	Y	Z
C	0.00000000	0.68800800	-0.30112600
C	0.66751800	-1.43026600	-0.92768600
C	-0.66751800	-1.43026600	-0.92768600
H	1.32449200	-2.20337800	-1.28508200
H	-1.32449200	-2.20337800	-1.28508200
N	-1.15564700	-0.15784800	-0.57732100
N	1.15564800	-0.15784800	-0.57732100
C	2.37001700	-0.01507700	0.26302900
C	2.79965600	1.45661100	0.27343000
H	2.03832300	2.10251000	0.70909300
H	3.71321500	1.56694300	0.86032900
H	2.98571600	1.80828100	-0.74148700
C	3.49468200	-0.84941700	-0.36249000
H	3.29454800	-1.91945900	-0.29731700
H	3.62992100	-0.58272900	-1.41178000
H	4.42989900	-0.66006500	0.16606300
C	2.10617700	-0.50378300	1.69871800
H	3.01739800	-0.45303000	2.29764900
H	1.35016600	0.10703100	2.19539900
H	1.75430500	-1.53697400	1.68982100
C	-2.37001700	-0.01507700	0.26302900
C	-3.49468200	-0.84941700	-0.36249000
H	-3.29454800	-1.91945900	-0.29731700
H	-4.42989900	-0.66006500	0.16606300
H	-3.62992100	-0.58272900	-1.41178000
C	-2.10617700	-0.50378200	1.69871800
H	-1.75430500	-1.53697300	1.68982200
H	-1.35016600	0.10703100	2.19539900
H	-3.01739800	-0.45302900	2.29764900
C	-2.79965600	1.45661100	0.27342900
H	-2.98571600	1.80828100	-0.74148700
H	-3.71321500	1.56694300	0.86032800
H	-2.03832300	2.10251000	0.70909300
O	0.00000000	1.88110700	-1.06820700
H	0.00000200	1.61649900	-1.99751000
H	0.00000000	1.06137900	0.72704500

E = -617.4005819, ZPE = 0.3218928

Table A64. Cartesian coordinate of S-**60**...ICF₃ (**67**).

Atom	X	Y	Z
C	1.48180600	0.00019500	0.00089100
C	3.64510500	0.67524600	-0.00269400
C	3.64561800	-0.67321500	-0.00268200
H	4.47752800	1.35098600	-0.00403800
H	4.47854900	-1.34832900	-0.00401500
N	2.31884200	-1.07263100	-0.00047200
N	2.31803000	1.07366300	-0.00049300
C	1.86285600	-2.49754700	0.00021500
C	1.86098900	2.49825200	0.00021700
C	1.03928000	-2.75389500	-1.26665400
H	0.70515500	-3.79253200	-1.28575000
H	0.16350400	-2.11254500	-1.30791500
H	1.64407800	-2.56931100	-2.15637500
C	3.07481500	-3.43540500	-0.00100600
H	3.69275500	-3.30379800	-0.89058600
H	3.69494200	-3.30327200	0.88697400
H	2.71374200	-4.46353600	-0.00028000
C	1.04213200	-2.75351500	1.26900300
H	1.64894600	-2.56881800	2.15732500
H	0.16657600	-2.11196800	1.31202500
H	0.70795400	-3.79212300	1.28904200
C	1.04017100	2.75361200	1.26906100
H	0.16522700	2.11124100	1.31223100
H	1.64726400	2.56956900	2.15733100
H	0.70500900	3.79190100	1.28900800
C	3.07224900	3.43701300	-0.00108100
H	3.69023600	3.30586500	-0.89069500
H	2.71039600	4.46487000	-0.00034000
H	3.69252500	3.30535600	0.88686500
C	1.03715000	2.75401600	-1.26659700
H	0.70212900	3.79236300	-1.28556900
H	1.64208900	2.57002300	-2.15634800
H	0.16191600	2.11192800	-1.30788900
C	-3.62996500	-0.00044700	-0.00108500
F	-4.12853600	-0.21967900	1.23020300
F	-4.12603900	-0.95766800	-0.80778700
F	-4.12606800	1.17650700	-0.42781700
I	-1.42030300	-0.00063000	0.00129900

E = -1176.5202346, ZPE = 0.310223

Table A65. Cartesian coordinate of radical pair **68** between **60** and ICF₃.

Atom	X	Y	Z
C	0.86091300	0.00007400	0.21686800
C	2.98844900	0.67440900	0.42616500
C	2.98856800	-0.67388500	0.42616700
H	3.81142000	1.35611200	0.51935500
H	3.81165900	-1.35544200	0.51936100
N	1.66752300	-1.08081700	0.31574000
N	1.66733200	1.08110700	0.31573600
C	1.23988200	-2.51648900	0.31704100
C	1.23943600	2.51670300	0.31703400
C	1.32363900	-3.05658500	-1.11481600
H	1.04638000	-4.11191300	-1.12762000
H	0.65043400	-2.51170600	-1.77384800
H	2.34044000	-2.96535600	-1.50196300
C	2.18343200	-3.30922700	1.23285800
H	3.19563300	-3.37690000	0.83312500
H	2.22692400	-2.86921300	2.23028500
H	1.80666100	-4.32760000	1.32504500
C	-0.18173000	-2.62641400	0.87058800
H	-0.24114800	-2.20196500	1.87313300
H	-0.90245700	-2.11917000	0.23719600
H	-0.45735300	-3.68038900	0.92289500
C	-0.18219500	2.62637800	0.87058100
H	-0.90283200	2.11900500	0.23718900
H	-0.24153900	2.20192000	1.87312600
H	-0.45800500	3.68030400	0.92288600
C	2.18284600	3.30961200	1.23284700
H	3.19503600	3.37746200	0.83311400
H	1.80589500	4.32791900	1.32503000
H	2.22641600	2.86961000	2.23027600
C	1.32309600	3.05680900	-1.11482500
H	1.04564900	4.11208800	-1.12763300
H	2.33991300	2.96576100	-1.50197300
H	0.64998800	2.51180800	-1.77385500
C	-2.52897300	-0.00022100	1.47839500
F	-1.74302100	-0.00014600	2.55288900
F	-3.27993300	-1.09152200	1.45650600
F	-3.28005000	1.09099800	1.45644000
I	-1.06019300	-0.00010000	-1.72908300

E = -1176.4580422, ZPE = 0.308974

Table A66. Cartesian coordinate of C–I insertion product **69** between **60** and ICF₃.

Atom	X	Y	Z
C	-0.00002900	-1.08783700	-0.18840500
C	-0.67574700	-0.13533200	-2.03935600
C	0.67573900	-0.13536100	-2.03935300
H	-1.34355700	0.30246400	-2.75113300
H	1.34357100	0.30240400	-2.75112700
N	-1.10411500	-0.72002300	-0.87986300
N	1.10407500	-0.72007300	-0.87986000
C	-2.58262300	-0.64756200	-0.45234700
C	2.58258700	-0.64769700	-0.45234800
C	2.69025300	-0.40406100	1.05643100
H	3.72199800	-0.12982100	1.27396200
H	2.04794900	0.42839000	1.34965100
H	2.46299200	-1.27970000	1.65331600
C	3.28698500	-1.92514900	-0.91200900
H	2.90093300	-2.81219300	-0.41803600
H	3.18893400	-2.05373200	-1.99152900
H	4.34908200	-1.84033800	-0.67906300
C	3.20093000	0.57164400	-1.15500800
H	3.29979300	0.43174000	-2.23186000
H	2.62553500	1.47430300	-0.94102400
H	4.20810900	0.70155900	-0.76165300
C	-3.20089800	0.57181200	-1.15501000
H	-2.62545500	1.47444000	-0.94102800
H	-3.29976800	0.43190900	-2.23186200
H	-4.20807100	0.70178300	-0.76165700
C	-2.69027500	-0.40391600	1.05643200
H	-3.72200300	-0.12960600	1.27395900
H	-2.46307200	-1.27956900	1.65332000
H	-2.04792000	0.42849600	1.34965200
C	-3.28709700	-1.92497500	-0.91200100
H	-2.90109700	-2.81204000	-0.41802400
H	-4.34918900	-1.84009900	-0.67905200
H	-3.18905700	-2.05356900	-1.99152000
C	-0.00005400	-2.04945600	0.98561700
I	0.00006900	2.51958800	0.45822800
F	-1.07090600	-2.86246600	0.92700500
F	1.07075900	-2.86251800	0.92701300
F	-0.00004300	-1.45245500	2.17607600

E = -1176.552922, ZPE = 0.3150267

Table A67. Cartesian coordinate of S-58.

Atom	X	Y	Z
C	0.00000000	0.97879600	0.00000100
C	-0.67580600	-1.20886000	0.00000000
C	0.67580600	-1.20886000	0.00000000
H	-1.37658100	-2.02580100	0.00000000
H	1.37658100	-2.02580100	0.00000000
N	-1.06004100	0.12322600	0.00000000
N	1.06004100	0.12322600	0.00000000
C	2.43977200	0.56828800	0.00000000
H	2.43834700	1.65483600	0.00000000
H	2.96224600	0.20771400	0.88848600
H	2.96224500	0.20771400	-0.88848800
C	-2.43977200	0.56828800	0.00000000
H	-2.96224500	0.20771500	0.88848700
H	-2.43834700	1.65483600	-0.00000200
H	-2.96224600	0.20771300	-0.88848700

E = -304.9210804, ZPE = 0.126183

Table A68. Cartesian coordinate of S-58···H₂O.

Atom	X	Y	Z
C	0.16881000	0.36985600	0.01232100
C	-0.93746500	-1.61999000	-0.00066600
C	-1.87165500	-0.64226600	-0.00374600
H	-1.04307600	-2.69080800	-0.00620100
H	-2.94619000	-0.69788800	-0.01162300
N	0.29149300	-0.98225100	0.00940800
N	-1.17579600	0.55572500	0.00404500
C	-1.80367200	1.86376100	-0.00164900
H	-1.01746700	2.61353100	-0.01796200
H	-2.43248900	1.98317100	-0.88557500
H	-2.41578600	2.00092400	0.89161800
C	1.57159100	-1.67367000	0.00536100
H	1.66075000	-2.29759600	-0.88537200
H	2.36283200	-0.92755300	0.00366300
H	1.66392200	-2.30384700	0.89167100
O	2.83735400	1.53637600	-0.10284200
H	1.87506900	1.30581900	-0.08093700
H	3.01807000	1.92277200	0.75956400

E = -381.4027263, ZPE = 0.1507387

Table A69. Cartesian coordinate of S-58···ICF₃.

Atom	X	Y	Z
C	-1.96665700	-0.00009600	0.00040400
C	-4.13042800	-0.67475500	-0.00067000
C	-4.12961800	0.67715000	-0.00066600
H	-4.94571000	-1.37666000	-0.00107100
H	-4.94406000	1.38003100	-0.00106400
N	-2.80143500	-1.06494700	-0.00001400
N	-2.80016200	1.06575700	-0.00000600
C	-2.35358400	2.44919500	0.00013500
H	-1.26755100	2.45923400	0.00086700
H	-2.71785200	2.96452800	-0.88940500
H	-2.71907900	2.96473200	0.88905300
C	-2.35649300	-2.44890000	0.00013900
H	-2.72144500	-2.96384200	-0.88934800
H	-1.27046700	-2.46012100	0.00075200
H	-2.72247600	-2.96397300	0.88912600
I	0.75567900	-0.00090700	0.00047900
C	2.98458300	0.00009300	-0.00027300
F	3.48856200	-0.78134700	-0.97842900
F	3.48623700	1.23895000	-0.18896900
F	3.48986900	-0.45511900	1.16533200

E = -940.5254942, ZPE = 0.1409142

Table A70. Cartesian coordinate of S-70.

Atom	X	Y	Z
C	0.00000000	0.00000000	1.27175000
C	0.00000000	-0.67523100	-0.93488100
C	0.00000000	0.67523100	-0.93488100
H	0.00000000	-1.37716500	-1.74963000
H	0.00000000	1.37716500	-1.74963000
N	0.00000000	-1.04794800	0.40285800
N	0.00000000	1.04794800	0.40285800
H	0.00000000	1.99970600	0.72365500
H	0.00000000	-1.99970600	0.72365500

E = -226.268388, ZPE = 0.0712612

Table A71. Cartesian coordinate of S-70···H₂O.

Atom	X	Y	Z
C	-0.21578600	-0.70087700	0.02111800
C	1.20431200	1.09933100	0.00344200
C	1.97355000	-0.01244400	-0.01152500
H	1.47625300	2.13959700	0.00062500
H	3.04240900	-0.12833400	-0.02837700
N	-0.10499900	0.65099800	0.02425100
N	1.08702000	-1.08049300	-0.00015500
O	-2.98034500	0.03706600	-0.10045300
H	-2.22659800	-0.59401400	-0.08864200
H	-3.52579600	-0.20517600	0.65395900
H	1.36261800	-2.04639100	-0.01109900
H	-0.93273200	1.22819900	0.03026900

E = -302.7492581, ZPE = 0.0959234

Table A72. Cartesian coordinate of S-70···ICF₃.

Atom	X	Y	Z
C	-2.27841700	-0.00020400	0.00014800
C	-4.46064000	0.67598300	-0.00029500
C	-4.46101600	-0.67517800	-0.00029400
H	-5.27369100	1.37925200	-0.00045600
H	-5.27445800	-1.37799600	-0.00045200
N	-3.12549000	1.05242600	-0.00002100
N	-3.12607400	-1.05236200	-0.00001800
H	-2.79839900	-2.00309300	0.00001900
H	-2.79728200	2.00297500	0.00001300
I	0.46907500	-0.00031700	0.00034600
C	2.68788900	0.00014600	-0.00012500
F	3.18937000	-0.97676300	-0.78295300
F	3.18849800	1.16675900	-0.45532300
F	3.19068000	-0.18880300	1.23674100

E = -861.8698877, ZPE = 0.0858612

Table A73. Cartesian coordinate of T-71.

Atom	X	Y	Z
C	2.48630300	2.02129600	0.00000000
C	2.11524800	0.67558900	0.00000000
C	0.76595800	0.38757000	0.00000000
C	-0.16266400	1.48006500	0.00000000
C	1.50067100	3.01192100	0.00000000
C	-1.39408400	-0.52310200	0.00000000
C	0.00000000	-0.85840900	0.00000000
C	0.35220600	-2.19237000	0.00000000
H	1.38934600	-2.50554600	0.00000000
C	-0.68098900	-3.13105500	0.00000000
C	-2.00990900	-2.69889100	0.00000000
H	3.52989900	2.30621600	0.00000000
H	2.86292700	-0.10844700	0.00000000
H	1.78799700	4.05774900	0.00000000
H	-0.46403500	-4.19086600	0.00000000
H	-2.81335300	-3.42744600	0.00000000
C	-1.46488100	0.90050200	0.00000000
N	-2.38204400	-1.41898400	0.00000000
N	0.19062300	2.76607600	0.00000000

E = -532.3654545, ZPE = 0.1390516

Table A74. Cartesian coordinate of S-71.

Atom	X	Y	Z
C	3.02203600	1.04883400	-0.04739300
C	3.32826800	-0.31038300	-0.14944500
C	1.15008000	-0.89948600	0.02681700
C	0.73537700	0.46238700	0.05206200
C	1.69164800	1.45617700	0.07045100
H	3.82216100	1.77735700	-0.05940100
H	4.35972300	-0.62327600	-0.26874400
H	1.43341400	2.50489600	0.15431200
C	0.00000000	-1.73337300	0.33815300
C	-1.15007900	-0.89948600	0.02681500
C	-3.32826800	-0.31038300	-0.14944400
C	-3.02203600	1.04883400	-0.04739200
C	-1.69164800	1.45617700	0.07045300
C	-0.73537700	0.46238700	0.05206300
H	-4.35972300	-0.62327500	-0.26874600
H	-3.82216100	1.77735700	-0.05940100
H	-1.43341400	2.50489600	0.15431300
N	-2.42148600	-1.28628900	-0.07937000
N	2.42148600	-1.28628900	-0.07936900

E = -532.3450693, ZPE = 0.1382139

Table A75. Cartesian coordinate of S-71...NH₃.

Atom	X	Y	Z
C	3.23781000	-0.88910500	0.48606400
C	3.47923000	0.25633100	-0.27546500
C	1.26589400	0.61477200	-0.58581100
C	0.92710900	-0.57882700	0.10847500
C	1.92676000	-1.32029300	0.70118500
H	4.07264600	-1.43374400	0.90758600
H	4.49874500	0.57561600	-0.46164200
H	1.71822500	-2.20212100	1.29460500
C	0.04714400	1.36876400	-0.84963000
C	-1.01626300	0.37748500	-0.73420600
C	-3.13767900	-0.40900600	-0.66856800
C	-2.76541700	-1.48854100	0.13472100
C	-1.42918900	-1.65411700	0.50483400
C	-0.53349900	-0.72863900	0.01552200
H	-4.17207500	-0.29449000	-0.97363100
H	-3.52052800	-2.18749100	0.47011600
H	-1.12271000	-2.47640400	1.13962400
N	-2.29365900	0.54103900	-1.07699000
N	2.51730800	1.02980200	-0.78288000
N	-1.46481300	2.27373400	1.79898600
H	-2.39049300	2.19015900	1.39257300
H	-0.88006300	2.68193600	1.07492300
H	-1.52699400	2.94155800	2.55931400

E = -588.9386982, ZPE = 0.1741088

Table A76. Cartesian coordinate of T-71...NH₃.

Atom	X	Y	Z
C	-3.40641300	-0.77332500	0.00000000
C	-3.42583500	0.62398300	-0.00000100
C	-1.16605000	0.74467800	-0.00000200
C	-1.03632100	-0.68332000	0.00000300
C	-2.18451500	-1.44831500	0.00000400
H	-4.33965800	-1.32047800	-0.00000300
H	-4.37498900	1.14898000	-0.00001400
H	-2.14637900	-2.53109600	0.00001000
C	0.15544900	1.28681800	-0.00000100
C	1.11402700	0.23044500	-0.00000300
C	3.11264700	-0.83820400	-0.00000800
C	2.49950300	-2.09319300	-0.00000100
C	1.10581100	-2.18464500	0.00000600
C	0.39031700	-1.00487700	0.00000400
H	4.19440700	-0.76447800	-0.00001100
H	3.11121900	-2.98532800	0.00000000
H	0.61226200	-3.14908000	0.00001200
N	2.44618100	0.31683200	-0.00000600
N	-2.33451900	1.38949800	-0.00000600
N	1.99200700	3.52847300	0.00000800
H	1.39973000	3.58411800	0.81961600
H	2.46625800	2.62937500	0.00001700
H	1.39974600	3.58411200	-0.81961300

E = -588.9600187, ZPE = 0.1754868

Table A77. Cartesian coordinate of triplet radical pair TS(T-71...NH₃).

Atom	X	Y	Z
C	-3.25242700	-1.09269100	-0.02248400
C	-3.40409700	0.29592700	0.01170600
C	-1.16465800	0.62906100	0.03106400
C	-0.90192600	-0.77873700	-0.00290500
C	-1.97168900	-1.64919700	-0.03109700
H	-4.12972800	-1.72547300	-0.04233200
H	-4.39866700	0.72883900	0.01813100
H	-1.83163600	-2.72320000	-0.05839700
C	0.09301300	1.31368500	0.04952700
C	1.13932200	0.34113300	0.03260000
C	3.23736600	-0.51102200	0.01529100
C	2.75777700	-1.82296900	-0.01906700
C	1.38090400	-2.05994800	-0.02918400
C	0.54890500	-0.95983700	-0.00158600
H	4.30635300	-0.32807500	0.02259700
H	3.45940700	-2.64619800	-0.03828700
H	0.99115800	-3.07037100	-0.05765300
N	-2.38939900	1.16028200	0.03786200
N	2.45601700	0.56965400	0.04000300
N	1.02343200	3.65604000	0.02147800
H	0.84043100	3.88518400	-0.95839600
H	1.97751500	3.28370900	0.03394300
H	0.37987400	2.66132400	0.18180300

E = -588.9493344, ZPE = 0.1697962

Table A78. Cartesian coordinate of triplet radical pair 75 between 71 and NH₃.

Atom	X	Y	Z
C	-2.22796700	-2.28813000	0.00001000
C	-2.94556500	-1.09043500	-0.00001800
C	-1.04213900	0.14783500	-0.00002800
C	-0.22263700	-1.02186100	-0.00000200
C	-0.83077000	-2.25925400	0.00001700
H	-2.76138400	-3.22923700	0.00002700
H	-4.02984600	-1.11090600	-0.00002800
H	-0.25629100	-3.17755400	0.00004200
C	-0.20337500	1.30923700	-0.00004200
C	1.15336900	0.85361900	-0.00002100
C	3.41525100	0.96007000	-0.00000200
C	3.53301000	-0.43320300	0.00002400
C	2.38316700	-1.22634700	0.00002900
C	1.16791300	-0.57451500	0.00000600
H	4.30896900	1.57493900	-0.00000700
H	4.51583600	-0.88553300	0.00003900
H	2.45273000	-2.30736200	0.00004800
N	-2.38031000	0.11770200	-0.00003900
N	2.25406900	1.61370200	-0.00002400
N	-2.98029600	3.23238200	0.00006000
H	-0.53881100	2.33539000	-0.00005400
H	-3.94445700	3.58620700	0.00012600
H	-3.08253400	2.20545700	-0.00001500

E = -588.9740255, ZPE = 0.1723789

Table A79. Cartesian coordinate of N–H insertion product **74** between **71** and NH₃.

Atom	X	Y	Z
C	1.36202200	-0.09973300	-3.01822000
C	0.01903800	0.06524900	-3.34622100
C	-0.58035300	0.18668700	-1.17200200
C	0.74390300	0.01683900	-0.73036900
C	1.74437600	-0.12578600	-1.67969300
H	2.09579100	-0.20910900	-3.80588800
H	-0.28989200	0.08157500	-4.38552200
H	2.78201300	-0.25794500	-1.39840900
C	-1.52688500	0.33462900	0.00000000
C	-0.58035300	0.18668700	1.17200200
C	0.01903800	0.06524900	3.34622100
C	1.36202200	-0.09973300	3.01822000
C	1.74437600	-0.12578600	1.67969300
C	0.74390300	0.01683900	0.73036900
H	-0.28989200	0.08157500	4.38552200
H	2.09579100	-0.20910900	3.80588800
H	2.78201300	-0.25794500	1.39840900
N	-0.95530700	0.21303100	2.43770400
N	-0.95530700	0.21303100	-2.43770400
H	-1.92899400	1.36161900	0.00000000
N	-2.55690300	-0.69969200	0.00000000
H	-3.14036300	-0.60104800	0.82295200
H	-3.14036300	-0.60104800	-0.82295200

E = -589.0754028, ZPE = 0.1812862

Table A80. Cartesian coordinate of T-**71**⋯ND₃.

Atom	X	Y	Z
C	-3.40641100	-0.77332800	0.00000200
C	-3.42583400	0.62398100	-0.00000100
C	-1.16604900	0.74467400	-0.00000300
C	-1.03631900	-0.68332500	0.00000000
C	-2.18451400	-1.44831900	0.00000300
H	-4.33965600	-1.32048100	0.00000400
H	-4.37498800	1.14897600	-0.00000100
H	-2.14638100	-2.53110000	0.00000500
C	0.15544800	1.28681900	-0.00000500
C	1.11402500	0.23045000	-0.00000300
C	3.11264800	-0.83819700	-0.00000200
C	2.49950700	-2.09319000	0.00000100
C	1.10581600	-2.18464400	0.00000200
C	0.39032000	-1.00487600	0.00000000
H	4.19440800	-0.76447300	-0.00000300
H	3.11122700	-2.98532100	0.00000300
H	0.61226400	-3.14907800	0.00000500
N	-2.33451800	1.38949500	-0.00000300
N	2.44618200	0.31683500	-0.00000400
N	1.99199300	3.52846900	0.00000600
D	2.46625200	2.62937800	0.00000500
D	1.39973200	3.58412100	0.81962400
D	1.39973200	3.58412400	-0.81961100

E = -588.9600187, ZPE = 0.1657593

Table A81. Cartesian coordinate of triplet radical pair TS(T-71...ND₃).

Atom	X	Y	Z
C	-3.25242800	-1.09268900	-0.02249200
C	-3.40409800	0.29593000	0.01171000
C	-1.16465800	0.62906200	0.03107500
C	-0.90192700	-0.77873600	-0.00290600
C	-1.97169000	-1.64919500	-0.03110800
H	-4.12972900	-1.72547000	-0.04234700
H	-4.39866700	0.72884200	0.01813700
H	-1.83163800	-2.72319800	-0.05841700
C	0.09301300	1.31368600	0.04954600
C	1.13932100	0.34113300	0.03261400
C	3.23736500	-0.51102300	0.01529800
C	2.75777600	-1.82297000	-0.01907300
C	1.38090200	-2.05994800	-0.02919500
C	0.54890400	-0.95983600	-0.00158500
H	4.30635200	-0.32807700	0.02260700
H	3.45940500	-2.64619900	-0.03830000
H	0.99115600	-3.07037000	-0.05767500
N	-2.38939900	1.16028300	0.03787600
N	2.45601700	0.56965300	0.04001800
N	1.02344000	3.65603600	0.02145000
D	0.84042800	3.88515600	-0.95842800
D	1.97752200	3.28370200	0.03391200
D	0.37987900	2.66132600	0.18180800

E = -588.9493344, ZPE = 0.161851

Table A82. Cartesian coordinate of triplet radical pair [D]-75 between 71 and ND₃.

Atom	X	Y	Z
C	2.22802800	-2.28809000	0.00000700
C	0.83083300	-2.25923600	0.00002000
C	0.22267800	-1.02185300	0.00000400
C	1.04215700	0.14786100	-0.00002700
C	2.94560400	-1.09037800	-0.00002300
C	-1.15336800	0.85359900	-0.00002100
C	-1.16788100	-0.57453700	0.00000800
C	-2.38311900	-1.22639800	0.00003400
H	-2.45265400	-2.30741400	0.00005600
C	-3.53298000	-0.43328000	0.00002800
C	-3.41525100	0.95999600	-0.00000100
H	2.76146400	-3.22918600	0.00001900
H	0.25636700	-3.17754400	0.00004300
H	4.02988600	-1.11083300	-0.00003200
H	-4.51579700	-0.88563200	0.00004600
H	-4.30898400	1.57484300	-0.00000600
C	0.20336800	1.30924700	-0.00004500
N	-2.25408500	1.61365300	-0.00002600
N	2.38032900	0.11774500	-0.00003900
D	0.53878500	2.33540700	-0.00007400
N	2.98002200	3.23240800	-0.00000500
D	3.08261200	2.20552100	-0.00006300
D	3.94403900	3.58662100	0.00060200

E = -588.9740255, ZPE = 0.1636544

Table A83. Cartesian coordinate of N–D insertion product [D]-**74** between **71** and ND₃.

Atom	X	Y	Z
C	1.36202200	-0.09973300	-3.01822000
C	0.01903800	0.06524900	-3.34622100
C	-0.58035300	0.18668700	-1.17200200
C	0.74390300	0.01683900	-0.73036900
C	1.74437600	-0.12578600	-1.67969300
H	2.09579100	-0.20910900	-3.80588800
H	-0.28989200	0.08157500	-4.38552200
H	2.78201300	-0.25794500	-1.39840900
C	-1.52688500	0.33462900	0.00000000
C	-0.58035300	0.18668700	1.17200200
C	0.01903800	0.06524900	3.34622100
C	1.36202200	-0.09973300	3.01822000
C	1.74437600	-0.12578600	1.67969300
C	0.74390300	0.01683900	0.73036900
H	-0.28989200	0.08157500	4.38552200
H	2.09579100	-0.20910900	3.80588800
H	2.78201300	-0.25794500	1.39840900
N	-0.95530700	0.21303100	2.43770400
N	-0.95530700	0.21303100	-2.43770400
D	-1.92899400	1.36161900	0.00000000
N	-2.55690300	-0.69969200	0.00000000
D	-3.14036300	-0.60104800	0.82295200
D	-3.14036300	-0.60104800	-0.82295200

E = -589.0754028, ZPE = 0.1711543

Calculated at B3LYP/6-31+G(d) level of theory onwards**Table A84.** Cartesian coordinate of S-**77**.

Atom	X	Y	Z
C	0.10784700	0.98823600	-0.00000500
C	-0.18164600	-0.40891700	-0.00000100
C	0.90911400	-1.32299100	-0.00000600
C	2.22218400	-0.86824000	0.00000600
C	2.47358500	0.51041800	0.00000500
C	1.41944700	1.43898500	-0.00000300
H	-0.71817800	1.69468700	-0.00000500
H	0.67671200	-2.38354800	-0.00001200
H	3.04950200	-1.57203600	0.00000700
H	3.50041500	0.86822600	0.00001000
H	1.63535900	2.50377700	-0.00000800
C	-1.49532500	-0.96565100	-0.00000100
C	-2.59290300	-0.11127500	0.00000000
N	-3.61680400	0.47507300	0.00000600

E = -362.5016243, ZPE = 0.1025558

Table A85. Cartesian coordinate of protonated cation of **77** (**77H⁺**).

Atom	X	Y	Z
C	-0.12734800	-1.02788300	-0.00000100
C	0.14576000	0.38933700	0.00000100
C	-0.95153800	1.32679400	0.00000000
C	-2.24832500	0.86402300	0.00000100
C	-2.48594000	-0.52760300	0.00000000
C	-1.43076200	-1.46853300	-0.00000100
H	0.70003600	-1.73187900	-0.00000100
H	-0.73894000	2.39237400	-0.00000100
H	-3.08356500	1.55680500	0.00000300
H	-3.51204500	-0.88716800	0.00000000
H	-1.65412100	-2.53052000	-0.00000100
C	1.43846300	0.88549400	-0.00000200
C	2.60192300	0.08381300	-0.00000100
N	3.57544500	-0.55927800	0.00000200
H	1.60712600	1.96268300	-0.00000200

E = -362.8950089, ZPE = 0.1159138

Table A86. Cartesian coordinate of S-78.

Atom	X	Y	Z
C	0.84939700	-0.94803400	0.00000100
C	0.52453900	0.44684300	0.00000000
C	1.60547200	1.37863300	-0.00000100
C	2.92909900	0.95544200	-0.00000300
C	3.20752200	-0.41645100	-0.00000100
C	2.17102800	-1.36550900	0.00000200
H	0.05526700	-1.68558600	0.00000200
H	1.34837100	2.43323900	-0.00000100
H	3.74043400	1.67758300	-0.00000400
H	4.24096800	-0.75512900	-0.00000100
H	2.40972900	-2.42545500	0.00000400
C	-0.77042600	1.03961900	0.00000100
C	-1.93736000	0.09111300	-0.00000100
F	-1.95081700	-0.71770700	-1.10708100
F	-1.95083900	-0.71766600	1.10710800
F	-3.12838700	0.73153000	-0.00002600

E = -607.2981331, ZPE = 0.1082777

Table A87. Cartesian coordinate of protonated cation of 78 (78H⁺).

Atom	X	Y	Z
C	0.89139900	-0.99872500	-0.00000100
C	0.56512900	0.41336400	-0.00000200
C	1.64011100	1.38566900	-0.00000100
C	2.95072700	0.96823000	0.00000000
C	3.23241300	-0.41507700	0.00000100
C	2.20931800	-1.39097300	0.00000000
H	0.09740500	-1.73703100	-0.00000100
H	1.39240700	2.44362800	-0.00000100
H	3.76286900	1.68794100	0.00000000
H	4.26978500	-0.74128800	0.00000100
H	2.46971700	-2.44449100	0.00000100
C	-0.72308000	0.88471900	-0.00000100
C	-1.98387700	0.02615000	0.00000000
F	-2.00953300	-0.75897300	-1.09379900
F	-2.00954500	-0.75894800	1.09381700
F	-3.06686700	0.80613700	-0.00001500
H	-0.91151900	1.95715900	0.00000100

E = -607.7046774, ZPE = 0.1221426

Table A88. Cartesian coordinate of S-79.

Atom	X	Y	Z
C	0.47041300	-0.82430000	0.00000100
C	0.03937800	0.54353800	0.00000100
C	1.05757500	1.54281800	0.00000100
C	2.40515800	1.21230200	0.00000100
C	2.80528200	-0.13483500	0.00000100
C	1.81448400	-1.14376200	0.00000100
H	-0.26577000	-1.61992700	0.00000200
H	0.73296100	2.57879200	0.00000100
H	3.15970000	1.99475500	0.00000100
H	2.12275800	-2.18701400	0.00000100
C	-1.29035800	1.04115700	0.00000000
C	-2.38493300	0.01145200	0.00000000
F	-2.34236800	-0.79837900	-1.10685300
F	-2.34236800	-0.79838100	1.10685100
F	-3.62058400	0.56326700	0.00000100
C	4.26211500	-0.51349100	-0.00000200
H	4.50594200	-1.12041800	0.88134500
H	4.50594300	-1.12039800	-0.88136200
H	4.91165400	0.36637600	0.00000900

E = -646.6200739, ZPE = 0.1357181

Table A89. Cartesian coordinate of protonated cation of 79 (79H⁺).

Atom	X	Y	Z
C	0.51728800	-0.87469800	-0.00800400
C	0.08611400	0.51010000	-0.00350100
C	1.10003400	1.54645000	-0.00250100
C	2.43054600	1.22000500	-0.00696000
C	2.83949800	-0.14342500	-0.01125600
C	1.85279600	-1.17442700	-0.01242200
H	-0.22084100	-1.66893800	-0.00980900
H	0.78630800	2.58682000	-0.00033000
H	3.18582500	1.99998200	-0.00932400
H	2.17618800	-2.21122900	-0.01867100
C	-1.22807800	0.89094800	0.00130900
C	-2.42211900	-0.05392900	0.00258300
F	-2.39935200	-0.84114300	-1.09156600
F	-2.39427700	-0.84392500	1.09467800
F	-3.56030600	0.64590400	0.00609000
H	-1.49169600	1.94689200	0.00554200
C	4.28469100	-0.50029800	0.01021700
H	4.56816800	-0.77555000	1.04003000
H	4.49167100	-1.37958800	-0.60986100
H	4.92517800	0.32972800	-0.29718400

E = -647.0359354, ZPE = 0.1492815

Table A90. Cartesian coordinate of S-80.

Atom	X	Y	Z
C	0.09676000	0.09676000	0.09676000
C	-0.19368200	-0.19368200	-0.19368200
C	-0.34912500	-0.34912500	-0.34912500
C	-0.30779400	-0.30779400	-0.30779400
C	-0.04517500	-0.04517500	-0.04517500
C	0.18750700	0.18750700	0.18750700
C	-0.71634800	-0.71634800	-0.71634800
C	-0.23660100	-0.23660100	-0.23660100
C	0.99300700	0.99300700	0.99300700
C	-0.99590500	-0.99590500	-0.99590500
C	1.43094800	1.43094800	1.43094800
H	1.60194000	1.60194000	1.60194000
C	-0.58725700	-0.58725700	-0.58725700
H	-1.91030400	-1.91030400	-1.91030400
C	0.63257900	0.63257900	0.63257900
H	2.38087500	2.38087500	2.38087500
H	-1.19151700	-1.19151700	-1.19151700
H	0.97116900	0.97116900	0.97116900
F	0.02243100	0.02243100	0.02243100
F	0.47264000	0.47264000	0.47264000
F	0.28992400	0.28992400	0.28992400
F	-0.28897200	-0.28897200	-0.28897200
F	-0.64109400	-0.64109400	-0.64109400

E = -997.4832919, ZPE = 0.1434549

Table A91. Cartesian coordinate of protonated cation of 80 (80H⁺).

Atom	X	Y	Z
C	3.01473500	-0.38612100	0.03531700
C	2.01042500	-1.35236000	-0.13177700
C	0.68353800	-0.96269900	-0.18392100
C	0.29093100	0.40327100	-0.08043100
C	1.35745200	1.34806400	0.04966800
C	2.68700400	0.97315600	0.12665700
C	-1.02518000	0.93702400	-0.19291300
C	-2.32163600	0.40300700	-0.04270100
C	-2.64936500	-0.84815200	0.56968700
C	-3.39451800	1.24707100	-0.48588400
C	-3.97035400	-1.23352100	0.69370600
H	-1.87129700	-1.48149100	0.97289500
C	-4.71022500	0.83483800	-0.38520100
H	-3.16002500	2.21397200	-0.92294000
C	-4.99904600	-0.40652800	0.20393900
H	-4.21710500	-2.17455300	1.17499500
H	-5.51348200	1.47038400	-0.74384600
H	-6.03296100	-0.72724700	0.29909600
F	1.06643200	2.64418100	0.13627100
F	3.64514300	1.87691100	0.28087700
F	4.27347000	-0.76109000	0.09684400
F	2.34515800	-2.63037400	-0.25685000
F	-0.22237300	-1.91199400	-0.41284300
H	-1.01816600	1.99793000	-0.43576700

E = -997.9109046, ZPE = 0.1583794

Table A92. Cartesian coordinate of S-**81**.

Atom	X	Y	Z
C	3.68341700	1.12165800	0.83651200
C	2.48920500	1.68169600	1.29499700
C	1.26796300	1.08644900	0.98419500
C	1.21055400	-0.13859600	0.25995700
C	2.43565700	-0.73178900	-0.14349100
C	3.62823800	-0.07089200	0.10544600
H	4.64328600	1.58015600	1.04290000
H	2.51695900	2.59822500	1.87748200
H	0.34444200	1.53613200	1.33638800
H	2.42618900	-1.68831000	-0.65221000
C	-0.00000200	-0.86192800	-0.00001200
C	-1.21055500	-0.13859100	-0.25998200
C	-1.26797100	1.08645800	-0.98421000
C	-2.43565300	-0.73179200	0.14347100
C	-2.48921700	1.68170900	-1.29499000
H	-0.34445400	1.53614500	-1.33640900
C	-3.62823800	-0.07089300	-0.10544300
H	-2.42617200	-1.68832200	0.65217300
C	-3.68342300	1.12166600	-0.83649400
H	-2.51698100	2.59824100	-1.87746800
H	-4.64329300	1.58017000	-1.04286500
N	-4.89356300	-0.67234200	0.36768700
N	4.89356900	-0.67233500	-0.36767700
O	4.82404100	-1.71282500	-1.01929900
O	5.94074200	-0.09032900	-0.08239800
O	-5.94074100	-0.09033100	0.08243200
O	-4.82402500	-1.71284300	1.01929000

E = -910.3313613, ZPE = 0.1893704

Table A93. Cartesian coordinate of protonated cation of **81** (**81H⁺**).

Atom	X	Y	Z
C	3.91519700	1.20492700	0.38439400
C	2.82473300	2.04923000	0.64906100
C	1.52850600	1.57377600	0.53545400
C	1.28561000	0.21988800	0.15280900
C	2.40075800	-0.64231900	-0.05765900
C	3.67867600	-0.12817500	0.03795700
H	4.93749800	1.56008100	0.46515500
H	3.00505500	3.07318300	0.96008800
H	0.70126300	2.22088600	0.80219100
H	2.26429500	-1.68723100	-0.31745700
C	0.00000000	-0.36282400	0.00001100
C	-1.28561000	0.21988700	-0.15279500
C	-1.52850300	1.57377400	-0.53544500
C	-2.40075900	-0.64231900	0.05766800
C	-2.82472900	2.04922900	-0.64906200
H	-0.70125700	2.22088500	-0.80217500
C	-3.67867600	-0.12817400	-0.03795900
H	-2.26430000	-1.68723000	0.31747100
C	-3.91519500	1.20492600	-0.38440200
H	-3.00504700	3.07318100	-0.96009300
H	-4.93749500	1.56008000	-0.46517200
N	-4.83488700	-1.02878800	0.21482300
N	4.83488500	-1.02879000	-0.21483100
O	4.57547700	-2.19184200	-0.50471400
O	5.95106300	-0.53495700	-0.11359200
O	-5.95106500	-0.53495700	0.11356400
O	-4.57548100	-2.19183700	0.50472200
H	0.00000000	-1.45300200	0.00001600

E = -910.7475711, ZPE = 0.2035798

Table A94. Cartesian coordinate of S-82.

Atom	X	Y	Z
C	0.00000000	3.03999100	1.33984100
C	0.00000000	1.67371800	1.68516000
C	0.00000000	0.74079500	0.66346900
C	0.00000000	1.13879300	-0.70845600
C	0.00000000	2.48772900	-1.04789200
C	0.00000000	3.42221100	0.00067100
C	0.00000000	-1.13879300	-0.70845600
C	0.00000000	-0.74079500	0.66346900
C	0.00000000	-1.67371800	1.68516000
H	0.00000000	-1.38663600	2.73318200
C	0.00000000	-3.03999100	1.33984100
C	0.00000000	-3.42221100	0.00067100
C	0.00000000	-2.48772900	-1.04789200
H	0.00000000	3.80702900	2.10593200
H	0.00000000	1.38663600	2.73318200
H	0.00000000	2.80835000	-2.08347300
H	0.00000000	-3.80702900	2.10593200
H	0.00000000	-2.80835000	-2.08347300
C	0.00000000	0.00000000	-1.64551900
N	0.00000000	-4.86137800	-0.32214400
O	0.00000000	-5.17546900	-1.51165200
O	0.00000000	-5.65927700	0.61654800
N	0.00000000	4.86137800	-0.32214400
O	0.00000000	5.17546900	-1.51165200
O	0.00000000	5.65927700	0.61654800

E = -909.1236482, ZPE = 0.1672886

Table A95. Cartesian coordinate of T-82.

Atom	X	Y	Z
C	0.00000000	3.03009200	1.34040700
C	0.00000000	1.66564600	1.64950500
C	0.00000000	0.73285700	0.61632200
C	0.00000000	1.17607100	-0.75625100
C	0.00000000	2.53939100	-1.06788100
C	0.00000000	3.43716800	-0.00180300
C	0.00000000	-1.17607100	-0.75625100
C	0.00000000	-0.73285700	0.61632200
C	0.00000000	-1.66564600	1.64950500
H	0.00000000	-1.35140000	2.68970100
C	0.00000000	-3.03009200	1.34040700
C	0.00000000	-3.43716800	-0.00180300
C	0.00000000	-2.53939100	-1.06788100
H	0.00000000	3.78167200	2.12037400
H	0.00000000	1.35140000	2.68970100
H	0.00000000	2.89943500	-2.08970900
H	0.00000000	-3.78167200	2.12037400
H	0.00000000	-2.89943500	-2.08970900
C	0.00000000	0.00000000	-1.55472800
N	0.00000000	-4.88057500	-0.29945900
O	0.00000000	-5.22120100	-1.48325400
O	0.00000000	-5.66200500	0.65303400
N	0.00000000	4.88057500	-0.29945900
O	0.00000000	5.66200500	0.65303400
O	0.00000000	5.22120100	-1.48325400

E = -909.1342925, ZPE = 0.1677794

Table A96. Cartesian coordinate of protonated cation of **82** (**82H⁺**).

Atom	X	Y	Z
C	0.00000000	3.05492900	1.34893200
C	0.00000000	1.67972400	1.70729500
C	0.00000000	0.74343300	0.69999100
C	0.00000000	1.15982600	-0.67409900
C	0.00000000	2.51429100	-1.03382600
C	0.00000000	3.44106000	0.01175900
C	0.00000000	-1.15982600	-0.67409900
C	0.00000000	-0.74343300	0.69999100
C	0.00000000	-1.67972400	1.70729500
H	0.00000000	-1.40505600	2.75756300
C	0.00000000	-3.05492900	1.34893200
C	0.00000000	-3.44106000	0.01175900
C	0.00000000	-2.51429100	-1.03382600
H	0.00000000	3.82412600	2.11481800
H	0.00000000	1.40505600	2.75756300
H	0.00000000	2.85278400	-2.06515800
H	0.00000000	-3.82412600	2.11481800
H	0.00000000	-2.85278400	-2.06515800
C	0.00000000	0.00000000	-1.49571500
N	0.00000000	-4.88848400	-0.32036800
O	0.00000000	-5.17655900	-1.51273600
O	0.00000000	-5.67396800	0.61943700
N	0.00000000	4.88848400	-0.32036800
O	0.00000000	5.17655900	-1.51273600
O	0.00000000	5.67396800	0.61943700
H	0.00000000	0.00000000	-2.58284800

E = -909.5357822, ZPE = 0.1806435

Table A97. Cartesian coordinate of **S-89**.

Atom	X	Y	Z
C	1.08884600	3.14562800	0.00000000
C	-0.09595300	2.38387000	0.00000000
C	0.00000000	1.00276600	0.00000000
C	1.28052700	0.36936700	0.00000000
C	2.45446000	1.10946900	0.00000000
C	2.32653300	2.50773400	0.00000000
C	-0.29548200	-1.35093700	0.00000000
C	-1.00828800	-0.07862800	0.00000000
C	-2.37189900	-0.08739300	0.00000000
H	-2.97163400	0.81848700	0.00000000
C	-3.02949400	-1.36731500	0.00000000
C	-2.29886700	-2.53964400	0.00000000
C	-0.88203000	-2.66191800	0.00000000
H	1.05434900	4.22898300	0.00000000
H	-1.05737400	2.88893200	0.00000000
H	3.43762200	0.65244800	0.00000000
H	-4.11457600	-1.40473300	0.00000000
C	1.06541800	-1.07039300	0.00000000
N	-3.11775400	-3.80795200	0.00000000
O	-2.52621700	-4.87661900	0.00000000
O	-4.34944100	-3.68607500	0.00000000
N	3.55001000	3.32921300	0.00000000
O	4.62962200	2.73697400	0.00000000
O	3.41841600	4.55305700	0.00000000
H	1.84414600	-1.82727800	0.00000000

E = -909.1024623, ZPE = 0.1657889

Table A98. Cartesian coordinate of T-89.

Atom	X	Y	Z
C	0.98866000	3.14418100	0.00000000
C	-0.15211700	2.33341900	0.00000000
C	0.00000000	0.94975700	0.00000000
C	1.30830800	0.35948400	0.00000000
C	2.45007300	1.16942800	0.00000000
C	2.25898500	2.55050400	0.00000000
C	-0.21711700	-1.37728600	0.00000000
C	-0.97481200	-0.14064600	0.00000000
C	-2.36663600	-0.15572100	0.00000000
H	-2.93341900	0.77104700	0.00000000
C	-3.05206400	-1.37907300	0.00000000
C	-2.32265400	-2.58070700	0.00000000
C	-0.94499500	-2.55095500	0.00000000
H	0.90953800	4.22449700	0.00000000
H	-1.13637900	2.79323200	0.00000000
H	3.45330700	0.75900000	0.00000000
H	-4.13598500	-1.42317000	0.00000000
C	1.17529100	-1.06740800	0.00000000
N	-3.01844100	-3.87136200	0.00000000
O	-2.31747800	-4.88388000	0.00000000
O	-4.25025300	-3.86266100	0.00000000
N	3.44513500	3.42467100	0.00000000
O	4.55348500	2.88635500	0.00000000
O	3.26004200	4.64270400	0.00000000
H	1.98418300	-1.78777700	0.00000000

E = -909.1354334, ZPE = 0.1669618

Table A99. Cartesian coordinate of S-90.

Atom	X	Y	Z
C	-3.22590400	-1.22118500	0.00000000
C	-2.41023900	-0.00555500	0.00000000
C	-1.04567500	-0.03470900	0.00000000
C	-0.34775700	-1.30953900	0.00000000
C	-1.08711100	-2.52928900	0.00000000
C	-2.46050600	-2.41584700	0.00000000
C	1.26255900	0.35230700	0.00000000
C	0.00000000	1.01686900	0.00000000
C	-0.06276200	2.39915800	0.00000000
H	-1.01262300	2.92509300	0.00000000
C	1.14087600	3.13134700	0.00000000
C	2.36186800	2.46206000	0.00000000
C	2.45555400	1.06122400	0.00000000
H	-2.93251700	0.95150700	0.00000000
H	-0.58726500	-3.49367300	0.00000000
H	1.13326900	4.21517800	0.00000000
H	3.42771500	0.58128200	0.00000000
C	1.01380800	-1.08374400	0.00000000
N	3.60685400	3.25099100	0.00000000
O	4.67049400	2.62983800	0.00000000
O	3.50817600	4.47749900	0.00000000
N	-3.20836900	-3.73121900	0.00000000
O	-2.52222800	-4.76213100	0.00000000
O	-4.42820700	-3.70904900	0.00000000
H	1.78788300	-1.84562000	0.00000000

E = -909.094036, ZPE = 0.1696269

Table A100. Cartesian coordinate of T-90.

Atom	X	Y	Z
C	-3.03314000	-1.28470900	0.00000000
C	-2.40243100	-0.05702100	0.00000000
C	-1.00408100	-0.09346100	0.00000000
C	-0.29849700	-1.35142400	0.00000000
C	-0.99653500	-2.56979400	0.00000000
C	-2.39146300	-2.51423500	0.00000000
C	1.28821100	0.33659100	0.00000000
C	0.00000000	0.96979000	0.00000000
C	-0.10778700	2.35719600	0.00000000
H	-1.07668600	2.84874200	0.00000000
C	1.05865100	3.13071600	0.00000000
C	2.30899000	2.49584300	0.00000000
C	2.45526400	1.10909000	0.00000000
H	-2.96014600	0.87586800	0.00000000
H	-0.49418800	-3.53211500	0.00000000
H	1.01478400	4.21300900	0.00000000
H	3.44489900	0.66678600	0.00000000
C	1.10334200	-1.08473200	0.00000000
N	3.52293800	3.33072200	0.00000000
O	4.61327200	2.75649400	0.00000000
O	3.37797900	4.55417500	0.00000000
N	-3.18710700	-3.74434400	0.00000000
O	-2.58607900	-4.81986000	0.00000000
O	-4.41204100	-3.61732700	0.00000000
H	1.89232600	-1.82790300	0.00000000

E = -909.1354922, ZPE = 0.1668426

Table A101. Cartesian coordinate of S-91.

Atom	X	Y	Z
C	-0.69420800	-0.11191700	-0.04178600
C	-1.43529200	1.11279500	-0.21662900
C	-2.85052700	1.06202900	-0.10176500
C	-3.49138500	-0.16216500	0.01681100
C	-2.77772600	-1.35690200	0.14547200
C	-1.38473700	-1.31663200	0.14278600
C	0.76686600	-0.10216800	-0.00020300
C	1.62253200	-1.14350100	-0.34213800
C	2.86807800	-1.21010500	-0.37691900
C	3.66569700	-0.15194500	0.02079300
C	2.95847600	0.99096900	0.43840300
C	1.55544100	1.00876000	0.43478000
H	-3.41478700	1.98513300	-0.15437200
H	-3.31276200	-2.29099700	0.27158900
H	-0.82486200	-2.23669000	0.28719200
H	3.51592900	1.86072400	0.77055700
H	1.04817300	1.88499600	0.83433900
N	5.13348200	-0.18951100	0.00941100
O	5.66066200	-1.23006100	-0.37560700
O	5.72862800	0.82131900	0.38674900
C	-0.92282200	2.39671600	-0.57685700
N	-4.96756200	-0.20379200	0.06503600
O	-5.49780600	-1.30584600	0.20662100
O	-5.57086000	0.86186100	-0.04054400
H	-0.02048000	2.27618500	-1.20468500

E = -908.9702449, ZPE = 0.1626601

Table A102. Cartesian coordinate of T-91.

Atom	X	Y	Z
C	-0.69806900	-0.02269200	-0.07725400
C	-1.49066100	1.17119800	-0.29101100
C	-2.91330400	1.04926700	-0.19890800
C	-3.49318300	-0.18083700	0.03145300
C	-2.73685000	-1.35259600	0.17760800
C	-1.35034400	-1.24886200	0.11747500
C	0.77127800	-0.01005500	-0.05305100
C	1.61051100	-1.03184500	-0.47803100
C	2.85396700	-1.14977900	-0.49443300
C	3.67378700	-0.15962600	0.01471300
C	2.98871000	0.96362600	0.52242800
C	1.58992400	1.02968900	0.48994000
H	-3.53544700	1.92535400	-0.33559100
H	-3.22950500	-2.30210200	0.34550000
H	-0.74731300	-2.14250700	0.25415100
H	3.56435000	1.77909000	0.94819500
H	1.10162200	1.89310800	0.93305400
N	5.13688900	-0.24187200	0.03446700
O	5.64738700	-1.26221000	-0.42221400
O	5.75250900	0.71610000	0.50905800
C	-0.96890000	2.40994600	-0.63990300
N	-4.96675400	-0.26771200	0.11247700
O	-5.45812500	-1.38115100	0.29611200
O	-5.61079200	0.77376100	-0.00707800
H	-0.01368000	2.83755000	-0.90709600

E = -908.9826439, ZPE = 0.1623414

Table A103. Cartesian coordinate of protonated cation of 91 (**91H⁺**).

Atom	X	Y	Z
C	0.65872700	-0.09943200	0.15412900
C	1.46548200	1.11348800	0.30313400
C	2.89771900	1.03994300	0.11878900
C	3.48396900	-0.18241900	-0.04465900
C	2.72117100	-1.37221600	-0.05420000
C	1.33347400	-1.32287100	0.04916200
C	-0.79424400	-0.07168500	0.08923000
C	-1.63088200	-1.10716900	0.51466200
C	-2.87686300	-1.12637600	0.49518100
C	-3.68023700	-0.14860100	-0.05049800
C	-2.96376900	0.94788900	-0.57042500
C	-1.56527600	0.98375900	-0.50676500
H	3.50582700	1.93807500	0.16572100
H	3.23638500	-2.32075400	-0.17420000
H	0.76109400	-2.24328200	-0.01392500
H	-3.51990400	1.76019300	-1.02931900
H	-1.05047100	1.81157500	-0.98728200
N	-5.15404900	-0.21298600	-0.09290500
O	-5.66202300	-1.21876900	0.38673200
O	-5.73346100	0.74223800	-0.60112800
C	0.95345200	2.27540300	0.82103000
N	4.96038500	-0.26943900	-0.20334600
O	5.42698700	-1.39133200	-0.35700900
O	5.57976500	0.78648200	-0.16929500
H	-0.06932900	2.35264000	1.17678100
H	1.58556400	3.15129400	0.94895500

E = -909.380425, ZPE = 0.1770506

Table A104. Cartesian coordinate of S-8.

Atom	X	Y	Z
C	1.11288900	-3.04952700	0.00000000
C	1.46882000	-1.67994900	0.00000000
C	0.45424000	-0.74258300	0.00000000
C	-0.91698900	-1.14007300	0.00000000
C	-1.24982700	-2.49401300	0.00000000
C	-0.22116300	-3.45501500	0.00000000
C	-0.91697600	1.14009100	0.00000000
C	0.45424000	0.74256400	0.00000000
C	1.46882000	1.67991600	0.00000000
H	2.51812800	1.39330800	0.00000000
C	1.11291200	3.04950600	0.00000000
C	-0.22113200	3.45503000	0.00000000
C	-1.24979700	2.49404000	0.00000000
H	1.90012100	-3.79966500	0.00000000
H	2.51812400	-1.39333000	0.00000000
H	-2.29615600	-2.78823700	0.00000000
H	-0.46317700	-4.51425200	0.00000000
H	1.90015700	3.79962900	0.00000000
H	-0.46313500	4.51426800	0.00000000
H	-2.29612300	2.78827700	0.00000000
C	-1.84902600	0.00001400	0.00000000

E = -500.1094175, ZPE = 0.163074

Table A105. Cartesian coordinate of T-8.

Atom	X	Y	Z
C	1.13107700	-3.03822600	0.00000000
C	1.44793300	-1.66968500	0.00000000
C	0.41904800	-0.73583000	0.00000000
C	-0.95120800	-1.18005500	0.00000000
C	-1.25463500	-2.54943800	0.00000000
C	-0.20421600	-3.47057100	0.00000000
C	-0.95120800	1.18005600	0.00000000
C	0.41904800	0.73583000	0.00000000
C	1.44793300	1.66968500	0.00000000
H	2.48854300	1.35290300	0.00000000
C	1.13107700	3.03822600	0.00000000
C	-0.20421600	3.47057100	0.00000000
C	-1.25463500	2.54943800	0.00000000
H	1.93253600	-3.77222500	0.00000000
H	2.48854300	-1.35290300	0.00000000
H	-2.28828400	-2.88447800	0.00000000
H	-0.42297700	-4.53505300	0.00000000
H	1.93253600	3.77222500	0.00000000
H	-0.42297700	4.53505300	0.00000000
H	-2.28828400	2.88447800	0.00000000
C	-1.74593800	0.00000000	0.00000000

E = -500.1153525, ZPE = 0.1631732

Table A106. Cartesian coordinate of protonated cation of **8** (**8H⁺** or **40**).

Atom	X	Y	Z
C	1.12702600	-3.05971100	0.00000000
C	1.49394100	-1.68372900	0.00000000
C	0.49161500	-0.74448000	0.00000000
C	-0.88038000	-1.16143200	0.00000000
C	-1.23414700	-2.52092800	0.00000000
C	-0.20642200	-3.47318200	0.00000000
C	-0.88038000	1.16143200	0.00000000
C	0.49161400	0.74448000	0.00000000
C	1.49394100	1.68372900	0.00000000
H	2.54445200	1.40842700	0.00000000
C	1.12702600	3.05971100	0.00000000
C	-0.20642200	3.47318200	0.00000000
C	-1.23414700	2.52092800	0.00000000
H	1.91429700	-3.80846000	0.00000000
H	2.54445200	-1.40842800	0.00000000
H	-2.27678000	-2.82693900	0.00000000
H	-0.44487000	-4.53166100	0.00000000
H	1.91429700	3.80846000	0.00000000
H	-0.44487000	4.53166100	0.00000000
H	-2.27678000	2.82693900	0.00000000
C	-1.69808600	0.00000000	0.00000000
H	-2.78528200	-0.00000100	0.00000000

E = -500.554007, ZPE = 0.1769359
